CHARGED PION EMISSION FROM ^{112}SN + ^{124}SN AND ^{124}SN + ^{112}SN REACTIONS WITH THE SπRIT TIME PROJECTION CHAMBER

By

Jonathan Elijah Barney

A DISSERTATION

Submitted to
Michigan State University
in partial fulfillment of the requirements
for the degree of

Physics — Doctor of Philosophy

2019

ABSTRACT

CHARGED PION EMISSION FROM ^{112}SN + ^{124}SN AND ^{124}SN + ^{112}SN REACTIONS WITH THE SπRIT TIME PROJECTION CHAMBER

By

Jonathan Elijah Barney

Heavy ion collisions provide a probe of nuclear matter in extreme conditions. A particular area of interest is the density dependence of the symmetry energy term of the nuclear equation of state. The symmetry energy term describes the difference in binding energy between pure neutron matter and symmetric nuclear matter, which has an equal number of protons and neutrons. The density dependence of the symmetry energy affects the structure of neutron stars, which reach densities far exceeding what can be observed in the laboratory. The emission of charged pions from heavy ion collisions is expected to be sensitive to the symmetry energy at densities which are typically not otherwise observed in the laboratory.

An experimental campaign to measure charged pion production was performed with the new SπRIT Time Projection Chamber, used in the SAMURAI spectrometer at RIKEN. The campaign included four secondary beams, produced from two primary beams. This work focuses on the measurement of pion emission from ^{124}Sn + ^{112}Sn and ^{112}Sn + ^{124}Sn systems, probing a single point of asymmetry at two center of mass energy points. This work serves to validate analysis methods, and to provide comparisons between the two experiments

The development of the SπRIT Time Projection Chamber is discussed in detail, from design considerations to construction methods. Upgrades performed after the experimental campaign are also described. The entire experimental setup is described, with position measurements discussed and tabulated.

The analysis of beam data from the BigRIPS fragment separator is described in detail,

providing the beam PID, momentum, and angle on target. The absolute cross section is determined and a basic filter of impact parameter is implemented.

We determine the pion spectra for ^{124}Sn + ^{112}Sn and ^{112}Sn + ^{124}Sn systems, comparing them to inform the range of pion kinetic energy which are consistently reconstructed for both systems. This informs the study of more asymmetric systems, where the pion ratio is expected to differ.

Dedicated in loving memory of:
Timothy Whitney Barney (1959-2016)
Nicholas Alexander Roosa (1989-2012)

ACKNOWLEDGMENTS

This body of work has been made possible because of many people, whose efforts I wish to acknowledge. This work began for me in November 2010, when Kim Crosslan suggested that I should join the research group of Professor Bill Lynch.

Professor Bill Lynch has been an excellent advisor, not only because of his vast knowledge and experience, but the patient approach he has had while mentoring me. From Bill, I've learned that sometimes the most important questions are the most simple. Neither Bill nor I could have predicted all the challenges that I encountered during my time in graduate school, but Bill has always listened and understood when I was operating at less than full capacity.

Professor ManYee Betty Tsang has also been closely involved with my advising and work. I'm very grateful to Betty for her experience in planning, record keeping, and facilitating communication within a collaboration. Many of the positive experiences and opportunities I had in graduate school were due to the recommendation or help of Betty.

I would like to thank the rest of my guidance committee: Pawel Danielewicz, Edward Brown, and Stuart Tessmer. Thank you for your time, expertise, thoughtful comments, and for looking out for my best interests.

It has been my pleasure to know and work with Justin Estee for the entirety of my time at MSU. We have shared failure and success, we have argued and agreed, but in all cases he has improved the quality of my time here. He is a stalwart researcher, and a loyal friend. Juan Manfredi made graduate school more enjoyable, and was a good travel companion. Also, Juan, you are welcome for the cat. Thank you for taking such good care of him. One of the greatest strengths of the HiRA group is how much help we give each other: I am grateful to all the HiRA students and postdocs that I have had the pleasure to know and work with, thank you for your help in my projects, and for teaching me while I helped in your endeavors.

I would like to thank my friends and family for supporting me on this journey. I'm truly blessed to have my siblings: Deborah, Daniel, Elizabeth, Hannah, Mary, and Sarah. Thanks to Korey Hurni for always having an open ear, and Jonathan Mayers for motivation. Thanks to Tommy Lee for teaching me it's alright to make mistakes on the way.

Many individuals have joined the SπRIT collaboration, but from the beginning, the leadership and vision of William G. Lynch (MSU), ManYee Betty Tsang (MSU), Tetsuya Murakami (Kyoto University), Sherry Yennello (TAMU), and Tadaaki Isobe (RIKEN) enabled the construction of the SπRIT Time Projection Chamber and the successful experimental campaign in which it was used. Alan McIntosh (TAMU) and Rebecca Shane (MSU) not only made the detector design and construction possible, they made it happen as Postdocs: through careful planning, long days, and weekly international conference calls. Justin Estee (MSU) and Suwat Tangwancharoen (MSU, KMUTT) shared responsibilities with myself for designing and constructing the SπRIT TPC, and we were joined for the assembly by William Powell (University of Liverpool), who also suggested the name for the SπRIT TPC. Rensheng Wang (THU, MSU) joined for the testing of the TPC, producing the first observation of cosmics in the TPC. We were assisted by many undergraduate students, whose efforts were invaluable. In particular, Corinne Anderson and Hananiel Setiawan were integral for the TPC project.

We had a great deal of help from many staff members at the MSU. In particular, I wish to thank John Yurkon, Jay Pline, John Puro, John Santana, Susan LeCureux, Ralph Witgen, Brian Drewyor, Barbara Pollock and Ben Shuart for their help and contributions to the project. Tom Palazzolo, Tom Hudson, Jim Muns, and Rob Bennett in the MSU Department of Physics and Astronomy machine shop helped with many design improvements, and taught me a great deal about machining. Jayne True and Bethany Hannon helped immensely with organizing all the travel required during this project, thank you!

Mizuki Kurata-Nishimura (RIKEN) coordinated efforts from the arrival of the TPC at RIKEN through the successful experimental campaign, and was a driving force behind the analysis of the experimental data. The software used for the data analysis (SπRITROOT) was developed by Genie Jhang (Korea University, MSU), JungWoo Lee (Korea University) and Giordano Cerizza (MSU). Masanori Kaneko (Kyoto University) was the graduate student responsible for the development of the Multiplicity Trigger Array used with the TPC, and has been a major driving force of the analysis efforts. Jerzy Łukasik (INP), Piotr Pawłowski (INP), Krzysztof Pelczar (JU), and Paweł Lasko (JU, INP) developed the KATANA trigger and veto array used with the TPC, as well as the trigger box used during the experiment. Yan Zhang (fmr. THU) and Zhigang Xiao (THU) designed and produced the Active Veto Array used with the TPC. Clementine Santamaria (MSU, LBNL) joined as a Postdoc and helped run the commissioning and experiments, afterwards doing a great deal of the beam analysis. She also taught me how to use ANAROOT and perform the beam analysis.

I would like to express my appreciation to Hideaki Otsu (RIKEN), project manager for the SAMURAI spectrometer, for helping us bring the SπRIT and SAMURAI together successfully. I also express my gratitude to the BigRIPS team for providing the rare isotope beams. I also am grateful to Hiroyoshi Sakurai (RIKEN) for hosting me as a student trainee for the EAPSI summer program. The RIBF secretaries, Yu Naya and Asako Takahashi helped so much for all the paperwork and training necessary for all our visits to RIKEN.

The TPC data analysis required a great deal of work, especially from Genie Jhang, Jung-

Woo Lee, Giordano Cerizza, Mizuki Kurata-Nishimura, Tadaaki Isobe, Masanori Kaneko, Chun Yuen Tommy Tsang (MSU), Rensheng Wang, and Justin Estee. The process involved developing physics analysis, in parallel testing and improving the reconstruction software. This required excellent communication between group members, and a lot of hard work.

Below, I list names of individuals who have contributed to the SπRIT project. This list cannot be entirely inclusive, so I express my gratitude to everyone who has helped along the way.

Michigan State University (MSU), USA

- William G. Lynch (Co-PI and Spokesperson)
- Manyee Betty Tsang (PI and Spokesperson)
- Rebecca Shane (Postdoc, 2011 – 2014)
- Giordano Cerizza (Postdoc, 2015 – 2017)
- Genie Jhang (Postdoc, 2016 –)
- Rensheng Wang (Visiting Scholar)
- Jonathan Barney (Undergraduate student, 2011 – 2013, Graduate student, 2013 – 2019)
- Justin Estee (Undergraduate student, 2011 – 2014, Graduate student, 2014 –)
- Suwat Tangwancharoen (Graduate student, 2011 – 2016)
- Chun Yuen Tommy Tsang (Graduate student, 2016 –)
- Zbigniew Chajecki (Postdoc)

- Clementine Santamaria (Postdoc, 2015 – 2017)
- John Yurkon (Staff)

Kyoto University, Japan

- Tetsuya Murakami (Japanese PI and Spokesperson)
- Masanori Kaneko (Graduate student 2014 –)

RIBF, RIKEN, Japan

- Hidetada Baba (Staff)
- Tadaaki Isobe (Spokesperson)
- Mizuki Kurata-Nishimura (Staff)
- Hiroyoshi Sakurai (Staff)
- Daisuki Suzuki (Staff)

Texas A&M University (TAMU), USA

- Sherry J. Yennello (Co-PI)
- Bob Olsen (Staff)
- Alan B. McIntosh (Postdoc 2010 – 2013, Assistant Research Scientist)

Korea University, South Korea

- Byungsik Hong (Faculty)
- Genie Jhang (Graduate student, 2013 – 2016)

- JungWoo Lee (Graduate student, 2014 –)

Institute of Nuclear Physics (INP), Poland

- Jerzy Łukasik (Staff)
- Piotr Pawłowski (Staff)
- Paweł Lasko (Graduate Student)

Jagiellonian University (JU), Poland

- Krzysztof Pelczar (Staff)

Tsinghua University (THU), China

- Zhigang Xiao (Faculty)
- Yan Zhang (Ph.D. 2017)

Additionally, I wish to thank members of the NeuLAND Collaboration:

Technische Universität Darmstadt, Germany

- Heiko Scheit (Senior Scientist)
- Leyla Atar (Postdoc)
- Dominic Rossi (Postdoc)
- Hans Törnquist (Postdoc)
- Andrea Horvat (Doctoral Researcher)

GSI Helmholtz Centre for Heavy Ion Research, Germany

- Thomas Aumann (Faculty)
- Konstanze Boretzky (Senior Scientist)
- Yvonne Leifels (Senior Scientist)

Ruđer Bošković Institute, Croatia

- Igor Gašparić (Research Associate)

Computing resources for analysis in this work were provided by the HOKUSAI-GreatWave at RIKEN, the High Performance Computing Center (HPCC) at MSU, and the NSCL computing cluster.

Finally, I want to thank the funding sources which have made this possible: this work was supported by the U.S. DOE under Grant Nos. DE-SC0014530, DE-NA0002923, US NSF Grant No. PHY-1565546, and the Japanese MEXT KAKENHI grant No. 24105004. The NSF EAPSI fellowship supported my travel and research at RIKEN for the summer of 2014 (NSF award 1414979).

TABLE OF CONTENTS

LIST OF TABLES

LIST OF FIGURES

Chapter 1

Introduction

A fundamentally useful property of physical laws is that they are universal: the laws of physics are the same on Earth as they are in the cosmos. Discoveries made in the cosmos increase our understanding of the pale blue dot we occupy, and measurements in Earth-based laboratories can shed light on the stars. To learn more about the processes which occur in stars, we turn to nuclear physics. Nuclear physics is the study of the nucleus of an atom, the basic building block of all matter. By studying the physics of these tiny systems, we gain information about the entire universe, from nuclear processes on Earth to the nuclear processes occurring in astrophysical environments.

Every atom consists of three types of particles: protons, neutrons, and electrons. The protons and neutrons are localized at the core of the atom, comprising the nucleus of the atom. The electrons, which weigh almost 2,000 times less than a proton or neutron, form a cloud around the nucleus which extends many times beyond the size of the nucleus: typically, an atom has a radius about 10,000 times larger than the radius of its nucleus. Nuclear physics focuses on studying the nucleus of an atom: the protons and neutrons which are bound together by the strong nuclear force. The number of protons is fixed for a given chemical element, but the number of neutrons can vary, resulting in the existence of different isotopes of the same element. One isotope of an element may be radioactive, while another is stable. The chart of the nuclides, shown in Figure 1.1, depicts isotopes as a function of proton number (along the Y-axis) and neutron number (along the X-axis). Stable isotopes are shown in black, and radioactive isotopes are shown with color corresponding to half life.

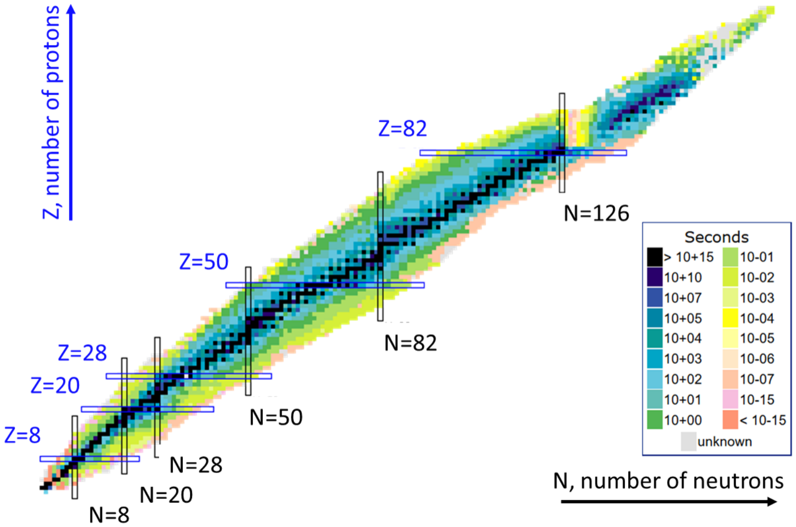

Figure 1.1: The chart of nuclides, with proton number (Z) on the Y-axis, and neutron number (N) on the X-axis. Stable isotopes are shown in black, and unstable isotopes with color corresponding to lifetime. Figure modified from [1]. For interpretation of the references to color in this and all other figures, the reader is referred to the electronic version of this thesis.

The stability of a nucleus depends on its binding energy BE: the amount of energy required to dissociate the nucleus. If we model the nucleus as an incompressible drop of nuclear matter [13], the binding energy can be approximated using the Bethe-Weizsäcker liquid drop model, a semi-empirical formula which gives the binding energy as a function of the number of protons Z, neutrons N, and mass $A = N + Z$:

$$BE = a_V A - a_S A^{2/3} - a_C \frac{Z^2}{A^{1/3}} - a_A \frac{(N-Z)^2}{A} + \mathcal{O}. \tag{1.1}$$

The first coefficient a_V is the volume term: the nuclear interactions between nuclei are attractive, binding the drop together. The energy contribution from volume scales linearly with A. The surface term a_S is a correction to the volume term, necessary since nucleons at the surface of the drop interact with fewer neighbors than those inside the nucleus, reducing the attractive interactions and thus the binding energy. The Coulomb term a_C accounts for the repulsive effect of the Coulomb force, scaling with Z^2 to account for proton charge, and divided by $A^{1/3}$ to account for the radius of the drop, providing a scale for the distance between protons. The asymmetry term a_A is necessary to describe the decrease in binding energy that occurs due to asymmetry in the number of protons and neutrons. Baryons in the drop cannot occupy the same quantum states, as required by the Pauli exclusion principle. However, a neutron and a proton in a nucleus can occupy the same spatial and spin states, as they have different isospin projections (+1/2 and -1/2, respectively). An imbalance of nucleon types causes one nucleon type in excess to occupy higher single particle energy levels than the deficient nucleon type, resulting in a reduced binding energy than for a nucleus with symmetric proton and neutron numbers. Additionally, the strong nuclear force interactions prefer symmetric ($N = Z$) systems, leading to reduced binding energy for asymmetric systems. This energy difference is modeled with the asymmetry term a_A. Other terms such as pairing ($\mathcal{O}$) can be added to refine this model, but for our purposes, it is sufficient to only discuss up to the asymmetry term.

If we extend our liquid drop to a macroscopic nuclear system (such as a neutron star), we can consider the limit where $A \to \infty$. The surface term becomes negligible, and we can neglect long-range Coulomb forces (in systems such as a neutron star, the Coulomb forces are screened by the presence of mobile electrons), giving binding energy per nucleon

$$\frac{BE}{A} = a_V - a_A\delta^2, \tag{1.2}$$

with δ as the asymmetry: $\delta = (N - Z)/A$. For a symmetric system, BE/A is described by only the volume term a_V, while for pure neutron matter, $BE/A = a_V - a_A$. To describe astrophysical systems that exist at a range of densities, we must move beyond the liquid drop model, since its modeling of a macroscopic system as an incompressible fluid at normal nuclear density is not valid. For example, the gravitational force of a neutron star compresses the nuclear matter to extreme limits of much higher nucleon densities, requiring an Equation of State (EoS) to describe properties of nuclear matter over a range of densities. An equation of state relates an important property of a system, such as its energy/nucleon, to state variables, such as pressure, temperature, and asymmetry. For large nuclear systems, the asymmetry can be described in terms of the neutron and proton densities,

$$\delta = \frac{\rho_n - \rho_p}{\rho}. \tag{1.3}$$

As a starting point, we use the insights learned from the liquid drop model to form a nuclear EoS:

$$E(\rho, \delta) = E(\rho, \delta = 0) + S(\rho) \cdot \delta^2, \tag{1.4}$$

with separable contributions from symmetric matter ($E(\rho, \delta = 0)$) and asymmetric matter ($S(\rho) \cdot \delta^2$). The term $S(\rho)$ is the symmetry energy: the difference between the EoS for pure neutron matter ($\delta = 1$) and symmetric nuclear matter ($\delta = 0$). From such an equation of state, the pressure can be calculated,

$$P(\rho) = -E(\rho)/V, \tag{1.5}$$

at zero temperature, for a fixed number of particles. By modeling the thermal properties of nuclei, one can extrapolate to non-zero temperatures. Determination of the pressure-density relationship is necessary to model the structure of a neutron star where the nuclear matter is in hydrostatic equilibrium.

1.1 Density Dependence of the Symmetry Energy Term

The nuclear saturation density ρ_0 is defined to be the density which minimizes the binding energy per nucleon, and is experimentally determined as $\rho_0 = 0.16\ \mathrm{fm}^{-1/3}$. For densities at or below saturation density, the symmetry energy can be determined using information about bound nuclei and by studying nuclear collisions. Much work has been done to constrain the symmetry energy around the saturation density, but the value of symmetry energy for higher densities must also be constrained. In particular, the value of the symmetry energy at twice saturation density ($2\rho_0$) is crucial for determining the structure of neutron stars. The symmetry energy density dependence is often parametrized by defining the quantity

$$x \equiv \frac{\rho - \rho_0}{3\rho_0} \tag{1.6}$$

and performing a Taylor expansion around the symmetry energy at saturation density:

$$S(\rho) = J + Lx + \frac{1}{2}K_{\mathrm{sym}}x^2 + \frac{1}{6}Q_{\mathrm{sym}}x^3 + \ldots\ , \tag{1.7}$$

with $J = S(\rho_0)$, and L, K_{sym}, and Q_{sym} the slope, curvature, and third derivative of the symmetry energy at saturation density. This form can be very useful for investigations around saturation density, as well as for making comparisons to symmetric nuclear matter [14]. An alternative formalism is to describe the behavior as a power law, as in Reference [2]:

$$S(\rho) = S_{\text{kin}} \left(\frac{\rho}{\rho_0} \right)^{2/3} + S_{\text{int}} \left(\frac{\rho}{\rho_0} \right)^{\gamma}, \tag{1.8}$$

which has the advantage of using a single tunable parameter γ to describe the density dependence of the symmetry energy. The term $S_{\text{kin}} \approx 12.3$ MeV is the kinetic term, and $S_{\text{int}} \approx 20$ MeV the interaction term. Figure 1.2 shows the symmetry energy dependence using this formalism for three values of γ. A value of $\gamma = 1$ would indicate a nearly linear dependence on density. Within this work, a value of γ above 1 will be referred to as “stiff", and a value below 1 will be referred to as “soft".

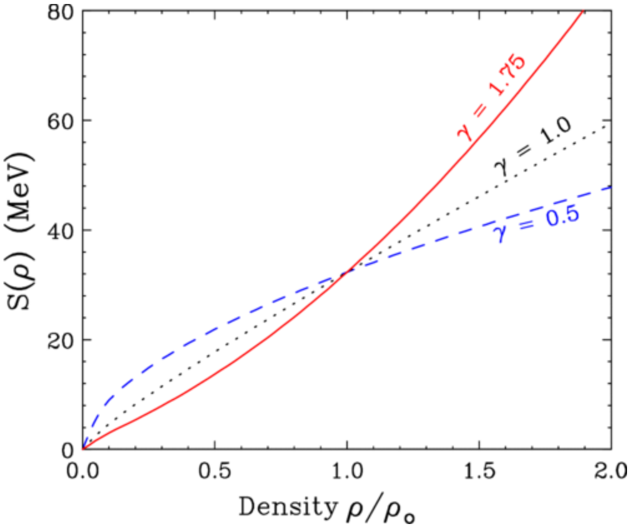

Figure 1.2: Parameterizations for density dependence of symmetry energy, for three values of γ. Figure from [2].

To study the symmetry energy at around twice saturation density, we turn to Heavy-Ion Collisions (HIC), which enable us to produce short-lived, high-density regions of nuclear matter. By employing Rare-Isotope (RI) beams, we can probe systems with a range of asymmetry. In the past, HIC have been successfully used to study the symmetry energy, using probes such as the neutron/proton ratio emitted from HIC [15], isospin diffusion [16], electric dipole polarizability and the ^{208}Pb neutron skin [17], and transverse flow [18]. The fundamental challenge that must be faced when using HIC to constrain the symmetry energy at higher density is to separate high density and low density effects.

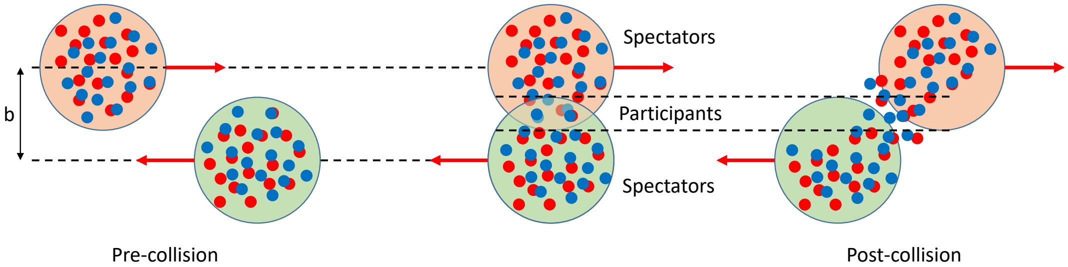

Figure 1.3: Cartoon graphic showing impact parameter b, and classification of spectator and participant nucleons.

In HIC, the relative centrality of a collision has a large effect on the reaction dynamics. Centrality is described by the impact parameter b, the transverse distance between the centers of a target nucleus and an approaching beam nucleus. The most central region of the collision will achieve the highest density, and models indicate that the density can reach $2\rho_0$ [19]. Nucleons in the most central region are referred to as participant nucleons, and nucleons outside this region are referred to as spectator nucleons. Figure 1.3 shows a cartoon representation of participant and spectator nucleons. Particles emitted from the central region of the collision can provide information about the symmetry energy at $2\rho_0$, but particles will also be produced from lower density regions. To specifically study symmetry energy effects, it is necessary to select a probe which will preferably be produced in the high-density region. One such probe is pions [20, 21, 22], which are predominately produced in the early stages of the reaction, when the high density matter is produced (as shown in Figure 1.4), which shows maximum density achieved in a pBUU simulation (discussed in Section 1.3) of a ^{124}Sn + ^{112}Sn reaction, with a central collision ($b = 3$ fm).

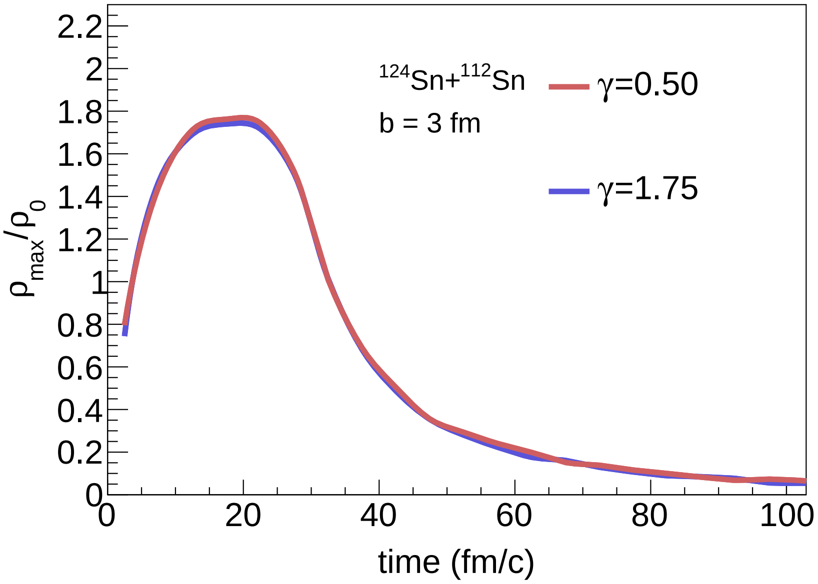

Figure 1.4: Maximum density achieved in collision as function of time, simulated for two values of γ.

1.2 Pion Production and the Symmetry Energy

Within a heavy ion collision, pions can be produced through nucleon-nucleon scatterings, or through the decay of Δ resonances. If our beam energy is below or slightly above the pion production threshold ($\sim$ 300MeV/u), most pion production will be due to the decay of Δ resonances [19]. There are four distinct Δ resonances: Δ^{++}, Δ^{+}, Δ^{0}, and Δ^{-}. These Δ resonances are produced by nucleon-nucleon interactions in the high density region of the HIC, where the collective motion of nuclei provides the energy required to form the Δ resonances. The type of Δ resonance (++, +, 0, -) produced depends on the nucleons involved in the production. The relative probabilities for a specific nucleon-nucleon interaction (p-p, n-p, n-n) to produce a Δ can be determined using conservation laws and Clebsch-Gordan coefficients (see Appendix A for derivation):

$$\begin{aligned}
p+p &\rightarrow \sqrt{\frac{3}{4}}\left(\Delta^{++}+n\right)-\sqrt{\frac{1}{4}}\left(\Delta^{+}+p\right) \\
n+p &\rightarrow \sqrt{\frac{1}{2}}\left(\Delta^{+}+n\right)-\sqrt{\frac{1}{2}}\left(\Delta^{0}+p\right) \\
n+n &\rightarrow \sqrt{\frac{1}{4}}\left(\Delta^{0}+n\right)-\sqrt{\frac{3}{4}}\left(\Delta^{-}+p\right).
\end{aligned} \tag{1.9}$$

Using the decay modes of Δs, we can determine the relative probabilities of different pions being produced, for a specific nucleon-nucleon interaction,

$$\begin{aligned}
p+p &\rightarrow \sqrt{\frac{5}{6}}\left(\pi^{+}+p+n\right)-\sqrt{\frac{1}{6}}(\pi^{0}+p+p) \\
n+p &\rightarrow \sqrt{\frac{1}{6}}(\pi^{+}+n+n)+\sqrt{\frac{2}{3}}(\pi^{0}+n+p)+\sqrt{\frac{1}{6}}(\pi^{-}+p+p) \\
n+n &\rightarrow \sqrt{\frac{1}{6}}(\pi^{0}+n+n)-\sqrt{\frac{5}{6}}\left(\pi^{-}+n+p\right).
\end{aligned} \tag{1.10}$$

From this, we can see that the production of π^- will largely depend on *n*-*n* collisions in the high density region, while π^+ production will largely depend on *p*-*p* collisions. The production of π^- and π^+ is equally likely for *n*-*p* collisions. It follows that the relative production of π^- and π^+ should depend on the relative numbers of neutrons and protons in the high density region.

The symmetry energy will affect the relative number of protons and neutrons in the high density region. A large symmetry energy (i.e., stiff) will favor symmetry in the number of protons and neutrons, and will compete with the Coulomb force which affects only the expulsion of protons from the high density region. A small symmetry energy (i.e., soft) will lead to comparatively fewer protons in the high density region. Therefore the relative numbers of π^- and π^+ produced should provide an indication of the relative numbers of neutrons and protons present in the high density region, and thereby provide a measure of the symmetry energy. This qualitative argument must be modeled to account for reaction dynamics and differences in the π^- and π^+ production. The symmetry energy directly affects the relative quantities and expulsion of protons and neutrons within the high density region, but inferring the symmetry energy at $2\rho_0$ from expelled protons and neutrons is difficult, most notably because neutrons and protons are emitted from all regions of the reaction, regardless of density. Measurements of n-p spectra will therefore be affected by the symmetry energy at a range of densities.

1.3 Measuring Pion Multiplicities, and the Proposed Experiment

Measuring charged pions requires a magnetic field to separate positive and negative charge. To measure a range of asymmetry (δ), large isotopes are preferable. Many charged particles are produced in the HIC, and we must be able to resolve the momenta and Particle Identification (PID) of these particles to distinguish pions, especially positive pions, from other charged particles. To determine the kinetic energy of the particles in the reaction center-of-momentum frame, the angle of emission must be determined in addition to the momenta and PID. The measurement of protons, deuterons, tritons, ^{3}He and ^{4}He can be used for complimentary measurements of the symmetry energy, and provide necessary systematic information.

The use of a Time Projection Chamber (TPC) suits the desired measurement perfectly. A TPC, used in conjunction with a magnetic field, is able to distinguish between positively and negatively charged particles. A TPC covers a large solid angle, and can be used to distinguish individual tracks in a high multiplicity collision. Since the experiment will be performed at sub-threshold energies, theory predicts that the pion production will be a relatively rare process compared to light charged particles such as hydrogen and helium isotopes [2], so it is important to maximize the detection efficiency of pions. The EOS TPC [23] has previously been employed to measure charged pion spectra for ∼1 GeV/A Au + Au collisions [24], thus demonstrating the feasibility of using a TPC for such measurements.

For the purpose of constraining the symmetry energy, a new TPC, called the SπRIT (SAMURAI Pion-Reconstruction and Ion-Tracker) TPC [3], a joint project between Texas A&M University and Michigan State University, was constructed at the National Superconducting Cyclotron Laboratory (NSCL) and used in an experimental campaign at the Radioactive Isotope Beam Factory (RIBF) at the RIKEN Nishina Center for Accelerator-Based Science in Wako, Japan. Two primary beams (^{124}Xe and ^{238}U) were used to produce four beams (^{108}Sn, ^{112}Sn, ^{124}Sn, and ^{132}Sn) which were impinged on two isotopic targets (^{112}Sn and ^{124}Sn), to probe a large range of asymmetry. Additionally, two beams were produced consisting of low-charge particles (Z ranging from 1 to 3) for momentum calibrations. The beam-target systems used is listed in Table 1.1.

Primary Beam		Secondary Beam		
Isotope	Energy (AMeV)	Desired Isotope	Target Isotope	Energy at mid target (MeV/u)
^{238}U	345	^{132}Sn	^{124}Sn	∼270
^{238}U	345	^{124}Sn	^{112}Sn	∼270
^{124}Xe	345	^{112}Sn	^{124}Sn	∼270
^{124}Xe	345	^{108}Sn	^{112}Sn	∼270

Table 1.1: Beams used in the SπRIT TPC experimental campaign

This dissertation will focus on the pion measurement from the ^{124}Sn+^{112}Sn system and the ^{112}Sn+^{124}Sn system, providing initial results from the SπRIT TPC campaign and demonstrating the capabilities of the TPC. The heavy ion collisions are modeled with a transport code, which predicts the pion production for given parameterizations of the symmetry energy [19, 2]. In this dissertation, a preliminary comparison of our data to the predictions of one transport model (pBUU) by Pawel Danielewicz [25, 26], which uses the Boltzmann-Uehling-Uhlenbeck equation, is performed. There has been ongoing efforts to compare to a suite of transport codes [27], which may be used in the future to interpret pion production spectra, and thereby constrain the symmetry energy.

1.4 Organization of Dissertation

This dissertation begins with a description of the design and construction of the SπRIT TPC in Chapter 2. The TPC shipping process is also detailed in Chapter 2, along with a description of upgrades that were performed to the TPC after the experimental campaign. The experimental setup is described in Chapter 3, including the position measurement of the setup. A description of ancillary detectors and the experimental trigger is included in Chapter 3. Analysis of the beam and TPC data is presented in Chapter 4. The beam analysis involves beam particle identification and trajectory reconstruction. The absolute cross section is determined using scaler information, TPC information, and the beam information. An overview of the TPC analysis software is presented, with details on the pion extraction and analysis. A summary is provided in Chapter 5, along with an outlook for future work.

Chapter 2

Development of the SπRIT Time Projection Chamber

The SAMURAI pion Reconstruction and Ion Tracking Time Projection Chamber (SπRIT TPC) [3] was designed to detect pions and other light charged particles, observables which are sensitive to the symmetry energy. The operation principle is shown in Figure 2.1, with the field cage and pad plane illustrated, although not to scale. The SπRIT TPC was designed to be placed inside the magnet gap of the SAMURAI Spectrometer [28], which provides the indicated magnetic field. The field cage produces a uniform electric field anti-parallel to the magnetic field, and is filled with P10 gas (90%Argon, 10%CH_4) at just above atmospheric pressure. A Rare-Isotope (RI) beam is impinges on a fixed target at the entrance of the field cage. When a beam nucleus collides with a target nucleus, neutrons and charged particles are released. As the charged particles pass through the field cage, they ionize the P10 gas, creating electron-ion pairs. The positive ions drift downwards towards the cathode plate, while the electrons drift upwards towards the ground wire plane, located 8 mm below the pad plane. The electrons are multiplied between the ground plane and the anode wire plane, which is located 4 mm below the pad plane. The high voltage potential between these two wire planes accelerates the drift electrons, giving them sufficient energy to liberate additional electrons from the gas. The additional liberated electrons will also be accelerated, liberating

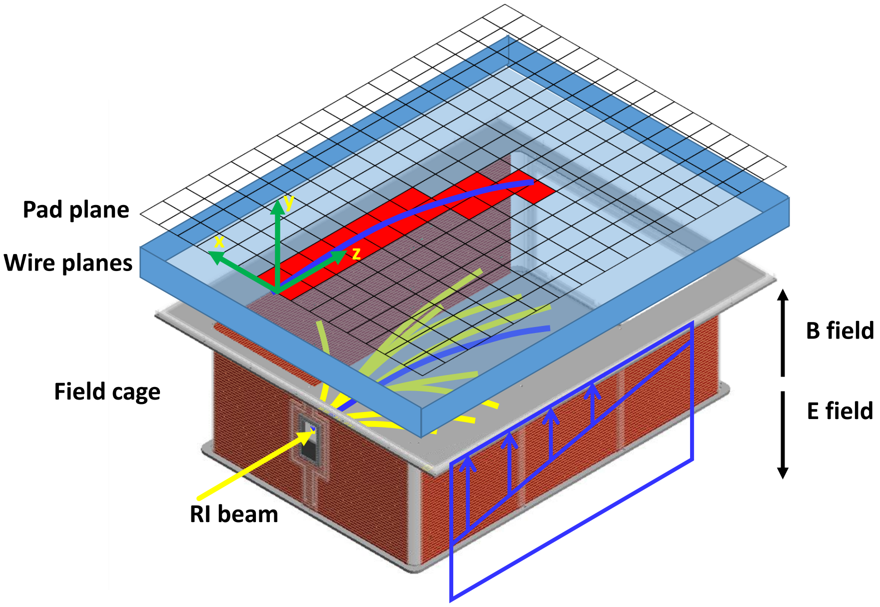

Figure 2.1: Operation principle of the SπRIT TPC, modified from [3].

further electrons. This chain effect causes an avalanche of electrons; therefore, the region between the ground and anode wire planes is referred to as the avalanche region. The electrons terminate on the anode plane, but the motion of the positive ions produced in the avalanche region induces an image charge on the pad plane, creating a signal large enough to be amplified and digitized by readout electronics.

The highly-segmented pad plane allows determination of the trajectory of a particle in the x-z plane, while the third dimension, y, is inferred from the relative timing of induced signals. The anti-parallel electric field, in combination with the encompassing magnetic field, causes the electrons to drift in tight spirals along the field lines, mitigating diffusion that would otherwise occur. A combination of magnetic rigidity ($B\rho$) and energy loss (dE/dx) provides the necessary information to determine particle identification, along with momenta of the charged particles created in the RI collision. The magnetic field separates the charged particles by magnetic rigidity, while the energy loss per unit length is determined from the amount of charge liberated beneath a pad. This chapter describes the design and construction of the SπRIT TPC. It should be noted that this chapter shares overlap with Reference [7], which was written before the first experimental run of the SπRIT TPC.

2.1 General Design Considerations

To achieve the desired physics results, the TPC must be able to resolve light charged particles in reactions which can include projectile-like fragments and intermediate mass fragment particles in high multiplicity [29]. To this end, the design was based on the EOS TPC [23]. To take advantage of the 2 m pole face of the SAMURAI spectrometer, the SπRIT TPC has a large pad plane (1344 mm by 864 mm). Structural bolt covers within the pole gap of SAMURAI reduce the available pole gap to 75 cm (of 80 cm maximum). The pad plane is read out by front-end electronics, which must be mounted as close as possible to the pad plane to avoid signal loss and noise pickup. The combination of readout electronics and available pole gap limits the drift length of the field cage to 50.49 cm.

The SπRIT TPC was designed to study central, heavy-ion collisions at around $E = 300$ MeV/u, which result in a high multiplicity of produced particles. The particle identification and momentum measurement for pions, hydrogen isotopes, and helium isotopes are necessary for the physics goals. Specific goals focused on within this work are measuring charged-pion spectra and ratios, as well as determining multiplicity cross sections. As discussed in Chapter 1, the pion ratio measured with different beam/target systems is expected to provide constraints of the density dependence of the symmetry energy. Measurements of multiplicity cross sections provide impact parameter constraints, which is important for comparison to theory.

Typically, a larger pad plane size is required for a larger range of momentum acceptance, while a smaller individual pad size allows a finer resolution of higher momentum values. The total number of pads is limited by channel cost, and a small pad size requires high density electronics for readout. The design of the pad plane had to optimize the momentum measurement over a range of momentum acceptance, without using a cost-prohibitive number of channels. Additionally, the pad plane should fit inside the region of uniform magnetic field of the SAMURAI spectrometer.

To safely operate within the SAMURAI magnet at 0.5T, all parts had to be made of non-magnetic materials. Many stainless steel parts and screws can be used, but must be checked for magnetism. Type 316 stainless steel, which contains a small amount of molybdenum, is typically non-magnetic, but can become magnetic when the metal is worked. To avoid using any magnetic electrical components, we avoided components which were nickel coated or had iron pins. Each component used was checked for magnetism using a rare-earth magnet.

An additional consideration made for materials used was to avoid introducing impurities in the field cage gas. Oxygen and halogenides have a relatively large electron affinity, and thus can absorb drift electrons, which do not typically have enough energy to form negative ions with noble gases or most organic compounds [30]. Materials were specifically chosen to be halogen free, to avoid introducing such impurities.

2.2 Design Overview

An exploded view of the SπRIT TPC is shown in Figure 2.2. The pad plane and wire planes are mounted to the top plate, which is kept flat with ribs. The field cage seals against the top plate, forming a gas tight detection volume. Clean P10 gas enters the field cage through an inlet at the bottom of the field cage, and exits the field cage through an outlet on the top,

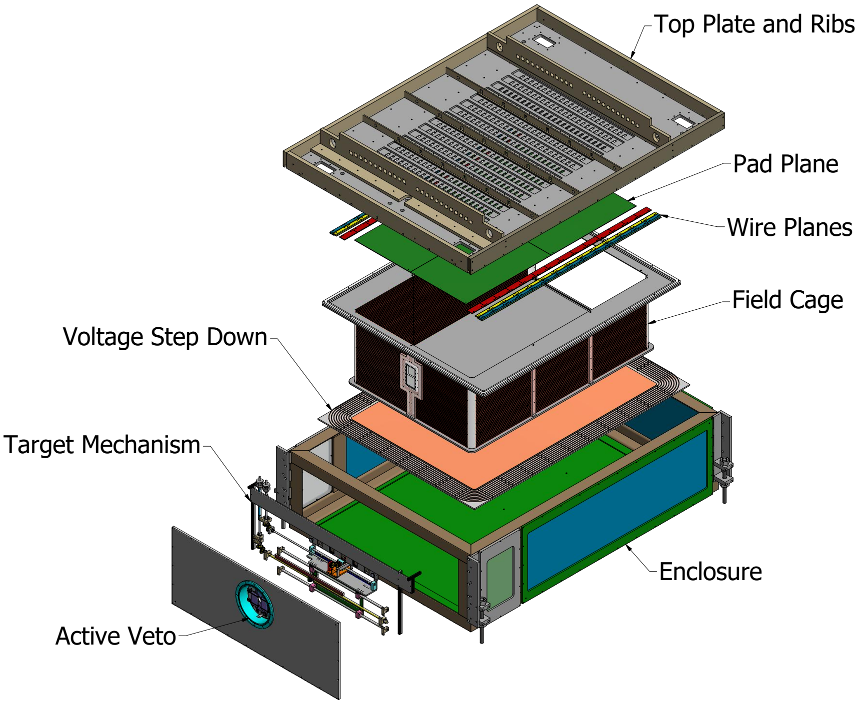

Figure 2.2: SπRIT exploded view.

flowing through the rest of the enclosure volume, and exiting via a bubbler. The voltage step down bridges the electric potential between the field cage cathode and the ground potential of the enclosure. These parts, along with the target mechanism, are housed within the enclosure. An entrance window is mounted on the front flange of the TPC, allowing RI beams to enter the enclosure.

2.3 GET Electronics

For the pad plane readout, the Generic Electronics for TPC (GET) system is employed [31]. This section draws heavily from References [31] and [5]. The Application-Specific Integrated Circuit (ASIC) and Analog-to-Digital Converter (ADC) board, or AsAd board, is used to amplify, shape, and digitize the signals from pads. Each AsAd board has 4 ASIC for GET (AGET) chips, which amplify and shape the signals from 64 input pads. A schematic diagram

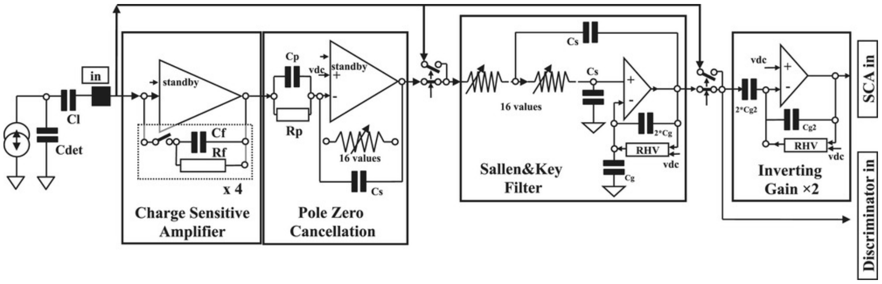

Figure 2.3: Schematic of AGET function, from [4].

of the AGET function is shown in Figure 2.3. Each of the 64 shaper outputs is sampled and stored on a 512-cell switched capacitor array, which provides a circular buffer for the analog signal. Upon receiving a trigger, these sampled signals are sent sequentially to a four channel ADC on the AsAd board, with one channel handling signals from one AGET chip. A single AsAd board therefore handles up to 256 input signals, with each input signal containing as many as 512 samples of the signal induced on the corresponding TPC pad. The sampling frequency is adjustable from 1 MHz to 100 MHz, allowing a time range from 512 µs to 5.12 µs to be sampled. Each of the 512 cells of the switched capacitor array store the amplified and shaped charge signal for its pad during the time corresponding to the sampling frequency, forming a granular “timebucket" with associated signal height. In addition to the input signals, each AGET has 4 Fixed Pattern Noise (FPN) channels, which can be used to determine noise levels. There is also a discriminator for each input signal that can be used for partial readout of pads with data above the threshold values. As the channel occupancy rates for the TPC are high, this feature was not used. Instead, all channels are written to disk on every event.

The digitized data from the AsAd boards are concentrated by Concentration Boards (CoBo). Each CoBo can handle signals from 4 AsAd boards, for a total of 1024 input signals. These CoBo boards send the concentrated data to a DAQ server, which writes the

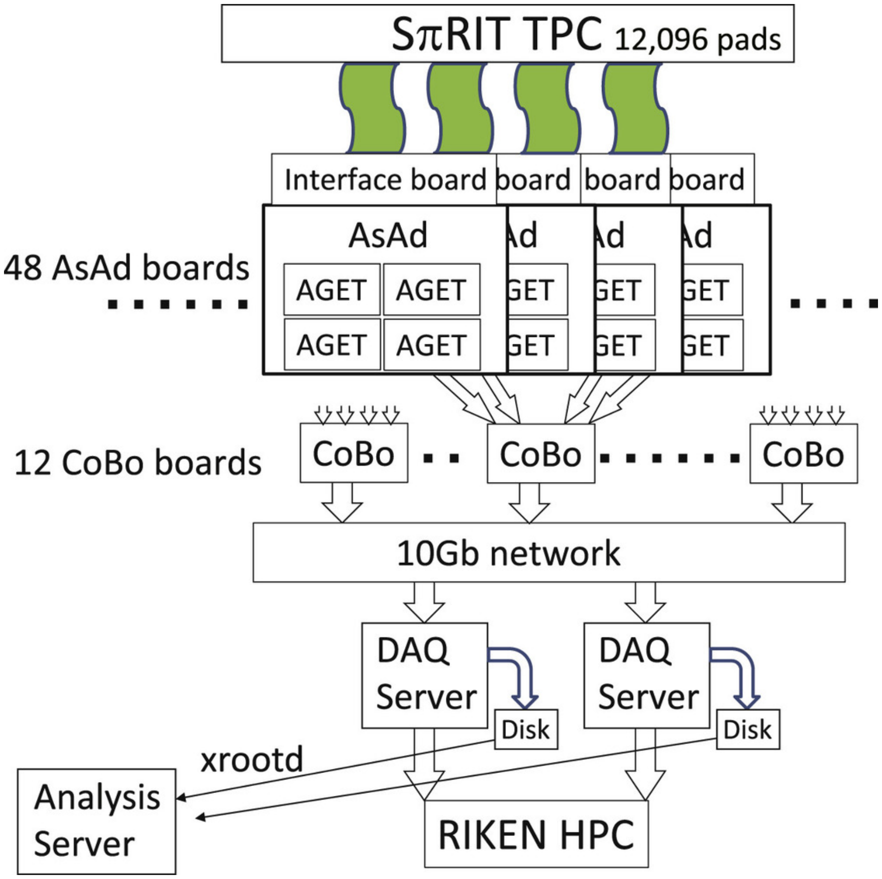

Figure 2.4: GET architecture employed for SπRIT TPC, from [5].

event to disk. The CoBo have DDRAM for event buffering, storing the time sequenced, digitized data from the 512-cell switched capacitor arrays. A control path on the CoBos is used to receive the trigger from the Multiplicity, Trigger and Time (MuTanT) module (see [4] for further details) and transfer it to the AsAd boards, and to configure the AsAd boards prior to data taking. When an event trigger is received, the buffered data from the CoBo modules are written to disk.

For the SπRIT TPC, 48 AsAd boards are used with 12 CoBos. The CoBos are mounted in 2 µ-TCA crates located outside the magnetic field, with 8 CoBos and one MuTanT module in one crate and 4 CoBos and one MuTanT module in the other. The AsAd and CoBo were connected with 8 m long commercial Very-High-Density-Cable Interconnect (VHDCI) cables.

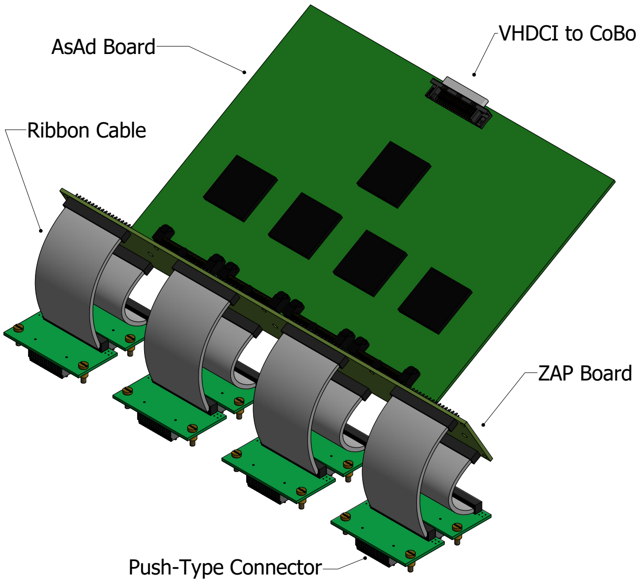

Figure 2.5: Adapter and ZAP boards.

The µ-TCA crates send data from the CoBo modules through a 10 Gbps network switch to 2 DAQ servers, which employ NARVAL [32] as the DAQ framework. The GET architecture as employed for the SπRIT TPC experiment is shown in Figure 2.4. During experimental runs, the AsAd sampling frequency was 25 MHz, with 270 of the 512 timebuckets digitized [5].

The connection between AsAd and pad plane is handled with custom made interface boards, as shown in Figure 2.5. The interface uses 2 types of rigid circuit boards, connected with flexible ribbon cables. Push-type connectors on the smaller rigid boards are used to interface to the pad plane, and the larger board is connected to the AsAd. Spacers are used to ensure that the force on the SAMTEC connector is sufficient to ensure electrical contact on all signal and ground lines, but not any more. Excessive force on the pad plane can break the gas seal between the pad plane and the top plate. The larger board is called a ZAP board, as it uses low capacitance diode arrays to protect the AsAd from huge signals which could be caused by sparking around the pad plane. The flexible ribbon cables allow the AsAd board to be installed in a tilted fashion, maximizing the limited space budget.

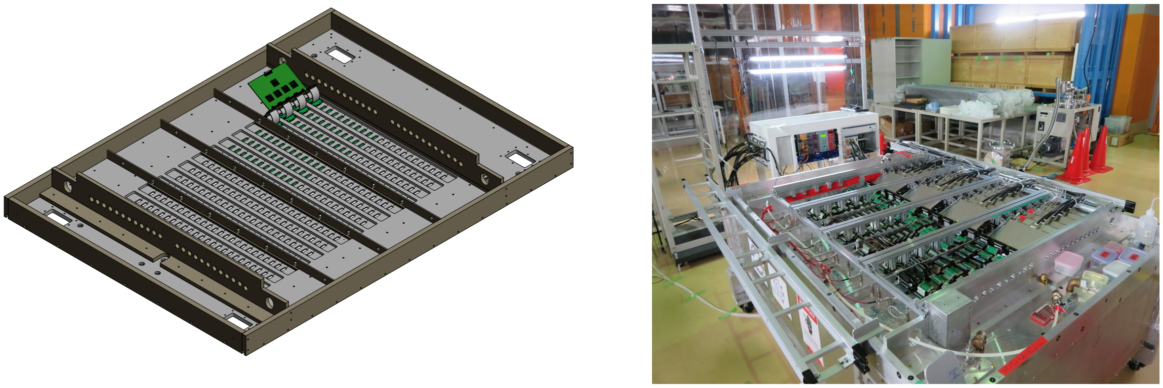

(a) (b)

Figure 2.6: Schematic view of top plate and ribs (a), and photograph of TPC with GET electronics partially installed (b).

2.4 Top Plate

A rigid aluminum plate is used as a flat reference surface for the pad plane, wire planes, field cage, and target mechanism, and as the mounting point for the readout electronics. This plate is referred to as the “top plate". The top plate is made of a 3/4 inch thick aluminum plate, 2035.2 mm long and 1498.6 mm wide. A recess is machined on the bottom side to fit the pad plane, and slots through the plate are machined for the interface boards (described previously) to connect to the pad plane. Machining the feed-throughs and recesses causes the plate to warp, as the machining process relieves stress within the metal, so a series of ribs is installed on the top plate to maintain planarity. The top plate and supporting rib structure is shown in Figure 2.6a, with a single AsAd and interface board installed. The ribs are used to hold a support structure for readout electronics, made of 80-20 aluminum extrusion. Figure 2.6b shows the TPC with GET readout electronics (described previously) installed on half of the pad plane.

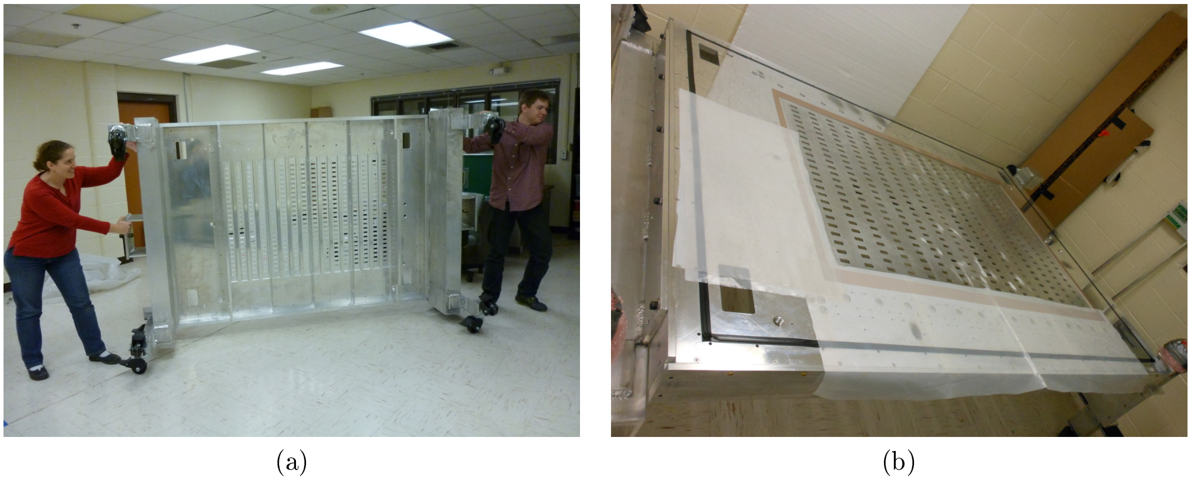
(a) (b)

Figure 2.7: The top plate and motion chassis in (a) doorway configuration and (b) table configuration.

2.4.1 Motion Chassis and Table Configuration

A motion chassis for the TPC was designed and fabricated at Texas A&M University. The motion chassis connects directly to the ribs of the top plate, allowing the top plate to be moved and worked on easily and safely. The motion chassis is shown installed on the top plate in Figure 2.7a, in the “doorway motion" configuration. Casters on the motion chassis allow smooth motion across floors and through doors. An additional set of casters are employed for a “table" configuration, shown in Figure 2.7b. In this configuration, the bottom of the top plate can be worked on easily, and motion is also possible, although in the table configuration, the assembly will not fit through a typical doorway.

2.5 Pad Plane

An array of conductive, charge-sensitive pads called the “pad plane" is mounted to the bottom of the top plate. Each pad is 11.5 mm in the beam direction and 7.5 mm in the transverse direction, with 0.5 mm isolation between each pad. An electron avalanche will induce a signal on the nearest charge-sensitive pads: if an avalanche occurs over an isolation area, the signal will spread over the two neighboring pads. Therefore, each pad covers an effective area of 12 mm × 8 mm. The pad plane spans 112 pads in the beam direction and 108 pads in the transverse direction, for 12,096 pads and overall dimensions of 1344 mm × 864 mm. The pad dimensions matched the EOS TPC, which had previously been used to measure pions. The overall pad plane size is somewhat smaller than that of the EOS TPC, but is a reasonable match to the available region of uniform magnetic field inside the SAMURAI spectrometer.

The effect of pad dimension on momentum resolution can be investigated for a fixed number of channels. For an array of 108 × 112 pads of fixed length, we examine the relative error in determining momentum for pads of different widths. For particles starting at the origin of the pad plane with momentum aligned along the Z-axis, the magnetic rigidity can be used to determine the path length and number of pads crossed. We assume the error of point measurement varies as $\varepsilon^2 \propto W^2 + L^2$, with W and L the pad width and length, respectively. The momentum resolution is determined from the ability to measure track curvature. From [30], the variance for curvature measurement can be described as

$$\sigma^2 = \frac{\varepsilon^2}{L^4} \frac{720N^3}{(N-1)(N+1)(N+2)(N+3)}, \tag{2.1}$$

where ε is the error of measurement for each point along the curve, L is the track length, and $N+1$ is the number of points measured.

Using the 8 mm × 12 mm pad size as a reference, relative momentum measurement error is shown in Figure 2.8 as a function of magnetic rigidity (in MeV/c/e). For low rigidity particles, wider pads increase the path length (by increasing the total pad plane

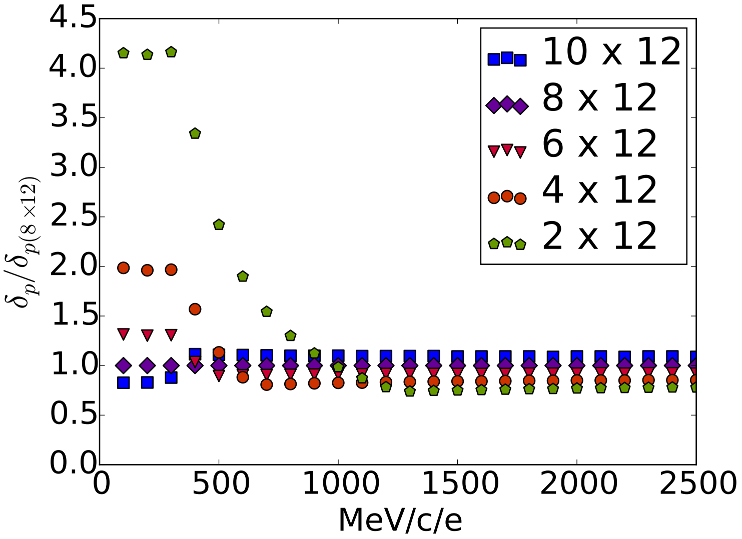

Figure 2.8: Relative error of momentum measurement for different pad sizes.

size), which increases the momentum resolution. For higher rigidity particles, the narrow pads increase the number of measurement points along the path, increasing resolution. A narrow pad size (and therefore narrow pad plane) drastically reduces the path length for low rigidity particles, disproportionately increasing the momentum error. Since our pions will typically be of rigidity less than 1000 MeV/c/e, the wider pads are better suited for our pion measurement.

The pad plane is made from a 6-layer Printed Circuit Board (PCB), with conductive surfaces coated in gold. Due to the complexity and size of the pad plane, it is technically difficult and cost-prohibitive to produce as a single board, so instead 4 different pieces were produced that could be combined to form the pad plane. The perimeter of the pad plan is bounded by a ground strip, causing an asymmetry which requires 2 designs for the 4 pieces. Opposing corners share the same design, as illustrated in Figure 2.9. The width of the ground strip is exaggerated in the figure. Dowel pin holes in the three outer corners are used to set the relative position of the 4 boards when mounting to the rigid top plate.

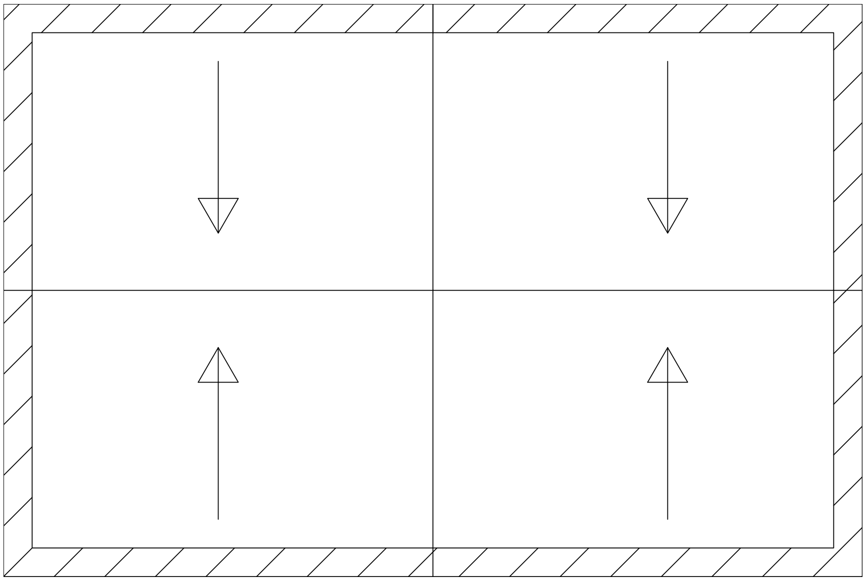

Figure 2.9: Pad plane symmetry, with hatched regions representing the ground strip, and arrows representing the symmetry of the pad layout. Not to scale.

2.5.1 Unit Cell

The pads are grouped into “unit cells" which span 7 pads in the beam direction and 9 pads in the transverse direction for a total of 63 pads. The unit cell is designed to be read out using either two STAR Front End Electronics (FEE) cards or by one AGET chip (described in Section 2.3). The layout and signal routing of the unit cell is shown in Figure 2.10. Pads are shown in blue, with pad number in white shown for one row and one column. The pad number increases from left to right, and top to bottom. The signal layer is shown in yellow. The signal routing was chosen to minimize the typical trace length. The green circles represent Vertical Interconnect Access (VIA) holes which transport signal between circuit board layers. The footprint for two SAMTEC FSI connectors are shown in red. These connectors are spring-loaded, and must be held against the pad plane circuit board. For a numbering convention, we have defined 4 rows from the 2 connectors, and labeled the pins in each of these rows from 0 - 24. This numbering is indicated in gray in the figure. The unit

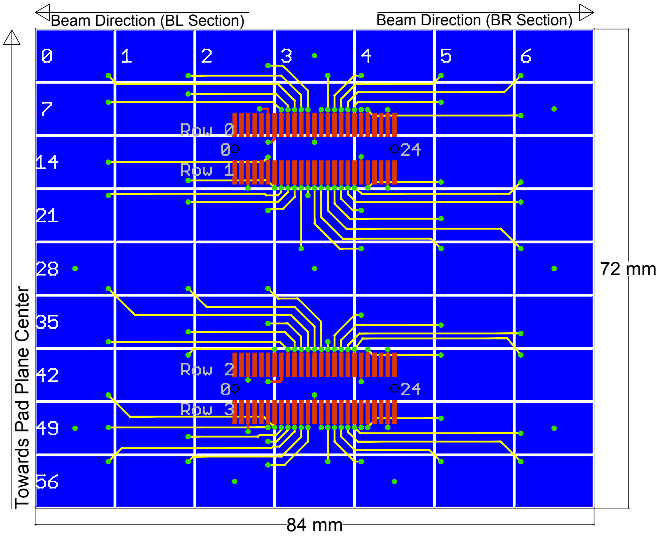

Figure 2.10: Circuit schematic of the pad plane unit cell.

cell pattern is repeated across the pad plane, and has mirror symmetry across the Z-axis (oriented along the typical beam direction).

Since each AsAd board has 4 AGET chips, 4 unit cells are serviced by each AsAd board. The pad plane dimensions are illustrated in Figure 2.11 along with the profile of a unit cell and the area serviced by a single AsAd board. The pad plane spans 16 unit cells in the beam direction, and 12 unit cells in the transverse direction. There are 196 unit cells in the pad plane, and 48 AsAd boards are used to read it out.

2.5.2 Layer Cross Section

To avoid crosstalk, we use a multi-layer circuit board. The signal plane is in the middle, shielded on either side by ground planes, with the pad side and readout side on the outside layers. This puts a requirement of a minimum of 5 layers, but it is best to use an even number of layers in a circuit board due to the manufacturing process, so a total of 6 layers were used. The cross section is shown in Figure 2.12, not drawn to scale. The layers of

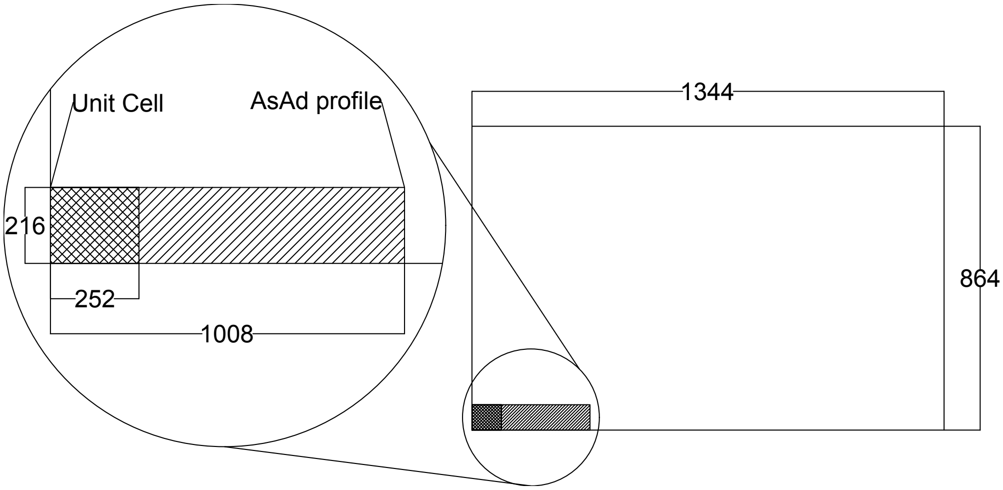

Figure 2.11: Pad plane overall dimensions in mm, with the profile of a unit cell (cross hatched), and the area serviced by one AsAd board (hatched).

copper are all 0.7 mil (1 mil = 0.001 inch) thick, and are drawn in an orange color. To simplify the manufacturing process, there are only two VIA routes with one route running through the entire board, and one route going from the top layer to layer 5. The insulating layers, drawn in green have thickness indicated with units of mil. The insulating materials are made of non-brominated G10 glass-epoxy resin. The VIA route which runs through all layers is used to connect the pads to the signal layers. On the top layer, the VIA is covered with insulating soldermask material to avoid grounding to the top plate. The VIA route which runs from the top layer to layer 5 is used to bring the signal from the signal layer to the top layer, as well as to interconnect all ground layers.

2.5.3 Pad Plane Signal Mapping

The interface board connecting the AsAd boards to the pad plane was described previously, and shown schematically in Figure 2.5. The signal mapping from one AGET chip to one unit cell is enumerated in Table 2.1, with pad numbers following the convention in Figure 2.10. In addition to 64 signal channels, the AGET chip has 4 Fixed Pattern Noise (FPN) channels,

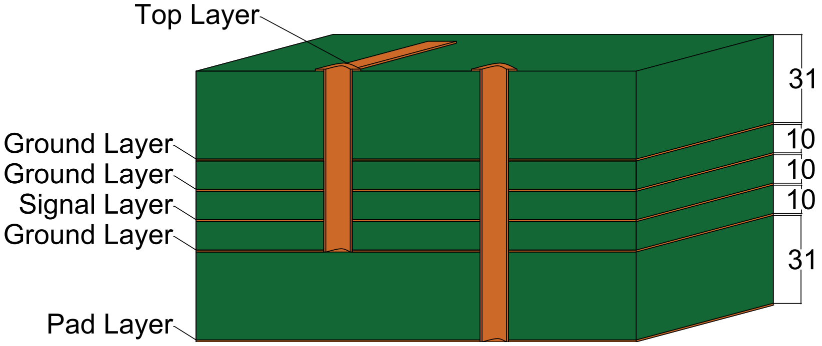

Figure 2.12: Cross sectional view of the pad plane. The green hatched layers are G-10, with the thickness indicated in mil.

which are included in the map. Since each unit cell has 63 pads instead of 64, one channel is Not Connected (NC). The mapping is the same for each unit cell/AGET chip in the pad plane.

2.6 Pad Plane Gluing

The pad plane was fastened to the top plate using Araldite 2013 epoxy. Since the pad plane forms a gas tight barrier, the gluing procedure was designed with redundancy for leaks. A double gasket fabricated from polycarbonate was glued to the top plate around each set of holes used for the GET electronics, as shown in Figure 2.13a. For this gluing, EZ-poxy was used. An aluminum jig was used to apply each gasket, to ensure uniform application. Uniform pressure was applied to the gaskets while the epoxy cured using teflon-coated, weighted aluminum plates. This made a gas-tight seal between the gaskets and the top plate. EZ-poxy does not provide the strongest structural bond to either aluminum or polycarbonate, but it is low viscosity, which allows the gaskets to be pressed flat against the top plate. This is essential to ensure a gas-tight seal.

With the gaskets installed, the pad plane was secured to the top plate using Araldite

AGET	Pad	AGET	Pad	AGET	Pad	AGET	Pad
0	14	17	33	34	49	51	52
1	9	18	10	35	NC	52	30
2	15	19	34	36	42	53	59
3	16	20	3	37	43	54	38
4	21	21	26	38	50	55	60
5	7	22	FPN	39	44	56	FPN
6	22	23	4	40	51	57	39
7	8	24	25	41	35	58	61
8	23	25	5	42	56	59	40
9	0	26	27	43	36	60	62
10	31	27	6	44	57	61	41
11	FPN	28	20	45	FPN	62	55
12	1	29	12	46	37	63	48
13	24	30	18	47	58	64	53
14	2	31	11	48	28	65	46
15	32	32	19	49	45	66	54
16	17	33	13	50	29	67	47

Table 2.1: AGET channel to Pad signal mapping. The convention for pad number is detailed in Figure 2.10. Four Fixed Pattern Noise (FPN) channels are present per AGET card, but they are not connected to the pad plane. Channel 35 is Not Connected (NC) to any pad.

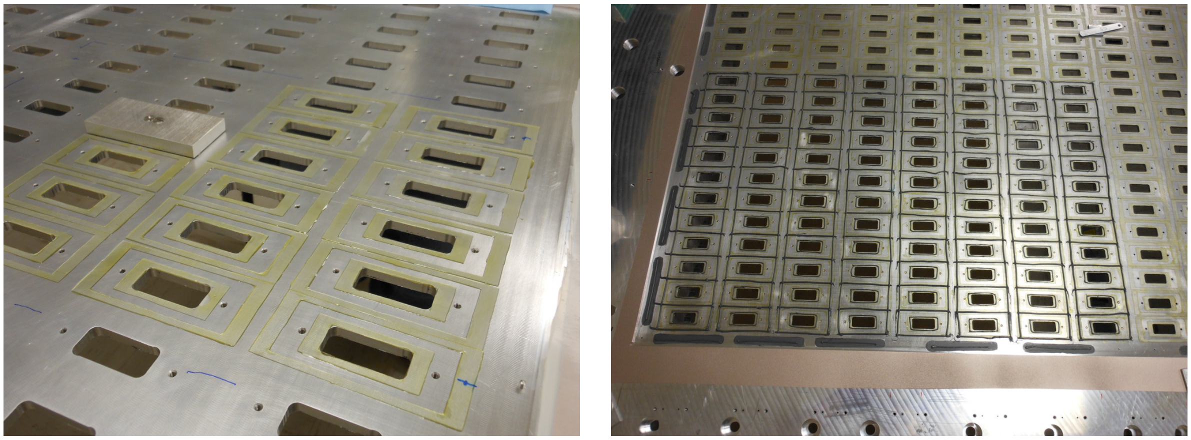

(a) (b)

Figure 2.13: Gluing double gaskets to top plate (a) and application of Araldite epoxy for pad plane installation (b).

2013 epoxy, which bonds strongly to the pad plane circuit board and to the aluminum top plate. The pad plane corners were installed one at a time, using a vacuum table to ensure planarity. The epoxy was applied to the top plate as shown in Figure 2.13b, in square patterns covering each of the previously described gaskets. Although most of the Araldite application is not directly on the aluminum surface, it is squeezed over the aluminum when the pad plane is pushed against it. Each screw hole was filled with Teflon-coated screws to prevent the Araldite 2013 epoxy from flowing into them. Kapton tape was placed over the electrical connections of the pad plane, to keep them clean of epoxy.

With the epoxy applied, the pad plane corner is lowered into place using a vacuum table, as shown in Figure 2.14. The vacuum table has a precision flat surface with many holes which, when used with a vacuum pump, holds the pad plane circuit board flat while the epoxy cures. Precision shims are used to set the height and level of the vacuum table. Metal weights on top of the vacuum table apply pressure to the pad plane and epoxy. The epoxy was cured in this configuration for 24 hours for each pad plane corner.

With this pad plane gluing procedure, each gasket was glued by two rectangular beads

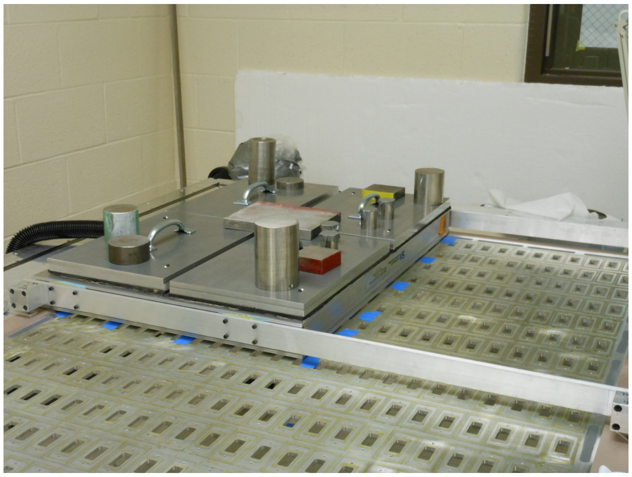

Figure 2.14: Vacuum table in use for pad plane installation.

of Araldite 2013 epoxy to the top plate. The innermost rectangle surrounds the electrical contacts for the SAMTEC push connector, and the outermost rectangle surrounds two screw holes used to secure the SAMTEC connector to the top plate and pad plane. When testing the TPC with P10 gas, some leaks were detected on the top plate using a combustible gas detector with sensitivity to methane at the 5 ppm level. All such leaks were then sealed by injecting EZ-poxy through the two screw holes, into the captive volume between the two rectangular seals.

2.6.1 Pad Plane Flatness Measurement

After the pad plane was installed on the top plate, the flatness of both the pad plane and top plate were checked. The top plate was moved to a clean tent, and secured in table configuration. A FARO brand laser alignment system was used to probe the relative height of many points over the surface of the pad plane and top plate. A picture of the measurement in progress is shown in Figure 2.15a, and the resulting measurement is shown in Figure 2.15b, with dimensions in inches. The measurement indicated deviation from planarity of up to ± 0.125 mm for the pad plane, and up to ± 0.203 mm for the top plate. The pad plane is offset from the bottom surface of the top plate by 1 mm.

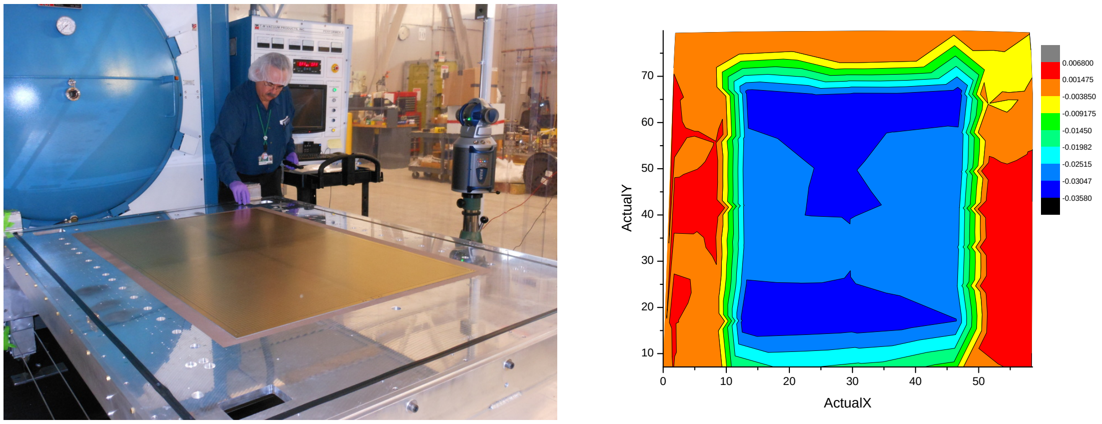

(a) (b)

Figure 2.15: Dave Sanderson (NSCL staff) measuring top plate and pad plane flatness (a), with topographical map of measured flatness (b).

2.7 Wire Planes

The wire planes are used to create an electron avalanche and produce a signal on the pad plane that is read out by the front end electronics. Each wire plane is divided into 14 sections, which allows us to replace or repair individual sections without replacing the entire wire plane. The wires from each wire plane are mounted under the pad plane, running transverse to the beam direction. For each section, a pair of circuit boards are mounted on spacer bars on either side of the pad plane, screwed to the top plate. The wires are epoxied and soldered to these circuit boards to form a section of the wire plane. Figure 2.16 shows the wire planes mounted on the top plate. The properties for the wire planes are listed in Table 2.2.

The amplification occurs between the ground and anode wire planes, and the gating grid plane is used to prevent amplification of events which are not of interest. The relative

Plane	Wire material	Diameter (µm)	Pitch (mm)	Distance to pad plane (mm)	Tension (N)	Nominal voltage (V)
Anode	Au-plated W	20	4	4	0.5	1420
Ground	BeCu	76	1	8	1.2	0
Gating	BeCu	76	1	14	1.2	-110±70

Table 2.2: Wire plane properties.

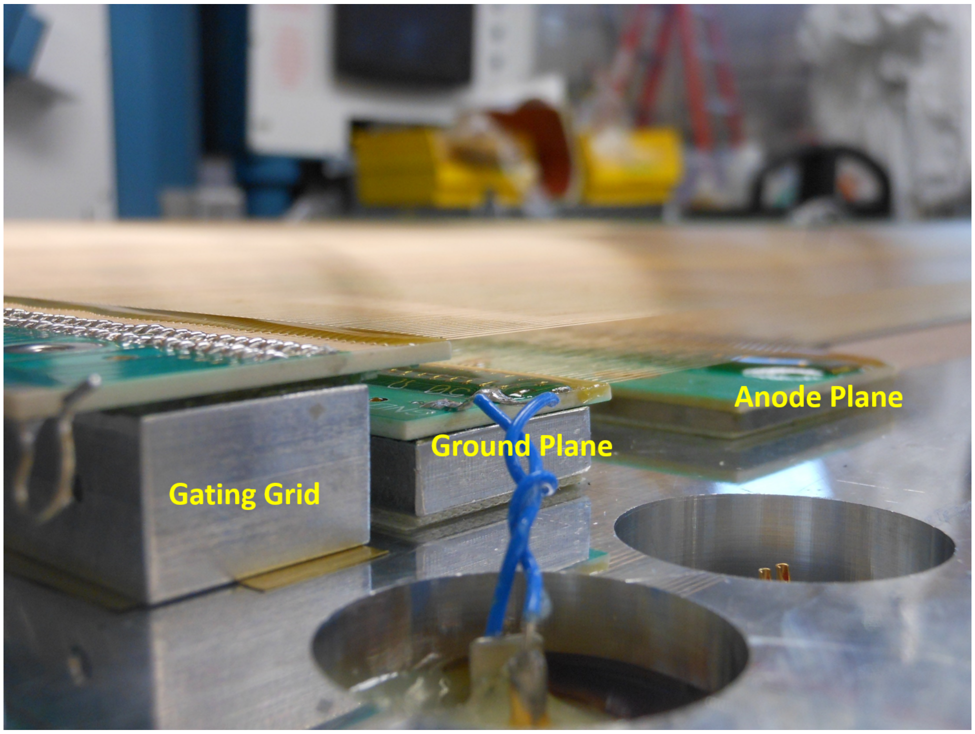

Figure 2.16: Wire planes mounted on the top plate.

voltage between ground and anode planes determines the electron multiplication, and since the ground plane remains fixed at ground potential, the gain is adjusted by varying only the anode voltage. The average voltage of the gating grid is set to match the local electric field, with alternating wires offset in opposite polarity from the average voltage when the gating grid is closed.

The wire planes are connected to feed-throughs in the top plate, with the feed-through mapping shown in Figure 2.17. The figure perspective shows the top plate from underneath, with the wire planes visible and numbered 1-14, with 1 at the upstream end and 14 at the

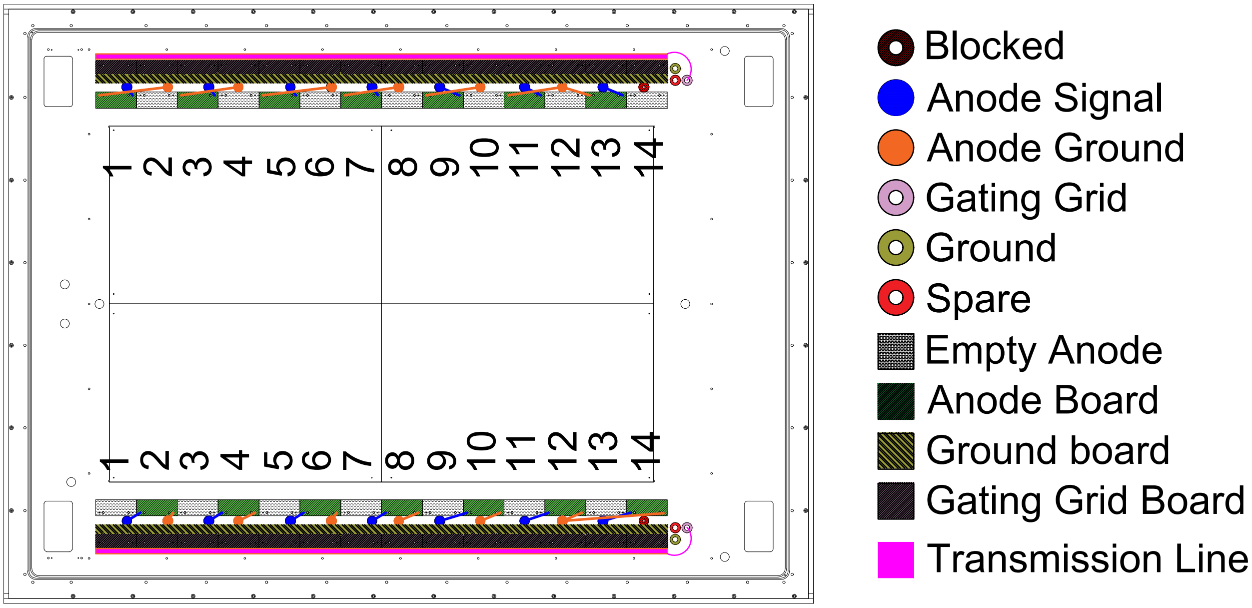

Figure 2.17: Wire plane feed through mapping.

downstream end. A design error blocked two anode plane feed-throughs, as indicated by red hatched feed-throughs. Due to this, the high voltage supplies for two pairs of anode planes were provided through the same feed-throughs, thus, the voltages on anode planes 12 and 14 are linked together, as are the voltages on anode planes 11 and 13. The anode high voltage is supplied using MHV feed-throughs (Amphenol model 10400), and the ground is supplied using BNC feed-throughs (Amphenol model 031-4237). The ground plane is connected on both left and right sides with BNC feed-throughs (Amphenol model 031-220H), with two spare feed-throughs. The gating grid plane is connected on both left and right sides using Dual-Lemo feed-throughs (LEMO model HGP.0S.302.CLLPV) and transmission lines that are shown alongside the gating grid boards.

2.7.1 Anode Plane

The anode plane consists of 364 gold-plated tungsten wires, 26 wires on each of the 14 sections. The thin diameter of 20 µm is necessary for a high gain, and although the wires are biased to a high electrical potential, they are vulnerable to a high electric current. Therefore, the anode plane circuit requires protection against sudden electrical discharge, which can occur when an electron avalanche terminates on a wire. The circuit for a single anode section is shown in Figure 2.18, with wires represented by arrows.

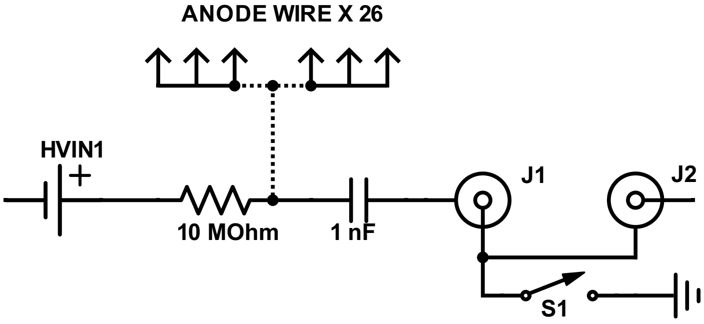

Figure 2.18: Anode plane circuit and termination. This circuit is repeated for each of the 14 sections.

The bias is provided on one side of the pad plane through a 10 MΩ resistor, with a virtual ground made using a 1 nF capacitor. When negative charge is deposited on an anode wire, the positive charge on the capacitor cancels the negative charge, partially discharging the capacitor. The capacitor is recharged through the resistor, with an RC time constant of 10 ms. This maintains the voltage on the wire while gas-amplification occurs on the anode wire during an event. It also limits the current on the wire in the event of a spark and allows a controlled recharging of the anode wires. The high voltage for each section is supplied using an SHV feed-through in the top plate, and a BNC feed-through, J1, is located on the top plate, which allows the individual anode signals to be observed or grounded. A switchboard installed to allow this configuration to be remotely switched between ground and a LEMO terminal, which can be attached to a pre-amp readout. The complementing circuit board on the opposite side of the pad plane is left unconnected to high voltage or ground.

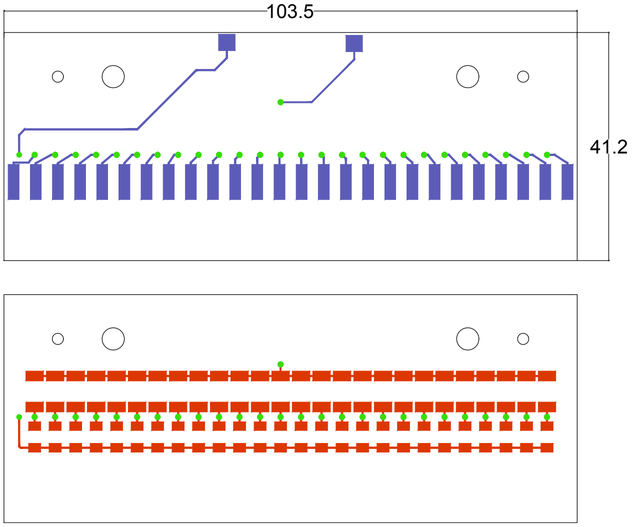

Figure 2.19: Anode plane circuit board. Dimensions in mm.

The layout of the anode boards is shown in Figure 2.19. Each section consists of 26 wires, and includes pads for installing the resistor and capacitor. The top (blue) is the signal layer, to which the wires are affixed. The bottom (red) is the layer to which the resistors and capacitors are soldered. VIAs are shown in green which link the two layers.

2.7.2 Ground Plane

The ground plane consists of 1456 beryllium-copper wires, 104 wires on each of the 14 sections. The main purpose of the ground plane is to define a ground potential for electron amplification. Additionally, the ground plane can be pulsed so as to induce regular signals on the pad plane. This is a very useful feature for testing and calibration. The wires for each section are connected to an impedance line which is built into the circuit board. The impedance was introduced to match the intrinsic capacitance of the ground plane wires. This impedance line has a set impedance per unit length, and is represented as an individual capacitor and inductor for each wire in Figure 2.20. The arrows represent wires from either side, and the dashed lines indicate repetition for the 1452 wires which are not shown. The

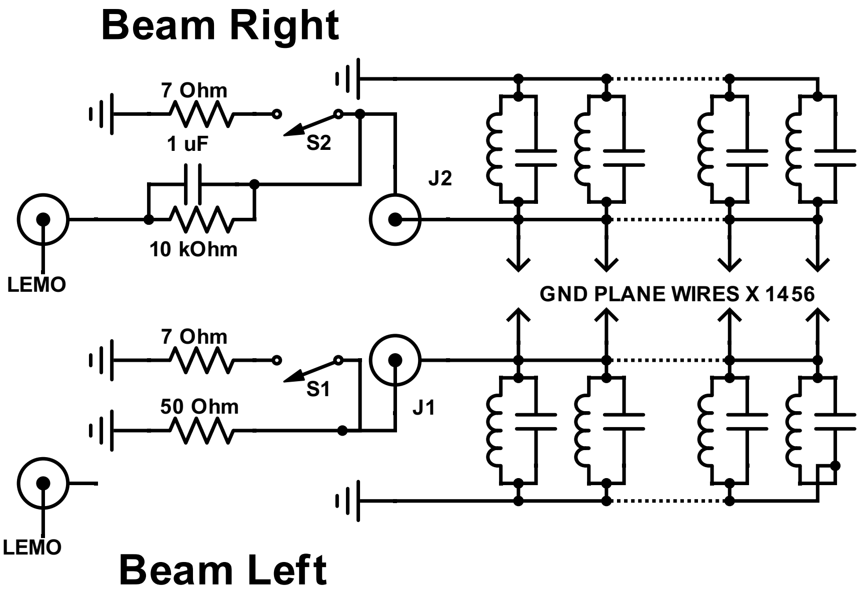

Figure 2.20: Ground plane circuit. Dashed lines indicate the pattern repeats over the entire plane.

circuit is mirrored on the opposite side of the pad plane, so that there are 2 BNC feed-throughs used to control the ground plane. The BNC feed-throughs are also connected to switchboards, allowing a pulser signal to be injected on the beam right side, or allowing the ground plane to be shorted to ground through a 7Ω resistor. The beam left side can be shorted through a 50 Ω resistor, or through the 50Ω and a 7Ω resistor, or effectively 6.14Ω.

The signal line runs across the top of the board, with the signal line of each board connected to adjacent sections in series. The ground line runs along the bottom side of the board, and this line is also connected to the ground lines of adjacent sections. The ground line and the signal line for a section can be seen in Figure 2.21. The bottom (blue) layer is at ground potential, and the top (red) layer is the signal layer. The wires are affixed to the signal layer. VIAs, shown in green, connect the signal and bottom layer.

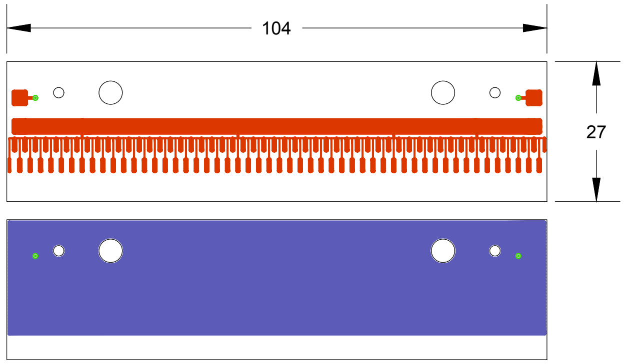

Figure 2.21: Ground plane circuit board. Dimensions in mm.

2.7.3 Gating Grid Plane

The gating grid wire plane is used to block drift electrons from reaching the avalanche region. During an experiment, reactions occur within the detector that are either not of scientific interest, or are not able to be recorded while the data acquisition is writing the last event. One particularly problematic situation is that of unreacted beam particles that pass through the field cage. The high charge and energy of the beam particle results in heavy ionization within the field cage. If the ionized electrons pass to the avalanche region, there are undesirable results. The first problem arises from the production of positive ions within the avalanche region. A sustained production of positive ions can cause a buildup of "space charge", net charge within the gas which distorts the electric field within the field cage, affecting the drift speed of electrons, drift path of electrons, and the detector gain, all in an unpredictable manner. Further, the buildup of positive ions can lead to the production of polymer chains which bind to the thin anode wires, changing their effective radius and irreversibly reducing the gain. This effect is commonly known as detector aging [33]. Finally, the amplification of a highly ionizing event produces a saturating signal on corresponding pads, causing the corresponding readout channel to be unresponsive for up to 35 ms [5].

For the reasons outlined above, it is necessary to have a gating grid wire plane which

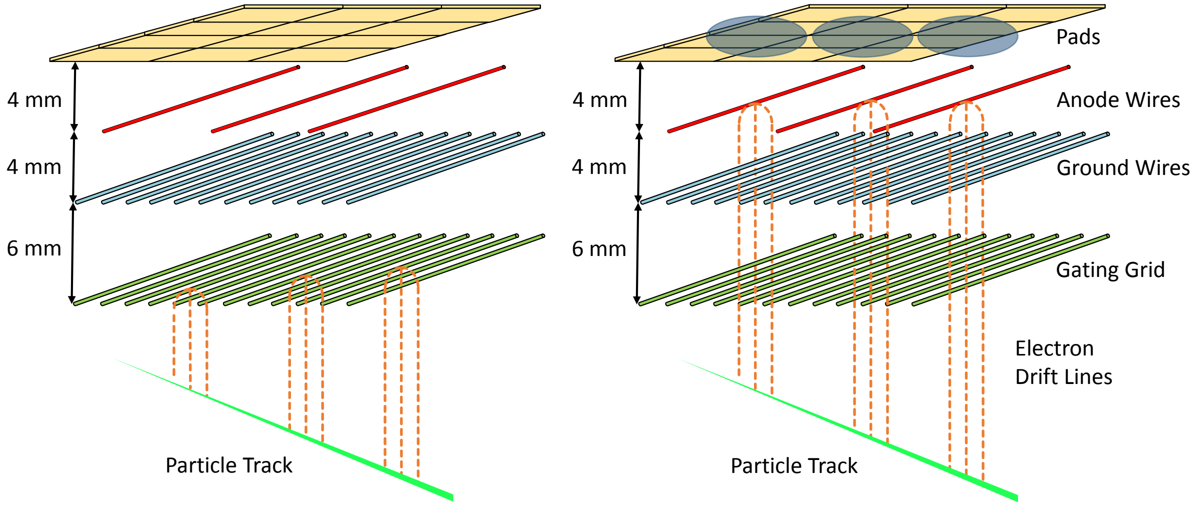

Figure 2.22: Gating grid operation principle [6].

serves to close the avalanche region to drift electrons from undesired events. This is achieved by using two alternating sets of wires, with each wire neighbored by wires of the opposite set. In the “open" configuration, both sets of wires are biased to a voltage V_{avg}, allowing drift electrons to pass through unimpeded. The best value of V_{avg} was determined using GARFIELD simulations. In the “closed" configuration, both sets are offset from V_{avg} by a voltage ΔV, with one set above the average voltage at $V_H = V_{avg} + \Delta V$ and one set below the average voltage at $V_L = V_{avg} - \Delta V$. This causes an electric field between wires, so that drift electrons are attracted to the set at V_H. The closed and open states are illustrated in Figure 2.22, with the open state allowing electrons to pass through, and the closed state resulting in electron drift lines terminating on the V_H set of wires.

The choice of ΔV must account for two factors: ΔV must be sufficiently high to prevent drift electrons from passing through, but as ΔV is increased, the time required to switch to the open state increases. A gating grid driver is used to change the state of the gating grid, and is described in Reference [6]. GARFIELD simulations were used to determine the minimum necessary offset voltage to close the gating grid. Figure 2.23 shows the electron

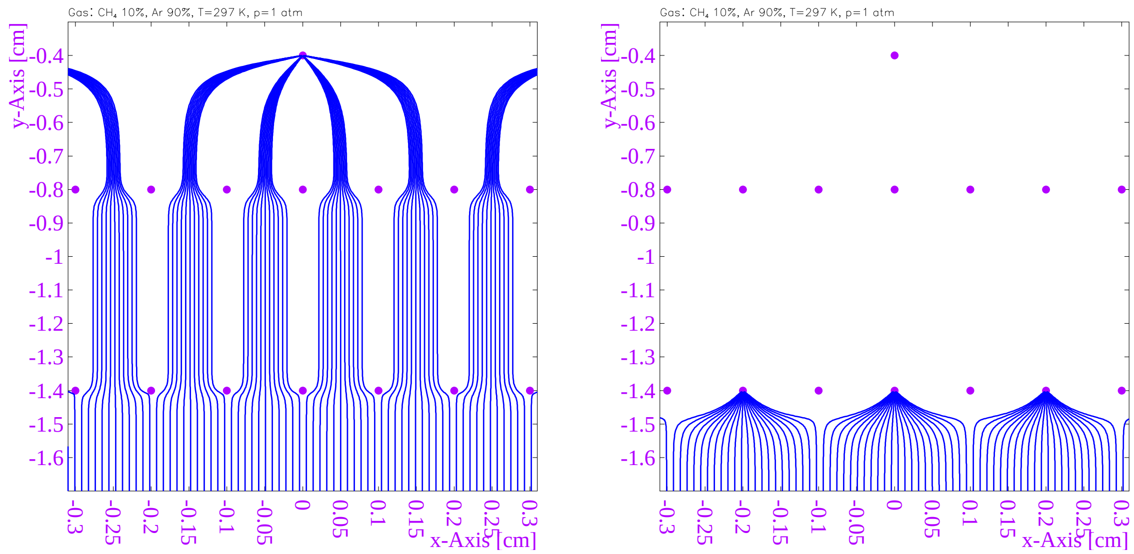

Figure 2.23: Garfield simulation of gating grid [6]. The left panel shows the opened gating grid, allowing electrons to reach and terminate on the anode wires. The right panel shows the closed gating grid, which causes electrons to terminate on the V_H wires.

drift lines for the open (left) and closed (right) states, from a GARFIELD simulation [6]. The simulation assumes P10 gas at atmospheric pressure, with $V_A = -110$ V and $\Delta V = 70$ V. The drift field is 131 V/cm and the simulation is performed without magnetic field. The quantification of open or closed is determined by "electron transparency". For example, if 1000 electrons were initialized, and 995 passed through the gating grid, terminating on the anode plane, the configuration would have an electron transparency of 0.995, or 99.5%.

The inclusion of a magnetic field increases the difficulty to close the gating grid. Since the drift field and magnetic field are anti-parallel, the Lorentz force suppresses transverse diffusion and causes the electrons to follow the anti-parallel electric and magnetic field lines closely as they drift upwards. These electric field lines terminate on the gating grid when it is closed. As electrons approach the region where the electric field has a large transverse component due to the closed gating grid, they are guided away from the electric field lines by the $\mathbf{E}\times\mathbf{B}$ effect, in a direction parallel to the wires, with some electrons missing the

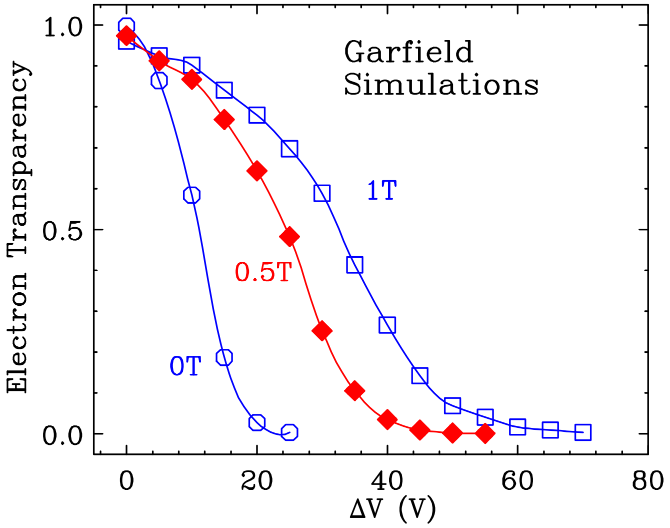

Figure 2.24: Gating grid closing with magnetic field [6].

gating grid wires biased at V_H. This results in a higher electron transparency, which must be overcome by increasing ΔV [30]. To determine the ΔV required for closing with magnetic field, GARFIELD simulations were performed using 4000 electrons per simulation and determining the electron transparency for various values of ΔV with a magnetic field set at 0, 0.5, and 1.0 T [6]. The results are shown in Figure 2.24.

The effective circuit for one of the gating grid boards is shown in Figure 2.25. The matching gating grid board on the opposite side of the pad plane mirrors this circuit. Two distinct sets of wires are used ($\mathrm{V_H}$ and $\mathrm{V_L}$), and they are connected to the opposing polarities of the transmission line (shown in Figure 2.17). The transmission line is represented by the capacitor and inductor in Figure 2.25, and is described in the next Section.

The gating grid circuit boards are shown in Figure 2.26, with a relatively straightforward circuit board layout. The main consideration that must be taken is to allow sufficient space between the front row of pads and the wires from the rear row that run between those pads. The electrical connections made to the board must be done on both the top and bottom

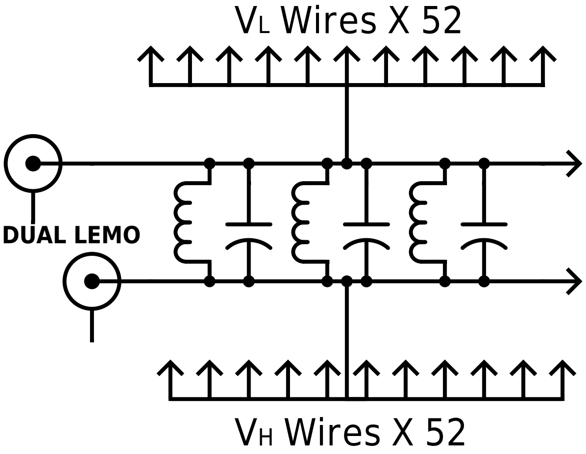

Figure 2.25: Gating grid circuit for a single section of the wire plane.

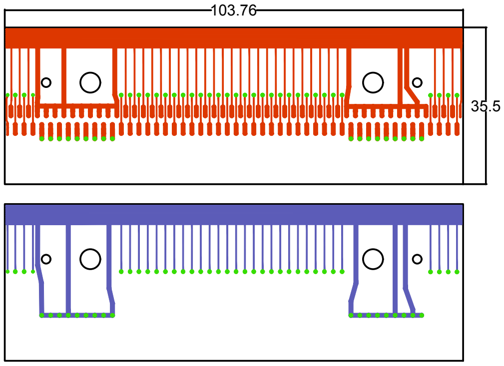

Figure 2.26: Gating grid plane circuit board. Dimensions in mm.

sides, and so it is required that the boards are larger than the spacer bars that they are mounted on.

2.7.4 Gating Grid Transmission Line

A bi-polar gating grid driver[6] is used to drive the gating grid between open and closed states. The gating grid plane has an inherent impedance due to capacitance with neighboring gating grid wires as well as neighboring ground plane wires, and thus a transmission line must be used between the gating grid driver and the gating grid wires to improve the impedance matching. Opening of the gating grid must be done as rapidly as possible without introducing large signals on the pad plane, as every 1 µs required to open the gating grid results in 5.5 cm of drift distance being not detectable, or approximately 9% of the detection volume.

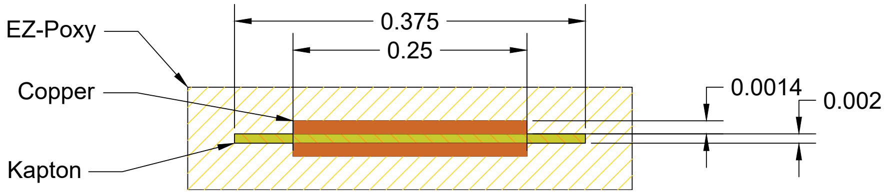

Figure 2.27: Cross section of gating grid transmission line. Dimensions in inches.

Two transmission lines, one for each side of the wire plane, run the length of the pad plane as shown in Figure 2.17, and are connected to each section of the gating grid plane through connections for each V_H and V_L, placed every 104 mm. The design copies the dimensions of commercially available transmission line. For the signal lines, a 1.4 mil thick by 0.25 inch wide copper foil was used. A 2 mil thick Kapton strip was used to set the distance between signal lines. The cross section is shown in Figure 2.27. The Kapton has a dielectric constant of 3.4, so the transmission line has capacitance of 3.8 nF/m, or 5.5 nF per transmission line. The entire assembly is encapsulated in EZ-poxy for insulation, and the signal lines are supplied through a dual-Lemo feed-through on the downstream end of the top plate. The EZ-poxy insulation is wrapped with copper for shielding; however, this changes the impedance characteristics of the transmission line in a non-uniform manner.

2.7.5 Wire Plane Installation

The first step of the wire plane assembly is to attach the circuit boards to spacer bars using epoxy. The circuit boards and spacer boards are aligned to each other using dowel pins. Uniform pressure is applied to the circuit boards and spacers while the epoxy cures, using a vacuum bag. The anode spacer boards have cutouts to accommodate the electrical components used. After the circuit boards have been attached to the spacers, these cutouts are filled with epoxy to provide electrical insulation, as shown in Figure 2.28. Note that half the anode boards do not have electrical components, as the wires are biased from only one side.

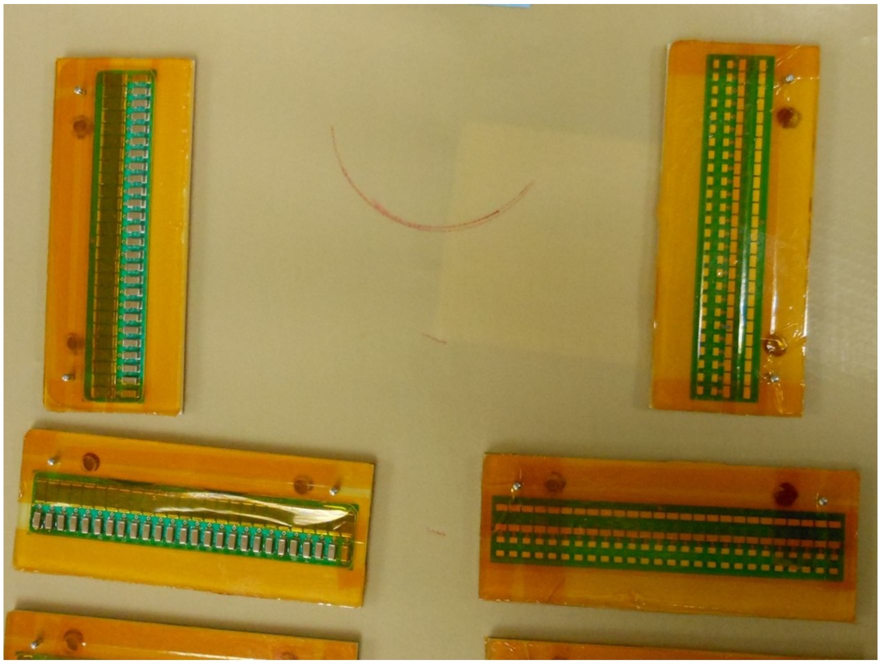

Figure 2.28: Anode circuit boards attached to spacer boards.

The wires are wound to a precise tension and approximate spacing before they are mounted to the circuit boards. The wire winding was performed in the NSCL detector lab, using the wire winding machine shown in Figure 2.29. A wire-feeding table uses a spring tensioning system to feed the wire at a set tension. This machine spins two wire plane frames at a constant rate, wrapping the wire around the frames. The machine moves the wire-feeding apparatus along the frame at a rate to set the initial pitch of the wires. When the wire is wound to the frames, it is secured using 5-minute epoxy. The wire between the two frames is then trimmed, and the wire plane frames are removed from the machine for installation on the wire bars. The tension of the wire planes was verified using a speaker

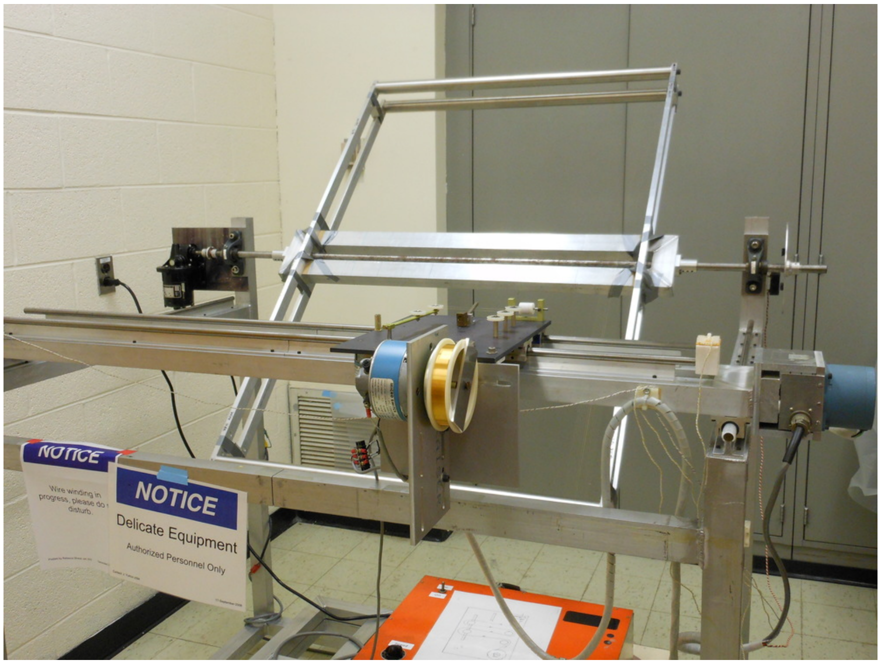

Figure 2.29: Winding machine for wire planes.

to vibrate the wires. The diffraction pattern of a low power laser incident on the middle of a wire indicates when the speaker was tuned to form a standing wave on the wire. The frequency that forms the second harmonic is used to infer the wire tension.

The wire bars are numbered and installed on the top plate. The height of each bar is set individually using shim stock and a height gauge, with the top plate as a reference surface. The gating grid and ground plane bars are removed to install the anode wires. The wire plane frame, with wound wires, is set above the anode bars. Figure 2.30 shows the the anode wires being glued to the anode bars. A wire comb, made with an electrical discharge machine to 1/10,000 inch precision, is used to align the wires while they are glued. After the epoxy has cured, each wire is soldered to the circuit board. Excess wire is trimmed away, and the wire combs and wire plane frame are removed. The soldered region is then covered with EZ-poxy to cover any sharp edges or points.

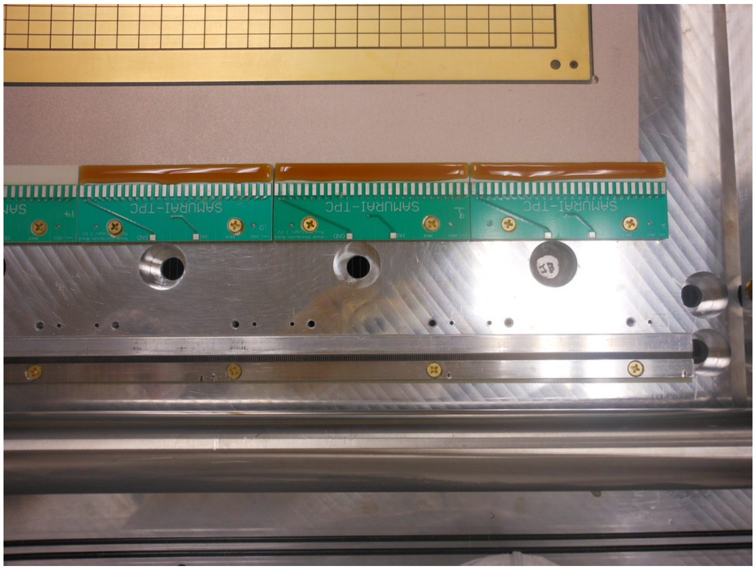

Figure 2.30: Gluing the anode wires to the anode bars.

2.7.6 Wire Plane Repair

Repairing a broken wire or wire plane requires one to remove all wire planes above the damaged portion. Thus, to replace a single section of the anode wire plane, the corresponding gating grid and ground plane sections must both be removed. During fabrication, we discovered that the tensioning of one anode plane was incorrect and therefore it needed to be replaced. Ideally, replacing such an anode wire plane section should be done without having to remake the ground and gating gird plane sections. A procedure to remove ground and gating grid wire planes was planned and implemented to correct the wrongly tensioned anode plane. Thus we tested this procedure during the construction of the TPC to replace anode plane 6, which exhibited sparking issues.

First, the electrical connections are removed from the wire plane sections that must be removed. A removal fixture, shown in place in Figure 2.31, was designed which would screw to the wire bars from either end. This maintains the wire plane section tension and overall shape when the wire plane section is removed from the top plate. To install the removal

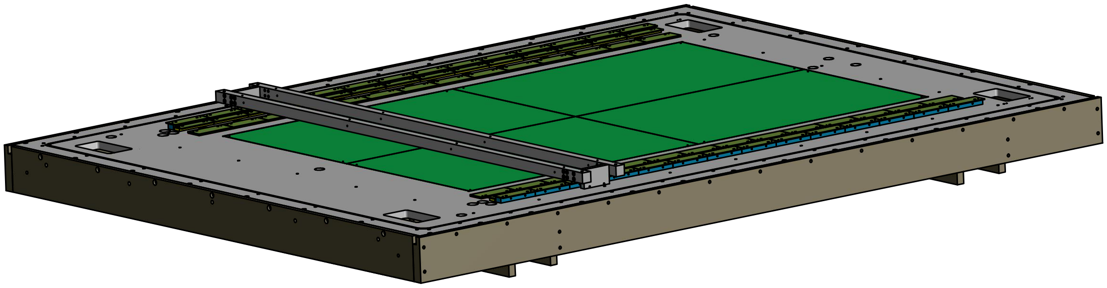

Figure 2.31: Schematic of wire plane removal fixture on upside-down top plate.

fixture, the gating grid transmission line must first be removed. Swivel-tip set screws on each corner of the removal fixture are used to control the height, allowing us to lift the wire plane section off the top plate in a controlled manner. Once the wire plane section is raised above neighboring sections, the entire fixture is removed from the top plate. The left and right sides can be marked on the removal fixture using a marker. A Lexan cover is installed on the removal fixture, keeping the wires safe until they are reinstalled. Both the gating grid and then the ground wire plane section can be removed in this way.

When the repairs are finished, the wire planes are reinstalled, returning the left and right bars to their original position, using the dowel holes and pins to reproduce the original position. The first step is to remove the Lexan cover. Then the removal fixture and wire plane can be placed on the top plate above the position for the wire plane. The wire plane is lowered into position using the swivel-tip screws.

2.8 Field Cage

The field cage provides a containment box for the counter gas, and produces a uniform electric drift field for the electrons ionized from the counter gas. Together with the rigid top plate, the

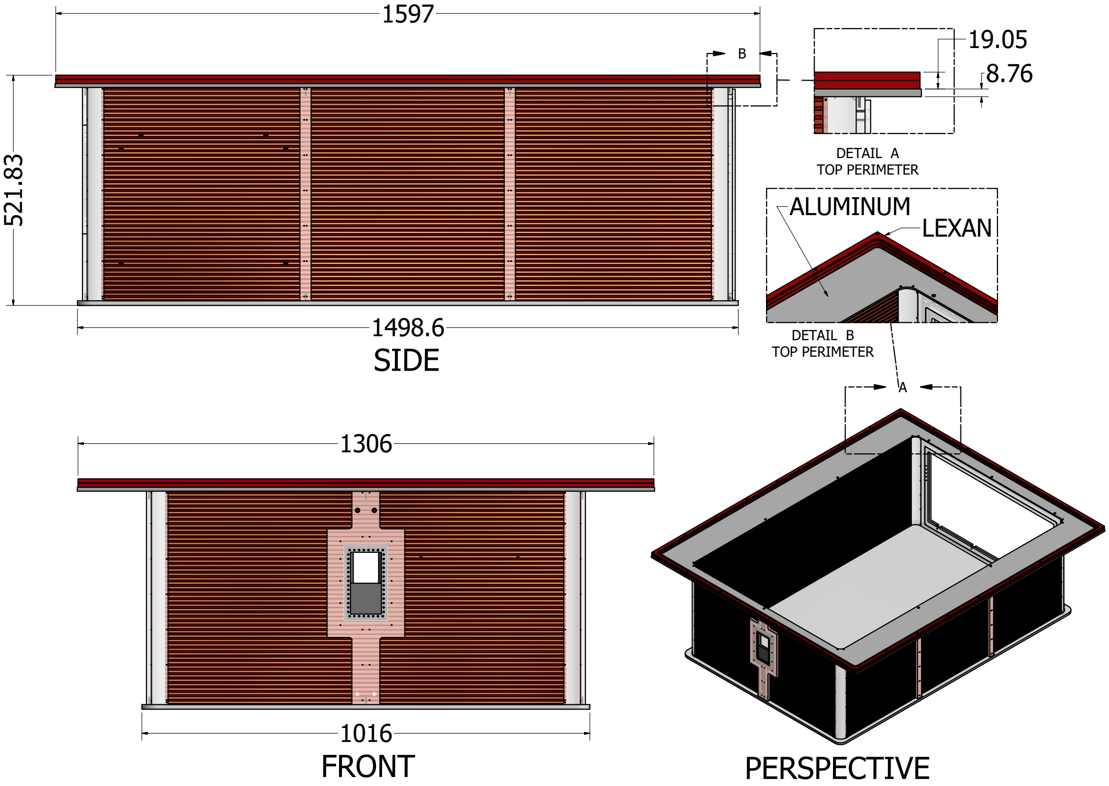

Figure 2.32: Dimensions of field cage in mm, with details A and B highlighting the top perimeter.

field cage forms a sealed rectangular box which contains P10 gas at just above atmospheric pressure. P10 gas is used in the STAR TPC[34], and performance properties have been studied in detail [35]. Key design considerations included maximizing the drift distance while still fitting inside the magnet gap of the SAMURAI spectrometer, and maintaining a uniform electric field throughout the detection volume underneath the pad plane. The overall exterior dimensions are shown in Figure 2.32, which shows views of the field cage from the front, side, and a perspective from the top.

The field cage interfaces with the top plate using an assembly called the top perimeter. A Lexan ring, formed of two pieces, surrounds the wire planes, while an aluminum perimeter forms the seal between field cage walls and the Lexan ring. The field cage and its enclosed drift volume can therefore be made gas-tight allowing the gas mixtures in the drift region and the insulation gas to be different. The top perimeter is shown in Figure 2.32, with detailed closeups. O-ring grooves are machined on both sides of the Lexan ring, mating with the top plate on one side, and the aluminum perimeter plate on the other. The field cage walls are made with 1.575 mm thick G10 Printed Circuit Boards (PCBs). Copper strips on the PCBs define the electric field, and using PCBs allows us to make the field cage gas-tight. Each side wall is made using 3 PCBs, while the front wall is made with 2 PCBs, as well as the entrance window. The rear wall is formed entirely using the exit window and frame. The cathode plate (detailed in the following section) seals the field cage on the bottom.

The height of the field cage is constrained by the vertical space budget. The usable pole gap of the SAMURAI spectrometer is 75 cm, due to a set of bolt covers inside the magnet. Above the field cage there must be space for the AsAd boards, and below the field cage there must be space for the Voltage Step Down (VSD), which is described in a following section, and the enclosure structure. The space used above and below was minimized so that the field cage height could be maximized. The resulting drift length, between the interior face of the cathode plate and the gating grid wires, is 497.3 mm.

The high voltage is supplied to the cathode through a 10 MΩ resistor, as shown in Figure 2.33. There are two paths to ground from the cathode: through the VSD (discussed in Section 2.8.1), and through the field cage resistor chain. The effective resistance of the VSD is $\mathrm{R_{VSD}}$= 700 MΩ. Each field cage strip is connected to the next through two 10 MΩ resistors, one on the beam left side and one on the beam right side. Thus, the effective resistance between adjacent strips is R = 5MΩ. There are 49 resistor pairs in the field cage resistor chain between the cathode and top perimeter, providing a total resistance of $\mathrm{R_{FC}}$ = 245 MΩ. A fixed 20 MΩ resistor ($\mathrm{R_{TP1}}$) in parallel with an adjustable resistor ($\mathrm{R_{TP2}}$)

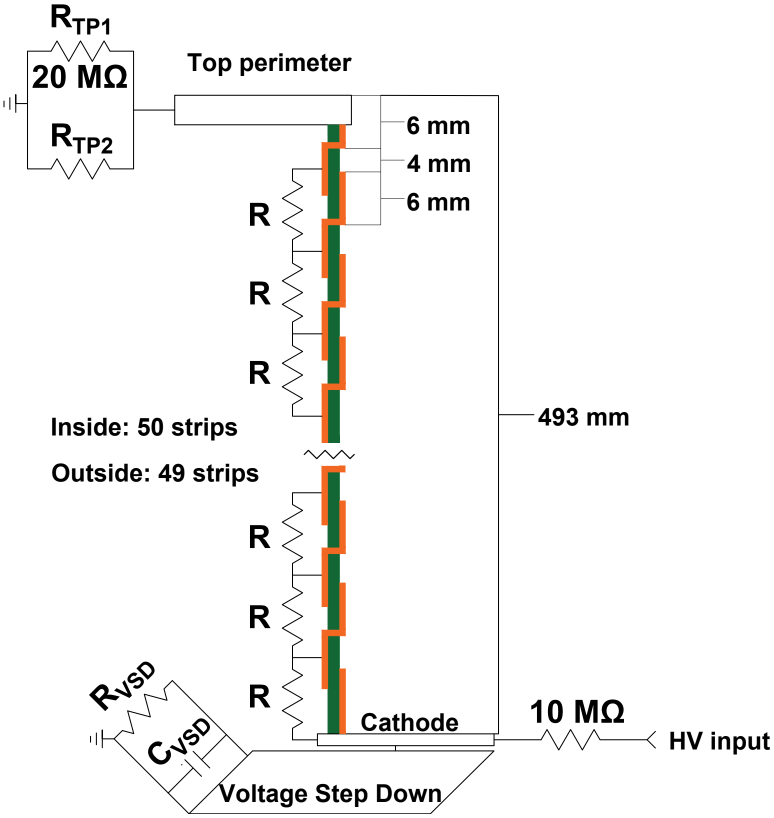

Figure 2.33: Field cage circuit layout. Modified from [7].

connects the top perimeter to ground. The effective circuit diagram is shown in Figure 2.34.

The choice of R_{TP2} is in principle made to tune the electric field between the top perimeter and gating grid, to match the electric field between the cathode and top perimeter. The field matching requires that

$$\frac{V_{\text{tp}} - V_{\text{cath}}}{y_{\text{tp-cath}}} = \frac{V_{\text{gg}} - V_{\text{tp}}}{y_{\text{gg-tp}}}, \tag{2.2}$$

where $y_{\text{tp-cath}} = 490$ mm is the distance between the cathode and the middle of the top perimeter equipotential, and $y_{\text{gg-tp}} = 7.3$ mm is the distance between the gating grid and the middle of the top perimeter equipotential. With this requirement, the resistance between top perimeter and ground, $R_{\text{TP}} = (R_{\text{TP1}}^{-1} + R_{\text{TP2}}^{-1})^{-1}$, can be determined using the standard voltage divider relation

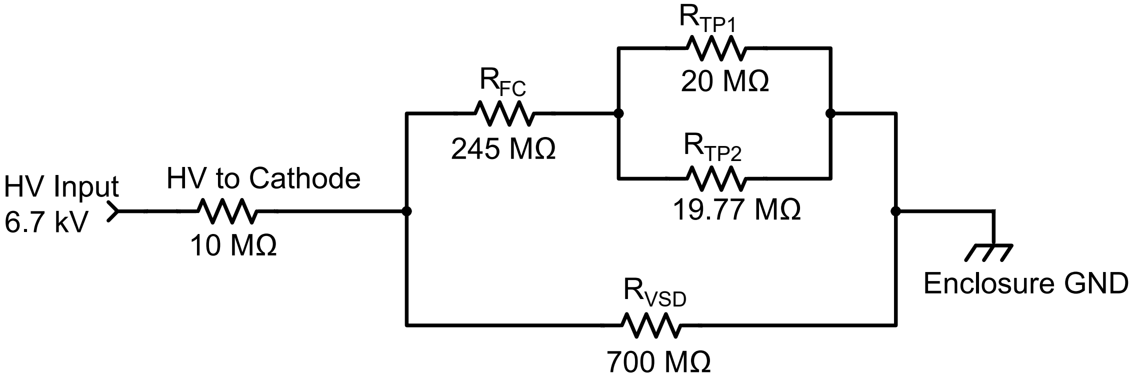

Figure 2.34: Effective circuit diagram for field cage.

$$R_{TP} = R_{FC} \frac{\frac{y_{\text{gg-tp}}}{y_{\text{tp-cath}}} V_{\text{cath}} + V_{\text{gg}}}{V_{\text{cath}} - V_{\text{gg}}}. \tag{2.3}$$

Tests of the electron transparency for various values of R_{TP2} were performed during the commissioning run, which indicated an ideal value of $R_{\text{TP2}} = 19.77$ MΩ. By our calculation, this corresponds to $V_{\text{gg}} = -165$ V, although for the experimental runs, the voltage supplied to the gating grid, V_{avg}, was set to -171 V.

2.8.1 Cathode Plate and Voltage Step Down

The cathode plate seals the bottom of the field cage, and defines the electric field. The cathode plate was designed to be lightweight and to mitigate sparking points. The cathode plate is made using a lightweight honeycomb aluminum plate, which has a machinable solid aluminum perimeter. Incident gamma rays can liberate electrons from the aluminum surface, which has a relatively low work function. To reduce the production of such electrons, the interior surface of the cathode is coated with graphite paint, which can be seen in Figure 2.35. An extrusion is machined in the cathode which matches with the field cage wall geometry. The cathode is fixed to the field cage walls using screws, and sealed with Araldite epoxy.

Figure 2.35: Justin Estee (GS) applies epoxy to the cathode plate.

During the experiment, the cathode plate was biased to 6.7 kV. The Voltage Step Down (VSD) was required to safely bridge the electric potential of the cathode plate to the grounded enclosure. A series of copper rings, each with 1.125 cm separation from neighboring rings, are mounted with standoffs to an insulating plate, with the innermost ring electrically connected to a conductive surface painted on a 0.375" polycarbonate insulating plate. The conductive surface has a 4 nF capacitance to the grounded enclosure. This geometry is shown in Figure 2.36. The cathode is connected to the conductive surface with Cu-Be spring-loaded connections. The innermost ring is connected directly to the conductive surface, and the outermost ring is connected directly to the enclosure. Each ring is connected to the neighboring ring(s) with a 100 MΩ resistor, creating an effective resistance between cathode and ground of 700 MΩ in parallel with the aforementioned 4 nF cathode to ground capacitance. The capacitance and the 10 MΩ HV to cathode resistor effectively serves as a low pass filter

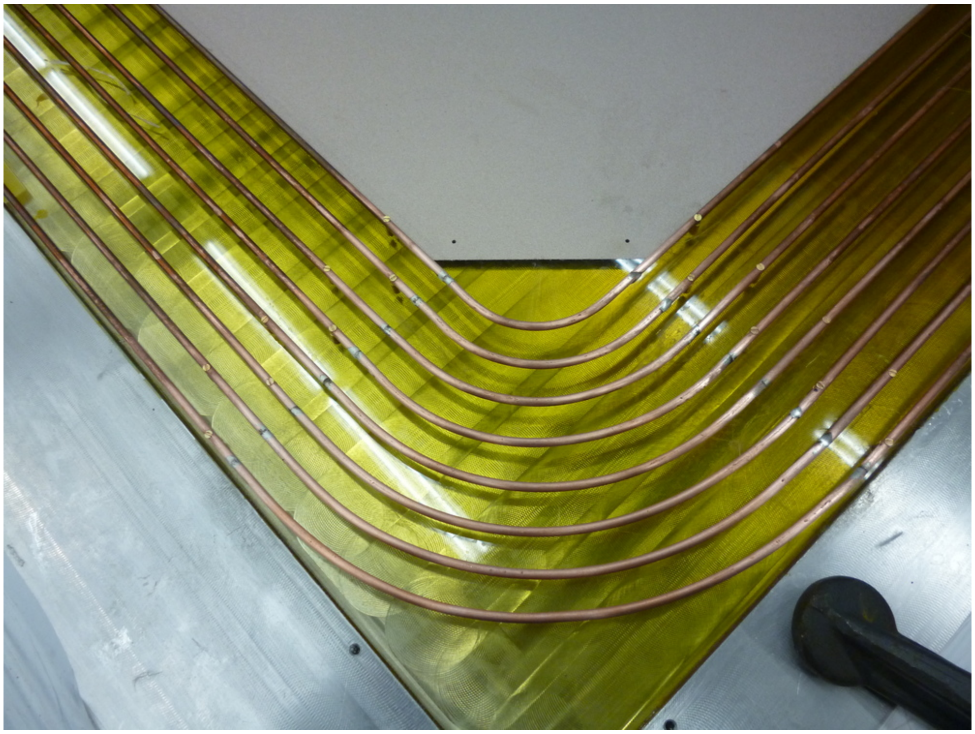

Figure 2.36: Corner of voltage step down. The painted conductive surface is visible inside the copper rings.

with a cutoff frequency of about 4 Hz, removing noise from the HV supply.

2.8.2 Field Cage Windows

The field cage has entrance and exit windows, to allow charged particles to enter and exit the field cage. A design drawing is shown in Figure 2.37, showing the field cage with windows and window frames accentuated. The windows are mounted to removable polycarbonate frames (yellow and turquoise in the figure), which in turn mount to fixed polycarbonate frames (green in the figure). This allows removal of field cage windows when needed.

The entrance window is made with 4 µm thick poly p-phenylene terephtalmide (PPTA), 5.73 cm wide by 7 cm tall. The removable polycarbonate frame is 9.9 cm wide by 16.9 cm tall. Figure 2.38 shows the entrance window, with (a) showing the window removed from the field cage, and (b) and (c) showing the window installed on the field cage. Note that

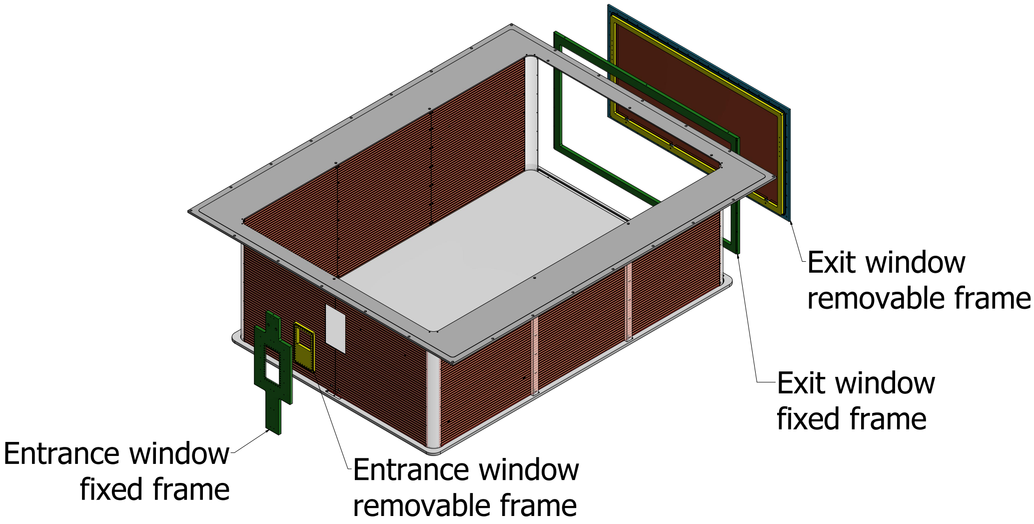

Figure 2.37: Exploded view of field cage windows and frames.

the window is inserted from inside the field cage. Aluminum strips are evaporated over the entire surface of the window and frame, with silver epoxy ensuring electrical contact between window strips and frame strips. Copper fingers are used to connect the strips on the frame to the strips of the field cage.

The exit window is made with 125 µm thick polyamide, 80.8 cm wide by 38.9 cm tall. Aluminum electrode strips are evaporated onto the polyamide, and the window is sandwiched between two polycarbonate frames, which have strips painted on with conductive paint.Figure 2.39a shows a close-up of the silver epoxy used to electrically connect the window strips and frame strips. Figure 2.39 (b) shows the fixed frame, with copper fingers on the outside to electrically connect the inner strips of the removable frame. A printed circuit board with copper strips is used to electrically connect the outside strips. This circuit board is shown in Figure 2.39b, with a white wire soldered to each strip. When the removable window frame is installed, this printed circuit board is screwed to the frame, as shown in Figure 2.39c, forming the electrical connection. To ensure the continuity of the electrical

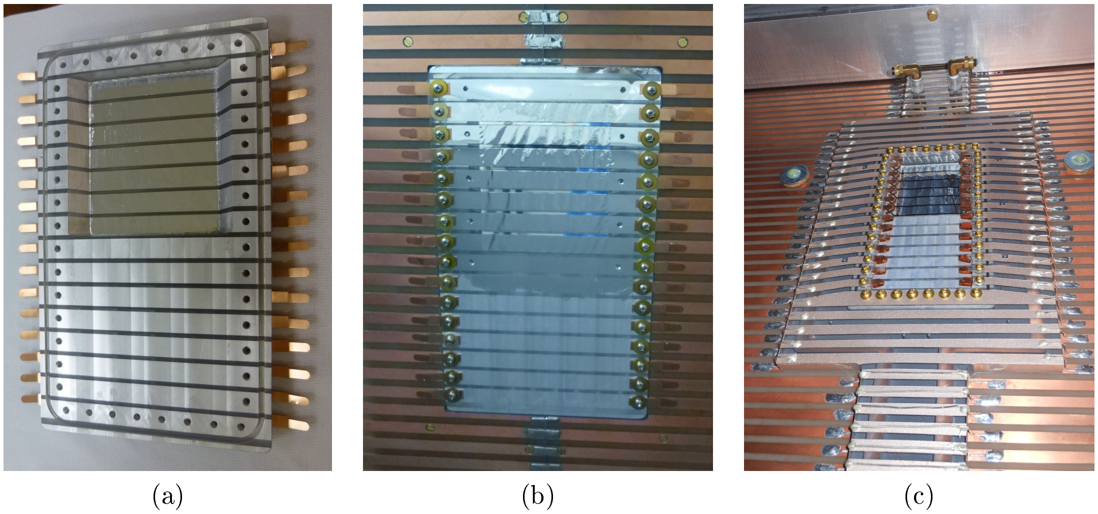
(a) (b) (c)

Figure 2.38: Field cage entrance window. Assembled window shown in (a), inserted window shown from (b) inside and (c) outside the field cage.

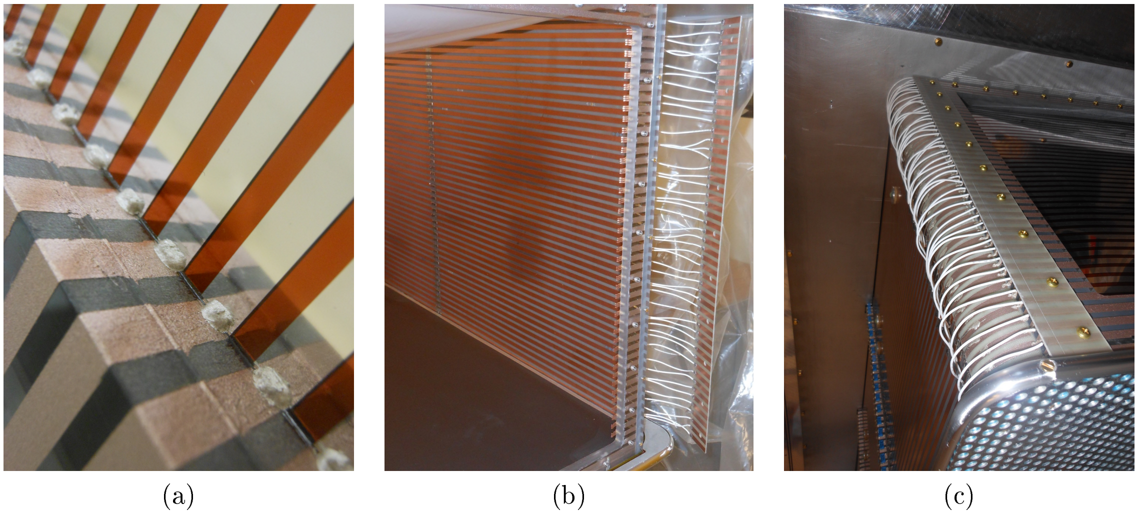
(a) (b) (c)

Figure 2.39: Field cage exit window. Silver epoxy connecting window and frame strips shown in (a), copper fingers and PC for electrical connection of window frame in (b), and installed window in (c).

connection around the field cage, 1 kΩ resistors are used at the front, beam right corner to complete the loop. If the strips on the window are not connected to the field cage strips on both sides, resistance measured across the 1 kΩ resistor will be 1 kΩ, but this resistance will be shorted if the window strips are properly connected.

2.8.3 Field Cage Gas

A suitable counter gas must be used within the field cage. The gas should have a fast drift velocity, and produce many ion pairs during primary ionization. The counter gas is typically a mix of a monatomic fill gas and a polyatomic quenching gas. During the avalanche, some gas molecules will be excited rather than fully ionized, and the photons emitted during de-excitation can ionize the fill gas, thereby causing ionization at points away from the avalanche location, and creating avalanches that are not associated with an actual hit. The quenching gas helps reduce this effect: the photons are preferentially absorbed by the polyatomic quenching gas, which has large photo-absorption coefficients over a wider range of wavelengths than that of noble gases, due to its many degrees of freedom [30].

The thin walls of the field cage and enclosure make it necessary to use a field cage gas around atmospheric pressure. P10 gas was chosen as the counter gas, following the counter gas choice for the EOS TPC and the STAR TPC. Properties of P10 have been studied in detail for gas detectors, and it is a common choice of counter gas. At atmospheric pressure, the drift velocity reaches a local maximum at an electric field to pressure ratio of E/p=0.146 V/cm/mbar [35]. Operating at this E/p results in a drift velocity which has small changes under small variations of the operating conditions. The maximal drift velocity is about 5.5 cm/μs, so for each event, it requires 9.2 μs for the drift electrons near the cathode to reach the avalanche region. This produces an strict upper limit on the rate which can be accepted by the detector. A faster drift velocity can allow a higher rate to be accepted; however, a gas with faster drift velocity will have a reduced interaction with charged particles, resulting in reduced primary ionization.

For the SπRIT experimental campaign, a 6.7 kV potential was applied to the cathode, producing an electric field of 124.73 V/cm. The gas flow was about 1 L/min, exhausting through a bubbler with 1 cm of mineral oil over atmosphere, corresponding to a pressure of 0.78 mbar over atmospheric pressure. Barometric pressure recorded during the experiment fluctuated between 995 mbar and 1020 mbar, corresponding to E/p values of 0.163 to 0.167 V/cm/Torr. Comparing to the MAGBOLTZ simulations performed by the STAR collaboration [35], this corresponds to drift speeds between 5.395 cm/µs and 5.403 cm/µs.

2.9 Target Ladder and Motion

To mount the fixed targets for the TPC, a target motion assembly was designed to hold 5 targets. The target ladder can be moved separately in the X and Z dimensions. The target ladder is fixed at a set height when it is installed; this height can only be changed by opening the TPC. The X and Z motion is controlled from outside the magnet, using a series of gears for motion transfer. The position of the target ladder is determined using potentiometers along the X and Z axis. The target ladder is shown in Figure 2.40. The entrance window frame prevents the target ladder from being positioned next to the window, so 3 of the 5 targets are mounted with standoffs, allowing them to be positioned inside the window frame. The width of the entrance window frame does not allow all 5 targets to be placed on standoffs.

The target ladder is mounted on the motion carriage, shown in Figure 2.41. The motion

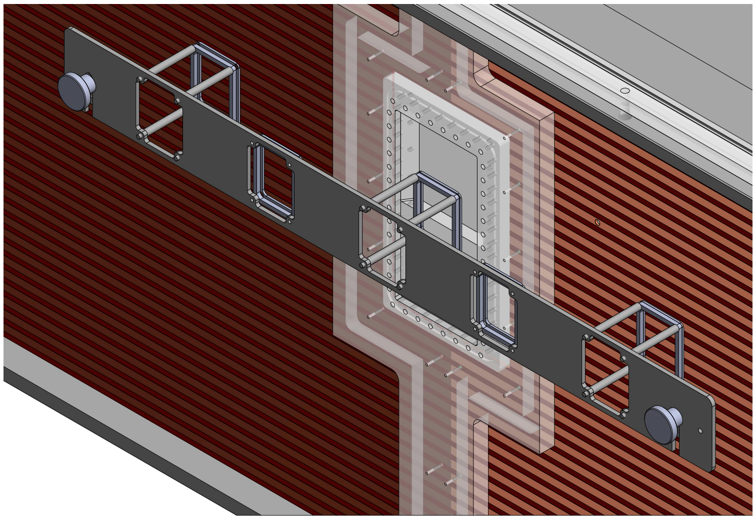

Figure 2.40: Target Ladder

carriage is able to traverse in the X-axis, with the carriage platform able to move in the Z axis. The Z motion mechanism is interfaced with the motion carriage through a bearing and aluminum rod, which are free to move in the X-axis, but constrained in the Z-axis through the Z motion mechanism, which uses a threaded rod to set the Z-position of the bearing. The X motion is controlled using a 102 cm long brass threaded rod. An Acetal nut couples the threaded rod and the motion carriage. The Acetal nut was initially fixed, but upgraded after the experiment to have freedom of motion in the Z and Y dimensions, to accommodate warping in the brass rod.

The motion control is patched out of the TPC using rotary feed-throughs on the top plate and brass gear pairs for corners. For the feed-throughs, 2 Lesker O-Ring Shaft Seals, model FMH-25A, were used. For the gears, 18 Boston miter gears, model G466Y, were used. For the Z-motion, 5 gear pairs are used to route the motion and for the X-motion, 4 gear pairs are used. The motion is directed out of the SAMURAI magnet with the gears, allowing the motion to be controlled from outside the magnet, consistent with safety rules of the RIBF facility.

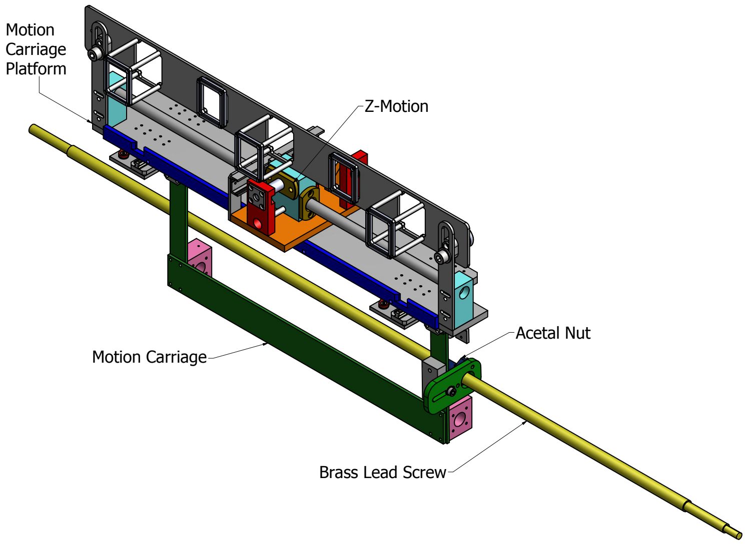

Figure 2.41: Target Motion Carriage.

2.10 Enclosure

The TPC enclosure serves as an electrically grounded, gas-tight box which keeps delicate components protected, and keeps potentially hazardous facets contained. The enclosure is made with an angle-aluminum frame, sealed with windows and plates. The enclosure is shown in Figure 2.42, with a clear plastic cover in place of the top plate. The angle-aluminum stock is welded to form the frame, with welds crossing the O-ring surfaces. These welds had to be ground and polished, to achieve O-ring sealing. Mounting points are welded to each corner, which can be used to mount wheels (as in Figure 2.42), or height-adjusting screws.

The design is shown in Figure 2.43, again with the top plate removed. The upstream end has a 1/2" thick aluminum plate, with a 25.3 cm diameter hole to accommodate the active veto array (discussed in Chapter 3) and entrance window. The bottom has a 1/2" plate, with a 1/4" deep recess for the voltage step down. Two clear plastic windows on the upstream end of the left and right sides provide views of the target mechanism. Three aluminum windows, 0.032" thick, are used on the left, right, and downstream ends of the

Figure 2.42: TPC enclosure with top plate removed.

TPC to allow charged particles to leave the TPC with minimal energy loss.

The thin aluminum windows are set in 1/2" thick aluminum frames. Screws are used to mechanically fix the window panels to the window frames, and epoxy is used to produce a gas-tight seal. The window frames have double O-ring grooves for 1/8" diameter Viton (a flouroelastomer) O-rings to seal against the enclosure frame. The clear plastic windows are set in 1/2" thick aluminum frames. These frames use single O-rings, with 1/4" diameter. The larger O-ring was chosen since these windows are designed to be removed and re-installed frequently. The O-ring grooves for all windows are made as dovetail grooves, which hold the O-rings captive during removal and installation.

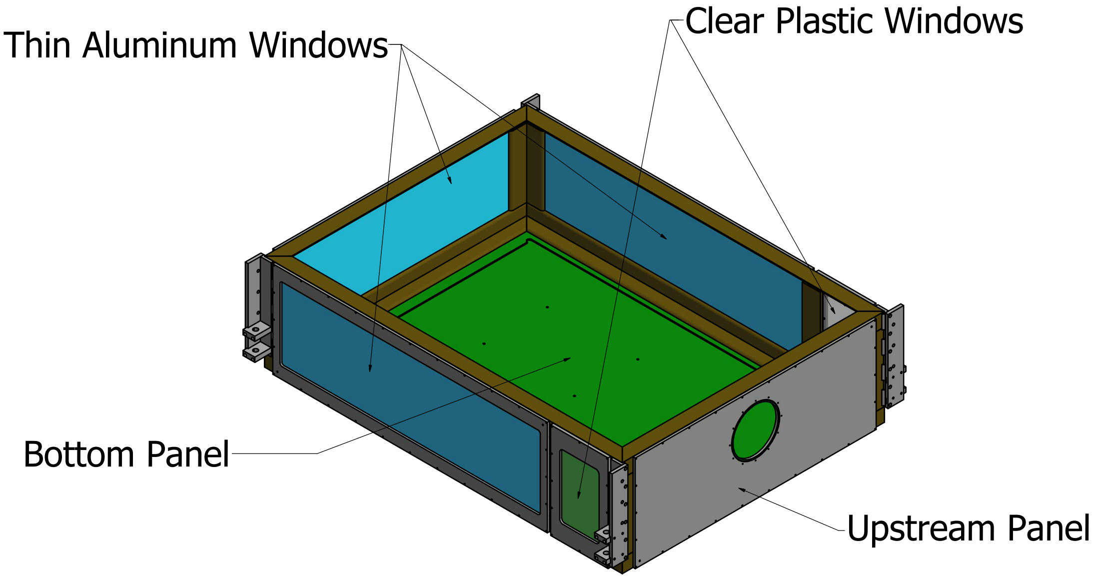

Figure 2.43: TPC enclosure design, without top plate.

2.11 Shipping

The TPC was shipped from the NSCL to RIKEN, where the SAMURAI Spectrometer is located, in February of 2014. A custom crate with vibration dampening and temperature control was used to ship the TPC. The journey involved transport by truck to Chicago, from Chicago to Narita international airport (NRT) by airplane, with a layover in Dallas. Upon clearing customs at NRT, the TPC was transported to RIKEN on a side-loaded truck, where it was lowered into the RIBF building and unpacked. The trucks used and the airplane cargo hold were partially temperature controlled.

The crate used to ship the TPC was custom fabricated by Delta Packaging International [36], of Lansing, Michigan, with guidance from Dennis Young of the MSU Packaging Department. The crate was pre-fabricated and shipped to the NSCL. The crate was built on an insulated base, which could be lifted by forklift from any side. A platform was mounted on the base using Stratocell S foam, dampening vibrations around 70 Hz, near the resonant

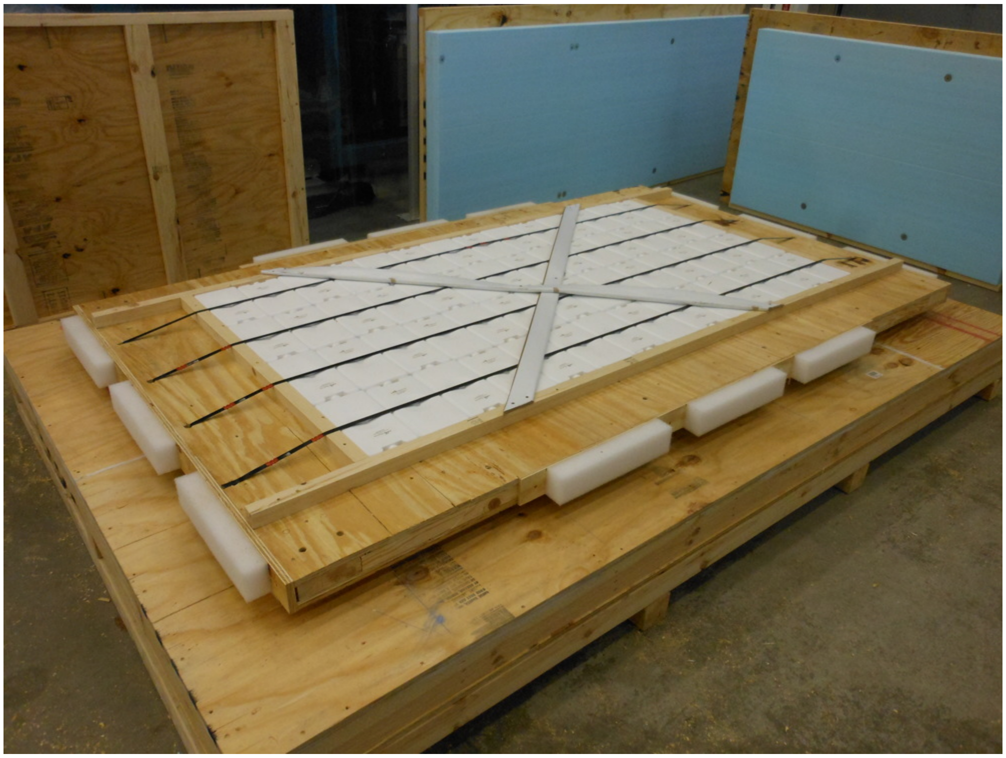

Figure 2.44: The crate base and platform. A bed of phase change material is secured to the platform with steel straps.

frequencies of the wire planes, as determined by their tension and length. The crate base and platform are shown in Figure 2.44. The sides of the platform are isolated from the walls using the Stratocell S foam, and the platform has a bed of PCM22P phase change material from RGEES [37], seen in white containers on the platform.

The TPC was mounted to the platform using the motion chassis and two I-beams as shown in the left panel of Figure 2.45. The crate walls, which must be removed to put the TPC on the platform, are visible in the picture background. The TPC could not be air tight during shipment, to accommodate changes in air pressure. During flight, the air pressure can drop from 14 psi to approximately 3-4 psi if the cargo hold is not pressurized, or loses pressure. An air-tight TPC would have to contain 2.25 m^3 of air at a 10 psi pressure differential, potentially damaging the TPC. A set of upstream windows with HEPA filters

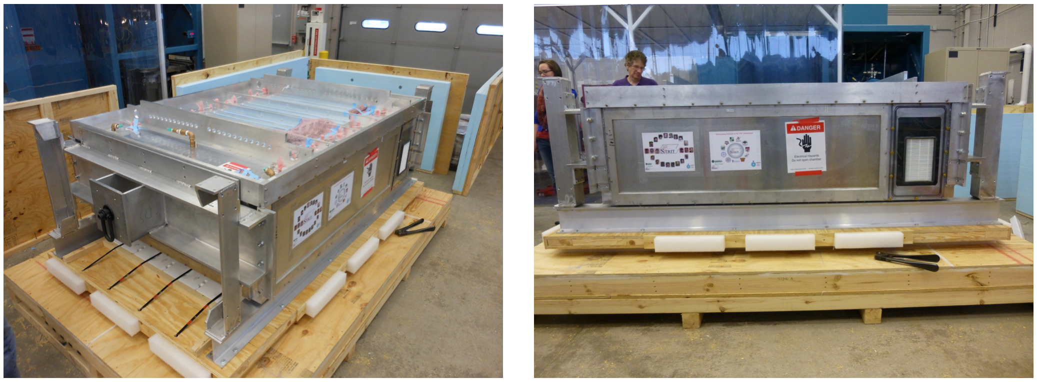

(a) (b)

Figure 2.45: The TPC installed on the crate platform. The bed of phase change material is visible in (a), and the side profile shown in (b) shows one of the HEPA window filters.

were produced specifically for shipment. One of these windows is seen in the right panel of Figure 2.45. The HEPA filters allow the TPC to breathe, while keeping it clean inside. In principle, the gas fittings of the TPC could be fitted with filters to provide breathability; however, the limited size of the gas fittings would restrict air flow. To ensure free exchange of air between the field cage and enclosure, the downstream window was installed with washers between the window frame and field cage, so that the field cage was not isolated from the enclosure volume.

The TPC is made of different materials, many of which are epoxied to each other. Of particular concern, the 4 pad plane sections are made of G10 circuit board and are epoxied to the aluminum top plate. The thermal expansion (or contraction) of these materials could cause the pad plane to separate from the top plate, or to damage the G10 board in such a way that the planarity of the pad plane is compromised. To maintain a constant temperature while shipping, the shipping crate was lined with foam insulation, and the platform had a bed of phase change material (shown in Figure 2.45). Calculations done by Gary Burgess of the MSU Packaging Department verified the quantity of 85 kg of PCM22P recommended

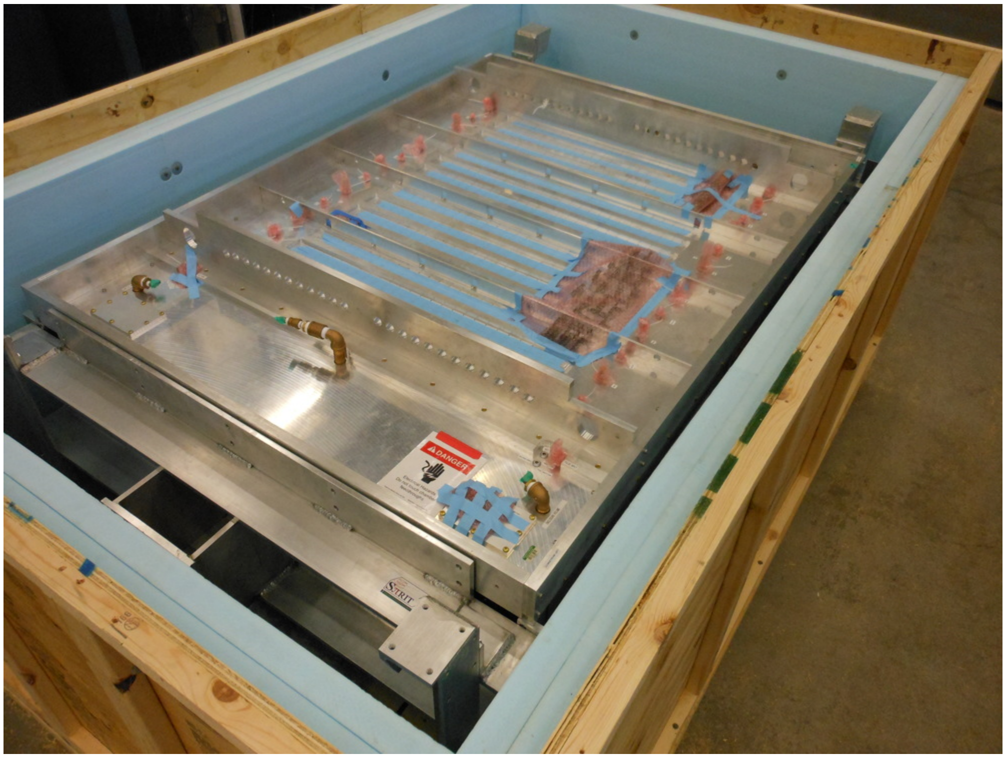

Figure 2.46: The TPC inside the crate with the crate walls installed.

by RGEES. The foam-lined walls are installed after the TPC has been secured to the crate platform, with the installed walls shown in Figure 2.46. The phase change material has a very high enthalpy of fusion, with a melting point just above room temperature. Temperature monitors were installed on the interior and exterior of the shipping crate, to record the minimum and maximum temperatures the TPC was subjected to during the journey.

With the walls and lid of the crate installed, the crate was fully packed and had to be weighed for shipment. The TPC had been previously weighed at about 1000 lbs, and the motion chassis at 294 lbs. The fully packed crate weighed approximately 3200 lbs. In addition to the overall weight, the crate was weighed from each side to determine the center of gravity (COG), which was then marked on the crate exterior. Figure 2.47 shows the crate being weighed (left panel), and one of the COG markings on the crate exterior (right panel). The left panel of Figure 2.47 also shows one of the “TIP N TELL™" indicators which were

(a) (b)

Figure 2.47: Weighing the packed crate. In addition to the overall weight, the crate was measured from each end (a) allowing us to determine and mark the center of gravity (marked with orange paint in (b)).

placed on the crate, and the temperature display, which is linked to the interior temperature monitors. Having these indicators on the outside of the crate allows inspection of the crate without unpacking, which is very important for liability purposes.

Loading and unloading the crate onto trucks required that the crate could be lifted by forklift from any side. When moving the crate with a forklift, it is necessary to strap the crate to the forklift, as a precaution against tipping. The straps are visible in Figure 2.48, prior to tightening. The straps were used regardless of if the crate was forked from the front or side, as is visible in Figure 2.49a, which shows unloading the crate from the side-loaded truck at RIKEN.

Upon arrival at RIKEN, the TPC was lowered to the B2F level of the RIBF building, approximately 22 m below ground level. The crate was allowed to acclimate for 24 hours before it was unpacked. The "TIP N TELL™" indicators did not have any sign of tipping, and the temperature within the shipping crate had varied by only one degree centigrade during shipping. Each wire plane was checked for shorting, and biased to check leakage

Figure 2.48: Strapping the crate to the forklift at the NSCL. Two lifting straps (yellow) are secured to the forklift with a chain, visible on the top of the crate.

(a)

(b)

Figure 2.49: Moving the TPC crate at RIKEN. (a) removing the crate from the side-loaded truck with a forklift, and (b) lowering the crate to the B2F area of RIBF using a crane.

current. The TPC was checked for leaks by pressurizing with P10 and checking all seams and screw holes with a combustible gas detector.

2.12 Disassembly and Reassembly of TPC

It is sometimes necessary to disassemble the TPC to perform repairs, or install upgrades. Structurally, the TPC is formed by two halves: the enclosure, with bottom and side plates attached, and the top plate, with pad plane, wire planes, and field cage attached. To work on components outside the field cage, side windows of the enclosure can be removed by hand for access. To work on components within the field cage, the top plate must be removed from the enclosure, and the field cage removed from the top plate. To work on the wire planes, the top plate should then be rotated to the table configuration.

To disassemble the TPC, care must be taken to avoid damaging any sensitive components. Prior to removing the top plate, gas connections, electrical connections, and target motion peripherals must be removed. If the top plate is to be rotated, the GET electronics must be removed, as well as the gating grid driver. The top plate should be inspected for any loose materials such as screws or tools before removal.

When it is desired to put the top plate in the table configuration, the motion chassis will be installed to the top plate prior to removal, as shown in Figure 2.50. Two lifting straps connect the motion chassis to an I-beam spreader for lifting the top plate, and two lifting straps connect a side of the top plate to a manual chain hoist, to control the rotation. The top plate is lifted from the enclosure using a crane, while at least one person watches from each side of the TPC, to ensure the top plate and field cage slide smoothly out of the enclosure. When the field cage is safely above the enclosure surface, the enclosure can be

Figure 2.50: Lifting the top plate and field cage out of the enclosure.

rolled away. The chain hoist is then used to lift one side of the top plate, rotating to the doorway configuration. Figure 2.51a shows the rotation in progress. With the top plate in the doorway configuration, it is lowered so that the motion chassis wheels are placed on the floor. Lead bricks are placed on the motion chassis as counterweights, to prevent tipping. With the top plate in doorway configuration, the lifting straps are removed and the detector is moved into a clean tent for further disassembly, as shown in Figure 2.51b.

The field cage is removed with the top plate in the doorway configuration. The gas and electrical connections to the top plate must be disconnected. Alternating screws are removed from the field cage, and replaced with set screws and wingnuts. The remaining screws are then removed. With the wingnuts loosened, sheet metal clips, covered with acrylic tape, are inserted around the top perimeter, to hold the O-rings captive. After removing the wing nuts, the field cage can be removed by three people, leaving the Lexan ring in place, as shown in Figure 2.52a. The field cage should remain in the clean environment, with the springs on

(a) (b)

Figure 2.51: Rotating the top plate and field cage (a), and moving the top plate and field cage in doorway configuration (b).

the cathode and the windows protected. A protective cover can then be placed over the wire planes, incorporating the Lexan ring. This cover is shown in Figure 2.52b. The rotation procedure is then repeated to bring the top plate to the table configuration. The reassembly follows the same procedure in reverse.

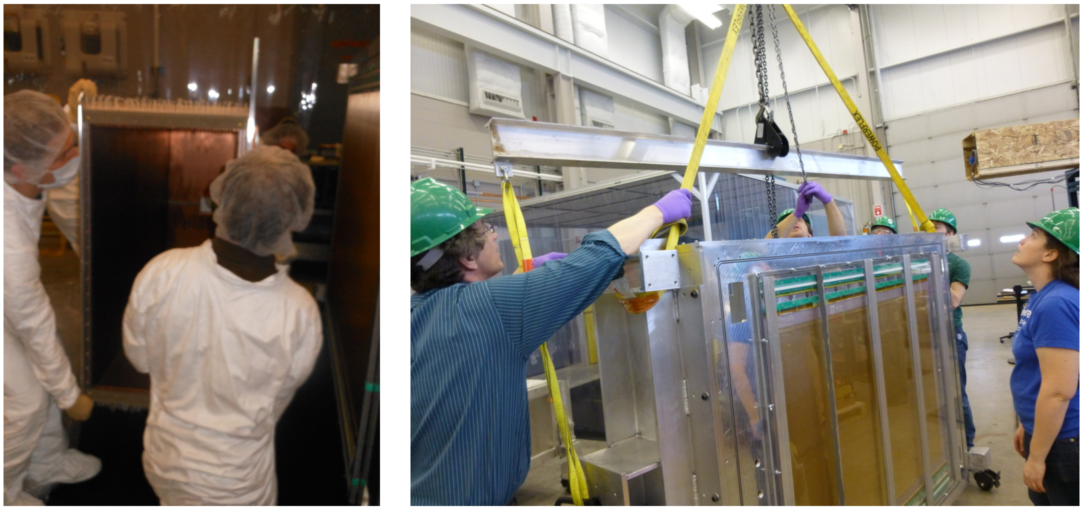

(a) (b)

Figure 2.52: Removing the field cage from the top plate (b), and rotating the top plate without field cage (b).

An alternative disassembly procedure, which did not require rotation, was developed

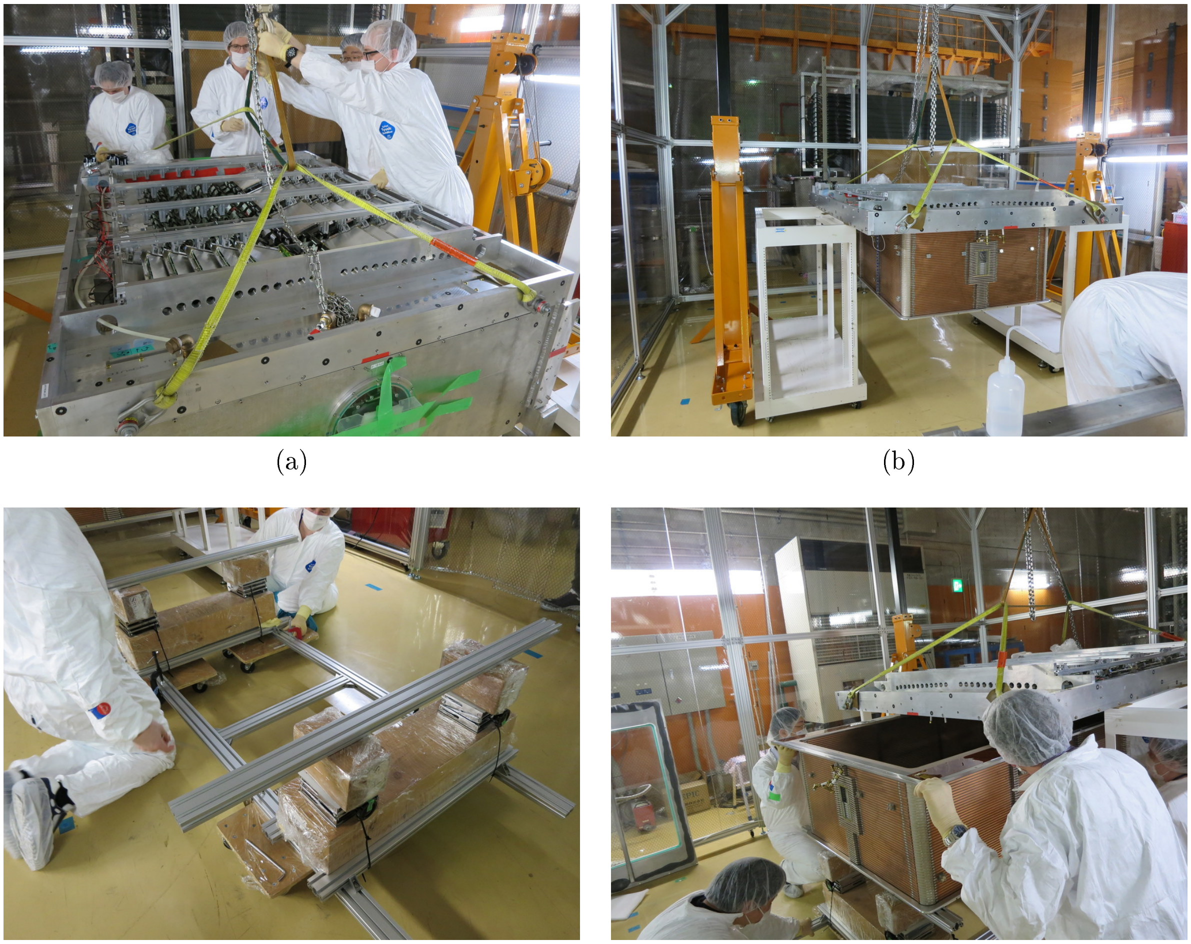
(a) (b) (c) (d)

Figure 2.53: Alternative procedure for removing field cage without rotation: lifting top plate (a), stabilized top plate (b), purpose-built cart for field cage removal (c), sliding the field cage away from top plate (d).

for upgrades to the field cage. This procedure was performed in a clean tent at RIKEN. Although the electrical and gas connections had to be disconnected, the GET electronics did not need to be removed (a significant advantage). A 1000 kg hoist is used, with lifting strap configuration shown in Figure 2.53a. Since the weight of the target mechanism displaces the center of gravity, counter weights are placed on the corners of the top plate to keep it level during the lifting process. The top plate and field cage are lifted above the enclosure, and the enclosure is pulled away on wheels. The top plate is lowered onto two electrical racks

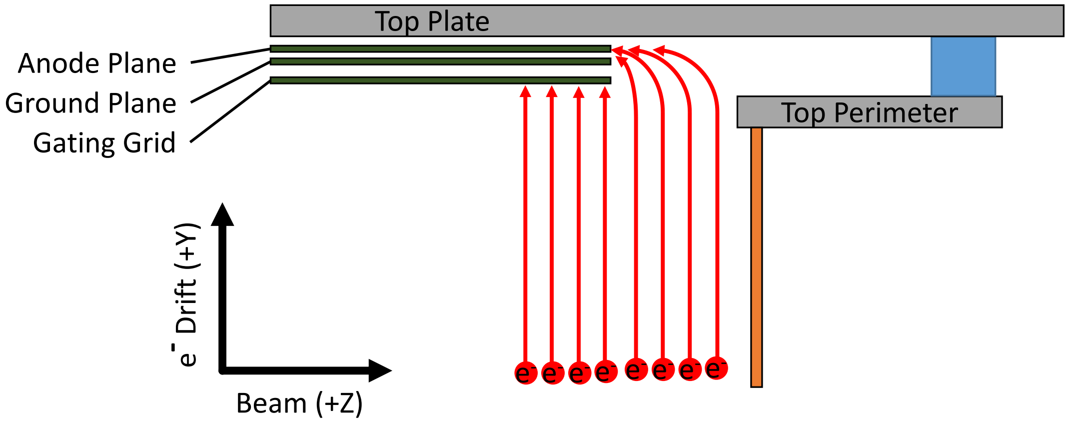

Figure 2.54: Illustration of electron leakage prior to repair.

for stability, as shown in Figure 2.53b. The field cage is lowered away from the top plate using a cart with 4 lab jacks (shown in Figure 2.53c). Aluminum tabs with threaded holes are used to secure the Lexan ring prior to fully removing the field cage. The field cage is then fully removed from the top plate. Figure 2.53d shows the field cage being pulled away.

2.13 TPC Upgrades

After the SπRIT experiment, specific areas for improvement were identified. Two issues were determined to be critical, and solutions were developed and implemented in early 2018. The first issue involved the specific geometry of the field cage, which allowed drift electrons to pass around the gating grid, entering the avalanche region on the downstream end of the wire planes. Thus the amplification in anode plane 14 occurred for all beam particles entering the TPC, potentially inducing space charge effects and detector aging. Further, due to the feed through sharing described in Section 2.7, this electron leakage induced extra current on anode planes 12 and 14. The second issue was difficulty and reliability of target motion. The brass lead screw for X-motion created friction in the motion, as did the motion carriage platform, which tilted when pushed in the Z-direction, causing the X-motion to seize.

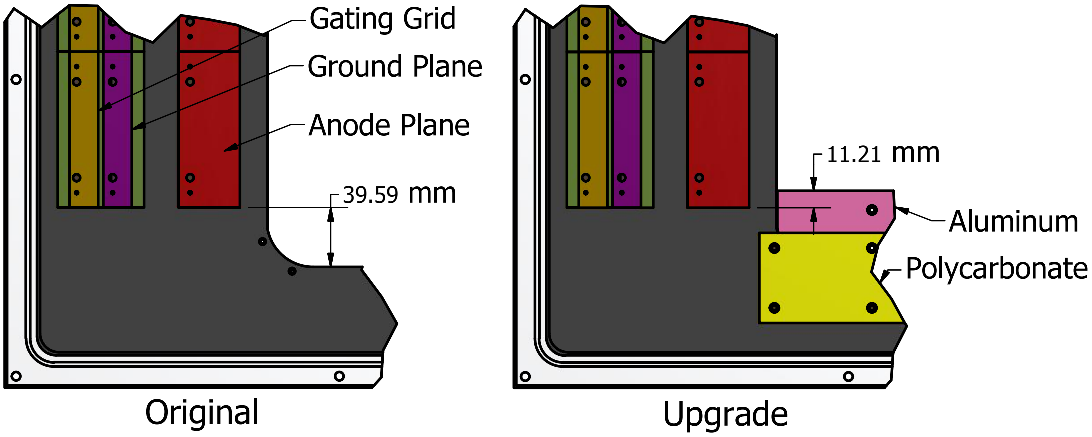

Figure 2.55: Upgrade to prevent leakage around gating grid.

The wire planes do not extend the entire length of the field cage. The gap of less than 4 cm between the wire planes and top perimeter is shown in the left side of Figure 2.55. The problem can be solved by extending the top perimeter to cover the gap, removing the leakage path for drift electrons. The designed upgrade is shown in the right side of Figure 2.55, with an aluminum plate clamped onto the top perimeter of the field cage.

The field cage is removed as described in Section 2.12. The installed aluminum blocking plate is shown installed in Figure 2.56. The polycarbonate plate is screwed to the top perimeter, and used as a reference point for clamping the aluminum blocking plate. The plate is electrically connected to the top perimeter, matching the electric potential.

The upgrades to the target motion focused on two principles: reducing motion resistance, and making the motion transfer structure more sturdy. Motion in the X-axis is controlled using a lead screw and nut, which is shown in Figure 2.57, with the upgraded design installed. The warped brass lead screw increased resistance, as the constrained motion of the motion carriage requires bending the lead screw. Figure 2.58 shows the original fixed nut design, and the updated design, where the nut is free to travel in the Y and Z axis. By accommodating the warping of the lead screw, the resistance is greatly reduced. Although a replacement

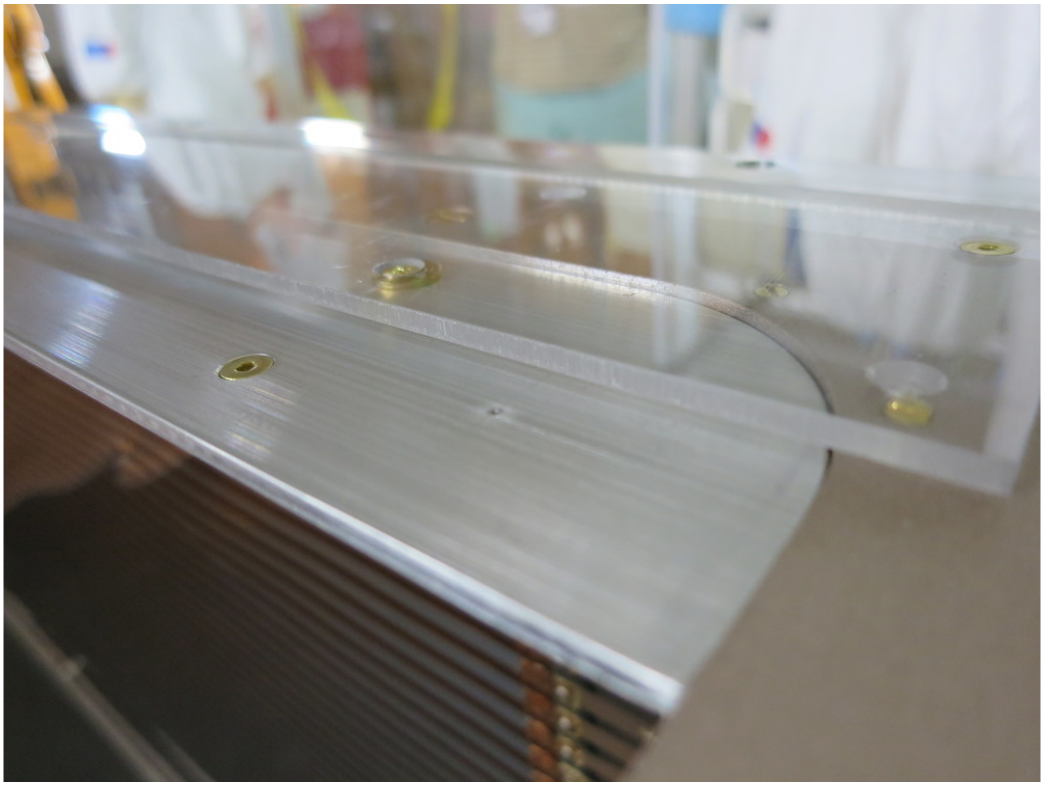

Figure 2.56: The installed field cage upgrade (April 2018).

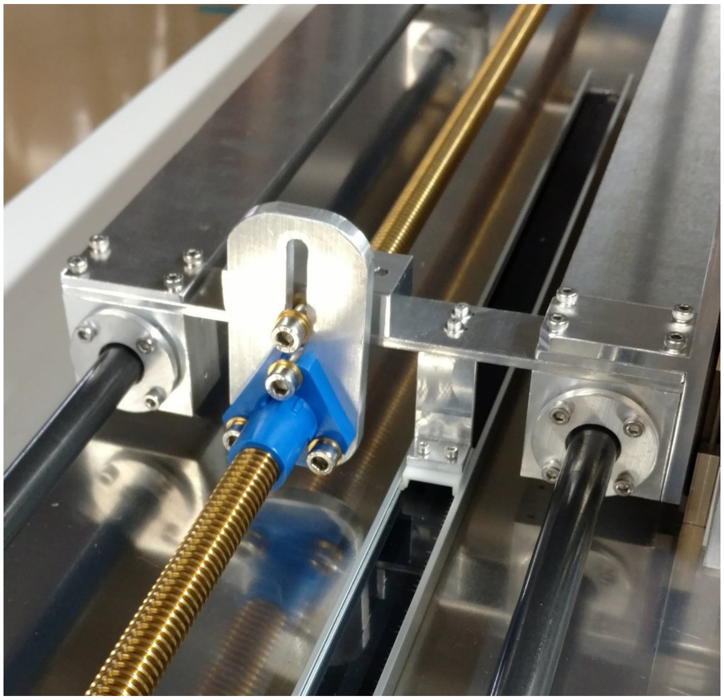

Figure 2.57: The installed target motion nut, which accommodates a warped lead screw (April 2018).

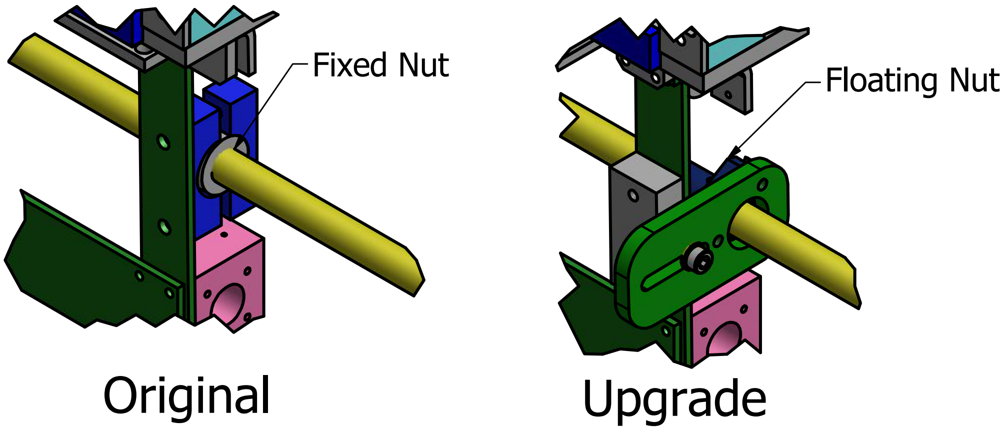

Figure 2.58: Floating lead nut design to accommodate warping of lead screw.

lead screw could be made, it is costlier to produce a new lead screw, and the replacement could also be warped from the machining process.

To traverse the Z-axis, the motion carriage platform moves on two rails on the motion carriage. When the platform is pushed from an off-center point, the platform twists on the rails, greatly increasing motion resistance. This problem also affects the X-motion: the twisting cinches a rod and bearing, causing friction during X-motion. This issue was addressed by creating a motion linking system (design shown in Figure 2.59a), which forces the platform to move equally along its rails. The red bars form a two halves of a rhombus linkage, and the purple bar connects them to form a modified rhombus linkage. The installed upgrade is shown in Figure 2.59b.

Finally, to make the entire design more sturdy, large brass gears were used for every corner, replacing gear boxes entirely. The motion was tested after upgrades and observed to be significantly improved.

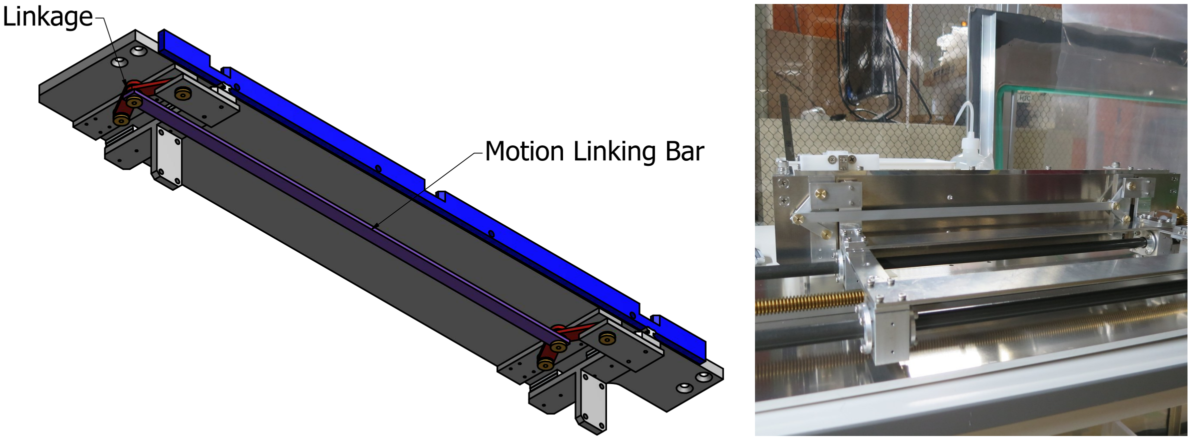

(a)

(b)

Figure 2.59: Motion linking system (a) design and (b) installed.

Chapter 3

Experimental Setup and Trigger Selection

3.1 SπRIT TPC inside the SAMURAI Spectrometer

The SπRIT TPC was previously described in Chapter 2. During the experiment, the TPC was installed inside the SAMURAI Spectrometer at RIKEN. The facility layout will be discussed in Chapter 4. The experimental layout within the SAMURAI area is illustrated in Figure 3.1, with dimensions in mm, and the origin of the SAMURAI coordinate system shown near the center of the figure. It is convenient to use two separate coordinate systems to describe the experimental layout: the SAMURAI coordinate system and the SπRIT TPC coordinate system. The relative position and orientation of these coordinate systems must be known to properly analyze the experimental data.

In the SAMURAI coordinate system, the z-axis is oriented along the beamline axis (not to be confused with the beam axis, which bends inside the magnet), the y-axis oriented anti-parallel to gravity, and the x-axis defined to form a Cartesian system, which sets the x-axis to the beam left side of the beamline axis. The origin lies in the center of the SAMURAI magnet. The SπRIT TPC coordinate system is defined relative to the pad plane, and is illustrated in Figure 2.1. The coordinate system of the SπRIT TPC is nominally aligned

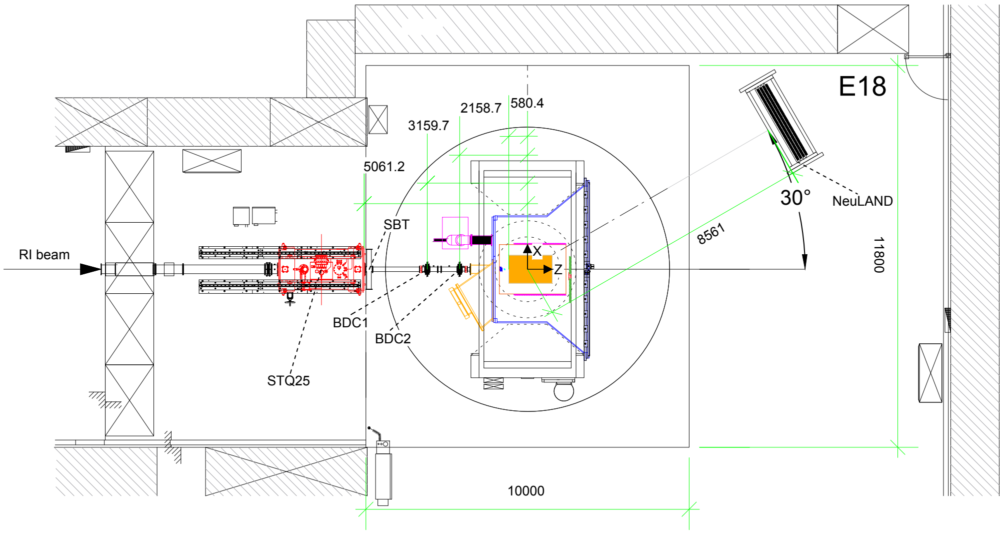

Figure 3.1: Schematic view of experimental layout.

with the SAMURAI coordinate system with some offset; however, some difference in the actual alignment of coordinate systems will be discussed in the following section. The x-z plane of the TPC coordinate system lies on the pad plane, with the y-axis extending above the pad plane, anti-parallel with gravity. The z-axis points towards the downstream side of the pad plane, and the x-axis points to the beam left direction of the pad plane. The origin is set to the center of the pad plane in x, and the upstream edge of the pads in z.

3.2 TPC alignment and Measurement

The initial placement of the detectors is performed using a laser alignment system. Rotating lasers were used to produce reference planes, allowing us to set the level and height of the TPC to match the reported beam height. Fixed markers in the SAMURAI area were used as references for the beamline axis. The TPC was aligned by scribe marks on the enclosure. The TPC enclosure is centered in x of the SAMURAI frame, and lifted to the top of the magnet gap, with a small clearance. The target height is adjustable within the enclosure, and is aligned to be centered at the beam height (y=0 in the SAMURAI frame). The alignment of the target height is shown in Figure 3.2. In the picture, a piece of graph paper was temporarily mounted in the target ladder, facilitating alignment with the laser.

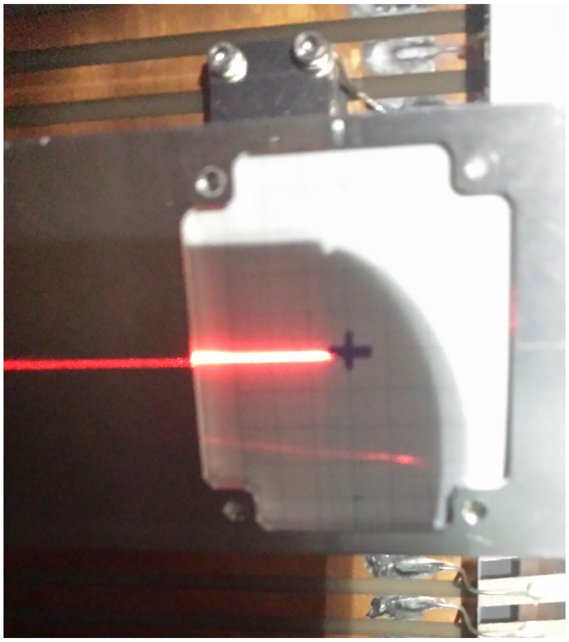

Figure 3.2: Laser alignment of target height

After alignment, the final position of detector systems was determined using a Photogrammetry Measurement (PGM) system called V-STARS, which is produced by Geodetic Systems, Inc. [38]. This technique uses flash photography to light retroreflective markers which are placed on the points to be measured. Figure 3.3 shows the SAMURAI area while the measurement was performed. Two yellow bars near the center of the photo have markers at precise distances, allowing the scale to be determined. Many photographs are taken using a camera which stores information about its angular orientation while taking a photo. The proprietary V-STARS software is used to combine information from the photographs into an array of 3 dimensional points. Fixed reference points in the SAMURAI area are used to transform the measurement into the SAMURAI coordinate system.

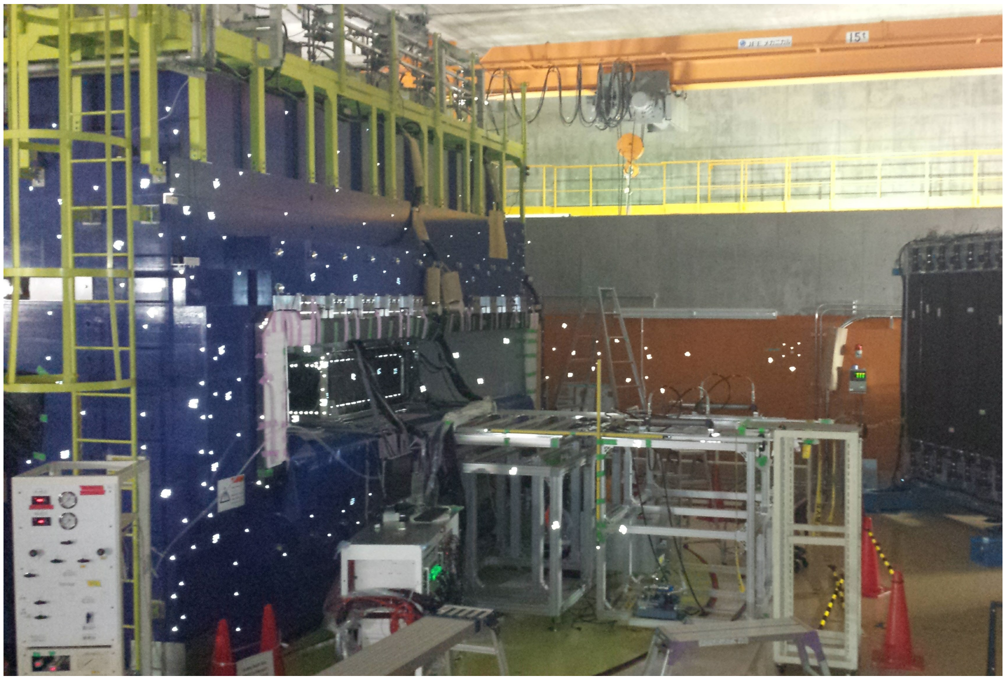

Figure 3.3: Flash photograph highlighting retroreflective photogrammetry markers

A previous PGM measurement of the TPC [39] provided reference points on the TPC, which are used to determine the TPC position in the SAMURAI frame. Even though the trigger detectors obscured most of the markers on the TPC, 15 of the TPC markers were found in the measurement of the TPC in SAMURAI. A numerical analysis was used to minimize the residuals between the two sets of measured points (TPC in SAMURAI, TPC standalone) using singular value decomposition [40], implemented with a Python script. This minimizes the residuals between the measured points in the SAMURAI coordinate system and the reference points, producing a best translation and rotation between the TPC and SAMURAI coordinate systems. Using this best translation and rotation, the origin of the SπRIT TPC pad plane is found to be:

$$(x, y, z) = (1.794, 205.502, -580.526) \text{ mm} \tag{3.1}$$

in the SAMURAI coordinates, defining the relative position of the the origins of the two frames. The error is evaluated as the standard deviation between the measured positions and reference positions, and was found to be

$$(\delta x, \delta y, \delta z) = (0.276, 0.090, 0.443) \text{ mm}. \tag{3.2}$$

The normalized $(\vec{x}, \vec{y}, \vec{z})$ vector pointing from the pad plane origin to the center of the downstream end of the pad plane is

$$(\vec{x}, \vec{y}, \vec{z}) = (3.3397 \times 10^{-4}, -5.946 \times 10^{-5}, 0.9999), \tag{3.3}$$

which defines the z axis of the TPC. The normalized vector pointing from the pad plane origin to the upstream, beam left corner of the pad plane is

$$(\vec{x}, \vec{y}, \vec{z}) = (0.9999, -3.616 \times 10^{-4}, -3.3397 \times 10^{-4}), \tag{3.4}$$

which defines the x axis of the TPC. The y axis thus lies along the normalized vector

$$(\vec{x}, \vec{y}, \vec{z}) = (3.606 \times 10^{-5}, 0.9999, 5.968 \times 10^{-5}). \tag{3.5}$$

The rotation matrix from SAMURAI frame to TPC frame is then

$$\begin{pmatrix} x'' \\ y'' \\ z'' \end{pmatrix} = \begin{pmatrix} 1 & 3.616 \times 10^{-4} & -3.34 \times 10^{-4} \\ 3.616 \times 10^{-4} & 1 & 5.934 \times 10^{-5} \\ 3.34 \times 10^{-4} & -5.946 \times 10^{-5} & 1 \end{pmatrix} \begin{pmatrix} x \\ y \\ z \end{pmatrix}, \tag{3.6}$$

where the unprimed coordinates align with the SAMURAI frame, and the double-primed coordinates are aligned with the TPC frame.

3.3 Trigger Detectors

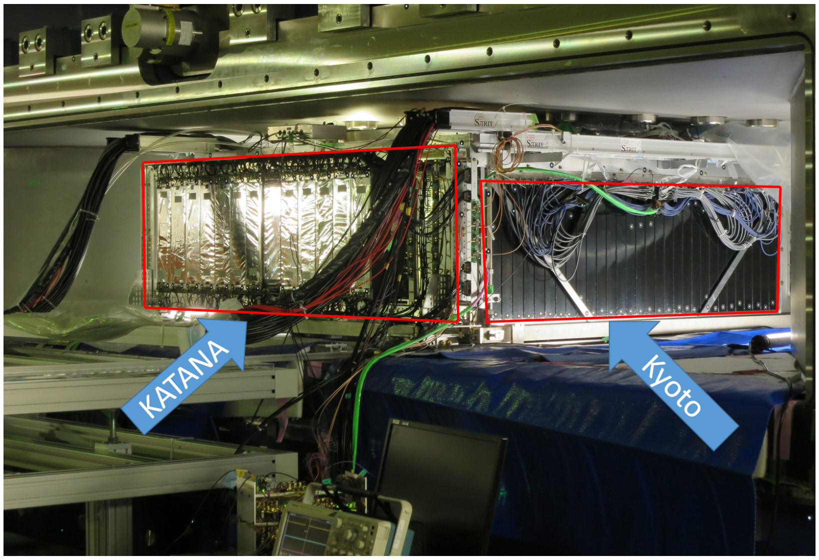

Figure 3.4: Photograph of the TPC and ancillary detectors installed in the SAMURAI spectrometer.

To create a physics trigger, ancillary detector systems are used. Figure 3.4 shows the TPC installed inside the SAMURAI spectrometer with the trigger detectors. The KATANA array scintillators are located on the downstream end of the TPC and are covered with a reflective wrapping, while the Kyoto Multiplicity Array scintillators are located on the beam left and right sides of the TPC and have an additional black plastic wrapping. The Active Veto Array and Scintillating Beam Trigger array are not visible in the figure.

3.3.1 Scintillating Beam Trigger

The Scintillating Beam Trigger (SBT) array serves as a start counter. The SBT array consists of two thick plastic scintillators mounted in parallel, as shown in Figure 3.5. Each scintillator is read out on the left and right by PMTs. The SBT is mounted approximately 4.5 m upstream of the target, transverse the beam pipe, shown in Figure 3.5. The logical OR of the PMTs is used to provide a start signal for the trigger.

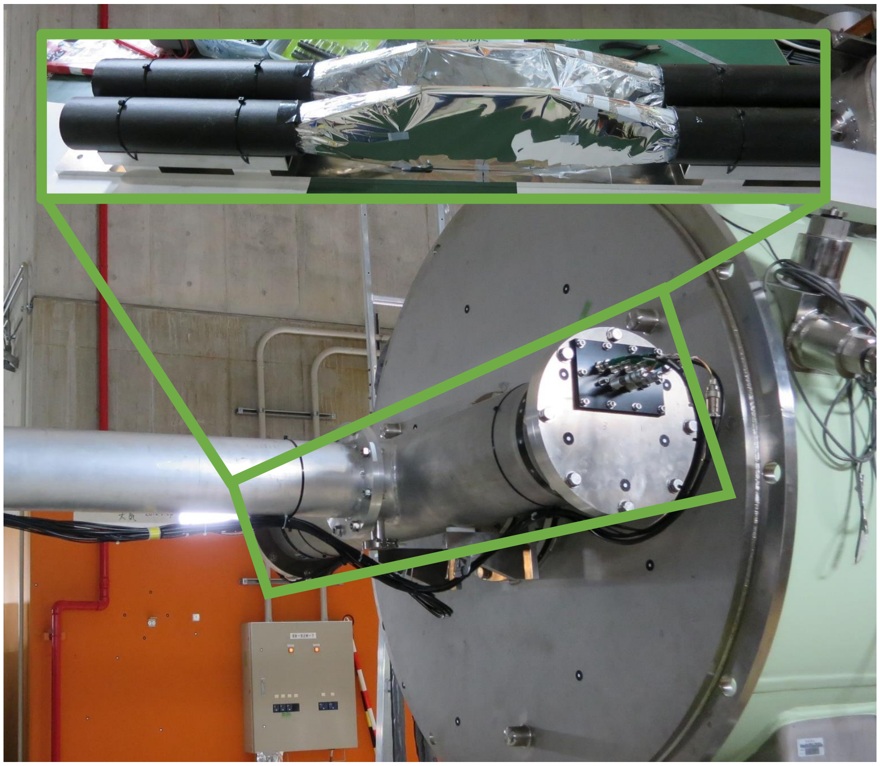

Figure 3.5: SBT array

3.3.2 Kyoto Multiplicity Array

The Kyoto Multiplicity Array [41] consists of two scintillator arrays, each containing 30 plastic scintillator bars. Figure 3.6 shows the schematic drawing of the TPC with the Kyoto Multiplicity Array installed. Only one side is visible, with the Kyoto Multiplicity Array bars shaded gray in the illustration. The second array is mounted on the opposite side of the TPC. The ∼1.5 mm thick G10 field cage walls and ∼0.8 mm thick aluminum enclosure windows allow charged particles from the heavy ion collisions to be detected by the scintillating arrays. Each scintillator bar is $450\times50\times10$ mm^3, with 1 mm diameter light guide fiber placed inside a 1.5 mm diameter hole running through the center of the bar. Each bar is coated with oxidized titanium for light reflection. The light from the light guide fiber is detected by a 1.3 mm^2 Hamamatsu Multi Pixel Photon Counter (MPPC), which, unlike normal photomultiplier tubes, can function inside the magnetic field.

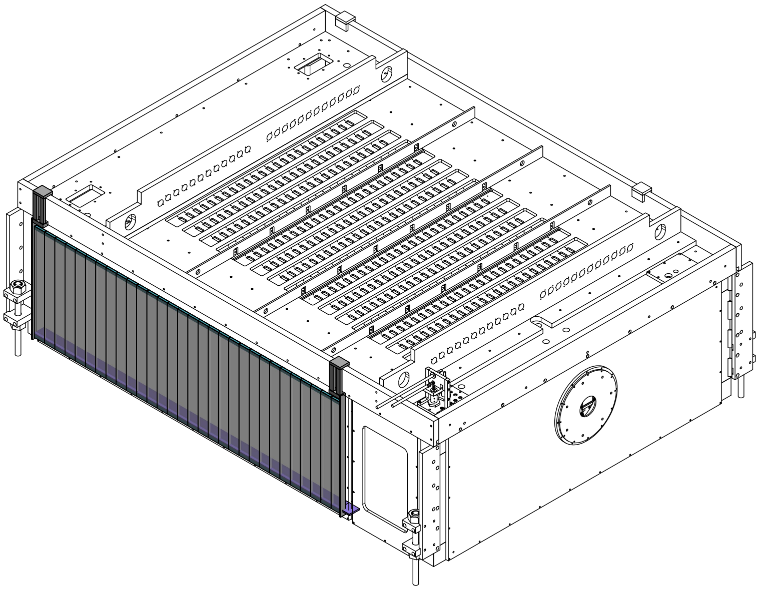

Figure 3.6: Design drawing of the Kyoto Multiplicity Array mounted on the TPC

The MPPC signals are shaped and discriminated using EASIROC [42] chips, ASIC chips designed specifically for silicon photomultiplier detectors. To process the digital outputs from the EASIROC chips, and to control the chips, an FPGA chip is integrated with each EASIROC chip. Discriminators within the EASIROC chip will produce a digital signal associated with each MPPC signal, and the FPGA chip will determine the total number of signals produced in each event, providing a multiplicity measurement from the Kyoto Multiplicity Array. The FPGA is able to achieve the fast response required for triggering by determining the multiplicity through ROM settings and adder circuits [41]. Additionally, a multi-hit TDC with 1 ns time resolution was implemented with the FPGA chip, allowing more detailed offline analysis of the hits on the Kyoto Multiplicity Array. For the SπRIT experiment, the typical multiplicity requirement was 4 or greater within the Kyoto Multiplicity Array.

3.3.3 Krakow KATANA Array

The KATANA array [43] consists of 12 plastic scintillating paddles, each $400\times100\times10$ mm^3 in size, and 3 thin plastic scintillating paddles, $400\times100\times1$ mm^3 in size, placed at the downstream edge of the TPC. The design of the KATANA array is shown in Figure 3.7, viewed from the downstream perspective. The left side shows the entire array, while the right side shows the array without thick paddles. The thin veto paddles are installed in an overlapping fashion to maximize detection efficiency. There are 7 thick paddles on the beam right side of the center veto paddle, and 5 on the beam left side. This asymmetry is chosen since most particles produced will have positive charge, and bend towards the beam right side. For each beam, the array position is optimized so that the center veto paddle intersects the path of the unreacted beam.

The threshold on the veto paddles is chosen to provide a veto signal whenever a beam particle or fragment with charge $Z \approx 20$ or greater passes through. The light signal in each scintillator is collected using MPPCs: on the thick paddles, a Hamamatsu S 12572-025P MPPC is placed on the top and bottom of each paddle, while on the thin paddles, a Hamamatsu S 12571-010P MPPC iss placed on all four corners of each paddle. The MPPCs are mounted to a printed circuit board with a preamplifier, to minimize noise.

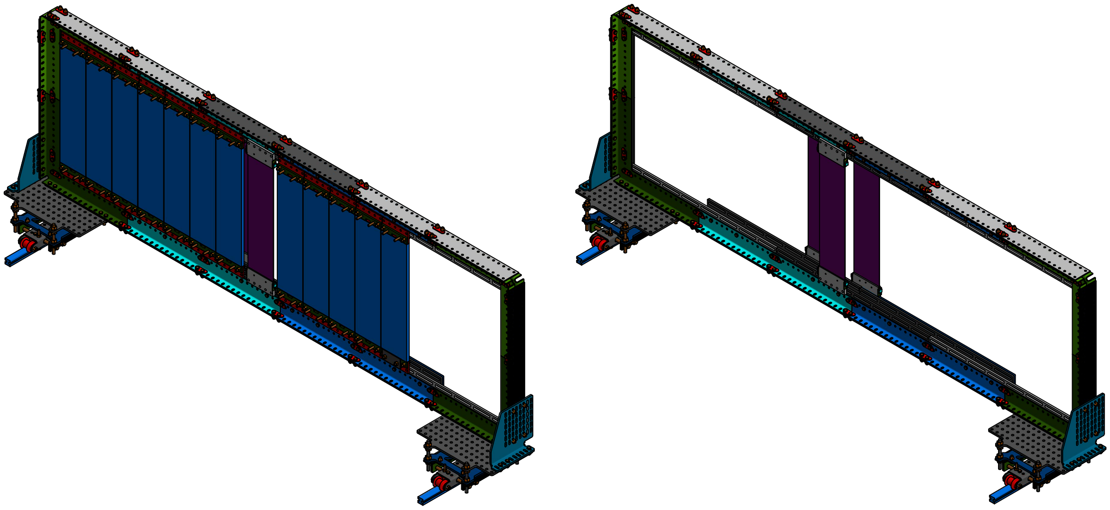

Figure 3.7: Design drawing of the KATANA array. Thick scintillators are shown in blue and veto scintillators are shown in purple. The left side shows the entire array, and the right side shows the array with veto paddles isolated

The analog MPPC signals from each paddle are summed to produce a single signal, with a normal and an inverted signal output. The negative signals are sent to a 20-channel discriminator board with leading edge discriminators, and compared to threshold levels which are set remotely. The resulting logic signal is analyzed with a logic circuit made with an FPGA board, which analyzes the 15 signals produced from KATANA paddles, as well as other logic signals used for the trigger. Gate&Delay (G&D) modules are programmed into the FPGA board, allowing proper synchronization of signals for logic processing. The delay durations, gate widths, as well as the KATANA multiplicity threshold, are controlled remotely with a RaspberryPi board [44]. The discriminator board, FPGA board, logic output buffers, and the RaspberryPi controller are integrated into a single unit, referred to as the “Trigger Box". The resulting “Trigger Box" trigger is incorporated into a separate trigger logic, described in Section 3.4.4. For further information on the KATANA array and the Trigger Box, readers are referred to Reference [43].

3.3.4 Active Veto Array

The Active Veto Array [45] consists of four plastic scintillators, each 90×50×6 mm^3 in size, placed on the upstream edge of the TPC entrance window to remove events where the beam particle is off-target. Each scintillator uses a Hamamatsu S10931-100P MPPC to generate a signal when a charged particle passes through, with the same preamplifier PCBs which were used for the KATANA array. Signals from the Active Veto Array were discriminated by the Trigger Box. The scintillators are arranged in an overlapping fashion, forming a profile around the beam path, with empty space. The Active Veto Array assembly is shown in Figure 3.8, with an aluminum housing fixture. The top and bottom scintillators are placed with 38 mm of separation, and the left and right are placed with 26 mm of separation. The overall position of the left and right was set to allow desired beams to pass through and hit the target without adjustment between settings. The paddle positions are all adjustable, to accommodate different target sizes as well as different beam rigidities.

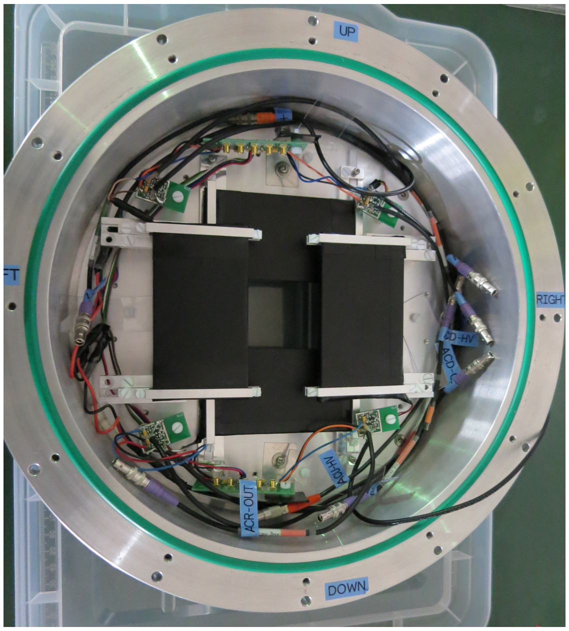

Figure 3.8: Photograph of the Active Veto Array.

The Active Veto Array is fixed to the front plate of the TPC, as shown in Figure 3.9 with a break-out view. The aluminum housing is shown in turquoise blue while the scintillators are shown in purple. In our setup, there is 23.8 cm between the field cage entrance window and the left/right scintillators, and 22.2 cm between the field cage entrance window and the up/down scintillators. The inner edge of the left scintillator is positioned 21 mm to the left of the center of the TPC, and the inner edge of the right scintillator is placed 5 mm to the right of the center of the TPC. The beam enters the TPC to the left of target center, and is curved to target center by the magnetic field.

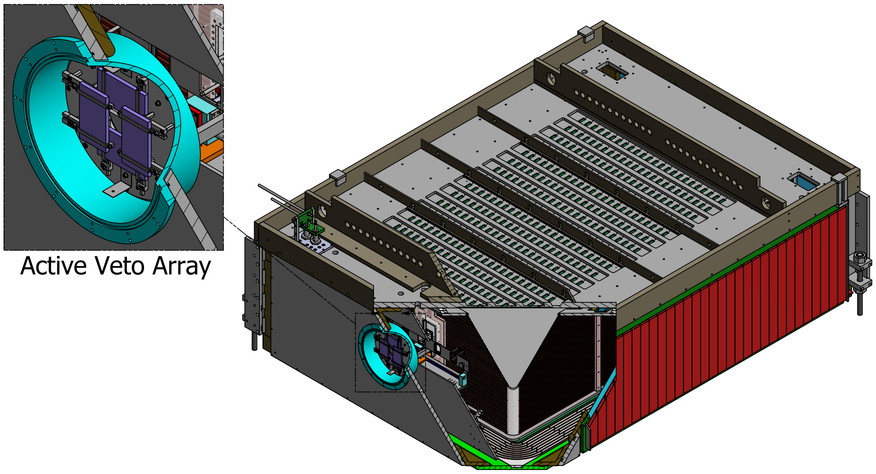

Figure 3.9: Break out view of the TPC with Active Veto Array installed

3.4 Trigger Selection

The trigger controls the selection of events and controls the opening and closing of the gating grid. The trigger is designed to maximize the selection of central, on-target reactions, while minimizing the selection of peripheral or off-target events. The Active Veto Array is used to reject off-target events from the trigger, while the KATANA Veto is used to reject events with unreacted beam particles. A minimum multiplicity requirement from the Kyoto Multiplicity Array is imposed, to select central events. A preliminary trigger, or Fast Trigger (Section 3.4.1), is produced with rack electronics. The gating grid is opened upon receiving a fast trigger, which must be validated by a trigger from the KATANA Trigger Box. If the latter is not produced, the trigger is fast-cleared, closing the gating grid. The trigger can also be vetoed by a KATANA Veto signal, which would indicate the presence of a second beam particle or heavy projectile residue. A busy circuit prevents the formation of a trigger while the DAQ is writing, or if the system is otherwise unable to record an entire event.

3.4.1 Fast Trigger and Fast Clear

The fast trigger is necessary to begin opening the gating grid as quickly as possible. The fast trigger is made with rack electronics, requiring a Scintillating Beam Trigger (SBT) signal in coincidence with the Kyoto multiplicity signal, without a KATANA Veto signal or a busy signal. The gate for the KATANA Veto is 4 µs wide. This introduces a deadtime of 4µs, which corresponds to the time for the charge induced by a beam particle to be safely collected by the closed gating grid. This is necessary to prevent the charge produced by an earlier beam particle from passing through the gating grid and reaching the anode plane in the case that a subsequent, otherwise trigger-satisfying, reaction occurs before the charge from the first beam particle has dissipated.

One key difference should be noted between the two experiments: for the ^{124}Xe primary beam (the first experimental run), the KATANA Veto signals are discriminated in the rack trigger, while for the ^{238}U primary beam (the second experimental run), the KATANA Veto signals are discriminated in the KATANA trigger box. The fast trigger is diagrammed in Figure 3.10.

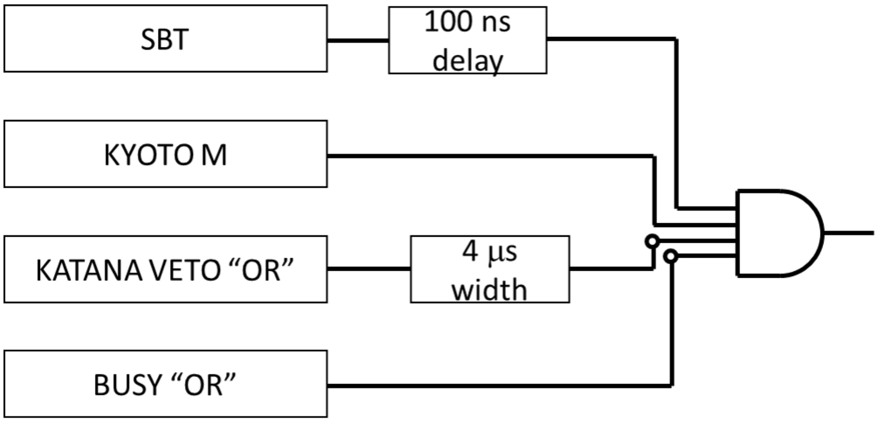

Figure 3.10: Fast trigger logic

If a fast trigger is produced without a Trigger Box trigger, the signal is fast cleared. The fast clear circuit allows the gating grid to be quickly closed if an event is not recorded, which prevents unnecessary charge amplification, and reduces the trigger deadtime by limiting unnecessary busy time. This occurred on the order of a 2-10 Hz, depending on beam rate. The fast clear logic is shown in Figure 3.11, with the KATANA Trigger Box abbreviated as K-Box Trigger.

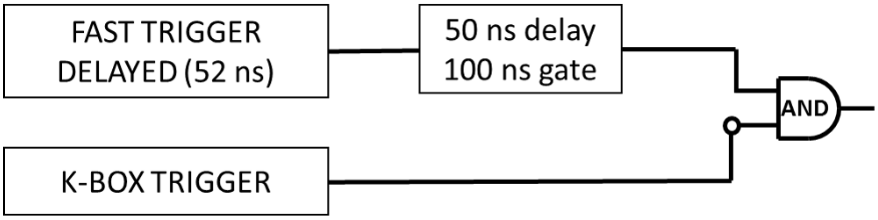

Figure 3.11: Fast clear logic

3.4.2 GGD Logic

The opening and closing of the GGD is controlled through Transistor-Transistor Logic (TTL) signals. The control circuit within the trigger was formed using two LeCroy Model 222 Dual Gate Generators, for a total of 4 distinct G&D modules. For clarity, these will be referred

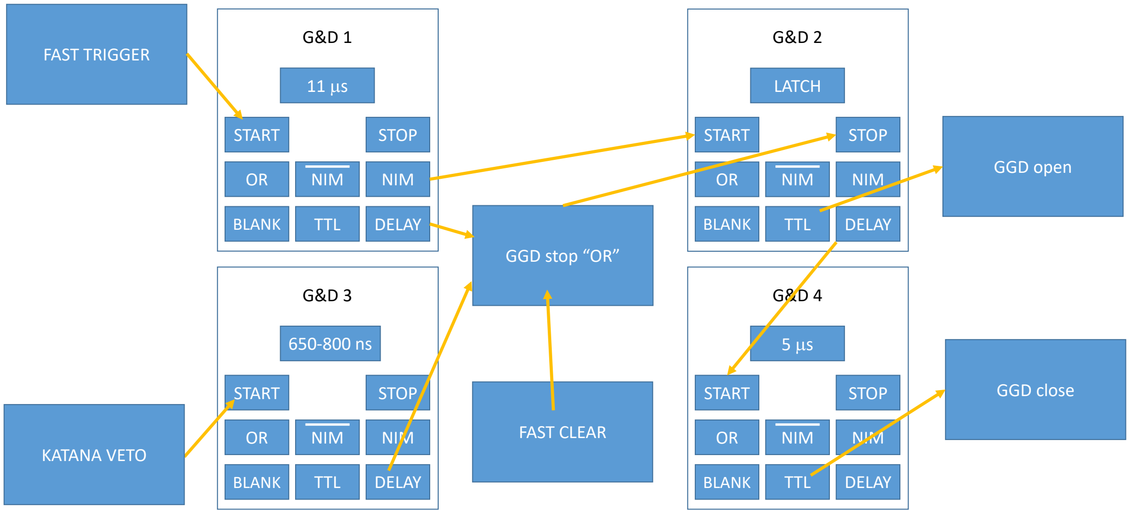

Figure 3.12: Gating Grid Driver Logic

to by G&D 1-4. The logic is illustrated in Figure 3.12. It is perhaps easiest to understand by examining G&D 2 first, which is a latch circuit. When the latch is open, a TTL signal is provided to the "open" input of the GGD. When the latch is closed, the TTL signal is removed from the GGD open, and the delay signal is sent to G&D 4, which sends a 5 µs wide signal to the "close" input of the GGD. The "start" for G&D 2 is provided by G&D 1, which sends a signal when a fast trigger is made. The "stop" for G&D 2 is provided by the GGD stop "OR" circuit. To summarize the logic so far: a fast trigger will start the opening process, and a GGD stop "OR" signal will remove the "open" signal, while sending a 5 µs wide "close" signal to the GGD.

The GGD stop "OR" circuit is triggered by any of three conditions: (i) the G&D 1 delay, which sends a signal 11 µs after a fast trigger is received, (ii) a fast clear, described in the previous section, or (iii) by the G&D 3 delay, which is triggered when a KATANA veto signal is provided. The G&D 3 delay was tuned to 650 ns during the ^{124}Xe primary beam experiment, and 800 ns for the ^{238}U primary beam experiment. An additional difference between the two primary beams was the discrimination of the KATANA veto signals: For the ^{124}Xe primary beam experiment, the KATANA Veto signals are discriminated in the rack trigger, while for the ^{238}U primary beam experiment, the KATANA Veto signals are discriminated in the KATANA trigger box. The thresholds for the rack and trigger box discriminators were similar, but the trigger box discriminators are remotely adjustable, and are used in the determination of the trigger for the DAQ.

3.4.3 Busy Circuit

The busy circuit prevents a trigger from being formed when the DAQ or the TPC is unable to handle a trigger. The DAQ produces its own busy, but this must be combined with busy signals for the GGD. The 11 µs gate from G&D 1 and the 5 µs gate from G&D 4 are both included in the busy circuit with the DAQ busy. The fast trigger will then produce an 11 µs busy, while any GGD stop “OR" signal will produce a 5 µs busy. When a master trigger is produced, it will produce a busy signal, bridging any delay between the formation of a trigger and the DAQ busy signal.

3.4.4 KATANA Trigger Box

The KATANA trigger box combines a 20-Channel discriminator board, an FPGA board, logic output buffers, and a RaspberryPi board to form a remotely programmable logic circuit [43]. A comprehensive diagram of the trigger box architecture is shown in Figure 3.13. This documentation focuses on the “Trigger Logic" portion of this diagram. The logic circuit used within the trigger box is similar to the fast trigger, with the addition of the Active Veto signal. The trigger logic is shown in Figure 3.14, with delays and gate widths.

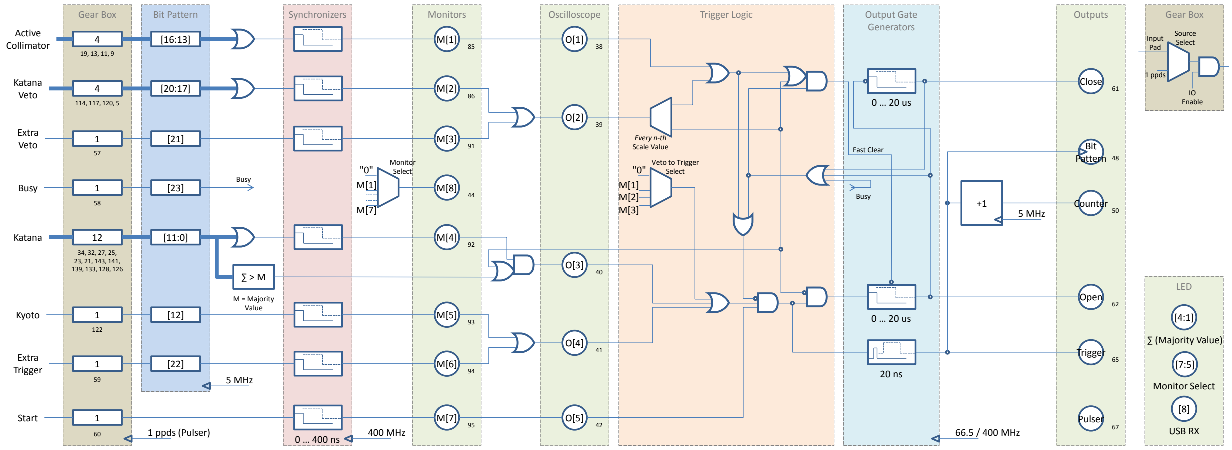

Figure 3.13: KATANA Trigger Box architecture

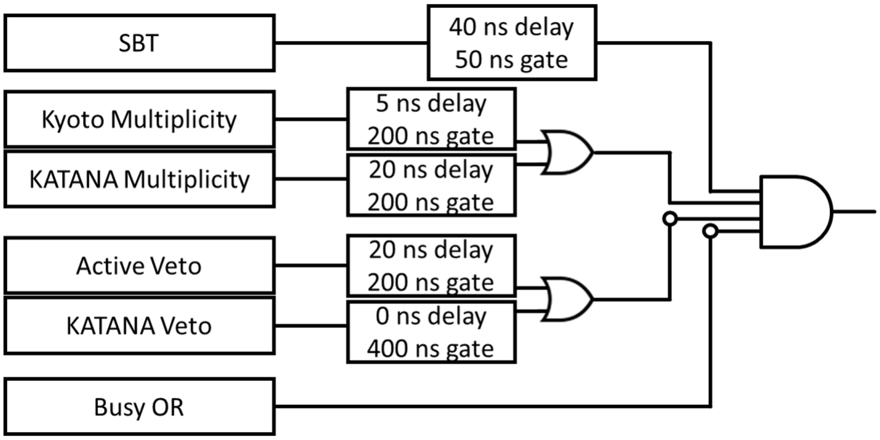

Figure 3.14: KATANA Trigger Box logic

3.4.5 Trigger for DAQ

The Master Trigger, or the trigger required for DAQ readout, closely resembles the fast trigger circuit, with the addition of the KATANA Box Trigger, and without the veto or busy as direct inputs. The veto and busy signals are processed within the KATANA box trigger. The logic for the ^{124}Xe primary beam experiment is shown in Figure 3.15, and the logic for the ^{238}U primary beam experiment is shown in Figure 3.16. The only difference is that for the second experiment, the Kyoto Multiplicity requirement is removed. The reason for this difference is discussed in the following section. For the function of the trigger, it is sufficient to note that this difference did not affect the data taken.

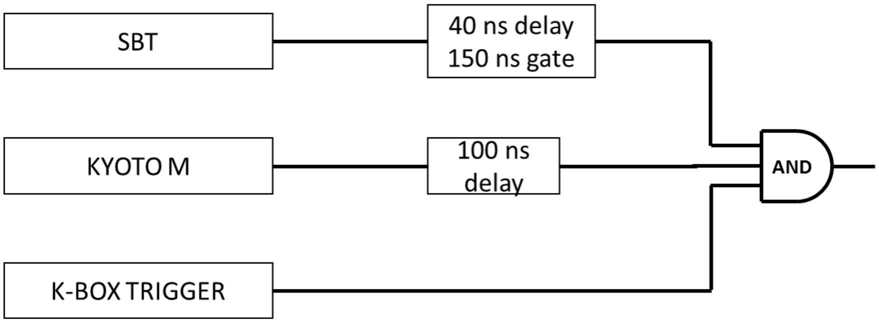

Figure 3.15: Logic for Master Trigger, or DAQ trigger, during the ^{124}Xe primary beam experiment

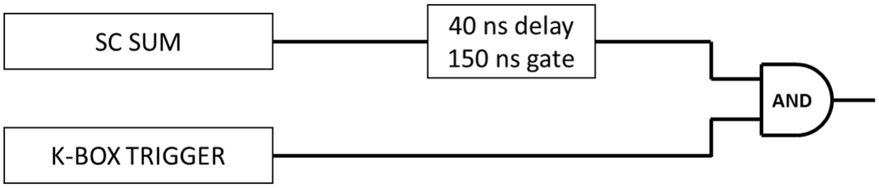

Figure 3.16: Logic for Master Trigger, or DAQ trigger, during the ^{238}U primary beam experiment

3.4.6 Differences Between Primary Beam Triggers

As discussed in the preceeding section, the trigger had some differences between the two experiments. A summary of the differences is provided here for ease in comparing the two triggers. For brevity, the ^{124}Xe primary beam experiment will be referred to as the first experiment, and the ^{238}U primary beam experiment will be referred to as the second experiment.

The first difference is the discrimination of the KATANA Veto: in the first experiment, the KATANA Veto is discriminated in the rack electronics for the fast trigger and the GGD closing, while it is discriminated in the trigger box for formation of the Master Trigger. If the discrimination in the rack electronics is more sensitive than in the trigger box, a

Master Trigger can be formed while the gating grid has not been opened. If the trigger box discrimination is more sensitive than the rack electronics, the gating grid may be opened for an event which will not form a Master Trigger. The first case can result in taking data which is not usable, while the second case will increase the rate of GGD opening and closing. In the second experiment, we addressed this issue by discriminating the KATANA Veto signal only within the trigger box, providing a consistent condition for the GGD and Master Trigger.

The second difference is the delay from the KATANA Veto OR to the GGD stop: in the second experiment, this delay was reduced from 800 ns to 650 ns, to account for any extra delay from the trigger box discrimination. This change is not likely to have a major influence on the data taken, but likely causes a small difference in the time required for a fast closing.

Finally, the Kyoto Multiplicity requirement was directly included in the Master Trigger for the first experiment, but was removed for the second experiment. During the first experiment, this requirement was necessary due to an issue within the KATANA trigger box, which “ORs" the KATANA multiplicity and Kyoto Multiplicity requirement. The KATANA Multiplicity requirement was initially set to $\geq$20, which would theoretically prevent the requirement from being satisfied; however, the multiplicity was stored as a 4-bit number in the trigger box. The binary number 00010100 = 20 was cut off to be 0100 = 4, resulting in triggers for multiplicity $\geq$4. This resulted in KATANA trigger box triggers without the Kyoto Multiplicity requirement being fulfilled. The addition of the Kyoto Multiplicity requirement directly in the Master Trigger circuit was necessary before solving this issue, but the problem was understood during the first experiment, allowing us to remove the requirement from the Master Trigger circuit for the second experiment.

3.5 Other Ancillary Detectors

3.5.1 Beam Drift Chambers

Two Beam Drift Chambers (BDCs) are employed around focal plane F13, upstream of the SAMURAI spectrometer. The detectors are Walenta-type wire chambers [46] with 2.5 mm drift lengths, allowing for high beam rates. A detailed description of technical properties of the BDCs can be found in Reference [28], along with schematic figures of the detectors. Key details include the effective area of 8×8 cm^2 and effective resolution of approximately 100 µm (rms). BDC1 and BDC2 are denoted in Figure 3.1, as well as their positions, measured relative to the origin of the SAMURAI coordinate system. The center of BDC1 is 3159.7 mm upstream of the SAMURAI origin, while the center of BDC2 is 2158.7 mm upstream of the SAMURAI origin. The information from these detectors is used to reconstruct the beam trajectory as it enters the SAMURAI spectrometer. This information, along with beam information from BigRIPS and the magnetic field map for SAMURAI, is used to determine the beam trajectory at the target plane. The BDC analysis is described in Chapter 4.

3.5.2 NeuLAND Array

The partial New Large-Area Neutron Detector(NeuLAND) [47] was positioned at a 30° angle relative to the beamline axis, as shown in Figure 3.1. The setup utilized 400 plastic scintillator bars [48]. Figure 3.17a shows the partial NeuLAND array. Each of these scintillators have a cross section of 5 cm × 5 cm, with a length of 250 cm. Each scintillator is read out with photomultiplier tubes at the far ends. There are 8 planes of 50 bars each, arranged with alternating horizontal and vertical orientations. A plane of 8 veto scintillators from NEBULA [49], each 1 cm thick, is fixed in front of the NeuLAND array, which is used to identify and remove signals from charged particles. The veto scintillator array is shown in Figure 3.17b. The minimum distance from the center of the SAMURAI spectrometer to the NeuLAND neutron walls was measured to be 85.6 cm, and the precise angle was measured to be 29.6°, providing angular coverage from approximately 22° to 43° in the laboratory frame.

(a) (b)

Figure 3.17: The partial NeuLAND array is shown in (a), and the charged particle veto array borrowed from NEBULA is shown in (b)

3.6 DAQ

The Data AcQuisition (DAQ) for the experiment consisted of three separate systems. The RIBFDAQ system using the babirlDAQ framework[50] collected data for BigRIPS detectors, SAMURAI detectors, the NeuLAND detector, and the Kyoto Multiplicity Array. The NARVAL [51] DAQ framework is employed to read out the GET electronics for the SπRIT TPC (see Section 2.3). The KATANA array and Active Veto array are handled by the KATANA system. Synchronization of the separate DAQs was achieved by supplying the same trigger to each subsystem with the General Trigger Operator (GTO) [52] event handling module.

The babirlDAQ framework is used for the RIBFDAQ, which handled event building for all beamline detectors, as well as the NeuLAND array and Kyoto Multiplicity Array. When the common trigger is provided by the GTO event handling module, the RIBFDAQ reads data from all modules in parallel. For each module, a Slave event builder creates a sub-event which is sent to a Master event builder, which writes all information in an event. A system busy is produced from the logical OR of all modules in the system.

The TPC data is handled with the NARVAL DAQ framework, which can handle the large amounts of data produced by the GET electronics. Up to 1.2 GByte/s of data from the GET electronics is saved to local DAQ servers using the NARVAL system, and the data is copied from the DAQ servers to the RIKEN HOKUSAI-GreatWave high performance computing cluster storage through a 10 Gbps network for offline analysis and tape backup.

Data from the KATANA array and Active Veto Array are saved by a separate DAQ, after signal processing by a Flash ADC board within the KATANA trigger box. For each paddle, the signals from all MPPCs for that paddle were summed and digitized, resulting in one data point for each paddle.

Chapter 4

Data Analysis

The data analysis can be divided into two main categories: beam analysis and TPC analysis. The beam analysis is necessary for tagging the PID of incoming beam particles and determining their energy and angle of incidence at the target. The TPC analysis is necessary to determine the PID, magnetic rigidity, and angle of emission for particles produced in the beam-target reaction. The TPC analysis also provides an event vertex, which is combined with the beam analysis when determining the absolute cross section for measured reactions.

4.1 RIBF Facility and Production of Primary Beam

The heavy-ion beams used for the experimental campaign with the SπRIT TPC were produced at the Radioactive Isotope Beam Factory (RIBF) at the RIKEN Nishina Center for Accelerator-Based Science in Wako, Japan. The beams used in the first SπRIT TPC experimental campaign are tabulated in Table 4.1. The ^{132}Sn and ^{108}Sn beams impinged on isotopic Sn targets are used to probe a wide range of asymmetry, $\delta = \frac{N-Z}{A}$, with the same Coulomb forces present in each system. The ^{124}Sn and ^{112}Sn beams are impinged on ^{112}Sn and ^{124}Sn isotopic targets, respectively, to provide direct comparisons between the two primary beams, and to provide a probe at the mid range of asymmetry probed by the other beams. The Z≈1-3 cocktail beams (tuned for α particles at specific momenta) provide momentum and energy loss calibrations for the TPC.

Primary Beam Isotope	Secondary Beam Desired Isotope	Energy at mid target (MeV/u)	Intensity (kHz)
^{238}U	^{132}Sn	269.2	9.5
^{238}U	^{124}Sn	270.3	9.1
^{124}Xe	^{112}Sn	270.4	7.6
^{124}Xe	^{108}Sn	269.3	7.5
^{238}U	Z≈1−3	≈300	0.6
^{238}U	Z≈1−3	≈100	0.09

Table 4.1: Beams used in the SπRIT TPC experimental campaign

The primary beams ^{238}U and ^{124}Xe were accelerated using mode 1 of the RIBF heavy-ion accelerator system, shown in Figure 4.1. The 28 GHz Superconducting Electron Cyclotron Resonance Ion Source (SC-ECRIS) [53] is used to provide either ^{238}U or ^{124}Xe ions to the RILAC II linear accelerator [54], after which they are accelerated by the RIKEN Ring Cyclotron (RRC) [55], the Fixed-frequency Ring Cyclotron (fRC) [56], the Intermediate-stage Ring Cyclotron (IRC) [57], and finally by the Superconducting Ring Cyclotron (SRC) [58]. Using this mode of acceleration, the primary beams are accelerated to a fixed energy of 345 MeV/u [59].

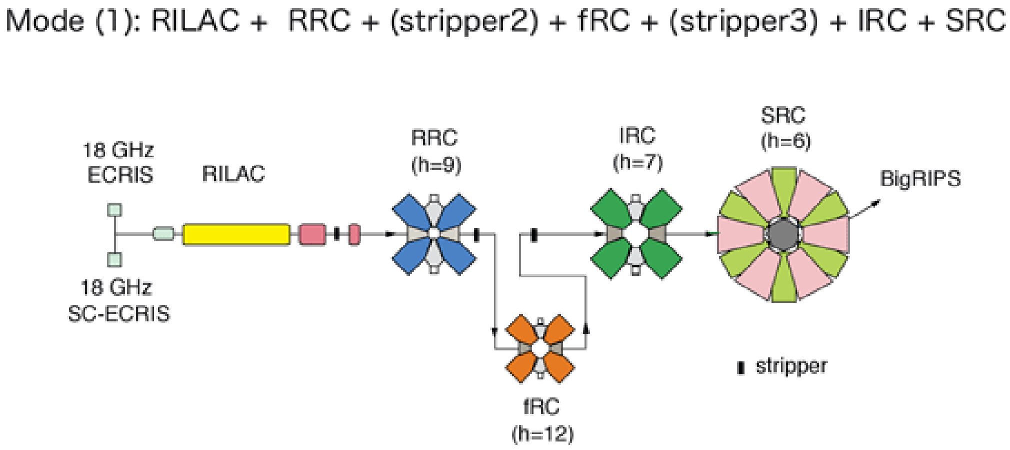

Figure 4.1: Mode 1 of the RIBF heavy-ion accelerator system [8]

4.2 Beam Analysis

The production of secondary beams is performed using the projectile fragmentation technique [60]. After its acceleration, the primary beam is impinged on a rotating, 3-mm-thick Be production target. Fragments from the reaction of primary beam on the production target are filtered in-flight, providing the desired secondary beam. The in-flight production of rare-isotope beams was performed by the BigRIPS two-stage fragment separator [61]. The RIBF beam line layout is shown in Figure 4.2 starting after the last two cyclotron stages, with the BigRIPS area labeled.

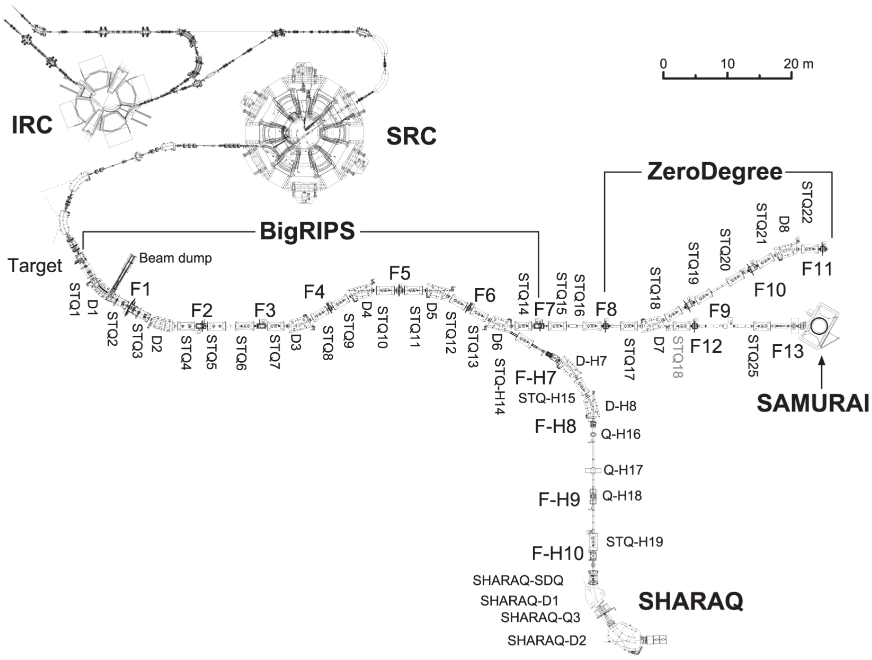

Figure 4.2: RIBF facility at RIKEN circa 2012. Although this figure will not represent the latest upgrades, it well represents the BigRIPS and SAMURAI beam line during the SπRIT experiment in 2016. Figure from [9].

A simplified schematic of BigRIPS is shown in Figure 4.3. Dipole magnets are denoted as D1-D6, and focal planes F3, F5, and F7 are shown. The naming convention follows that in Figure 4.2. The first stage of BigRIPS selects fragments, while the second stage provides beam identification, with additional filtering capabilities. The first stage is performed with dipoles D1 and D2, with a wedge energy degrader between the two dipoles. Separation is achieved in D1 with filtering by magnetic rigidity $B\rho$

$$B\rho = \frac{p}{Q}, \tag{4.1}$$

where B is a magnetic field which results in a radius of curvature ρ for a particle of momentum p and charge $Q = Ze$ (assuming a fully ionized nucleus). Slits before and after the dipole magnets are used to select a specific bending radius, providing a filter of magnetic rigidity. After D1, most unwanted particles are collected in a beam dump. Remaining beam particles pass through the wedge degrader, with the thickness encountered dependent on $B\rho$. This creates dispersion in B/rho between different A/Q ratios. After the wedge degrader, an additional $B\rho$ selection is made using D2. The first stage of separation results in a secondary beam with the desired isotope, as well as a variety of contaminants, which have a mass-to-charge A/Q ratio similar to that of the desired isotope.

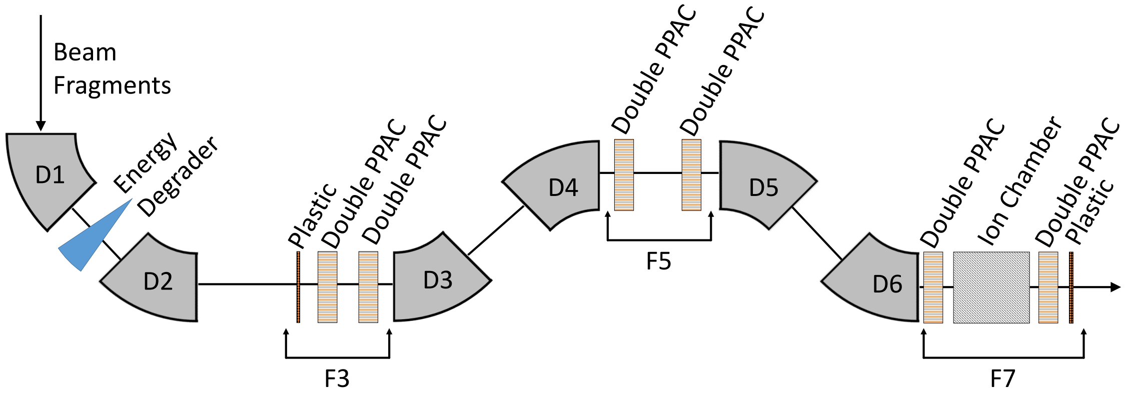

Figure 4.3: Simplified schematic of BigRIPS. Dipole magnets are labeled D1-D6. A single energy degrader was used between D1 and D2. Focal planes F3, F5, and F7 are shown with beamline detectors. Descriptions of these detectors are given in the text.

The second stage of BigRIPS provides beam identification, with additional filtering capabilities. A second wedge degrader is sometimes installed at focal plane F5, but this was not used for the SπRIT experiment, to achieve maximal energy. Beam analysis is required for beam identification, as well as to determine the beam energy and beam position on target. Plastic scintillators are located in focal planes F3 and F7, allowing the Time-Of-Flight (TOF) to be measured over a known distance. The F3 and F7 focal planes are fully achromatic, and the beam spot at these focal planes is small, allowing consistent and precise time measurements [62]. To determine the beam trajectory, double Parallel Plate Avalanche Counters (PPACs) [63] are used at focal planes F3, F5, and F7. This information provides the position and angle that the beam takes through dipole pairs D3 and D4, and D5 and D6. The magnetic field of these dipoles is measured using Nuclear Magnetic Resonance (NMR) probes. With the trajectory of beam particles and the knowledge of magnetic fields of the dipole magnets D3, D4, D5, and D6, the magnetic rigidity $B\rho$ can be determined for each beam particle [64, 65, 66]. Energy loss is determined using a segmented gaseous ion chamber, called the MUlti-Sampling Ionization Chamber (MUSIC) [11]. The TOF is used with the magnetic rigidity to determine the mass-to-charge ratio of each beam particle, while the energy loss is used to determine the atomic number of each beam particle (with slight corrections coming from velocity). Finally, Beam Drift Chambers (described in Section 3.5.1, located after BigRIPS) with high position resolution are used to determine the beam trajectory on target.

The particle identification method is described in detail in Reference [62], using the TOF-$B\rho$-ΔE method. There one can find additional details about how the Time-Of-Flight (TOF)

$$\mathrm{TOF} = \frac{L}{\beta c}, \tag{4.2}$$

magnetic rigidity ($B\rho$), and the energy loss (ΔE) are measured in BigRIPS [61], and how the atomic number and mass-to-charge ratio (A/Q) are determined from these quantities. A summary is presented here. From the TOF, the velocity $v = \beta c$ can be determined, given that the length (L) of the flight path is known. With $v = \beta c$ and $B\rho$ (Equation 4.1), one can determine the mass-to-charge ratio A/Q

$$\frac{A}{Q} = \frac{B\rho}{\beta\gamma}\frac{c}{m_u}, \tag{4.3}$$

where $\gamma = 1/\sqrt{1-\beta^2}$ and $m_u = 931.494$ MeV/c^2 is the atomic mass unit. Finally, since β has been determined, a measurement of energy loss can be used to determine the charge Z using the Bethe-Bloch formula,

$$\frac{dE}{dx} = \frac{4\pi e^4 Z^2}{m_e v^2} Nz \left[\ln\frac{2m_e v^2}{I} - \ln(1-\beta^2) - \beta^2\right] : \tag{4.4}$$

here e is the elementary charge, and m_e is the electron mass. The material through which the beam passes is described by its atomic density N, atomic number z (not to be confused with beam atomic charge Z), and mean excitation potential of the material I. With A/Q and Z determined, the particle identification is complete.

Raw information from the beam-line detectors is stored in RIBF Data Format (RIDF) files for offline analysis. The RIDF files are analyzed with the ANAROOT [67] toolkit, which was developed at RIBF for both online and offline analysis. ANAROOT is used to unpack the raw data, and built-in libraries are used to perform the particle identification methods. Finally, ROOT files are produced for the analyzed beam data, facilitating merging with the TPC data, indexed by event number (see Section 3.6 for further details on the DAQ).

4.2.1 Analysis of PPAC signals

Trajectory reconstruction within BigRIPS is performed with Parallel Plate Avalanche Counter (PPAC) [10] detectors located at the focal planes F3, F5, and F7. Ion-optical transfer maps, deduced experimentally [9], are used along with the trajectory information to calculate the value of $B\rho$ at the three specified focal planes. Additionally, corrections to the flight path length can be determined from the trajectory information. A total of 12 PPAC detectors were used in the beamline during the SπRIT campaign, with 4 PPACs located in each of the focal planes F3, F5, and F7 (see Figure 4.3). PPACs are doubled together for efficiency, making "double PPACs", at the fore and aft of the focal planes.

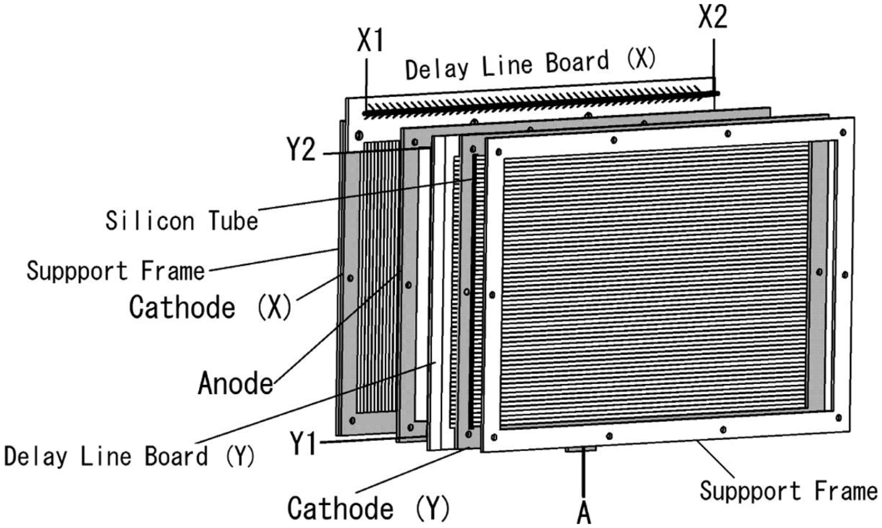

Figure 4.4: Structural schematic of BigRIPS 240×150 mm^2 PPAC, from Reference [10]

The following description of the PPAC detectors is summarized from Reference[63]. As seen in Figure 4.4, the PPAC detector is made by an anode plate, sandwiched between two cathode plates. The cathode plates are made of 1.5 µm thick Mylar foil, with 0.30 nm strips of either Au or Al evaporated on the surface. These strips are 2.4 mm wide with a pitch of 2.55 mm, and are connected to a delay line readout. There are 40 strips on each cathode plane, with one cathode plane containing strips separated in the x direction, and the other cathode plane containing strips separated in the y direction. The detector is filled with isobutane (C_4H_{10}) gas. The operating voltage difference between anode and cathode is variable, but is typically less than 2000 V. Throughout the experiment, the operating voltage of PPAC detectors was sometimes lowered to prevent electrical trips. Each PPAC layer outputs 5 time signals: T_{X1}, T_{X2}, T_{Y1}, T_{Y2}, and T_A. Calibration of these signals is performed to convert from TDC channels to ns, and we will only consider calibrated signals in this work. The strips are read out with a lumped-constant delay line, which enables the high-rate readout capabilities of the PPACs. The delay of a 100 mm delay line with 40 steps was measured to be 81.6 ns, consistent with a delay time of one step being 2.04 ns.

The time signals from the PPAC layers are recorded using a CAEN V1190 multi-hit Time-to-Digital Conversion (TDC) module [68], which records time signals for multiple hits. This TDC module does not have a sharp correlation between its gate and the TDC value for a given signal: there is a “jitter" between the gate and the TDC value, which varies event-by-event. This is done deliberately to correct for differential non-linearities in the TDC readout. Although this introduces inaccuracy in absolute measurements of a single channel, the relative time between TDC channels provides an accurate measurement [68]. This method is referred to as asynchronous time interval measurement, as opposed to synchronous time interval measurement [69]. With synchronous time interval measurement, TDC signal times are compared to a reference clock, which has some jitter, causing random, potentially non-Gaussian, measurement error. Thus, all measurements made with PPACs use the difference of two signals.

Since the multi-hit TDC modules record hits over a range of time, the hit associated with the event must be distinguished from other hits. A TDC overflow parameter is set for each PPAC, which is applied to the dimensional time signals (T_{X1}, T_{X2}, T_{Y1}, and T_{Y2}). In our analysis, any hits at times greater than the TDC overflow are ignored. The last signal below the TDC overflow limit is considered to be the real signal.

The difference between delay line signals is used to determine position. As an example, we consider position determination in the X dimension. Three signals will be used: T_{X1}, T_{X2}, and T_A, with T_A being the anode time signal. Aside from a fixed delay associated with the signal generation and cable delay, T_A is equal to the arrival time of the beam particle in the PPAC. T_{X1} and T_{X2} have additional delays, as they are read out through a delay line. The difference between the two dimensional time signals, $T_{\text{diff}} = T_{X1} - T_{X2}$, is basically equal to the difference in the delays of the two signals going out of the two ends of the delay line. This difference is proportional to the X displacement of the track relative to the center of the PPAC and is used to determine the position, given as

$$x = K_x \times T_{\text{diff}}/2 + x_{\text{off}}, \tag{4.5}$$

with an offset correction x_{off} in mm and a position coefficient K_x, in mm/ns. We used previously determined values for these constants, with each PPAC individually calibrated. We can also see that $(T_{X1}+T_{X2})/2$ is insensitive to X and is equal to T_A up to an additive constant.

To validate signals from the PPAC, we define the quantity T_{sum}:

$$T_{\text{sum}} = T_{X1} + T_{X2} - 2 \cdot T_A. \tag{4.6}$$

Since $T_{X1} + T_{X2} = 2T_A$ within an additive constant, we expect T_{sum} to remain constant, with some variation due to the timing resolution of the PPAC. If the value of T_{sum} is well established, we can use any two of the three signals (T_{X1}, T_{X2}, and T_A) to determine the third. This will be exploited in Section 4.2.1.1 for signal recovery. We show an example T_{sum} spectra in Figure 4.5, fitted with a Gaussian function. It can be seen that the distribution has a tail for lower values of T_{sum}.

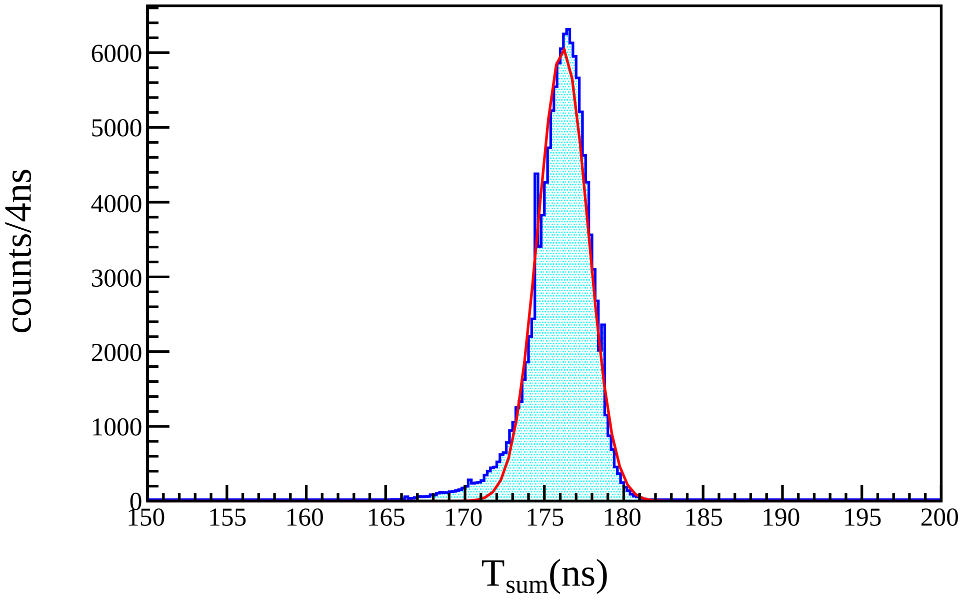

Figure 4.5: An example T_{sum} spectra. The distribution is fitted with a Gaussian function, shown in red.

Two effects typically contribute to the asymmetric tail of the T_{sum} distribution: δ-ray production within the PPAC (an electron which is liberated from the PPAC gas with sufficient energy to produce a signal on the delay line), or multiple hits (pile-up type events). These effects cause erroneous position measurements, as one of the timing signals is too small. We can identify these events by requiring a minimum value of T_{sum}. We fit the Gaussian portion of the T_{sum} distribution, using the mean to define the expected value $\langle T_{\text{sum}} \rangle$, and defining the upper and lower bounds of T_{sum} to be at $\langle T_{\text{sum}} \rangle \pm 2\sigma$. Events outside these bounds will often have compromised position information, and we attempt position recovery for such events in the following section.

One additional cause of information loss should be noted: the PPACs can experience electrical discharge between the anode and cathodes, especially with high beam intensity. This causes the high voltage module for a PPAC to trip, causing total loss of information for that PPAC until it is reset manually. Such tripping occurred with varying frequency throughout the experiment.

4.2.1.1 Position determination with partial information

In principle, a single dimensional signal from one end of the PPAC delay line can be combined with the anode time to reconstruct the position. With the expected value $\langle T_{\text{sum}} \rangle$ determined previously, we construct T_{diff} for the case of an erroneous T_{X1}:

$$T_{\text{diff}} = \langle T_{\text{sum}} \rangle + 2 \cdot T_A - 2 \cdot T_{X2}, \tag{4.7}$$

or if T_{X2} is erroneous,

$$T_{\text{diff}} = 2 \cdot T_{X1} - \langle T_{\text{sum}} \rangle - 2 \cdot T_A. \tag{4.8}$$

For events which do not satisfy the T_{sum} condition, we take the greater of T_{X1} and T_{X2}, and check if it satisfies the following:

$$\langle T_{\text{sum}} \rangle - 4\sigma \leq 2 \cdot (T_X - T_A) \leq \langle T_{\text{sum}} \rangle + 4\sigma, \tag{4.9}$$

where T_X is either T_{X1} or T_{X2}, and $\langle T_{\text{sum}} \rangle$ and σ are extracted from the fit on T_{sum} described previously. When these conditions are satisfied, the PPAC information can be safely reconstructed using the available timing information.

Issues with the PPAC signals are made evident by inspecting the relationship between $T_{X1} - T_A$ and $T_{X2} - T_A$. Since the sum of these quantities should be constant in principle, we expect to observe an anti-proportionality between them. The left panel of Figure 4.6 shows the behavior for the F7-1B PPAC, which exhibits the expected behavior.The right panel of the same figure shows the F7-2B PPAC, which exhibits non-standard behavior.

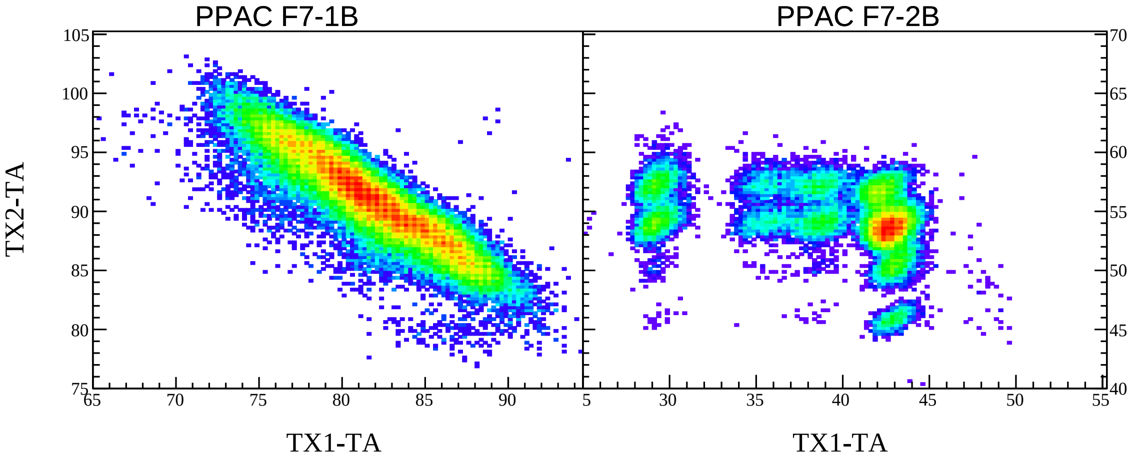

Figure 4.6: Correlation plot for PPAC signals for the F7-1B (left) and F7-2B (right) PPACs. Signal issues are evident for the F7-2B PPAC.

The distinct groupings seen in the F7-2B PPAC suggest that the data has been affected in a systematic fashion. A likely cause is crosstalk between the cables which run from the focal plane detectors to the DAQ room. The F3 and F7 focal planes house plastic scintillators as well as the PPACs, with the F7 focal plane also housing the ion chamber. The regularly timed signals within the cables for these detectors can cause regularly timed crosstalk in the data cables for the PPACs, corrupting the recorded data. By using proper T_{sum} gates in conjunction with partial information position recovery, we can estimate position information for some of the affected events.

To ensure that dependent quantities such as A/Q and projection on target are not adversely affected by using the partial information position recovery, we compare the reconstruction of a run using the position recovery to the reconstruction without position recovery. A single run from the ^{132}Sn beam will be used for this comparison. For simplicity, we will refer to the reconstruction without position recovery as method 1, and the reconstruction with position recovery as method 2. The run is reconstructed using both methods, and ^{132}Sn isotopes are selected with an elliptical cut for both reconstructions:

$$\frac{(A/Q - 2.64)^2}{(0.005)^2} + \frac{(Z - 50)^2}{(0.6)^2} < 1. \tag{4.10}$$

The PID for both methods are shown in Figure 4.7, with the elliptical cut overlaid. Method 2 shows nearly a 50% increase over method 1 of ^{132}Sn isotopes reconstructed within the PID cut. The numbers are listed in Table 4.2.

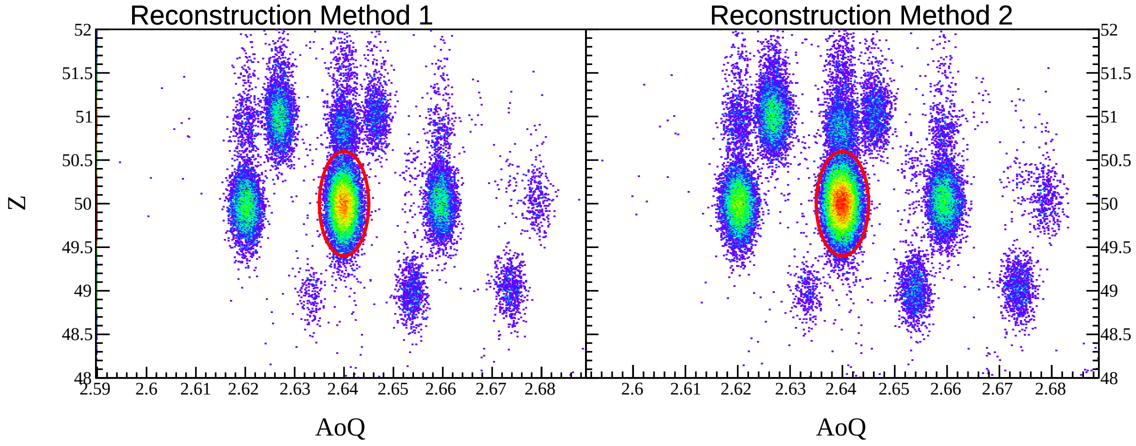

Figure 4.7: Beam PID from reconstruction without (a) and with (b) position recovery. Refer to Table 4.2 for numerical comparison of these two plots.

The A/Q distribution of the selected ^{132}Sn isotopes is fit with a Gaussian function for both methods. The Full Width at Half Maximum (FWHM) of the distributions are reported in Table 4.2. The PID is required to project the beam path to target (this projection is described in Section 4.2.8). The number of ^{132}Sn isotopes successfully projected on target is higher for method 2, since more ^{132}Sn isotopes are found by method 2. The FWHM of projected x position and yaw angle on target are listed in Table 4.2. The mean of the x distributions found by the two methods agree within 0.05 mm, and the mean of the yaw distributions agree within 0.2 mrad.

Observable	Method 1	Method 2
^{132}Sn	21719	31436
FWHM$_{A/Q}$	0.00336	0.00350
^{132}Sn on target	18490	27020
FWHM x on target (mm)	9.327	9.367
FWHM yaw on target (mrad)	4.78	4.72

Table 4.2: Resulting quantities for PPAC reconstruction without (method 1) and with (method 2) PPAC position recovery

4.2.1.2 Beam Rate Calculation with PPAC

The typical scaler estimation of beam rate provides a time-averaged rate, which does not account for fluctuations in the beam intensity. An alternative estimate of the beam rate comes from the multi-hit information of the PPACs. After an event is triggered, the probability that an additional beam particle will pass through is directly related to the beam rate. We can set a window of time with width W_{after} after the TDC overflow limit and take the ratio of hits within this window (N_{after}) to the number of triggered events (N_{events}) to calculate the beam rate

$$\text{Rate}_{\text{beam}} = \frac{N_{\text{after}}}{N_{\text{events}} \cdot W_{\text{after}}}. \tag{4.11}$$

This rate is calculated using the F7-2 PPACS, and can be compared to the scaler rate for the F7 plastic. The relative rates can be used to correct the scaler rate for the SBT start counter (described in Chapter 3).

4.2.2 Analysis of Beam Time of Flight

To determine the velocity, β, and mass-to-charge ratio, A/Q, of the beam particles, an accurate and precise measurement of the TOF must be performed. The TOF was measured using plastic scintillators located at focal planes F3 and F7. An example raw spectra is shown in the left panel of Figure 4.8, and the same spectra after calibration in the right panel of Figure 4.8. The raw spectra must be converted from TDC channels to ns, and corrected with an offset to produce the actual TOF. A mesytec MTDC-32 module was used to record the scintillator signals, and the conversion factor from TDC to ns for the setup was 64 TDC = 1 ns. The calibrated TOF value is estimated using the beam energy and distance between focal planes F3 and F7 (roughly 46.6 m) [9], and is fine-tuned by adjusting the offset to produce correct A/Q values. The TOF is recorded between focal planes F3 and F7, as the F5 scintillator was removed to achieve higher beam energies. We can estimate the expected TOF using the expected beam velocity with Equation 4.2.

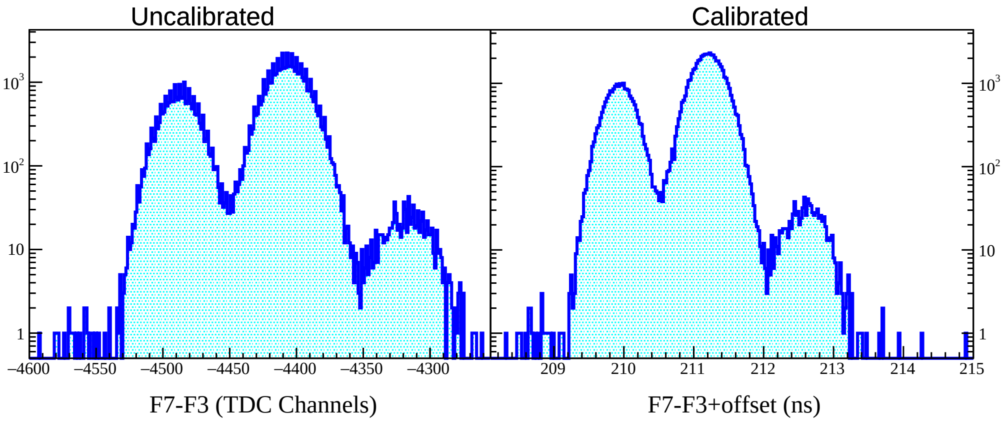

Figure 4.8: The uncalibrated (a) and calibrated (b) time-of-flight spectra from run 2894.

The conversion of TOF to velocity β is performed using ANAROOT, which uses PPAC information to correct for the flight path. The ion-optical transfer maps that are used to determine $B\rho$ are also used to determine a particle's trajectory, producing small corrections to the flight length. ANAROOT scales β to account for energy loss between F3 and F7, providing an estimate for β at F7. With β and $B\rho$ determined, the A/Q ratio is calculated using Equation 4.3.

A time offset is required to calibrate the time signals between the F3 and F7 plastic detectors. An estimate is made using the expected TOF, which is then iteratively corrected to reproduce the expected A/Q ratio for the main Sn isotope. An example is shown in Figure 4.9, with the reconstructed A/Q ratio plotted as a function of the TOF offset.

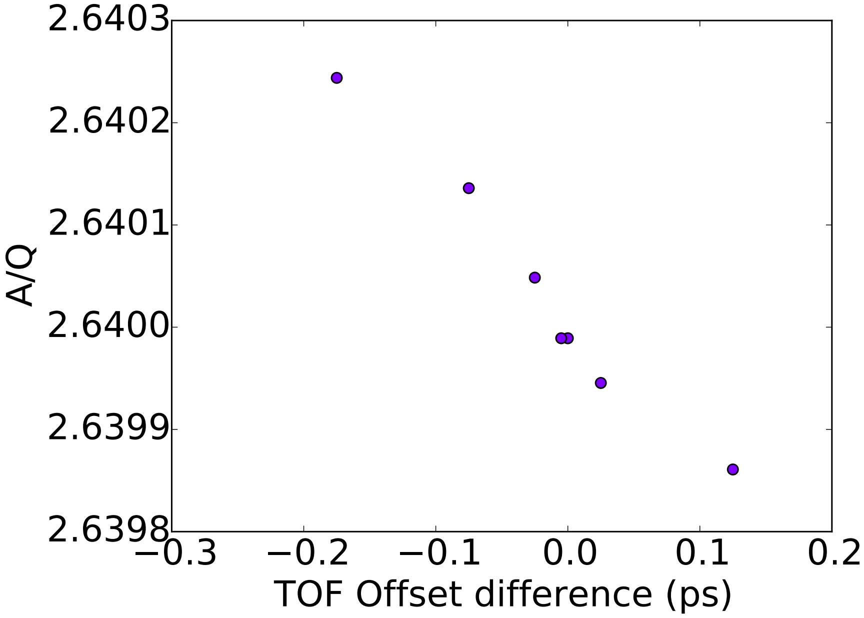

Figure 4.9: Relationship between TOF offset used and reconstructed A/Q ratio of ^{132}Sn.

Radiation from the heavy-ion beam damages the plastic scintillators, changing the light output over time. The scintillator at F3 is subjected to a higher beam intensity than the scintillator at F7, causing the damage to occur unevenly. In addition to the slow degradation, the physical position of the scintillators were periodically adjusted to place the beam spot on an undamaged section. A slewing correction similar to that described in Reference [62] is performed, with slight differences. We perform the slewing correction with two equations,

$$\tau = t + \Delta t_{\text{slew}} \tag{4.12}$$

and

$$\Delta t_{\text{slew}} = \frac{c_1}{\sqrt{q}}, \tag{4.13}$$

where τ is the actual time, t is the observed time, and q is the integrated charge signal. The slewing effect Δt_{slew} is a function of parameter c_1, which is determined empirically for each run. The effect of the slewing correction can be observed in Figure 4.10, which shows a ^{112}Sn PID reconstructed with and without the slewing correction.

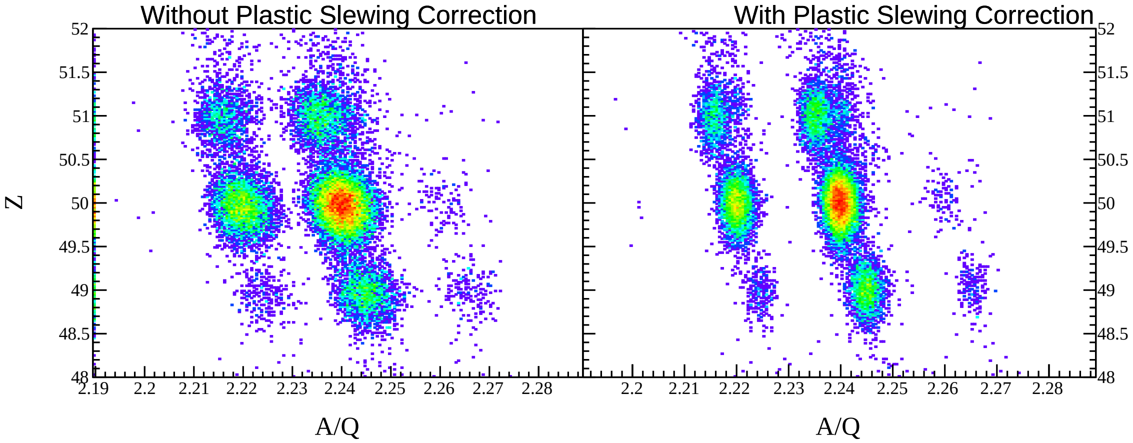

Figure 4.10: PID reconstructed without (left) and with (right) plastic slewing correction. Resolution in A/Q is visibly improved by using the slewing correction.

4.2.3 Determination of Charge with the Ion Chamber

The charge of each beam particle is determined using energy loss information from the Multi-Sampling Ionization Chamber (MUSIC)[11], and from the beam velocity. The combined energy loss and beam velocity information is used in the Bethe–Bloch formula (Equation 4.4) to determine charge. A schematic view of MUSIC is shown in Figure 4.11. The chamber is filled with P10 gas at approximately 760 Torr (this pressure differs slightly from the pressure used in Reference [11]). A series of 4 µm thick aluminized Mylar foils are alternated as anode and cathode plates, with the cathode set to ground potential, and pairs of anode signals linked together, with a total of 25 aluminized Mylar planes. A total of 6 ADC signals are read out from anode planes, providing the multi-sampling capabilities. Each ADC signal is proportional to the amount of energy lost in 4 Mylar planes and 80 mm of counter gas. MUSIC is located in focal plane F7, between two PPACs and prior to the plastic scintillator at F7.

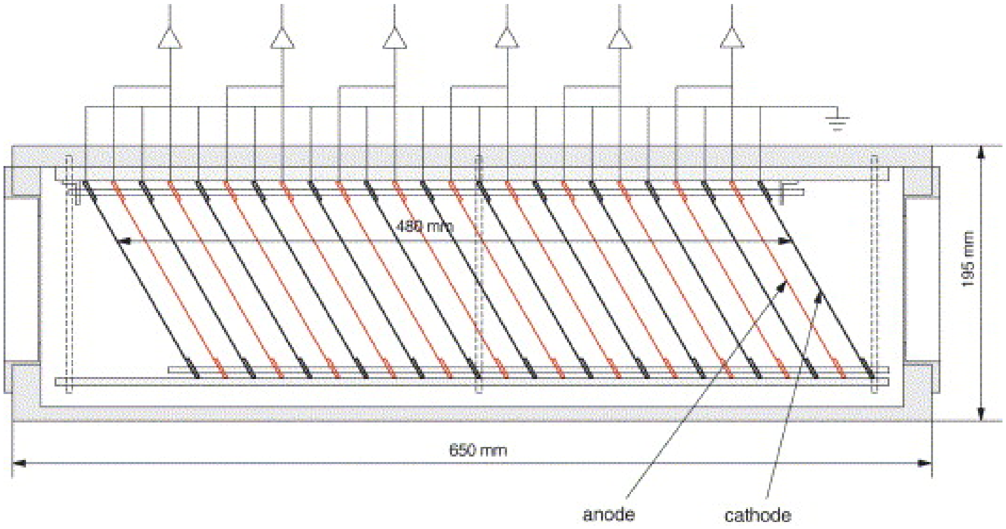

Figure 4.11: MUSIC side-view schematic, from Reference [11]

The energy loss within MUSIC is tabulated as a geometric mean, to reduce statistical fluctuation. The geometrical mean for 6 ADC channels is given as

$$\overline{ADC} = \sqrt[6]{\prod_{i=0}^{i=5} ADC_i}. \tag{4.14}$$

An analysis program, LISE++ [70], was used to calculate the expected energy loss of the major particle species present in the isotopic Sn beams. The geometrical mean of the observed energy loss in ADC is plotted against the geometrical mean of simulated energy loss in MeV in Figure 4.12, for an array of selected isotopes. A linear relationship is observed between these values, with the slope representing the gain.

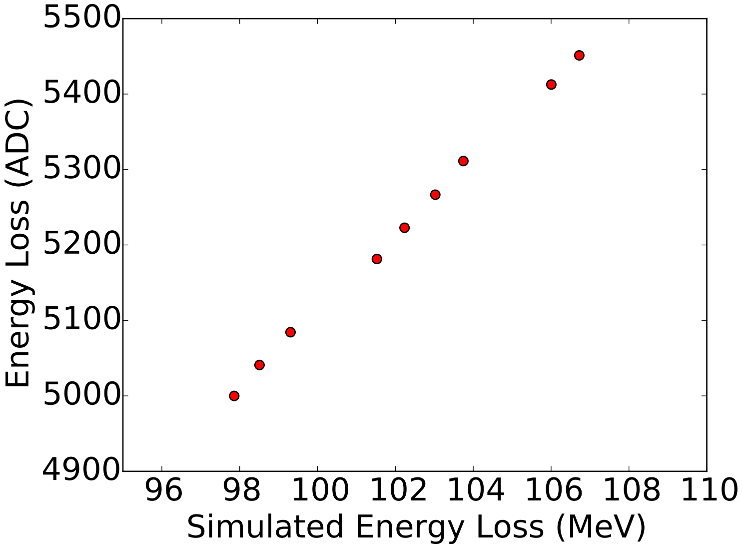

Figure 4.12: Geometrical mean of ADC response compared to simulated energy loss

It is common that a detector will register a non-zero signal, even if there is no particle present. The typical signal size for a non-event is called the pedestal, a baseline value which corresponds to no signal. The pedestal for each ADC channel is determined using the gain. For each channel, the measured ADC signal and simulated energy loss are compared for several isotopes. The combined results are plotted in Figure 4.13, with the left panel showing results before pedestal subtraction. For each channel, the pedestal can be calculated as

$$\text{pedestal} = \text{Measured Energy (ADC)} - E_{\text{Loss}} \cdot \text{gain}. \tag{4.15}$$

For each channel, the average pedestal is calculated using an array of isotopes. After applying pedestal subtraction, the relationship between pedestal-subtracted measured ADC signal and simulated energy loss is shown in the right panel of Figure 4.13. A linear fit is applied to this distribution to determine the final calibration between ADC channels and energy loss in MeV.

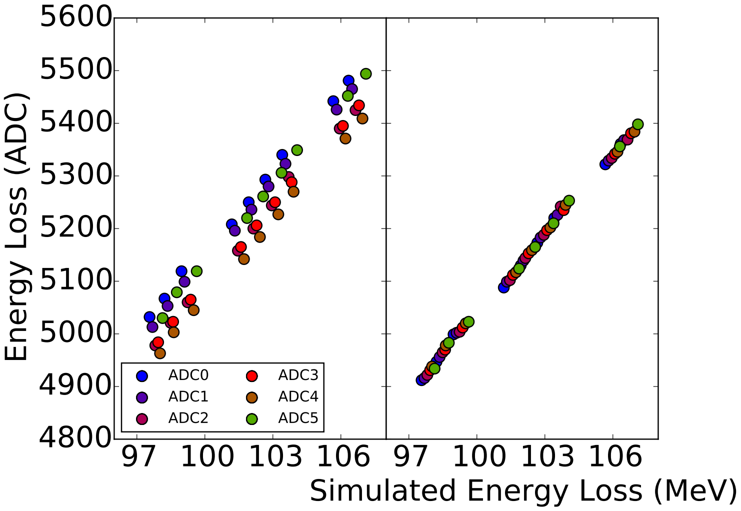

Figure 4.13: Ion chamber signal and simulated energy loss before (left panel) and after (right panel) pedestal subtraction.

The final step is to determine particle charge from energy loss and beam velocity. This is done in ANAROOT with the equation

$$Z = \text{slope} \cdot \beta \cdot \sqrt{\frac{E_{\text{Loss}}}{\ln(4866 \cdot \beta^2) - ln(1-\beta^2) - \beta^2}} + \text{offset}, \tag{4.16}$$

where 4866 corresponds to $2 \cdot m_e/(I \cdot c^2)$, with m_e the mass of an electron, c the speed of light, and I as the mean excitation potential of the combined Mylar and ion chamber gas. The energy loss, E_{Loss}, is determined using the geometrical mean of all fired ADC channels, with the conversion from ADC to MeV detailed earlier in this section. The slope and offset are calibrated by fitting data for selected isotopes.

For the ^{108}Sn and ^{112}Sn beams, ADC channels 1, 3, and 4 (of the 6 total channels) had drifting gains. To perform run-by-run calibration in an automated manner, the runs were

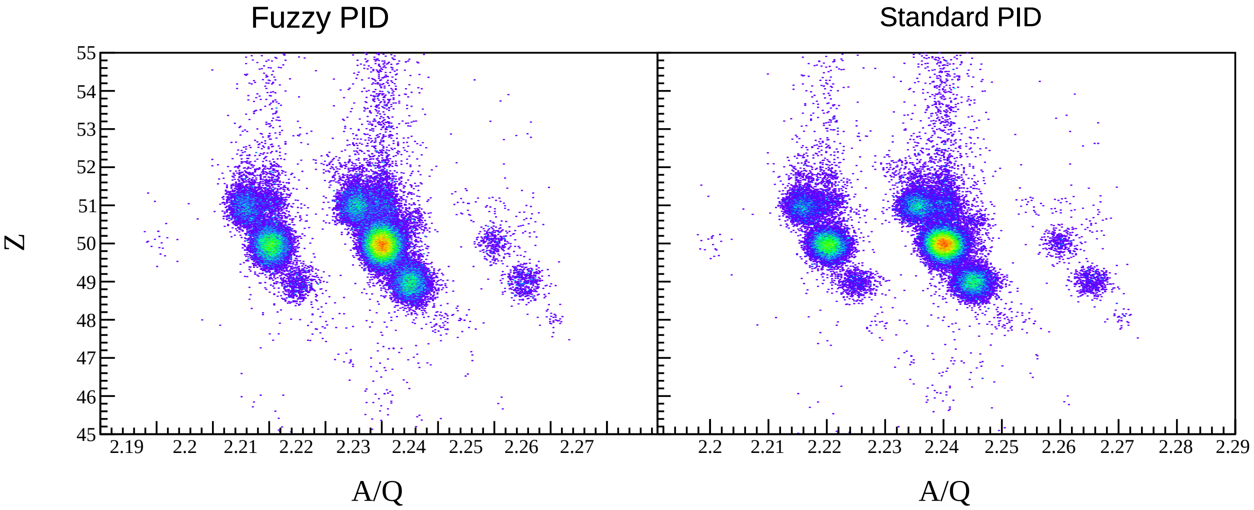

Figure 4.14: ^{112}Sn beam PID plot for run 2580, using 3 ADC channels (left), and all 6 ADC channels (right).

first reconstructed using ion chamber ADC channels 0, 2, and 5 only, producing “fuzzy" PID plots, as shown in the left panel of Figure 4.14. These can be produced using a single calibration, as the selected ADC channels exhibited stable behavior. The ADC response for a single run is determined by selecting isotopes using the fuzzy PID plot, and performing the standard calibration with a script that collects the ADC response for each channel, sorted by isotope, and performs the calibration as described previously within this section.

The beam PID plots shown in Figure 4.14 also indicate the presence of beam pileup: beam particles passing through the ion chamber in close succession alter the ion chamber response, causing the smeared, seemingly high-Z distribution above the main isotopic peaks. The ion chamber response for a typical data run with the ^{124}Sn beam is shown in Figure 4.15. The main peak, which is associated with properly identified charge, can be seen at approximately 4000 ADC channels. The tailing function at higher ADC values is caused by beam pileup. Other sources for aberrant ion chamber signals could be reactions within the ion chamber, or crosstalk in the ion chamber data cables.

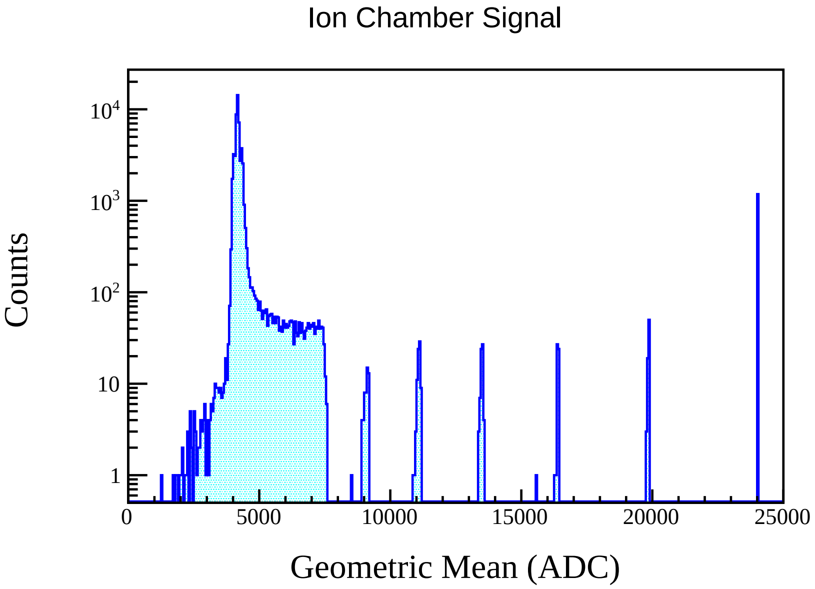

Figure 4.15: Ion chamber signal for ^{124}Sn beam

4.2.4 Beam Pileup and Background

Two beam particles in close proximity will cause a large ion chamber response, resulting in a non-physical reconstructed value of Z. The pileup can be seen in the beam PID plots as a smeared distribution above the properly reconstructed isotope peaks. These tails can overlap with other isotopes, altering the statistics. An additional indicator of pileup comes from the multi-hit TDC modules used for the PPACs. An example TDC spectrum is shown in Figure 4.16, with the main peak at approximately 32,500 TDC channels, which is constrained by trigger timing. Each hit in this spectrum is made from a particle passing through the PPAC, so hits before or after the main peak are associated with pileup events. The pileup occurs for all beams, but this section will focus on analysis of the ^{132}Sn beam.

For the ^{124}Sn and ^{132}Sn beams, the extra hits before the main peak are suppressed by the trigger, while for the ^{108}Sn and ^{112}Sn beams, the rate of extra hits is the same before and after the main peak. This was due to differences in the discrimination of signals for the KATANA Veto array, and is explained in the trigger description in Chapter 3.

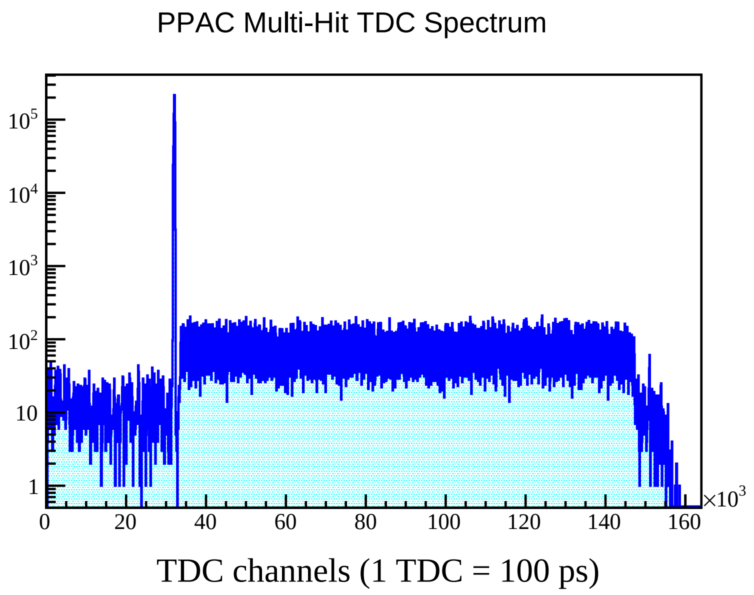

Figure 4.16: Multi-hit TDC spectra, from a PPAC at the F7 focal plane, for ^{132}Sn beam

The multi-hit information from the F7 PPACs is used to identify pileup, as multiple hit events in F3 and F5 can be caused by particles which are filtered out by BigRIPS. We gate on multiple hits in at least 2 PPACs, to prevent δ-ray production from causing an event to be identified as pileup. The ion chamber response is related to the time difference between the main particle and a pileup particle, as can be seen in the left panel of Figure 4.17. Pileup particles which arrive within 3 µs before or after the initial particle saturate the ion chamber, and result in non-physical A/Q reconstruction. For pileup events separated from the main peak by more than 3 µs, the ion chamber response converges to a value just above the typical response for a non-pileup event. The resulting PID spectrum from these events is shown in the right panel of Figure 4.17. The distribution is smeared in reconstructed Z for pileup which occurs within 6 µs of the initial particle, and a peak just above the expected Z is formed from pileup at times later than 6 µs.

Pileup which occurs before the main particle is also present, but more difficult to identify. Figure 4.16 shows a TDC spectrum for the ^{132}Sn beam, with counts before the main peak

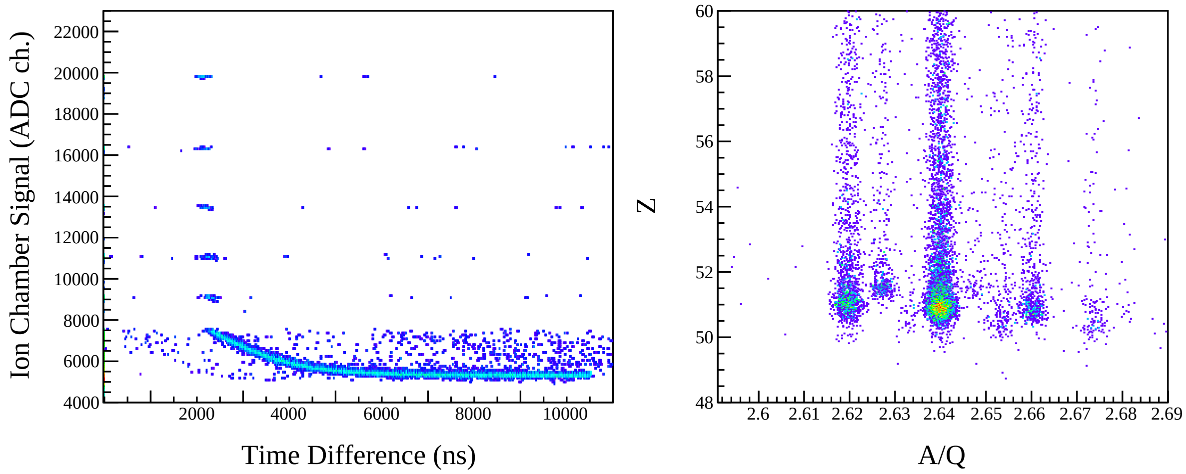

Figure 4.17: (Left) Ion chamber response plotted against pile-up time after main particle, for ^{132}Sn beam. (Right) Resulting PID spectrum for these events. Both plots are restricted to events with time difference greater than 3 µs.

corresponding to pileup before the main particle. The pileup rate before the main peak is partially suppressed by the trigger. The limited multi-hit TDC window does not provide information less than 3 µs before the main peak. Pileup within 6 µs of the main peak can be identified directly by the ion chamber response, while pileup separated by more than 6 µs cannot easily be separated from the main ion chamber response. The pileup which cannot be identified by the multi-hit TDC information and which is not clearly distinguishable from the beam PID must be estimated.

Other sources of background can be caused by poor reconstruction. The background due to poor reconstruction is estimated by inspecting the focal plane reconstruction and the reconstructed beam velocity. The reconstructed event must pass through a 100×100 mm^2 area formed around the focus of each of the focal planes F3, F5, and F7. Reconstruction outside the set limit corresponds to a non-physical position, indicating the reconstruction is compromised, and cannot be trusted. Events which are poorly reconstructed can result in a non-physical value of A/Q, providing a clear indication of mis-reconstruction.

4.2.5 Reconstructed Beam PID plots

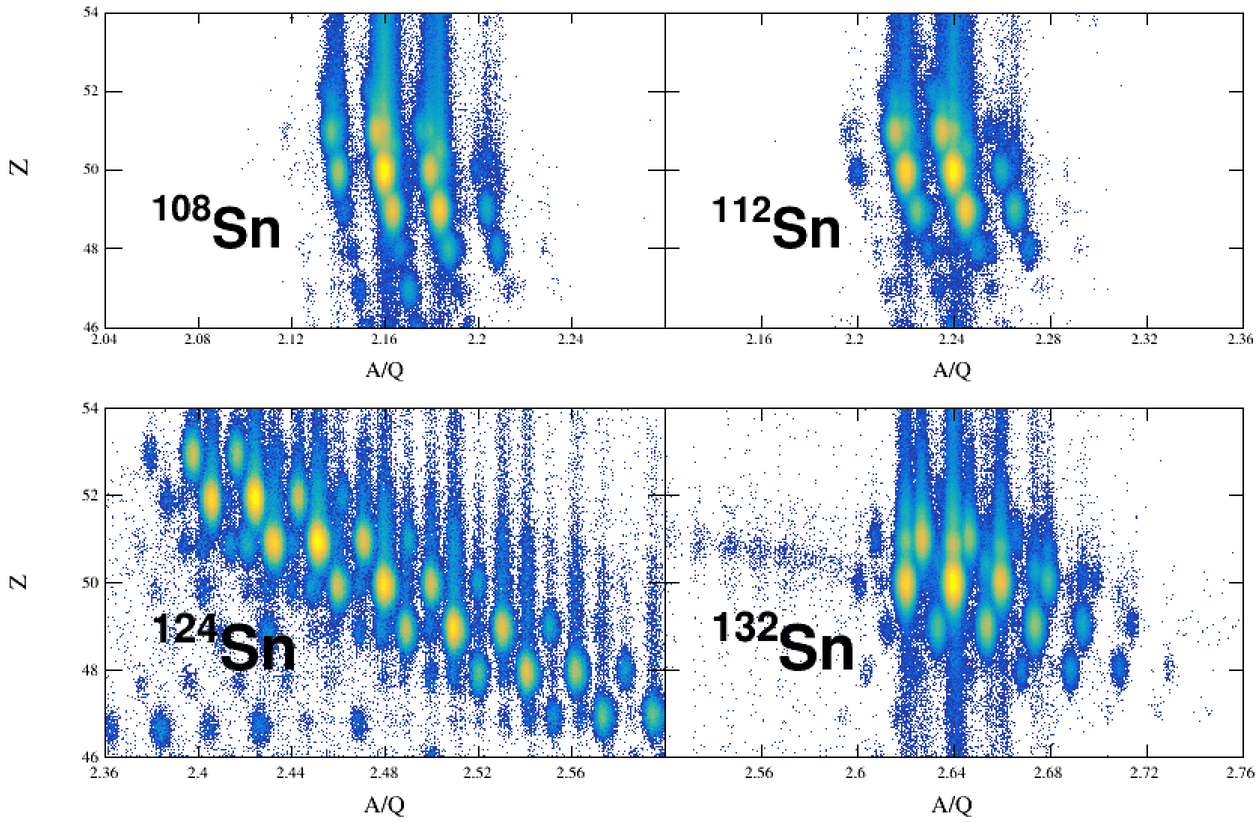

Figure 4.18: From top to bottom, left to right, beam PID plots for ^{108}Sn (TL) , ^{112}Sn (TR), ^{124}Sn (BL), and ^{132}Sn (BR).

The reconstructed beam PID plots of the 4 main beams (^{108}Sn, ^{112}Sn, ^{124}Sn, and ^{132}Sn) are shown in Figure 4.18. Pileup is evident in all of the systems, with ^{132}Sn exhibiting an additional pileup peak in addition to the smeared pileup distribution. Low-Z (Z <45) contaminants are evident in Figure 4.19, which shows the beam PID plots over a wide range of Z and A/Q values. The width of the Z and A/Q plotting ranges is consistent for all subplots in Figure 4.19, and was chosen to show all contaminants in the ^{124}Sn beam. Although low-Z beam particles are present in all systems, they do not contribute more than 1% to the statistics of any system, although during some minimum bias runs of ^{124}Sn, low-Z

particles accounted for more than 10% of particles.

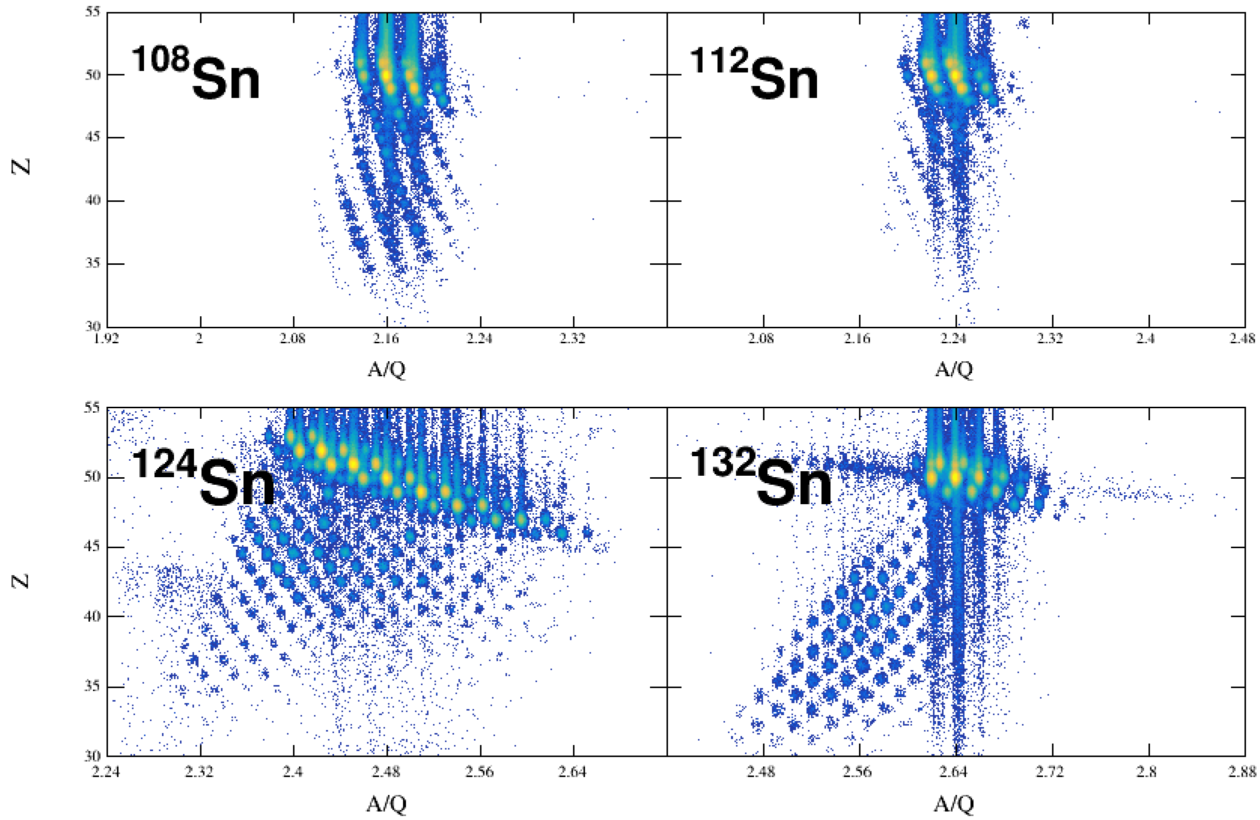

Figure 4.19: From top to bottom, left to right, wide perspective beam PID plots showing lighter beam particles for ^{108}Sn (TL) , ^{112}Sn (TR), ^{124}Sn (BL), and ^{132}Sn (BR).

4.2.6 Beam Purity

The beam purity must be measured for each run. The trigger settings can affect the purity, as can the slit settings or other changes to the beam settings. We begin by identifying isotopes using the reconstructed PID. Since the reconstruction efficiency varies by run, we define the relative purity of an isotope $^{\mathrm{A}}$Sn as:

$$\mathrm{Purity}_{A_{\mathrm{Sn}}} = \frac{N_{A_{\mathrm{Sn}}}}{N_{\mathrm{found}}} \tag{4.17}$$

where N_{found} is the total number of isotopes found within isotope gates. This is smaller than the number of collected triggers, due to reconstruction inefficiencies.

To determine the main isotopes present, a run with low beam rate is chosen to mitigate pileup. For each particle in this run, the reconstructed A/Q ratio and charge Z are checked against possible isotope combinations nearby. If a good agreement is found ($\delta Z \leq 0.1$, $\delta A/Q \leq 0.002$), the matching isotope is added to a list of main isotopes. An example is shown in Figure 4.20, for ^{124}Sn. Ellipses are drawn representing the sampling range for isotope. A graphical cut for low-Z particles is used to collect isotopes which are reconstructed, but may not be reconstructed well enough to be tagged automatically.

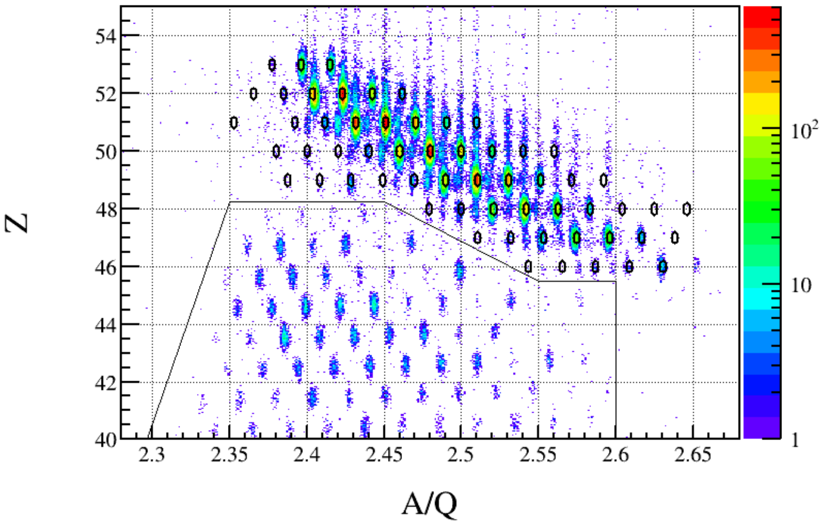

Figure 4.20: Beam PID from low-intensity ^{124}Sn runs, used to determine main contaminants.

For each of the identified isotopes, a 2D Gaussian fit is determined using the accumulated statistics of all data runs. Elliptical cuts are determined individually for each isotope using these fits, with widths up to 7σ, but not exceeding half the distance to any neighboring isotopes, preventing overlapping cuts. The large cuts are necessary to compensate for accumulated differences in reconstruction for different runs. For each beam, a loose graphical cut is used to count the overall sum of low-Z particles, rather than applying individual isotope cuts. In Figure 4.21, the beam PID for ^{124}Sn is plotted with non-identified events in black, and identified isotopes in color.

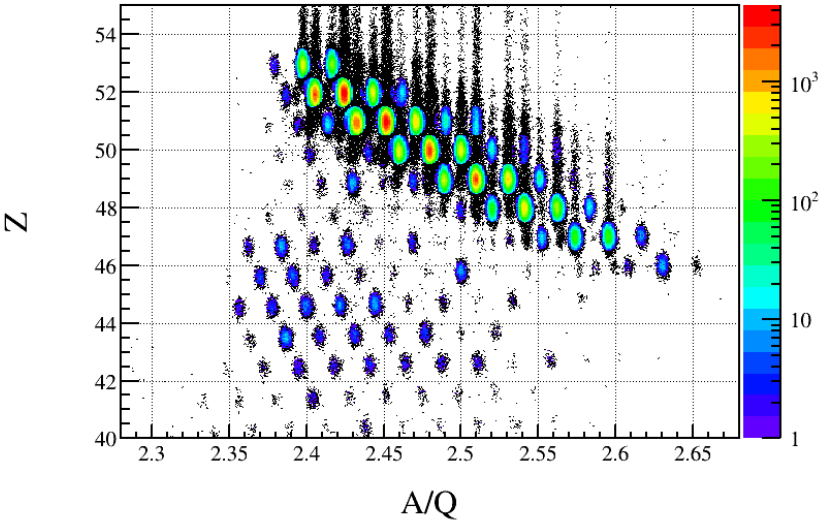

Figure 4.21: Beam PID for ^{124}Sn, with found isotopes highlighted in color

The measured purity for ^{132}Sn is shown run-by-run in Figure 4.22. Sharp changes in beam purity correspond to breaks where the beam was lost and recovered, often due to ion source issues. From run 3015, minimum bias runs introduced changes to the trigger and slit conditions, causing changes to the purity.

The purity selected by the trigger may not be the same as the incident beam purity, since the cross section of contaminants is not necessarily the same as the desired isotope. For cross section determination, the relative purity of gated triggers to incident beam should be established. Some runs were taken with a beam trigger, which can be used to compare to runs with the data trigger. The relative purities are listed in Table 4.3, and these are used for the determination of the absolute cross section.

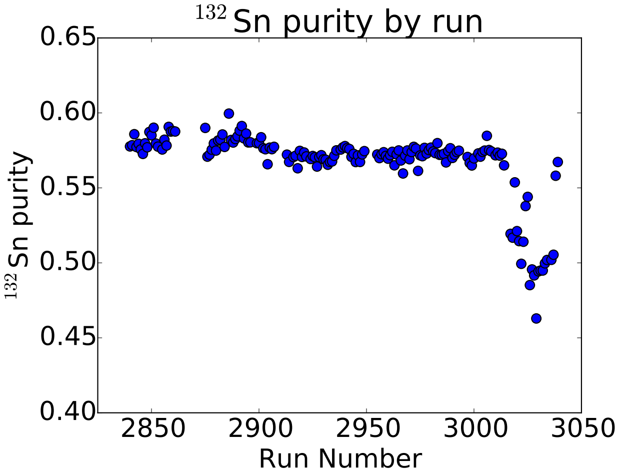

Figure 4.22: Beam purity for ^{132}Sn by run

Primary Beam	Secondary Beam	Purity Beam (%)	Purity Data (%)
^{238}U	^{132}Sn	53.5	56.9
^{238}U	^{124}Sn	9.78	10.97
^{124}Xe	^{112}Sn	47.8	46.9
^{124}Xe	^{108}Sn	51.5	50.8

Table 4.3: Beam purities and triggered purities for the secondary beams

4.2.7 Reconstruction Efficiency

The reconstruction efficiency is defined by the number of isotopes that can be identified. This is affected mainly by pileup and beam-line detector performance. The efficiency is tabulated in Table 4.4. During the ^{108}Sn beam setting, the F3 PPAC HV settings were lowered, reducing the reconstruction efficiency. During the ^{124}Sn beam setting, the F7 plastic and F5 PPACs were replaced, increasing reconstruction efficiency. Therefore, two distinct reconstruction efficiencies are reported for both the ^{108}Sn and ^{124}Sn settings. A reconstruction efficiency of 100% would indicate proper reconstruction of each event.

Beam	Reconstruction Efficiency (%)
^{132}Sn	62.2
^{124}Sn	20.5, 30.4
^{112}Sn	73.5
^{108}Sn	85.6, 66.4

Table 4.4: Event reconstruction efficiency for each beam, ^{108}Sn and ^{112}Sn both had two distinct reconstruction efficiencies, described in the text.

4.2.8 Beam Drift Chambers and Projection to Target

After the production of the beam at BigRIPS, the beam is sent to the SAMURAI magnet and experimental setup. A pair of Walenta-type detectors, called Beam Drift Chambers (BDCs) were employed for trajectory reconstruction prior to the magnet. In Figure 3.1, these detectors are labeled BDC1 and BDC2. In the SAMURAI coordinate system, BDC1 is located at $(x_1, y_1, z_1) = (-0.72, 0, -3159.28)$ and BDC2 is located at $(x_2, y_2, z_2) = (-0.52, 0, -2158.7)$. The x and z positions are measured using photogrammetry (PGM) [38], but the y positions could not be determined from the measurements, so the nominal height (centered at $y = 0$) is assumed.

The BDC detectors measure the x–y position of a beam particle with precision of 120 µm [71] as it passes through 8 wire planes (4 planes in x, and 4 planes in y.) The beam position as well as angle can be determined individually from each BDC detector, but for our purposes, we only use the beam positions at the mid-planes of the two BDCs. The BDCs are situated well outside the SAMURAI magnetic field, so it is reasonable to assume the beam takes a straight path between the BDCs. To describe the beam location and momentum vector, a system similar to the Tait-Bryan convention used: the origin is the beam particle location, the roll axis is parallel to the SAMURAI z-axis, the pitch axis is parallel to the SAMURAI x-axis, and the yaw axis is parallel to the SAMURAI y-axis. The yaw angle is denoted as Ψ, and the pitch angle is denoted as θ_p, with both angles illustrated in Figure 4.23. In terms of momentum, these angles are defined as

$$\Psi = \tan^{-1}\left(\frac{p_x}{p_z}\right) \tag{4.18}$$

$$\theta_p = \tan^{-1}\left(\frac{p_y}{p_z}\right). \tag{4.19}$$

If the measured positions at BDC1 and BDC2 are written as (x_1, y_1, z_1) and (x_2, y_2, z_2), respectively, the starting position of the projection will be (x_2, y_2, z_2) and the starting angles Ψ_0 and θ_{p0} will be

$$\Psi_0 = \frac{x_2 - x_1}{z_2 - z_1} \tag{4.20}$$

$$\theta_{p0} = \frac{y_2 - y_1}{z_2 - z_1}, \tag{4.21}$$

where we have taken advantage of the accuracy of the small angle approximation for these calculations.

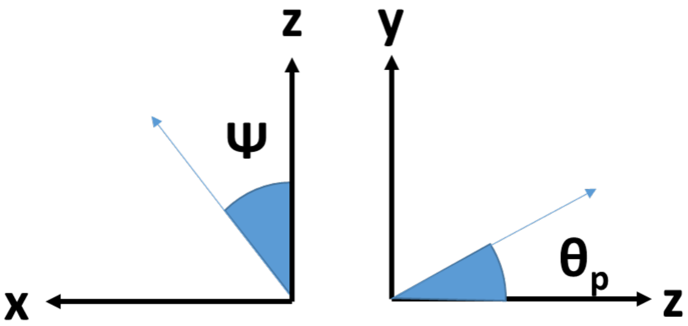

Figure 4.23: Yaw (Ψ) and pitch (θ_p) angles used for the BDC projection

Since we are dealing with a non-uniform magnetic field, we perform a step-wise projection. For fixed steps in z, the local magnetic field, particle energy, starting position and angle are used to determine the position, angle, and energy at the end of the step. The magnetic field is oriented mostly along y, and so non-y components were ignored. The final position will be expressed as (x_f, y_f, z_f), where z_f is chosen as the nominal target position.

Over a small step Δz, the local magnetic field can be approximated as constant and combined with the particle magnetic rigidity to determine the radius of curvature ρ in the x–z plane. Given starting yaw angle Ψ_1, the ending yaw angle Ψ_2 is given geometrically as

$$\Psi_2 = \sin^{-1}\left(\frac{\Delta z + \rho \cdot \sin(\Psi_1)}{\rho}\right). \tag{4.22}$$

The corresponding change in X, Δx, is given as:

$$\Delta x = \rho \cdot (\cos(\Psi_2) - \cos(\Psi_1)). \tag{4.23}$$

The change in Y, Δy, is found through a linear projection using pitch angle θ_p

$$\Delta y = \Delta z \cdot \tan(\theta_p). \tag{4.24}$$

The pitch angle θ_p remains constant through the projection, as the small non-y components of the magnetic field can be safely ignored.

After updating the position, the energy loss is estimated. For each beam, the energy loss is estimated for the isotope of interest using LISE++ [70]. The energy loss through each material is stored in array, as a percent of energy remaining. The starting and ending coordinates for each material are also stored in arrays. For each step Δz, the energy is updated based on the energy loss tables.

The projected position can then be compared to the vertex reconstructed by SπRITROOT.

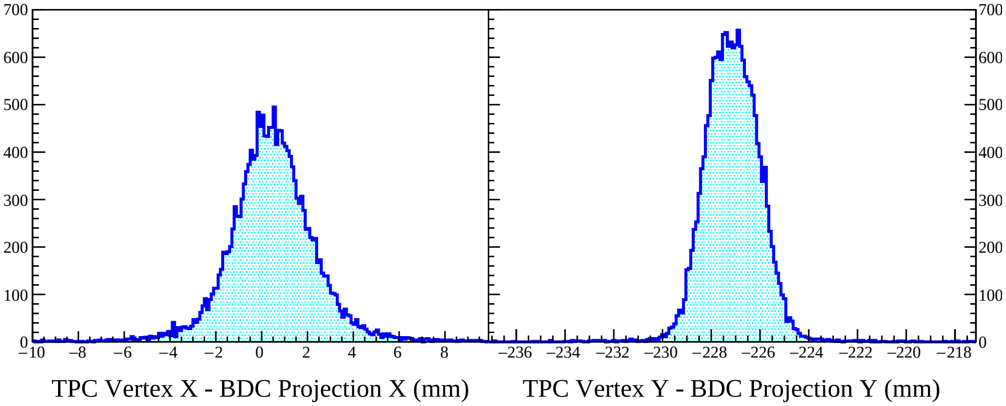

Figure 4.24: Differences between BDC projection and TPC vertex for x (left) and y (right).

We perform this comparison with ^{132}Sn events, limited to events with identified ^{132}Sn, with vertex located near the target. The differences TPC$_x$ - BDC$_x$ and TPC$_x$ - BDC$_x$ are shown in Figure 4.26. For each system we determine the typical offset between the TPC and SAMURAI coordinate systems:

$$\mathrm{TPC}_x = \mathrm{SAMURAI}_x + x_{\mathrm{offset}}; \tag{4.25}$$

$$\mathrm{TPC}_y = \mathrm{SAMURAI}_y + y_{\mathrm{offset}}. \tag{4.26}$$

The correlation between TPC and BDC is plotted in Figure 4.25 for x and y, applying offsets to x and y of the TPC vertex so that they are in SAMURAI coordinates.

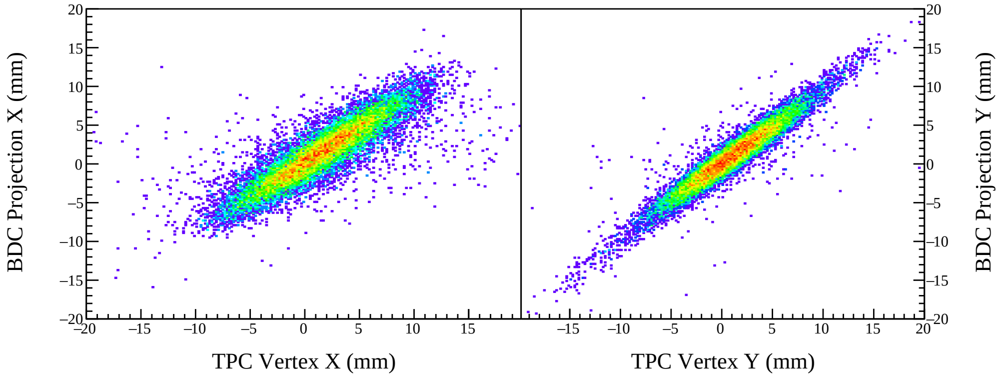

Figure 4.25: Correlations between BDC projection and TPC vertex for x (left) and y (right).

The calculated offsets are different for each system: differences in y_{offset} are most likely caused by slightly different delays in the trigger. Differences in x_{offset} are most likely caused by an error in the BDC projection. The average x and y offset for each system is listed in Table 4.5, and the x_{offset} is plotted for each system, with error bars of ± 1 standard deviation in Figure 4.26. Although the results are consistent within 2 standard deviations, it appears that systematic differences are affecting x_{offset}.

Beam	x_{offset} (mm)	y_{offset} (mm)
^{132}Sn	-0.299	-227.29
^{124}Sn	-0.609	-227.1
^{112}Sn	-0.757	-228.4
^{108}Sn	-0.706	-228.7

Table 4.5: Average x and y offsets between TPC vertex and BDC projected position, for each beam. These offsets also reflect the fact that the BDC and TPC vertices are defined in different coordinate frames.

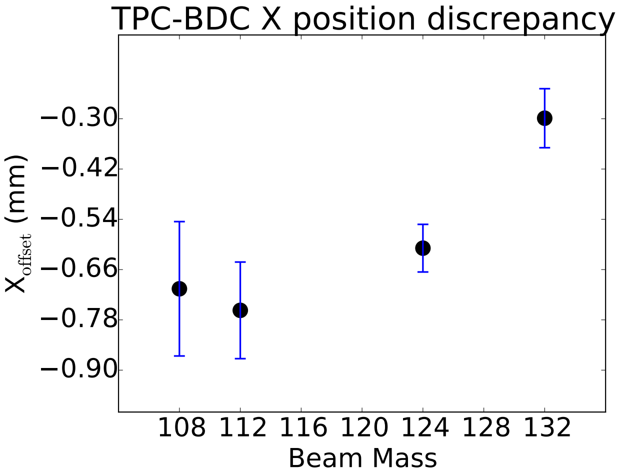

Figure 4.26: For each beam, typical x_{offset} with error bars of ± 1 standard deviation

To check the expected resolution, we perform an analytical error calculation. The BDCs have measurement resolution of $\delta_m \approx 120$ µm [71], and combining with uncertainty in the physical positions, the uncertainty of measurements by BDC1 and BDC2 is: $(\delta_x, \delta_y, \delta_z) =$

(0.32, 0.12, 0.32) mm, with the uncertainty in y reported as a function of measurement resolution, since systematic position difference can be calibrated away for the y projection. The error for x and y straight-line projections can be approximately found as

$$\delta_{x_f} \approx \sqrt{\delta_{x1}^2 + \delta_{x2}^2} \cdot \frac{z_f - z_2}{z_2 - z_1} = 0.708 \text{ mm}, \tag{4.27}$$

$$\delta_{y_f} \approx \sqrt{\delta_{y1}^2 + \delta_{y2}^2} \cdot \frac{z_f - z_2}{z_2 - z_1} = 0.265 \text{ mm}. \tag{4.28}$$

The differences in x_{offset} fall within this error, and the differences in y_{offset} within a primary beam setting also fall within this error.

The error for projected angles follows the error of the initial angle determination

$$\delta_{\Psi_0} = |\Psi_0| \cdot \sqrt{\left(\frac{\delta_{x_2-x_1}}{x_2 - x_1}\right)^2 + \left(\frac{\delta_{z_2-z_1}}{z_2 - z_1}\right)^2} = 0.639 \text{ mrad} \tag{4.29}$$

$$\delta_{\theta_{pf}} \approx \delta_{\theta_{p0}} = |\theta_{p0}| \cdot \sqrt{\left(\frac{\delta_{y_2-y_1}}{y_2 - y_1}\right)^2 + \left(\frac{\delta_{z_2-z_1}}{z_2 - z_1}\right)^2} = 0.240 \text{ mrad}, \tag{4.30}$$

where $\delta_{\theta_{pf}} \approx \delta_{\theta_{p0}}$ since $\theta_{pf} = \theta_{p0}$. To calculate δ_{Ψ_f} an approximation is made: the error is calculated for the case of a projection through constant magnetic field of 0.5 T. Further, beam type and momentum are held constant for this approximation. The radius of curvature ρ and associated error δ_ρ is calculated assuming $Z = 50$ and $B = 0.5$ T exactly. In this approximation, Ψ_f is given by

$$\Psi_f = \sin^{-1}\left(\frac{\Delta z + \rho \cdot \sin(\Psi_0)}{\rho}\right), \tag{4.31}$$

with $\Delta z \approx 0.642$ m set to reproduce the typical $\Psi_f = 45$ mrad found by the step-wise projection for the ^{132}Sn beam. Using $\beta = 0.6565$ and $\delta_\beta = 2.597 \times 10^{-4}$, we find momentum $p = 106.945$ GeV/c, $\delta_p = 0.07435$ GeV/c, $\rho = 14.269$ m, and $\delta_\rho = 0.00248$ m. Taking $\Psi_0 = 0$, we can find $\Psi_f = 45$ mrad, and $\delta_{\Psi_f} = 0.6397 \times 10^{-4}$ mrad. With these values, the error in yaw angle is dominated by the error in Ψ_0

$$\delta_{\Psi_f} = \sec(\Psi_f) \cdot \sqrt{\left(\frac{\Delta z}{\rho^2} \cdot \delta_\rho\right)^2 + \Big(\cos(\Psi_0) \cdot \delta_{\Psi_0}\Big)^2} = 0.6397 \text{ mrad}. \tag{4.32}$$

4.3 Absolute Cross Section

Determining the absolute cross section for each system is necessary to normalize comparisons between systems. For simplicity, we start with the cross section for collisions that satisfy the trigger. The cross section can be determined statistically from the ratio of the number of nuclear reactions that satisfy the trigger to the number of incident particles by the relation

$$\frac{N_{\text{reactions}}}{N_{\text{incident}}} = \frac{\rho_A \sigma}{m}, \tag{4.33}$$

where ρ_A is target area density in g/cm^2, σ is the cross section in cm^2, and m is the mass of the target nucleus in g. The two targets used in the SπRIT campaign were isotopically enriched ^{112}Sn and ^{124}Sn, with measured thicknesses of 0.836 mm and 0.828 mm, respectively. The area densities of the ^{112}Sn and ^{124}Sn targets were measured at 0.561 g/cm^2 and 0.608g/cm^2, respectively. To calculate the cross section, we must determine $N_{\text{reactions}}$ and N_{incident}.

4.3.1 Measurement of Reacted Sn

The simplest measure of $N_{\text{reactions}}$ for a run is provided by correcting the number of gated triggers, N_{gated}, for purity and off-target reactions

$$N_{\text{reactions}} = N_{\text{gated}} \cdot \text{Purity}_{(\text{data})} \cdot R_{(\text{on target})}. \tag{4.34}$$

The value $\text{Purity}_{(\text{data})}$ was determined previously in Section 4.2.6. The average ratio of events on target

$$R_{(\text{on target})} = \frac{N_{\text{gated}}(\text{on target})}{N_{\text{gated}}} \tag{4.35}$$

was measured for each system using reconstructed vertex information from SπRITROOT. The Z position of reconstructed vertices for ^{132}Sn is shown in Figure 4.27, along with a Gaussian fit to the peak at the target position. Events within a 5σ cut of the target peak are counted as on-target. The average value is used, rather than the run-by-run value. The vertex reconstruction for all of the four systems is discussed later in Section 4.5.

4.3.2 Measurement of Incident Sn

The measurement of N_{incident} is made using the counts from the SBT scaler, but correction for Active Veto Array hits, the “liverate", reactions upstream of target, beam purity, and a normalization between the two primary beams is required. The beam purity, $\text{Purity}_{(\text{beam})}$, is tabulated in Section 4.2.6. The beam particles which hit the Active Veto Array produce a scaler count AVA which is subtracted from the SBT counts. The liverate is calculated using

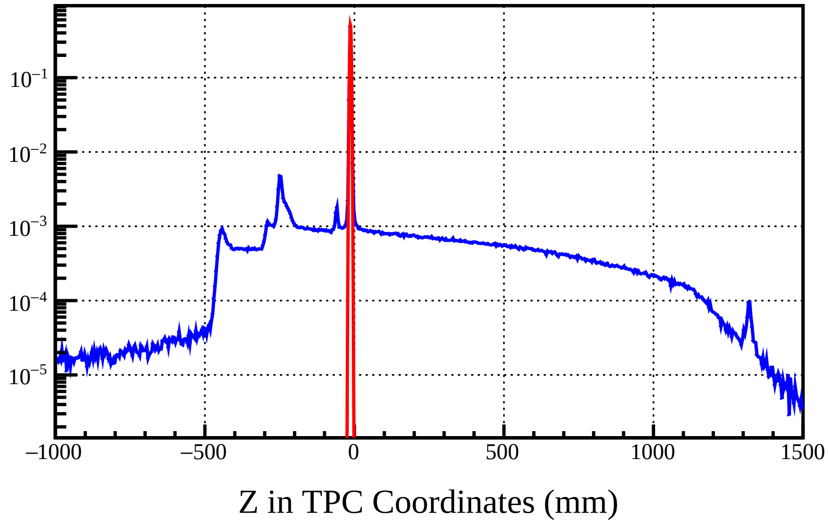

Figure 4.27: Vertex Z probability distribution for ^{132}Sn data. A fit on the target peak is shown in red.

the SBT scaler and the SBT & BUSY scaler

$$\text{liverate} = \frac{\text{SBT} - \text{SBT \& BUSY}}{\text{SBT}}. \tag{4.36}$$

Reactions upstream of target were estimated using the total absorption cross section., which is determined geometrically by treating each nucleus as a hard sphere with set interaction radii R_B and R_T for beam and target. It is assumed that when the impact parameter is less than or equal to $R_B + R_T$, a reaction will occur. Interaction radius is estimated as $R = 1.2 \times A^{1/3}$ fm, and cross section for reaction is given as $\sigma = \pi(R_B + R_T)^2$. The probability for collision is then given by

$$P_{\text{rxn}} = \sigma N_A \rho_A / A_T. \tag{4.37}$$

The reaction probabilities are tabulated in Table 4.6, with the background rate estimate coming from P_{bkgd} between the SBT and the target (TGT). This probability is multiplied by the number of SBT hits to determine the number of upstream reactions.

Start	End	$\mathrm{P_{bkgd}}$ (%) ^{108}Sn	$\mathrm{P_{bkgd}}$ (%) ^{112}Sn	$\mathrm{P_{bkgd}}$ (%) ^{124}Sn	$\mathrm{P_{bkgd}}$ (%) ^{132}Sn
SBT	TGT	1.12	1.30	1.36	1.40
TGT	TGT	1.25	1.28	1.31	1.36
TGT	$\mathrm{FC_{exit}}$	0.293	0.298	0.312	0.322
SBT	$\mathrm{FC_{exit}}$ (no TGT)	1.41	1.59	1.67	1.72

Table 4.6: Total absorption cross sections for the Sn beams used in the SπRIT experiment

The normalization between the two primary beams is required to account for trigger differences. As described in Chapter 3, the discrimination of the KATANA veto was performed differently between the two primary beams. For the ^{108}Sn and ^{112}Sn beams, pileup before the trigger is not suppressed, whereas for the ^{124}Sn and ^{132}Sn beams, pileup before the trigger was partially suppressed. The pileup suppression reduces the number of candidate incident Sn. To determine the suppression, the pileup rate is determined before and after the trigger using the F7 PPAC information as described in Section 4.2.4. This rate is used to determine the probability that a suppressed pileup event occurs. With the triggered pileup rate before as R_{before} and triggered pileup rate after as R_{after}, the suppressed rate $R_{\mathrm{suppressed}}$ is given as

$$R_{\mathrm{suppressed}} = R_{\mathrm{after}} - R_{\mathrm{before}}. \tag{4.38}$$

The probability that an incident Sn is suppressed due to pileup can be calculated using Poisson statistics. The veto window is 4 µs wide, so the probability that a suppression occurs is given as:

$$P_{\mathrm{suppression}} = e^{-\lambda}\frac{\lambda^2}{2!}, \tag{4.39}$$

where λ is calculated as:

$$\lambda = R_{\text{suppressed}} \cdot 4\ \mu\text{s}. \tag{4.40}$$

With the accumulated corrections, the number of candidate Sn can be determined as

$$N_{\text{incident}} = (SBT - AVA) \cdot (1 - P_{\text{suppression}} - P_{\text{bkgd}}) \cdot \text{Purity}_{(\text{beam})} \cdot \text{liverate}, \tag{4.41}$$

giving the final value for cross section determination.

4.3.3 Measured Cross Section

With $N_{\text{reactions}}$ and N_{incident} determined, the cross section can be determined using Equation 4.33. The average of the determined absolute cross sections for all data runs are shown in Figure 4.28 as a function of system mass, with error bars corresponding to the standard deviation of determined absolute cross sections for each beam. The values are tabulated in Table 4.7, along with the standard deviation.

Beam	Target	σ (barn)	stddev (barn)
^{132}Sn	^{124}Sn	1.775	0.012
^{124}Sn	^{112}Sn	1.679	0.013
^{112}Sn	^{124}Sn	1.687	0.009
^{108}Sn	^{112}Sn	1.598	0.010

Table 4.7: Average absolute cross section, σ, with standard deviation of the cross section measured for the data runs.

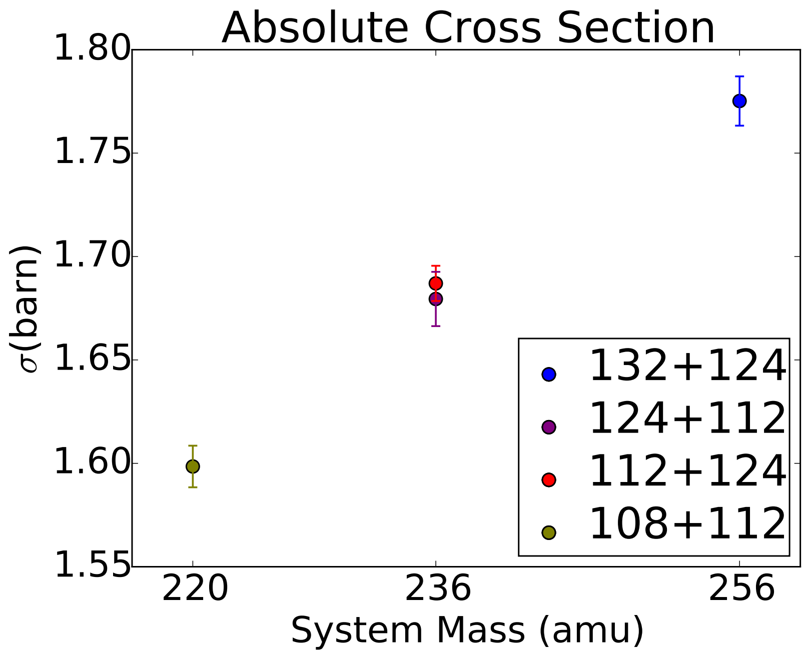

Figure 4.28: Calculated cross section for each system, organized by total system mass

4.4 Impact Parameter Selection

The measured cross section relates to the range of impact parameter measured. In the following, we use the number of charged particles measured in an event (i.e., the multiplicity) as a measure of the impact parameter. Generally, the average charged particle multiplicity of events at a given impact parameter decreases with increasing impact parameter. For simplicity, we assume this relationship is correct for individual events and discuss the validity of this approximation later. In this approximation, the cross section for events with a multiplicity greater than a given value is related geometrically to the maximum impact parameter $b_{\max}$

$$\sigma_{b_{\max}} = \pi \cdot b_{\max}^2. \tag{4.42}$$

The uncertainty associated with determining cross section $\sigma_{b_{\max}}$ causes an uncertainty in $b_{\max}$, discussed later.

The detected charged particle multiplicity provides a basic filter of the impact parameter. A reaction with a small impact parameter will in general produce a higher charged particle multiplicity than an otherwise similar reaction with a larger impact parameter. However, this relationship is not exact for many reasons. First, the charged particle multiplicity depends on whether the emitted particles emerge as nucleons or as bound clusters with $Z > 1$. At high temperatures, and high entropies/nucleon, the emission of individual nucleons and a high multiplicity are favored while at low temperatures and low entropies, the emission of clusters with $Z > 1$ and a low multiplicity are favored. The amount of heating is increased with the number of hard collisions per event, but the number hard collisions varies randomly from event to event, even when all events are at the same impact parameter. Second, we do not detect all charged particles; this introduces another uncertainty that can be assessed by simulating the event. Third, it is obvious that we cannot perfectly constrain the continuous impact parameter distribution with a discrete multiplicity distribution. These uncertainties, however, can all be explored and addressed by simulating the impact parameter filter theoretically and determining the uncertainties in the impact parameter for each choice of impact parameter filter. We return to this issue later.

The normalized charged particle multiplicity distributions for all systems are shown in Figure 4.29, with $\mathrm{P[N_C]}$ the probability of detecting a given number of charged particles. In contrast to a minimum bias trigger for which the most probable multiplicity is very low, the trigger suppresses low multiplicities. The requirement of multiplicity greater than or equal to 4 in the Kyoto Multiplicity Array is the most effective at suppressing peripheral collisions with low charged particle multiplicities. The events are selected with the same filter used to determine cross section: a 5σ cut around the vertex peak, and the beam PID cut used for particle selection. Tracks contributing to the multiplicity count must have a Point Of

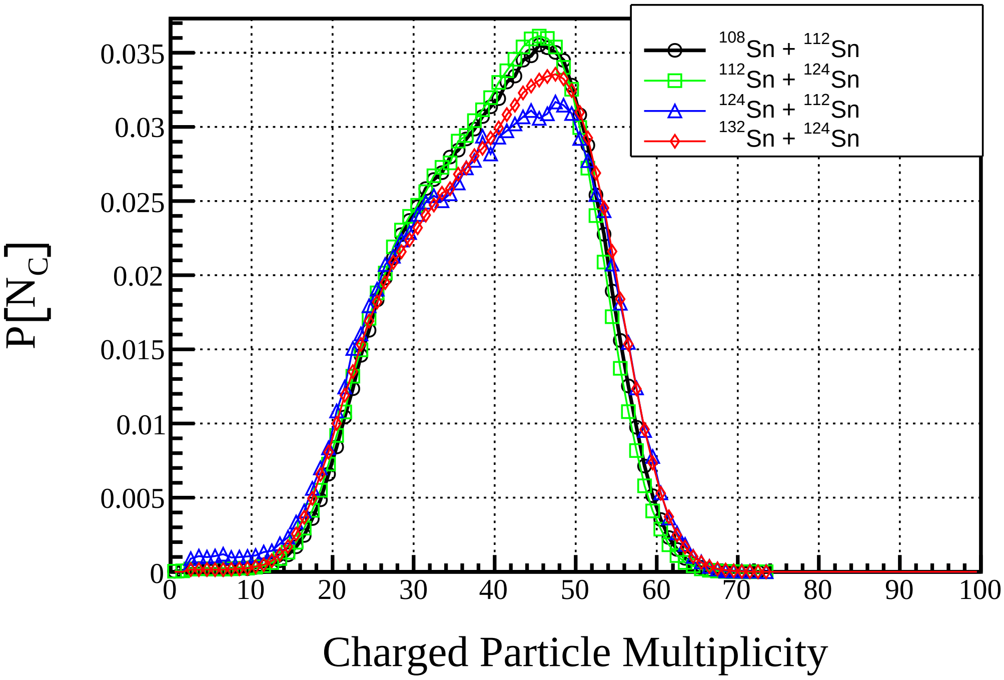

Figure 4.29: Charged particle multiplicity distribution for the four beam systems

Closest Approach (POCA) of 20 mm to the event vertex. The distributions are normalized by the number of entries.

Assuming a monotonic relationship between impact parameter and charged particle multiplicity N_C, with a smaller impact parameter associated with a larger charged particle multiplicity, we can calculate the cross section for a given multiplicity $N \geq N_C$:

$$\sigma_N = \frac{N \geq N_C}{N_{\text{total}}}. \tag{4.43}$$

It is common to define a reduced impact parameter as

$$\hat{b} = \frac{b(N_C)}{b_{\max}} = \left\{ \sum_{N_C}^{\infty} \frac{dP(N_C)}{dN_C} \right\}^{1/2}, \tag{4.44}$$

where $b_{\max}$ is the maximum impact parameter determined by the absolute cross section in

Section 4.3, and $dP(N_C)/dN_C$ is the normalized probability distribution for N_C. Values of $\hat{b}$ range from 0 for the most central events to 1 for the least central events. Values of $\hat{b}$ are multiplied by b_{max} to extract $b(N_C)$. The relationship between b and N_C is shown in Figure 4.30 for all four systems. The shaded regions represent error, which is discussed next.

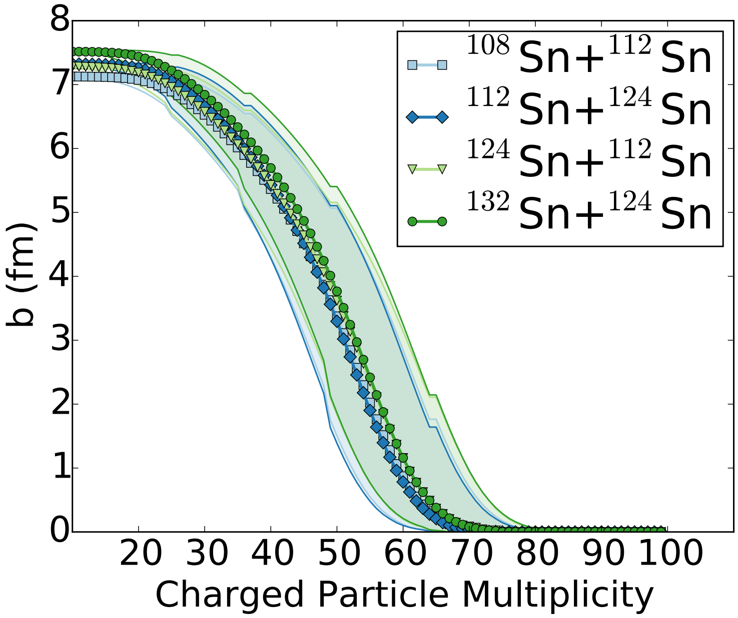

Figure 4.30: Relationship between b and N_C for the four beam systems, with error shown by shaded regions

There are two main sources of error that contribute to the determination of $\hat{b}$: the error in determining b_{max}, and the range of values of b which can result in measured N_C. A significant contribution to error in determining b_{max} comes from the uncertainty of the measured absolute cross section. This contribution is determined using standard error propagation,

$$\delta b_{\text{max}} = \sqrt{\left(\frac{\partial b_{\text{max}}}{\partial \sigma_{\text{tot}}} \cdot \delta\sigma_{\text{tot}}\right)^2} = \frac{\delta\sigma_{\text{tot}}}{2\sqrt{\pi\sigma}}. \tag{4.45}$$

The calculated error of b_{max} is listed for each system in Table 4.8, using one standard deviation of σ_{tot} for $\delta\sigma_{\text{tot}}$.

Beam	Target	b_{max} (fm)	δb_{max}
^{132}Sn	^{124}Sn	7.52	0.0254
^{124}Sn	^{112}Sn	7.31	0.0283
^{112}Sn	^{124}Sn	7.33	0.0195
^{108}Sn	^{112}Sn	7.13	0.0223

Table 4.8: Average absolute cross section, σ, with standard deviation of the cross section measured for the data runs.

An event at given impact parameter b does not produce a deterministic value of N_C. We assume that the values of N_C from a given b follow a Poisson distribution. A multinomial distribution is likely a better description of N_C, but this will require further analysis to model. The average value of $\overline{N_C}$ is determined using the relationship in Equation 4.44, and the standard deviation is then $\sqrt{\overline{N_C}}$ by standard Poisson statistics. This allows us to set error bars for b from $b\left(\overline{N_C} - \sqrt{\overline{N_C}}\right)$ to $b\left(\overline{N_C} + \sqrt{\overline{N_C}}\right)$. The error for b_{max} is included by adding $\pm\hat{b} \cdot \delta b_{\mathrm{max}}$.

4.5 TPC Analysis

The data produced by the GET electronics is stored as hardware-specific binary-encoded files, which are unpacked to ROOT files using the GETDecoder software [12, 72]. Each CoBo board produces a raw data file, and the unpacked ROOT files are maintained as files for each CoBo, resulting in 12 files for each data set. These unpacked ROOT files are then analyzed using SπRITROOT [73], a package based on the FairRoot framework [74]. The analysis flow is shown in Figure 4.31, with two branches: one for simulation, and one for analysis of experimental data. After digitization of a simulated event, the analysis follows the same flow as that of the data.

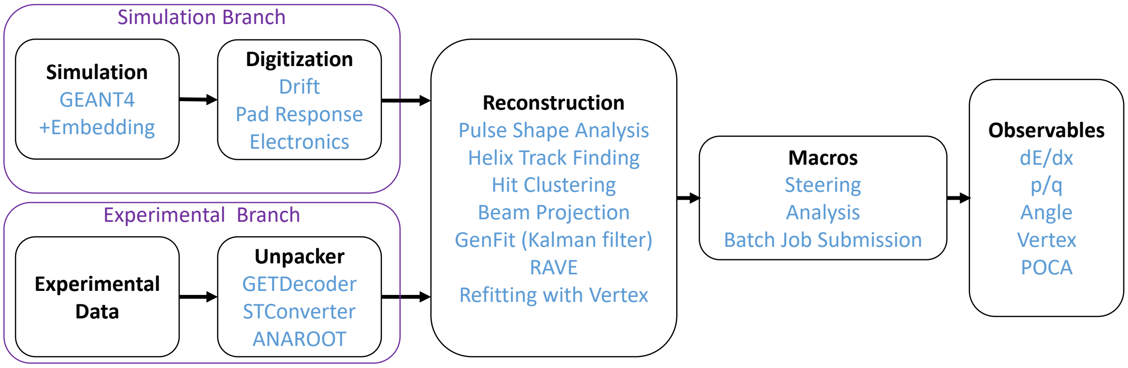

Figure 4.31: Analysis flow for the SπRITROOT software package, showing branches for experimental data as well as simulation

The reconstruction stage starts with the pulse finding task. The data for each pad consists of an amplitude over time spectra, divided into discrete bins of time. An example of the data from a single pad in a single event is shown in Figure 4.32. For the SπRIT experiment, the AsAd sampling frequency of 25 MHz resulted in time bins, or time buckets, of 40 ns width. Since the drift time for electrons in the TPC is roughly 9 µs, only 270 time buckets were used, which leaves a few time buckets for pedestal subtraction. The first task for reconstruction of an event is to analyze the hits on all pads. The Pad Response Function (PRF) describes the amplitude on a pad resulting from collected charge. A reference pulse was generated from experimental data which was used to fit the signals from each pad. Each pad is scanned from the earliest time to the latest time, searching for peaks. When a peak is found, it is fit using the reference pulse shape. The fitted pulse shape is subtracted from the spectra, and the peak finding continues the scan for additional peaks. Each fitted pulse is stored as a “hit", with position and amplitude information. In Figure 4.32, the individual fits are shown in red, the overall fit (sum of all individual fits) is shown in black, and the raw spectra is shown in gray.

Since the charge from an avalanche is spread out over multiple pads, a single hit does not contain the complete information for an avalanche. When an avalanche occurs over a

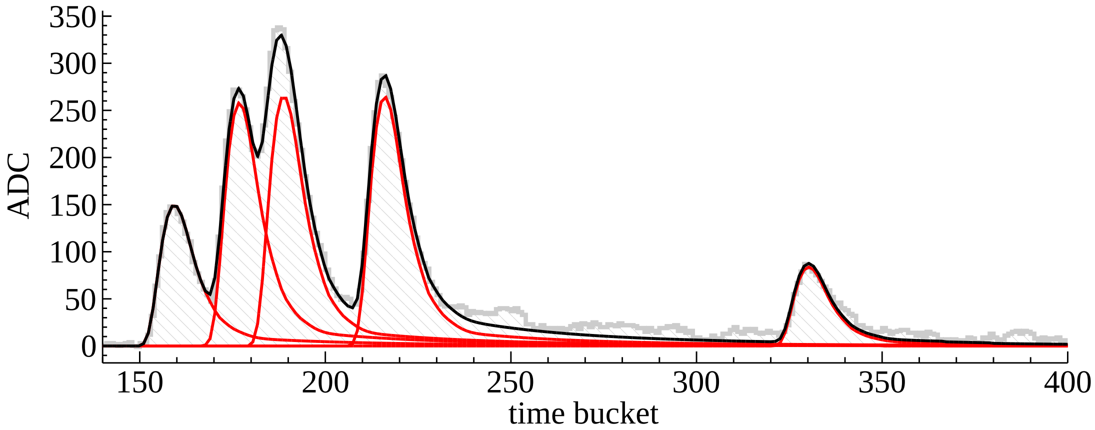

Figure 4.32: Example ADC spectra for a pad. Signal height is in ADC channels, and each time bucket corresponds to 40 ns. Figure from [12].

pad, the neighboring pads will have a signal proportional to their relative proximity to the avalanche. Neighboring hits are grouped into “clusters", which collectively provide more complete information about position and charge. The total charge Q for a cluster is determined by summing the charge q_i from all contributing hits, $Q = \sum_i q_i$. The position X is determined using the charge-weighted positions of each pad, $X = \frac{\sum_i q_i x_i}{\sum_i q_i}$.

The creation of clusters and the track finding process are intertwined. Clusters are ideally formed perpendicular to the track, so the cluster formation is integrated with the track finding task. Hits are mapped to a Riemann sphere, with radius R_R equal to twice the variance of hits in the pad plane. The sphere is centered with x_0 at the location of the average x hit position, $\langle x_{\text{hit}} \rangle$, y_0 at R_R, and z_0 at the center of the pad plane. The mapping of hits onto the Reimann sphere groups hits associated with a track near each other, allowing the formation of track candidates, which are parametrized with a helical equation. Remaining hits are compared against the track candidates, and are associated with the track based on their point-of-closest-approach (POCA) to the track's helical equation. With hits associated to a track, clusters can be formed from the hits. Clusters are ideally formed as a group of hits perpendicular to a track. Since the pads run in row (along the x direction) and layers (along the z direction), clusters must be formed along these directions. The decision of whether to cluster along a row or layer is determined by the track's crossing angle: if the track's yaw angle at a given point is greater than 45°, it is clustered along that row. Otherwise, it is clustered along the layer.

The final fit of tracks is performed using the GENFIT package [75]. GENFIT uses the least square Kalman filtering algorithm with the gas properties and magnetic field map as input parameters to fit the track momentum. Initial parameters are provided from the helix parametrization discussed above. We have the option to refit the track momenta including a point from the BDC vertex, but for this work, the initial momentum provided by GENFIT is used to determine particle momenta.

The RAVE toolkit [76] was implemented for vertex finding. RAVE was designed for the CMS experiment [77], which utilizes a large solenoidal magnet. RAVE performs best with the magnetic field aligned along the z-axis, as is the case for CMS. Thus, a cyclical change of coordinate system, (x,y,z) → (z,x,y), was made when providing tracks to RAVE, so that the magnetic field was aligned along the z-axis in the fitting environment. The reconstructed x and y positions can be compared to the BDC projection, as was shown earlier in Section 4.2.8. The distribution of reaction position in z is shown in Figure 4.33, for all four systems. A sharp peak corresponds to reactions on target. The position and width of the peak for each system are listed in Table 4.9, along with the measured physical position of the target. The event vertex found from the TPC is used to determine if the reaction occurred on target.

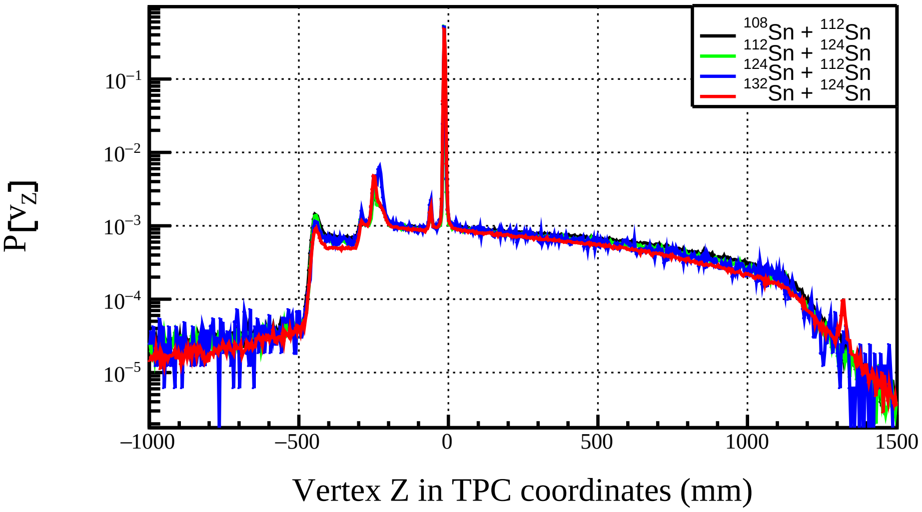

Figure 4.33: Normalized distribution of z position of reconstructed vertex, for all systems.

Beam	Target	Target center (measured) (mm)	Reaction Peak (RAVE) (mm)	Sigma (mm)
^{132}Sn	^{124}Sn	-13.12	-13.10	1.83
^{124}Sn	^{112}Sn	-13.27	-13.13	1.44
^{112}Sn	^{124}Sn	-13.12	-12.86	1.27
^{108}Sn	^{112}Sn	-13.19	-13.35	1.70

Table 4.9: Comparison of measured target position and reconstructed reaction vertex. Dimensions are in the TPC frame.

4.5.1 Track Validation

To remove background, we must remove tracks that are not associated with our event or cannot be reconstructed well. The GENFIT result provides a track fit that can be compared to the RAVE vertex to obtain the point of closest approach (POCA). Tracks which have POCA>20 mm are invalidated, as they are likely either a deflected particle, a false reconstruction, or an upstream reaction product. Tracks with few clusters can be caused by false reconstruction, or by short tracks for which the momentum and energy loss cannot be well resolved. A minimum of 15 clusters is required for tracks to be validated.

Figure 4.34 shows a typical event for the TPC, from (top panel) above and (bottom panel) the side. The region by the entrance window has a high occupancy probability. The clustering does not handle charge sharing, resulting in artificially high dE/dx values for clusters in this region. Also, pads for this high density region are often saturated. An ellipsoid cut, drawn on Figure 4.34 with a red line, is used to exclude clusters in this high density region as such clusters tend to make the track reconstruction less accurate.

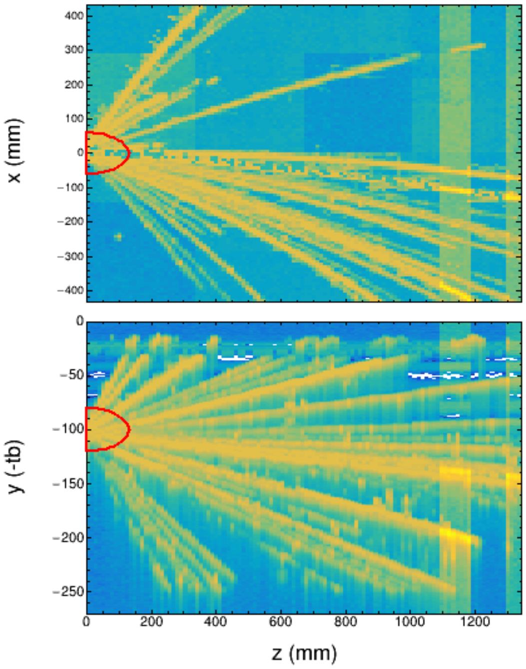

Figure 4.34: A typical event in the TPC viewed from (top panel) above and (bottom panel) the side. The high density region outlined in red is excluded from data analysis.

In addition to track cuts, event cuts are applied to the data. Isotopic cuts, described earlier in this chapter, are applied to select only reactions with the desired isotopes. The RAVE vertex is used to select reactions on target, excluding upstream and active target reactions. Events with reaction vertex within 3σ of the vertex z peak are considered to be on target. Additionally the x and y vertex position is required to be within the physical target location.

To demonstrate the effect of the track validation, the PID plot after determining $B\rho$ and dE/dx is shown in the left panel of Figure 4.35, for ^{124}Sn beam impinged on a ^{112}Sn target. Although PID lines are clearly evident, they are not clearly resolved, with pion lines almost impossible to discern. The PID plot after removing background with the filters defined above is shown in the right panel of Figure 4.35, for the same set of events. The PID shows drastic improvement in the resolution of particles, with pion lines clearly evident.

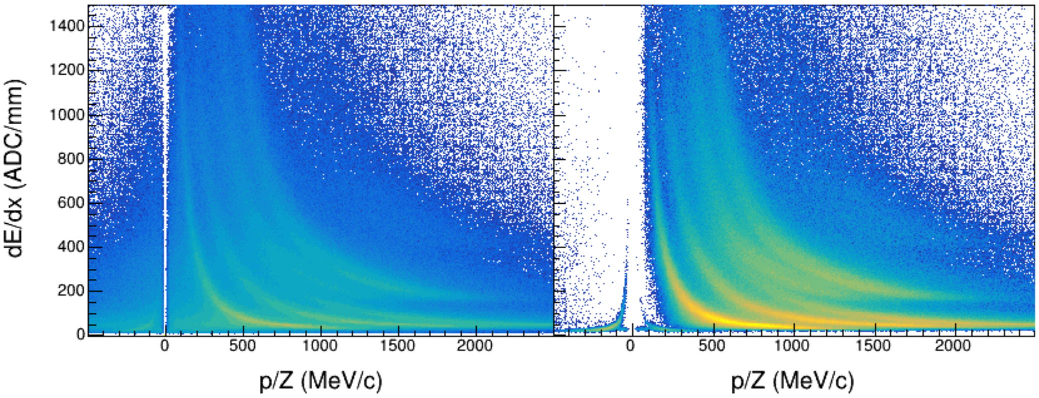

Figure 4.35: The PID for ^{124}Sn events, (left) without cuts, and (right) with cuts.

4.5.2 Detection Efficiency from Embedding Studies

The data contains high track multiplicity events, which are difficult to accurately reproduce with simulations. To determine reconstruction efficiency, an embedding simulation was developed. This method is used by the STAR collaboration [78], and involves embedding simulated particles into real data events. Single pion tracks were generated using GEANT4 [79] over a range of angles and momenta, and embedded into data events from the ^{132}Sn + ^{124}Sn system. As shown in Figure 4.31, the electron drift and pad response for each simulated track is determined in the simulation branch. After the simulated track is embedded in the real data event, the event is analyzed using the reconstruction software. The POCA<20 mm condition and minimum of 15 clusters condition are applied to tracks (including the embedded track), and if the embedded track is reconstructed and meets these conditions, it can be classified as “detected". The reconstruction efficiency is determined as a function of track angle, momentum, and event multiplicity by determining the proportion of detected to total tracks embedded with similar properties.

4.6 Calibration with Cocktail Beam

The ^{238}U primary beam was used to produce two $Z \approx$1–3 cocktail beams for calibration of the TPC. The beam energies were tuned for alpha particles: the higher energy cocktail beam produced alpha particles at 300 MeV/u, while the lower energy cocktail beam produced alpha particles at 100 MeV/u. Both of these beams were measured with an empty target in the TPC, and the 100 MeV/u beam was also measured with a 21 mm thick aluminum target, which served as an energy degrader. The combination of these setups provides 3 distinct energy calibration points for the TPC. The TPC is used to construct the PID of incoming particles, as the ion chamber energy loss is too low to produce a beam PID.

4.6.1 Cocktail Beam Settings

For the cocktail beam, plastic scintillators were used in focal planes F3, F8, and F13. The F8 plastic scintillator was used to trigger data acquisition. The final quadrupole, STQ25, is tuned to maximize acceptance of the expected rigidity. For the $E \approx$ 300 MeV/u beam, STQ25 was tuned to maximize acceptance around 5.3759 T·m, and for the $E \approx$ 100 MeV/u beam, STQ25 was tuned to maximize acceptance around 2.9239 T·m, corresponding to 300.11 MeV/u and 97.93 MeV/u alpha particles, respectively.

Since the particles are low charge, the plastic scintillators do not have 100% detection efficiency, although every triggered event will have a signal in the F8 plastic. We are not able to reconstruct a beam PID, but we can determine PID using the TPC, and examine the corresponding TOF from F3 to F8, and F8 to F13 scintillators. These TOF measurements are uncalibrated, but the offset should be the same regardless of isotope. Using ^{2}H and ^{4}He as test isotopes, the TOF offset between F8 and F13 is tuned to reproduce the expected $B\rho$ value. The TOF offset is set to 477.6 ns for the 300 MeV/u beam, and 479.4 ns for the 100 MeV/u beam. These offsets are expected to be different, as the plastic timing was adjusted for each setting. The average $B\rho$ value for each isotope is listed in Table 4.10. The particle rigidities are within +0.7%/-1.7% of the expected $B\rho$.

Particle	$B\rho$ (T·m) (100 MeV/u setting)	$B\rho$ (T·m) (300 MeV/u setting)
p	2.934	5.358
d	2.944	5.402
t	2.890	5.366
^{3}He	2.925	5.366
^{4}He	2.903	5.394
^{6}Li	N/A	5.322
^{7}Li	N/A	5.287

Table 4.10: Magnetic rigidity for each particle in cocktail beams

4.6.2 Rigidity within TPC

The TPC provides a measurement of magnetic rigidity, which can be compared to the expected rigidity. The measured magnetic rigidity in the TPC appears to be correct if we only analyze tracks over the first 90 layers of the TPC, corresponding to 108 cm along the length of the pad plane. More precise values for the rigidity can be obtained by utilizing the full 112 layers (134.4 cm) of the TPC, but the rigidity obtained using the full 112 layers became systematically higher than the expected rigidity. This discrepancy originates from the magnetic field, which has non-negligible horizontal components, and a reduced, non-uniform vertical component as it approaches the edge of the pole face. For the TPC analysis in this body of work, this discrepancy was patched by shifting the magnetic field center 22 cm upstream, effectively reducing the magnetic field strength for track fitting. The original PID is shown in the left panel of Figure 4.36, and the PID which results from using a shifted magnetic field is shown in the right panel. The differences are not substantial, but shifting the magnetic field better aligns the reconstructed momentum with the expected momentum.

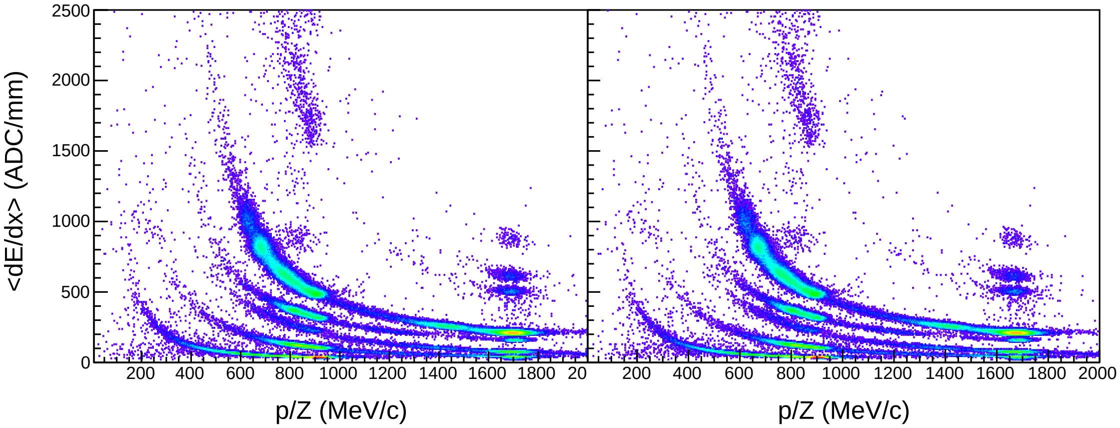

Figure 4.36: Cocktail PID using (left) proper geometry and (right) shifted magnetic field

A detailed analysis of the electron drift in this region reveals that non-negligible x and z components of the magnetic field in the original (correct) field map change the drift of electrons in the final 24.4 cm of the field cage. This shifts and straightens the image of the track on the pad plane and increases the rigidity values extracted from the track. A new correction that takes the resulting $\mathbf{E}\times\mathbf{B}$ component of the electronic drift velocity has been obtained and will be applied to all future analyses, although it was not ready to be applied to the analysis in this work.

4.7 Mixed ^{124}Sn-like beam

Because the statistics of the ^{124}Sn beam are limited, it is necessary to include additional beam particles in the analysis. The selection of isotopes is performed to match the average charge, mass, and asymmetry of the ^{124}Sn+^{112}Sn system, with asymmetry δ defined as:

$$\delta = \frac{N-Z}{N+Z}. \tag{4.46}$$

For example, if an equal number of ^{123}In, ^{123}Sn, ^{125}Sn, and ^{125}Sb beam particles are impinged on the ^{112}Sn target, the beam-target system's average charge, average mass, and average asymmetry will be the same as that of the ^{124}Sn+^{112}Sn system.

The selected isotopes, and relative proportions, are listed in Table 4.11. For the duration of this work, the mixed beam consisting of these isotopes will be denoted as the $^{124^*}$Sn beam.

Beam Isotope	Relative Composition (%)	Beam Isotope	Relative Composition (%)
^{121}Ag	1.3	^{124}Sn	16.71
^{122}Ag	1.43	^{125}Sn	4.41
^{121}Cd	1.08	^{124}Sb	7.19
^{122}Cd	5.44	^{125}Sb	22.48
^{123}Cd	2.93	^{125}Te	0.07
^{122}In	3.3	^{126}Te	5.67
^{123}In	13.1	^{127}Te	4.01
^{124}In	5.78	^{127}I	0.77
^{123}Sn	4.35		

Table 4.11: Beam isotopes included for mixed $^{124^*}$Sn beam

To check that these additions are reasonable, we plot the reduced impact parameter $\hat{b}$ (See section 4.4) spectra for the ^{124}Sn beam and the $^{124^*}$Sn beam. The reduced impact parameter is in good agreement for all beam types. When measuring the pion spectra in the following section, the ^{124}Sn and ^{124*}Sn spectra are evaluated for consistency.

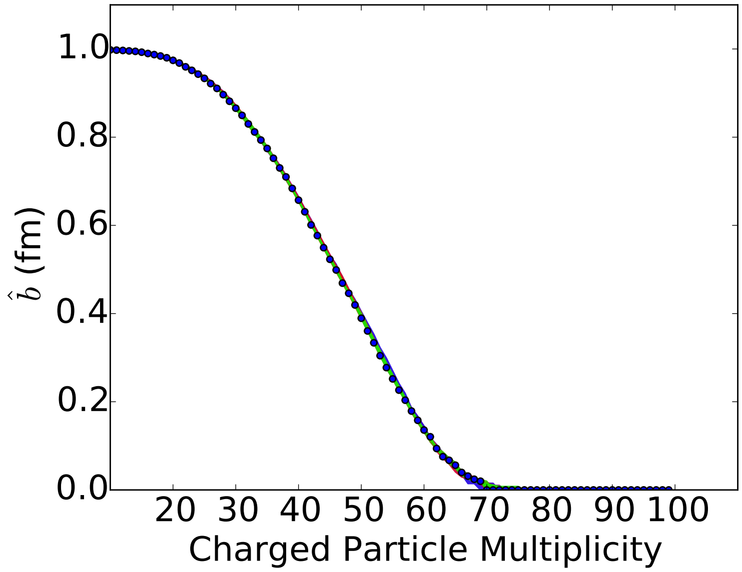

Figure 4.37: $\hat{b}$ spectra for ^{124*}Sn mixed beam.

4.8 ^{112}Sn+^{124}Sn and ^{124*}Sn+^{112}Sn pion production

The ^{112}Sn + ^{124}Sn and ^{124*}Sn + ^{112}Sn systems provide critical comparisons of the two primary beams, and the pion production from these systems is predicted to be sensitive to the symmetry energy. Since the systems are approximately mirror reactions, we expect that the physics will be similar and mainly affected by the interplay of each system's kinematics with the experimental setup. Incomplete stopping and incomplete equilibration may affect the reactions, that is, the beam nucleons may not fully mix with the target nucleons. This would cause the ^{124*}Sn reaction to be more representative of emission from a system that is more neutron rich, and cause the ^{112}Sn system to be more representative of a system that is more neutron deficient. This difference should be more manifest at high particle rapidities, which move at rapidities consistent with the beam velocity, and less so at particle rapidities consistent with emission from an equilibrated system, which move at rapidities consistent with the center-of-momentum of the projectile plus target system. Such effects would also be more evident in peripheral collisions, consistent with a higher degree of stopping in central collisions. Using the impact parameter described in Section 4.4, events are selected from the ^{112}Sn system and ^{124*}Sn with impact parameter up to 3.1 fm. The pion spectra for the two systems are produced and examined in this section.

4.8.1 PID fitting and pion selection

The particle identification depends on measuring each particle's momentum and energy loss. The energy loss is a function of a particle's relativistic velocity β and charge q. The TPC measures magnetic rigidity, or p/q. If the charge and mass of a particle are known, the momentum and velocity can be determined. The momentum is related to β by

$$\beta = \frac{p}{\sqrt{p^2 + m^2c^2}}. \tag{4.47}$$

The energy loss $dE/dx(Z, \beta)$ is approximated following the form used by Blum et al. [30]:

$$dE/dx = Z^2 \frac{p_1}{\beta^{p_4}} \left\{ p_2 - \beta^{p_4} - \ln \left[p_3 + \left(\frac{1}{\beta\gamma} \right)^{p_5} \right] \right\}, \tag{4.48}$$

where p_1–p_5 are free parameters. The energy loss curve was found to vary by pitch and yaw, so it is fit separately for different regions of angular emission, with 6 equal divisions of yaw and 12 equal divisions of pitch. This fit provides a function to describe energy loss dE/dx(typ.) of a typical pion, as a function of momentum in the lab frame. Figure 4.38

shows the quantity

$$\ln\left(\frac{dE/dx(\text{track})}{dE/dx(\text{typ.})}\right) \tag{4.49}$$

for pions as a function of track momentum in lab frame, where $dE/dx(\text{track})$ is the measured energy loss for a given track, and $dE/dx(\text{typ.})$ is the typical value of energy loss determined from the fits discussed above. The projection to the Y-axis is shown on the left for π^-, and on the right for π^+. A large contribution from protons is visible in the top-right corner of the plot of π^+. The top panels show the ^{124*}Sn system, and the bottom panels show the ^{112}Sn system. Electron (e^-) and positron (e^+) lines can be seen underneath the pion lines. Pions are selected from these spectra using graphical cuts.

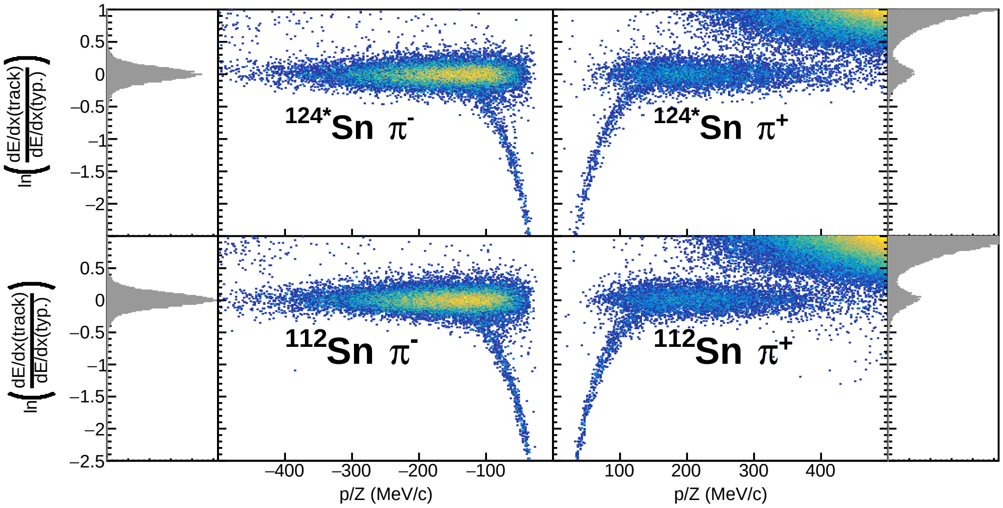

Figure 4.38: Comparison of energy loss to typical energy loss for (top) ^{124*}Sn system and (bottom) ^{112}Sn system. Y-projections are shown to the left for π^-, and to the right for π^+.

4.8.2 Background Estimation

Figure 4.38 shows the positron and electron lines intersecting with the pion line, as well as the proton line overlapping with the π^+ line, indicating that the pion lines contain background from other particles. This background is estimated as a function of momentum, using the

π^+ as an example. Slices of the flattened PID are made every 20 MeV/c, and projected to the y-axis. Figure 4.39 shows this projection for ^{124*}Sn+^{112}Sn between 380 and 400 MeV/c. The peaks from π^+ and protons are clearly visible and overlapping. The spectra is fit with the sum of two Gaussian functions, shown in red in the figure. The deconvolution of these Gaussians provides Gaussian estimates for π^+ (fit shown in green) and protons (fit shown in blue). These fits are used to estimate the relative contribution from pions and protons.

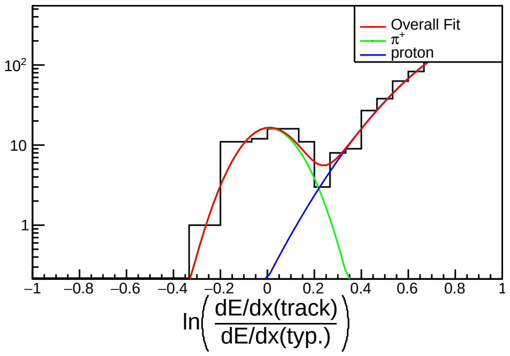

Figure 4.39: Projection of flattened PID between 380 and 400 MeV/c. The π^+ (green) and proton (blue) peaks are fit simultaneously, with the total fit (red) and separate contributions shown.

Within this section, we let x be

$$x = \ln\left(\frac{dE/dx(\text{track})}{dE/dx(\text{typ.})}\right), \tag{4.50}$$

thereby giving a variable name to the quantity defined by Equation 4.49. For the momentum range shown in Figure 4.39, a particle at a given x will have some probability of being a pion and some probability of being a proton. If we write the Gaussian fit for a pion as

$$G_\pi(x) = A_\pi e^{-\frac{(x-\mu_\pi)^2}{2\sigma_\pi^2}}, \tag{4.51}$$

and for a proton as:

$$G_p(x) = A_p e^{-\frac{(x-\mu_p)^2}{2\sigma_p^2}}, \tag{4.52}$$

then the probability that a particle is a pion can be found as

$$P(\pi) = \left(1 + \frac{A_p}{A_\pi} e^{-\frac{(x-\mu_p)^2}{2\sigma_p^2} + \frac{(x-\mu_\pi)^2}{2\sigma_\pi^2}}\right)^{-1}. \tag{4.53}$$

The error is estimated by propogating the fit error for each parameter:

$$\begin{aligned} &\left(\frac{\delta P(\pi)}{P(\pi)}\right)^2 = \\ &\left(\frac{\partial P(\pi)}{\partial A_p}\delta A_p\right)^2 + \left(\frac{\partial P(\pi)}{\partial \mu_p}\delta \mu_p\right)^2 + \left(\frac{\partial P(\pi)}{\partial \sigma_p}\delta \sigma_p\right)^2 + \\ &\left(\frac{\partial P(\pi)}{\partial A_\pi}\delta A_\pi\right)^2 + \left(\frac{\partial P(\pi)}{\partial \mu_\pi}\delta \mu_\pi\right)^2 + \left(\frac{\partial P(\pi)}{\partial \sigma_\pi}\delta \sigma_\pi\right)^2 \end{aligned} \tag{4.54}$$

Figure 4.40 shows the average background as a function of momentum bin, for tracks selected with a graphical cut. The background contribution is less than 5% for most of the momentum regions we investigate. Near 100 MeV/c, the background contribution rises to about 8%: this is where the positron line intersects the pion line.

4.8.3 Pion Multiplicities

With pions selected, we create the momentum spectra for pions in the lab frame and energy spectra in the COM frame, normalized by the number of candidate events (selected as described in Section 4.5.1). The pions are translated to the COM frame using a Lorentz boost, opposite the beam direction, with magnitude β_{COM}. The beam angle is determined using the BDC information (See Section 4.2.8), and the beam velocity is determined using

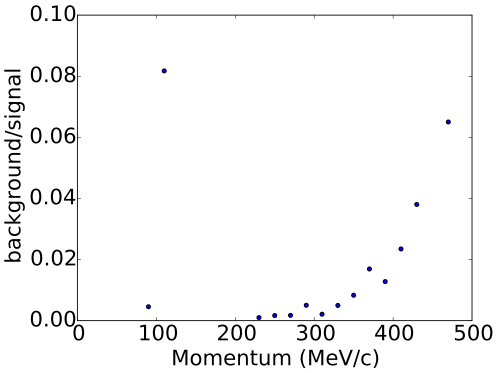

Figure 4.40: Average background/signal ratios for π^+, as a function of momentum. The effects of positron and proton contamination are evident.

the TOF information (see Section 4.2.2), with an energy loss correction, which is calculated with LISE++. The mass of the target is added to the beam energy, and the total energy and mass of the system used to determine β_{COM}. A rather restrictive cut is used, implemented in the COM frame, allowing us to compare the two systems in regions of similar acceptance and reconstruction efficiency:

$$\begin{aligned} -40^\circ \leq \phi_{\text{COM}} \leq 20^\circ, \\ 150^\circ \leq \phi_{\text{COM}} \leq 220^\circ, \end{aligned} \tag{4.55}$$

$$0^\circ \leq \theta_{\text{COM}} \leq 90^\circ. \tag{4.56}$$

Since the solid angle coverage is not complete, we must scale the results by a correction factor. We calculate the solid angle of the angular range selected,

$$\Omega_{\text{selected}} = \frac{130}{360} 2\pi \int_{0^\circ}^{90^\circ} \sin(\theta) d\theta = \frac{13 \cdot 2\pi}{36} \tag{4.57}$$

where the factor 130/360 comes from the ϕ_{COM} selection, which cuts out part of the solid angle. To obtain the correction factor, we divide $\Omega_{\mathrm{selected}}$ by 4π to obtain

$$\frac{\Omega_{\mathrm{selected}}}{\Omega_{\mathrm{total}}} = \frac{13 \cdot 2\pi}{36 \cdot 4\pi} \approx 0.18056. \tag{4.58}$$

Beam	Events	π^- (Raw)	π^+ (Raw)	π^- (Eff. Corr.)	π^+ (Eff. Corr.)
^{124*}Sn	74168	5321	1833	36567	12736
^{124}Sn	9112	637	201	4366	1397
^{112}Sn	115543	8561	2757	59220	19198

Table 4.12: Efficiency corrected (Eff. Corr.) pion yields for this work.

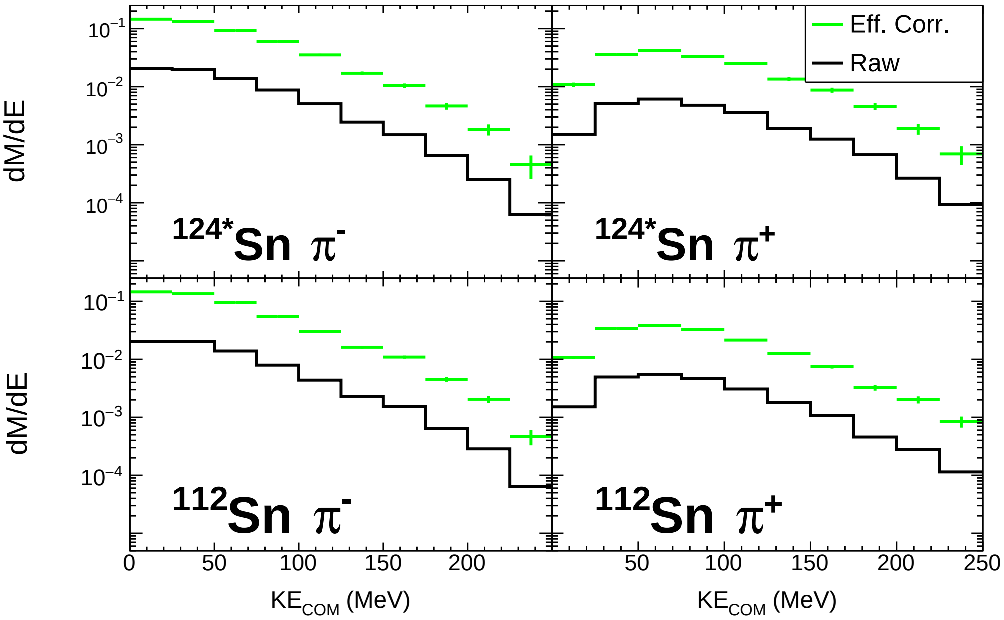

Figure 4.41: Pion kinetic energy spectra in COM frame. π^- are drawn on the left side, π^+ on the right. The top panels are for the ^{124*}Sn system, while the bottom panels are for the ^{112}Sn system.

The COM kinetic energy spectra for pions are shown in Figure 4.41, with π^- on the left side, π^+ on the right, from the ^{124*}Sn system on top, and from the ^{112}Sn system on the bottom. The raw spectra is drawn with black histograms, and the efficiency corrected spectra is drawn with green crosses. The efficiency correction incorporates the solid angle correction, background correction, and the embedded efficiency correction. The statistics are particularly limited for π^+ above 200 MeV. A direct comparison between the two systems is shown in Figure 4.42, for π^- (left) and π^+ (right). It is apparent that the ratio is close to 1, although there is not perfect agreement between the systems.

diverging for kinetic energy over 150 MeV for both π^- and π^+.

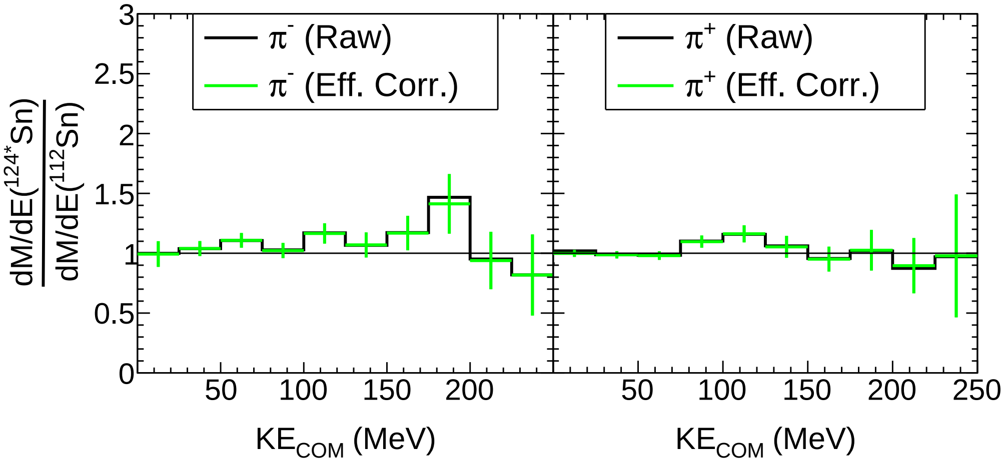

Figure 4.42: Relative pion production for the ^{124*}Sn system and the ^{112}Sn system, for π^- (left) and π^+ (right)

The rapidities y_{beam}, y_{COM}, and $y_{\pi COM}$ are all calculated, along with transverse momentum p_t, allowing us to plot the p_t-y_0 phase space distributions for the pions. We normalize the pion rapidity,

$$y_0 = \frac{y_{\pi COM}}{y_{\text{beam}} - y_{\text{COM}}}, \tag{4.59}$$

to determine rapidity relative to beam rapidity. This notation is consistent with y_0 as defined in Reference [80]. In this normalization, a rapidity of 1 corresponds to a particle moving at the beam rapidity. The transverse momentum indicates momentum directed away from the beam axis. Figure 4.43 shows the p_t-y_0 spectra for π^- (left) and π^+ (right) for ^{124*}Sn (top panels) and ^{112}Sn (bottom panels) beams. Note that these plots include data from a larger

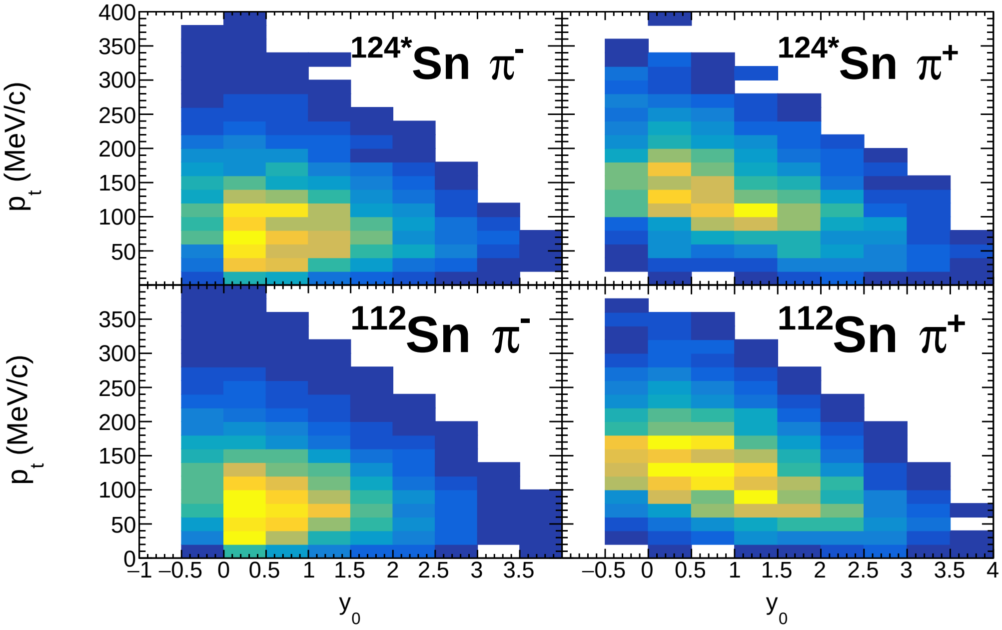

Figure 4.43: p_t-y_0 distributions, with rapidity normalized to beam rapidity. π^- are drawn on the left side, π^+ on the right. The top panels are for the ^{124*}Sn system, while the bottom panels are for the ^{112}Sn system.

cut in θ_{COM}, up to 100°, in order to demonstrate acceptance issues for $y_0 < 0$. Data used for other figures excludes tracks with $y_0 < 0$.

4.8.4 Comparison of Pion Spectra for ^{124}Sn-like beams and ^{124}Sn beam

To check that the results using the ^{124*}Sn system are representative of the ^{124}Sn system, we compare the pion spectra for both systems. Figure 4.44 shows the normalized pion $\mathrm{KE}_{\mathrm{COM}}$ spectra, with the top panel showing the efficiency corrected spectra, and the bottom showing the raw spectra. The mixed beam, ^{124*}Sn, is plotted with black circles, and the ^{124}Sn beam is plotted with magenta diamonds. Within statistical uncertainties, the distribution shapes for both systems match well.

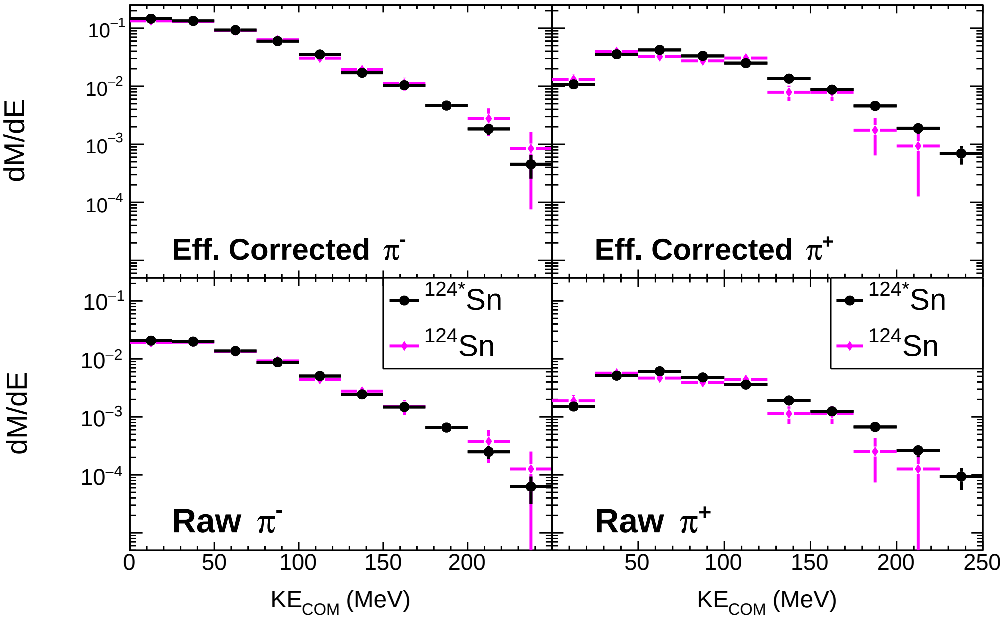

Figure 4.44: Pion $\mathrm{KE}_{\mathrm{COM}}$ spectra for ^{124*}Sn and ^{124}Sn beams. The top panel is efficiency corrected, and the bottom is the raw spectra.

4.8.5 Error in Pion Spectra

We need to combine the error associated with background and efficiency corrections with the statistical error for the pion spectra. The background and efficiency corrections are calculated for each track, and saved as fractional error. We denote the probability that track i is background as b_i, and the embedding efficiency correction as e_i. For a pion with weight $n_i = b_i \cdot e_i$, the square of the fractional error is

$$\left(\frac{\delta_{n_i}}{n_i}\right)^2 = \left(\frac{\delta_{b_i}}{b_i}\right)^2 + \left(\frac{\delta_{e_i}}{e_i}\right)^2. \tag{4.60}$$

As we fill the pion spectra, the weight of each track is added, and the square of the fractional error is saved. For bin j of the spectra, the pion count is N_j

$$N_j = \sum_i n_{ij}. \tag{4.61}$$

We must also include the variance $\sigma_{N_j} = \sqrt{N_j}$ of the pion count, so the final error of the pion count is:

$$(\delta_{N_j})^2 = (\sigma_{N_j})^2 + \sum_i (\delta_{n_i})^2. \tag{4.62}$$

We scale our spectra by the number of events N_{events}, and the solid angle acceptance, producing for each bin the probability p_j that a pion is produced in that bin:

$$p_j = \frac{N_j}{N_{\text{events}}} \cdot \frac{\Omega_{\text{total}}}{\Omega_{\text{selected}}}. \tag{4.63}$$

We take our event number and solid angle correction to be known exactly, therefore the error for p_j is

$$\delta_{p_j} = \frac{\delta_{N_j}}{N_{\text{events}}} \cdot \frac{\Omega_{\text{total}}}{\Omega_{\text{selected}}}. \tag{4.64}$$

This is assuming that the trigger selects a uniform azimuthal distribution of the reaction plane, and that the reaction is symmetric forwards versus backwards. The correction for solid angle reflects the limited acceptance of the TPC.

4.8.6 Pion Ratios

Figure 4.45 shows the π^-/π^+ spectral ratio as a function of KE_{COM} for ^{124*}Sn and ^{112}Sn beams. The efficiency corrected spectra is shown with green crosses, and the raw spectra with a black histogram. Both raw and efficiency corrected spectra match well. This ratio is expected to provide strong sensitivity to the symmetry energy for the most asymmetric system, ^{132}Sn + ^{124}Sn. For collisions between ^{124}Sn and ^{112}Sn, the sensitivity will be much less. If the collision mixes projectile and target nucleons well, we expect spectral ratios for the ^{112}Sn + ^{124}Sn collisions to be essentially the same as for the ^{124}Sn + ^{112}Sn collisions.

Two differences may affect the spectral ratio comparisons: the inclusion of additional ^{124}Sn-like beam nucleons, and the difference in the COM frame for the two systems, relative to the detector.

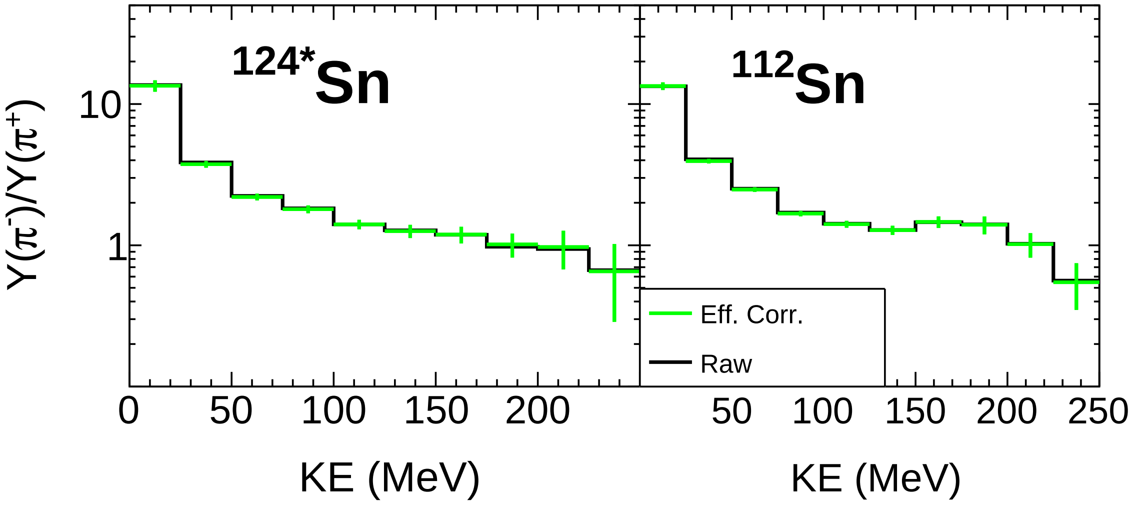

Figure 4.45: The π^-/π^+ spectral ratio for (left) the ^{124*}Sn system and (right) the ^{112}Sn system

We wish to reduce or eliminate as many systematic uncertainties as possible. In particular, the acceptance and detection efficiencies are in general different for π^- and π^+. Without knowing and correcting for these efficiencies, physics interpretations will be inaccurate. One method to mitigate this is to construct what is called the double ratio. If we denote the π^- and π^+ detection efficiency as ε_{π^-} and ε_{π^+}, the double ratio is

$$DR = \frac{\frac{Y(\pi^-)\varepsilon_{\pi^-}}{Y(\pi^+)\varepsilon_{\pi^+}}\left(^{124*}\mathrm{Sn}\right)}{\frac{Y(\pi^-)\varepsilon_{\pi^-}}{Y(\pi^+)\varepsilon_{\pi^+}}\left(^{112}\mathrm{Sn}\right)}. \tag{4.65}$$

If the efficiencies and acceptances are similar between the two systems, they will cancel out, leaving the double ratio as

$$DR = \frac{Y(\pi^-)/Y(\pi^+)\left({}^{124*}\mathrm{Sn}\right)}{Y(\pi^-)/Y(\pi^+)\left({}^{112}\mathrm{Sn}\right)}. \tag{4.66}$$

The double ratio is plotted in Figure 4.46 as a function of $\mathrm{KE}_{\mathrm{COM}}$. The efficiency corrected spectra is shown with green crosses, and the raw spectra with a black histogram. The double ratio measured is consistent with a double ratio of 1 for 7 of the 10 bins.

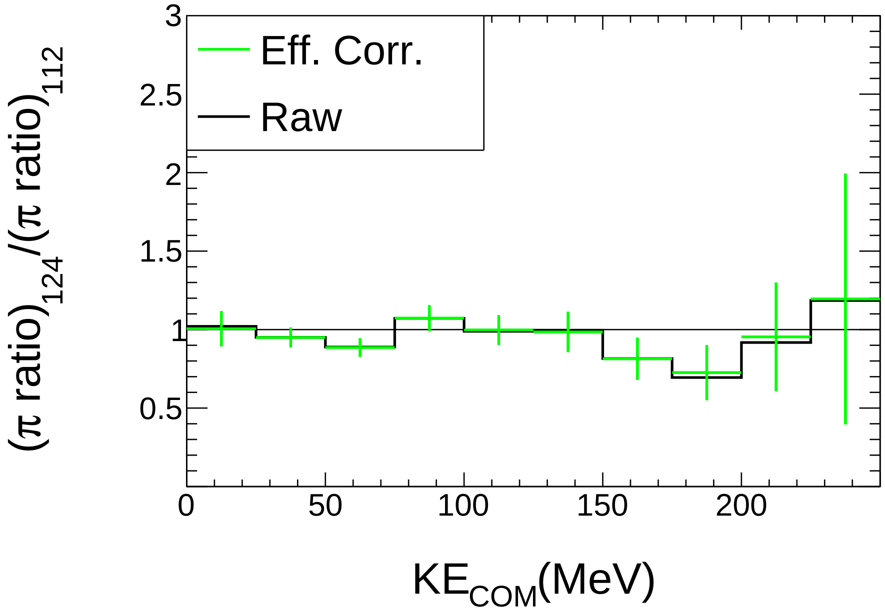

Figure 4.46: The double ratio as a function of $\mathrm{KE}_{\mathrm{COM}}$ for ^{124*}Sn+^{112}Sn and ^{112}Sn+^{124}Sn.

The left panel of Figure 4.47 shows the π^-/π^+ spectral ratio plotted as a function of y_0 (Equation 4.59), for the ^{124*}Sn beam system with black circles, and the ^{112}Sn beam system with green squares. The right panel shows the measured double ratio of the two systems, which is consistent with a ratio of1 for 4 of the 5 bins. A double ratio of 1 is consistent with complete mixing of the nucleons for these central collisions.

Based on a symmetry argument, we expect that the π^-/π^+ spectral ratio at positive rapidity for the ^{112}Sn beam should be equal to the π^-/π^+ spectral ratio at negative rapidity

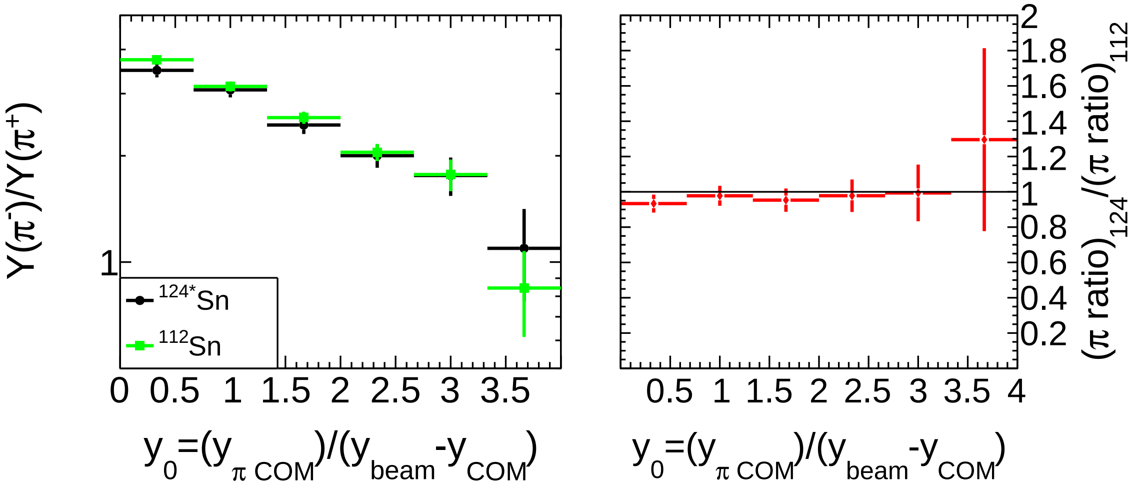

Figure 4.47: The π^-/π^+ spectral ratio as a function of rapidity (left) and the double ratio as a function of rapidity (right).

for the ^{124*}Sn beam. In principle, we can combine them to get the π^-/π^+ spectral ratio at all rapidities. This is shown in Figure 4.48. As we can see in the figure, the general trend is that the π^-/π^+ ratio is larger at 0 rapidity, and decreases monotonically with increasing $|y_0|$. Both systems are generally consistent with a Coulomb shift in the π^- and π^+ spectra whereby the π^+ are shifted to higher rapidity by the Coulomb force and the π^- are shifted to lower $|y_0|$ because of their negative charge.

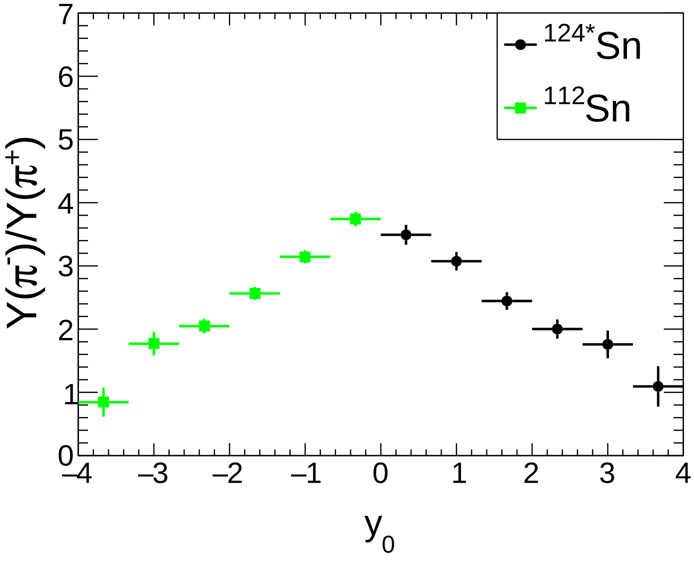

Figure 4.48: The π^-/π^+ spectral ratio, with the rapidity of the ^{112}Sn beam reversed.

We show the individual π^- and π^+ p_t-y_0 spectra in Figure 4.49, combining the ^{124*}Sn system with the rapidity-reversed ^{112}Sn system. Red lines are drawn corresponding to pion kinetic energy of 50 and 200 MeV in the COM frame (calculated separately for the ^{112}Sn and ^{124*}Sn systems). We can clearly see the effect of the Coulomb force: at low p_t and y_0, corresponding to the region of beam and target nucleon mixing, the π^- are abundant, and the π^+ are deficient.

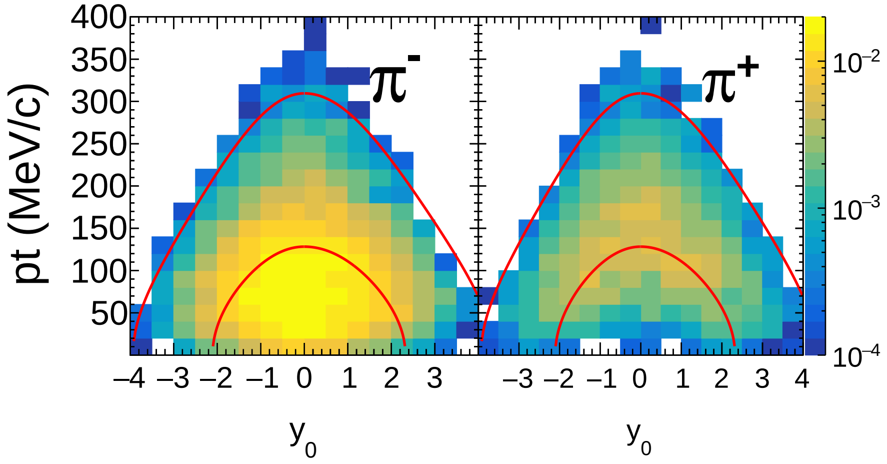

Figure 4.49: The π^- (left) and π^+ (right) p_t-y_0 spectra, with the rapidity of the ^{112}Sn beam reversed and added to the ^{124*}Sn beam to form a complete spectra. Red lines correspond to kinetic energies of 50 (bottom) and 200 (top) MeV in the COM frame.

Evaluating the spectra shown in this section indicates some differences and similarities between the pion ratios between the two systems. The pion ratios are very similar when examined as a function of rapidity, evident in Figure 4.47. This indicates complete mixing for central events. An examination of the double ratio as a function of kinetic energy in the COM frame (Figure 4.46) shows differences between the two systems. The double ratio differs from 1 for kinetic energy just below 200 MeV, which corresponds to just below the top red lines in Figure 4.49, and just above 50 MeV, which corresponds to just above the bottom red lines. We can see that around 200 MeV, our statistics are becoming limited. The double ratio differing from 1 is interesting, but it is not immediately evident what the statistical relevance is, so these differences bear further study. The deviation from 1 at just above 50 MeV may indicate that the kinetic energy determination is not fine enough: between 50 – 75 MeV, the double ratio trends below 1, while between 75 – 100 MeV, the double ratio trends above 1.

4.8.7 Examination of less central collisions

We can examine the emission of pions for less central collisions (5 fm $< b <$ 7 fm). Efficiency corrections are not applied to this analysis, and the error bars represent only the statistical uncertainty of the raw spectra. The pion yields are listed in Table 4.13, indicating a lower cross section for pion production for these more peripheral reactions. Figure 4.50 shows the π^-/π^+ ratios for ^{124*}Sn and ^{112}Sn beams in the left panel, and the double ratio in the right panel, analogous to Figure 4.47. Here we see that the double ratio is lower than 1, which qualitatively indicates more neutron-rich behavior from the ^{112}Sn system, seemingly in contradiction to our initial expectations. This result can be understood by examining the measured pion production cross sections, which are lower for both π^- and π^+ for the ^{112}Sn system compared to the ^{124*}Sn system, for these more peripheral reactions. The double ratio is lowered due to the overall reduction in pion production. This could indicate an issue with our impact parameter selection for more peripheral reactions.

Beam	Events	π^-	π^+
^{124*}Sn	73958	3642	1431
^{112}Sn	194686	8307	2852

Table 4.13: Raw pion yields for events with impact parameter 5 fm - 7 fm.

Figure 4.51 shows the combined p_t-y_0 spectra, again with ^{112}Sn rapidity reversed.

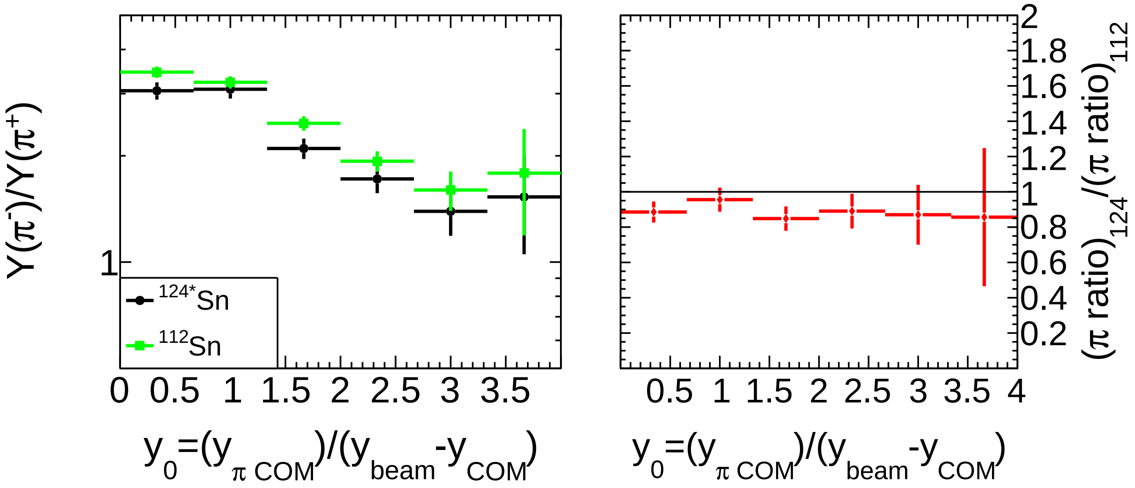

Figure 4.50: The π^-/π^+ spectral ratio as a function of rapidity (left) and the double ratio as a function of rapidity (right), for less central events.

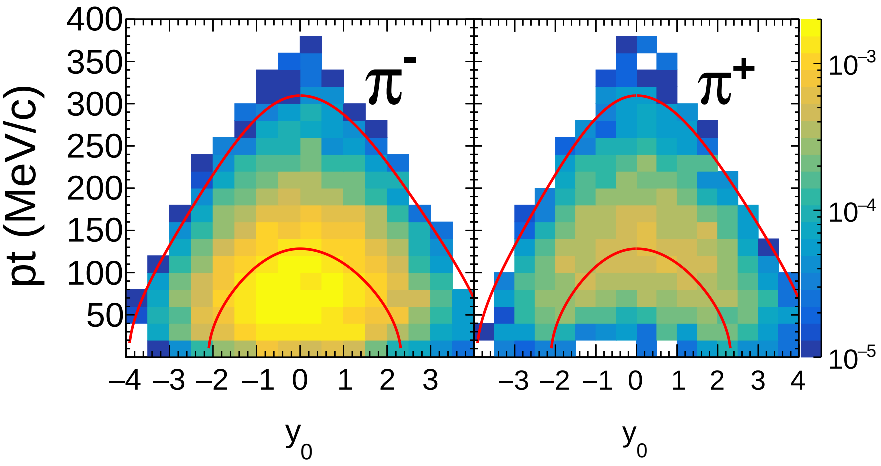

Figure 4.51: The π^- (left) and π^+ (right) p_t-y_0 spectra, with the rapidity of the ^{112}Sn beam reversed and added to the ^{124*}Sn beam to form a complete spectra, for less central events. Red lines correspond to kinetic energies of 50 (bottom) and 200 (top) MeV in the COM frame.

Figure 4.52 shows the combined ^{124*}Sn and ^{112}Sn (with rapidity reversed) π^-/π^+ spectra, analogous to Figure 4.48, but for less central events. We can see that the behavior is not monotonic, with rising tails at larger $|y_0|$, and the peak not as sharply defined near y_0=0.

For less central collisions, we can see differences between the two systems. The pion production probability is increased for the ^{124*}Sn system, and the pion ratio is increased for ^{112}Sn system. This may indicate issues with the impact parameter selection for more

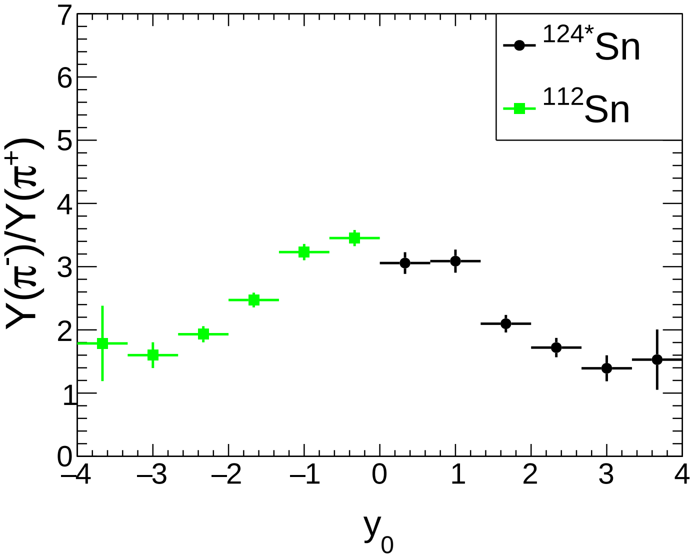

Figure 4.52: The π^-/π^+ spectral ratio, with the rapidity of the ^{112}Sn beam reversed, for less central events.

peripheral events, but the issue bears further study.

4.8.8 Preliminary Comparison to Transport Code

One of the main goals of the experiment was to use the pion emission to study the symmetry energy, as discussed in Chapter 1. Although the maximum sensitivity to the symmetry energy will come from the analysis of the more asymmetric beam + target system, we can compare our data to a transport code, for early indications of the results of the experiment. The ^{124}Sn+^{112}Sn and ^{112}Sn + ^{124}Sn reactions were modeled using the pBUU transport code, as described in Reference [2]. The simulations were performed at 270 MeV/u and impact parameter $b = 3$ fm, with clustering effects included. We compare the π^-/π^+ ratios and the double ratio to the results of this simulation. The simulation was performed for two different parameterizations of the symmetry energy (see Chapter 1 for explanation of parameterization), with $\gamma = 0.5$ (a softer EoS), and $\gamma = 1.75$ (a stiffer EoS).

The π^-/π^+ ratios are shown in Figure 4.53, for ^{124}Sn on the left and ^{112}Sn on the right.

The prediction from a softer EoS is shown as the shaded blue region, with the prediction from a stiffer EoS shown in the red shaded region. The data seems to favor the prediction from a stiffer symmetry energy, but it does not match the prediction perfectly.

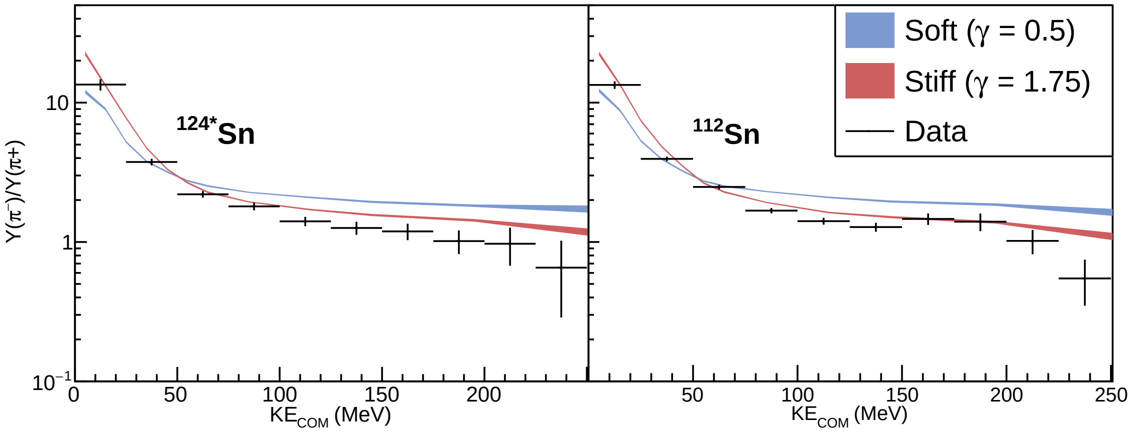

Figure 4.53: The π^-/π^+ spectral ratio for ^{124*}Sn (left) and ^{112}Sn (right), compared to simulation for soft (blue) and stiff (red)

Figure 4.54 shows the double ratio, with the blue shaded region showing the prediction from the softer EoS, and the red shaded region showing the prediction from the stiffer EoS. Here, we can see that the model predicts a double ratio close to 1 for both cases. This makes sense, because the asymmetry for both beam + target systems in this comparison is the same (on average, considering the mixed beam), although the energy of the COM frame is slightly different. Our data does not fit either prediction perfectly. The double ratio is expected to provide more sensitivity when comparing systems which have a difference in asymmetry.

Considering both the single and double ratios, it initially appears difficult to make even a qualitative claim on the relative softness or stiffness of the symmetry energy. The limited statistics of this experiment play a role in this uncertainty. The statistics could be increased by examining a larger solid angle, which would require further work to examine the differences in acceptance between the two systems for the increased solid angle.

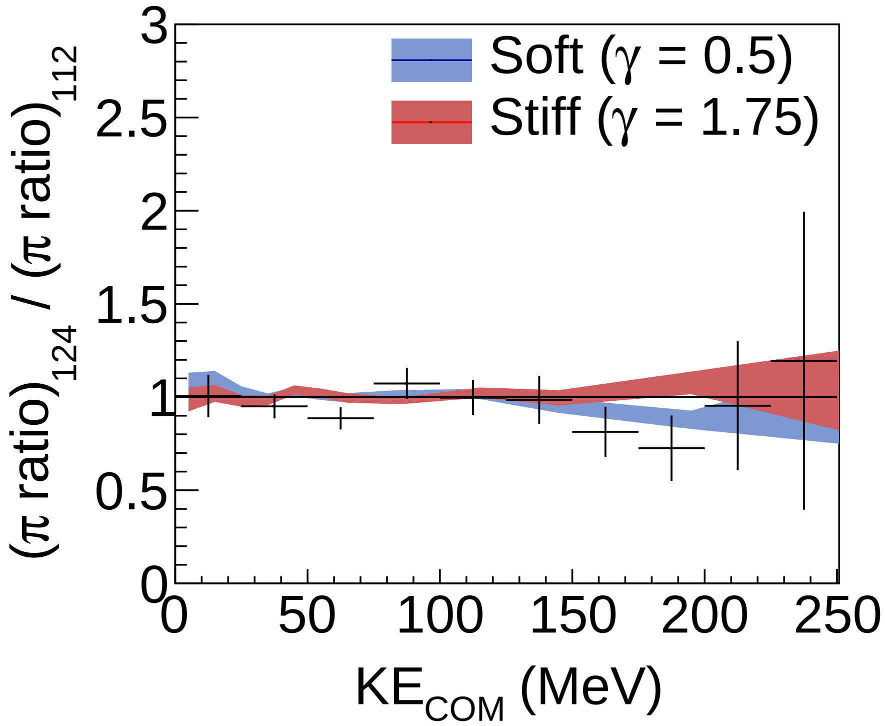

Figure 4.54: The double ratio for ^{124*}Sn and ^{112}Sn, compared to simulation for soft (blue) and stiff (red)

Chapter 5

Summary and Outlook

This dissertation presents part of a larger body of work. The SπRIT TPC was envisioned and created to place constraints on the symmetry energy at around twice saturation density, with the particular ability to measure charged pion emission and ratios. The ^{132}Sn + ^{124}Sn and ^{108}Sn + ^{112}Sn systems provide the greatest sensitivity to the symmetry energy, while the ^{124}Sn + ^{112}Sn and ^{112}Sn + ^{124}Sn systems provide measurements of the kinematic effects of using asymmetric beam + target systems. This work focuses on the ^{124}Sn + ^{112}Sn and ^{112}Sn + ^{124}Sn systems, along with other foundational analysis which is necessary to complete the analysis of more asymmetric systems.

The measurement of charged pion emission from systems with a wide range of asymmetry is a core part of this effort to constrain the density dependence of the symmetry energy. For this, it was necessary to construct a new detector: the SπRIT TPC. This TPC was designed for use in the SAMURAI spectrometer at RIKEN, where the large range of tin beams at the requisite energy and intensity were available. In addition to measuring pions, the TPC is able to measure other charged particles, providing a compliment of observables. The TPC was constructed at the NSCL, and shipped to RIKEN. The TPC was installed in the SAMURAI spectrometer and used in an experimental campaign with four beams: ^{108}Sn, ^{112}Sn, ^{124}Sn and ^{132}Sn, impinged on ^{112}Sn and ^{124}Sn targets.

The analysis of beam data was required to identify beam isotopes, and to determine the beam angle and velocity. This allows us to determine the center-of-momentum frame event-by-event, which is critical for the physics analysis. The beam analysis and careful treatment of scaler counts allow us to determine the absolute cross section, which provides a constraint on the impact parameter. We use the measured track multiplicity to establish an impact parameter selection filter, allowing us to select events which are more central or more peripheral.

Using events selected with the beam analysis, further limited to events with $b < 3$ fm, we measure the charged pion spectra for the ^{112}Sn + ^{124}Sn and ^{124}Sn + ^{112}Sn systems. We produce the spectra in the center-of-momentum frame, as a function of kinetic energy and as a function of rapidity. The ratio of π^- to π^+ production is expected to be sensitive to the symmetry energy, so these ratios are produced and compared to a transport code simulation. The pion spectra tend to agree more with a stiff parameterization of the symmetry energy, although the double ratio of the two systems does not show such a clear preference. This is due in part to the limited sensitivity of the double ratio in our selected systems: the double ratio will enhance effects due to differences in asymmetry between the systems, and our systems have, on average, the same asymmetry. The two systems presented are at the midpoint of asymmetry for the experimental campaign, and it is expected that analysis of the two more extreme systems will provide additional sensitivity to the symmetry energy.

For more peripheral ($b > 5$ fm) collisions, the ^{112}Sn + ^{124}Sn system produces fewer π^+ and π^+ than for the ^{124*}Sn + ^{112}Sn system. The pion ratio (π^-/π^+) is also lower for the ^{112}Sn + ^{124}Sn system. This is a puzzling result: we expect that for more peripheral collisions, particles detected in the TPC should be affected more by the beam composition than the target. As the beam nucleons enter the collision with velocity directed into the TPC, they, and the particles produced by their interactions, are more likely to achieve or maintain the required velocity to enter the TPC. By this reasoning, peripheral reactions from the ^{124*}Sn beam should be reflective of a more neutron rich reaction, while peripheral reactions from the ^{112}Sn beam should be more reflective of a neutron deficient system. This apparent contradiction is likely due to either the impact parameter selection or a bias from the trigger for these more peripheral reactions, as evidenced by the reduced pion production for the ^{112}Sn + ^{124}Sn system. Further study of this conundrum should be done, using $t/^3$He ratios to provide an additional indicator of the relative neutron-rich or neutron-deficient behavior of these more peripheral reactions.

Overall, this first analysis of the SπRIT experiment indicates that the TPC and experimental setup worked well, and we are able to measure the requisite pion spectra, although some work remains to obtain accurate spectra for larger values of kinetic energy. The analysis should incorporate a larger solid angle in the COM frame, which can be achieved with the data available but will require careful analysis of the acceptance and efficiency for each system, in the lab and COM frames. Effects of the impact parameter are not currently well understood, and a detailed study should be done, including analysis of minimum bias runs.

The pion spectra and ratios should be compared to a full suite of transport codes, as is being developed by a collaborative group effort [27], to place satisfactory constraints on the symmetry energy at twice saturation density. Other observables, such as anisotropic flow, n/p ratios, and $t/^3$He ratios, should be extracted from this experiment to provide the best constraints on the symmetry energy.

APPENDIX

Appendix A

A.1 Clebsch-Gordan Coefficients for Pion Production from Delta Resonance Decay

A.1.1 Production of Δ baryons

To investigate the production and decay of pions, it is necessary to assume the production of the Δ baryons (or resonances) accounts for the majority of our pion production. In our system, the energy is just reaching the threshold for pion production through the Δ resonance model, but at higher energies, this analysis may not be a valid representation of the whole system.

Most of our pions should be produced through nucleon-nucleon collisions, so we examine the Δ production from p-p, n-n, and n-p reactions using the isospin t and isospin projection t_3 as our quantum numbers to determine allowed reactions and resulting reaction rates. The isospin and isospin projection values for Δ baryons, π particles, and nucleons are tabulated below (using the particle physics convention for the sign of t_3).

particle	t	t_3
p	1/2	1/2
n	1/2	−1/2
Δ^{++}	3/2	3/2
Δ^{+}	3/2	1/2
Δ^{0}	3/2	−1/2
Δ^{-}	3/2	−3/2
π^{+}	1	1
π^{0}	1	0
π^{-}	1	−1

First, we examine the Δ states that a generalized nucleon-nucleon collision can produce. The generalized reaction is

$$\left|\frac{1}{2}, {}^{1}t_3\right\rangle \left|\frac{1}{2}, {}^{2}t_3\right\rangle \rightarrow |T, T_3\rangle\,. \tag{A.1}$$

From the initial values of ${}^{i}t$, we determine from the triangle rule the allowed final states of T,

$$\left|\frac{1}{2} - \frac{1}{2}\right| \leq T \leq \frac{1}{2} + \frac{1}{2}, \tag{A.2}$$

which allows states $T = 0, 1$. The isospin projection must equal the sum of the initial isospin projections, which must equal the sum of the isospin projections in the final state, so we have $T_3 = {}^{1}t_3 + {}^{2}t_3$. If the reaction results in two particles, we can write this more explicitly as:

$$\left|\frac{1}{2}, {}^{1}t_3\right\rangle \left|\frac{1}{2}, {}^{2}t_3\right\rangle \rightarrow \left|\frac{3}{2}, {}^{3}t_3\right\rangle \left|\frac{1}{2}, {}^{4}t_3\right\rangle\,. \tag{A.3}$$

We examine the allowed states resulting from the nucleon/Δ state,

$$\left|\frac{3}{2}, {}^{3}t_3\right\rangle \left|\frac{1}{2}, {}^{4}t_3\right\rangle \to \left|T, T_3\right\rangle , \tag{A.4}$$

which allows $T = 1, 2$ and $T_3 = {}^{3}t_3 + {}^{3}t_3$. Thus we want to investigate the case of $T = 1$ as it is the only case shared in both directions. This also provides the constraint $-1 \leq T_3 \leq 1$.

Decomposing the possible Δ-nucleon states using Clebsch-Gordan coefficients gives us

$$\begin{aligned}
\left|\frac{3}{2}, \frac{3}{2}\right\rangle \left|\frac{1}{2}, -\frac{1}{2}\right\rangle &\to \sqrt{\frac{1}{4}}\left|2, 1\right\rangle + \sqrt{\frac{3}{4}}\left|1, 1\right\rangle \\
\left|\frac{3}{2}, \frac{1}{2}\right\rangle \left|\frac{1}{2}, \frac{1}{2}\right\rangle &\to \sqrt{\frac{3}{4}}\left|2, 1\right\rangle - \sqrt{\frac{1}{4}}\left|1, 1\right\rangle \\
\left|\frac{3}{2}, \frac{1}{2}\right\rangle \left|\frac{1}{2}, -\frac{1}{2}\right\rangle &\to \sqrt{\frac{1}{2}}\left|2, 0\right\rangle + \sqrt{\frac{1}{2}}\left|1, 0\right\rangle \\
\left|\frac{3}{2}, -\frac{1}{2}\right\rangle \left|\frac{1}{2}, \frac{1}{2}\right\rangle &\to \sqrt{\frac{1}{2}}\left|2, 0\right\rangle - \sqrt{\frac{1}{2}}\left|1, 0\right\rangle \\
\left|\frac{3}{2}, -\frac{1}{2}\right\rangle \left|\frac{1}{2}, -\frac{1}{2}\right\rangle &\to \sqrt{\frac{1}{4}}\left|2, -1\right\rangle + \sqrt{\frac{3}{4}}\left|1, -1\right\rangle \\
\left|\frac{3}{2}, -\frac{3}{2}\right\rangle \left|\frac{1}{2}, \frac{1}{2}\right\rangle &\to \sqrt{\frac{1}{4}}\left|2, -1\right\rangle - \sqrt{\frac{3}{4}}\left|1, -1\right\rangle .
\end{aligned} \tag{A.5}$$

Using the Wigner-Eckart theorem, we can deduce the branching fractions of the $\left|T, T_3\right\rangle$,

$$\begin{aligned}
\left|1, 1\right\rangle &\to \sqrt{\frac{3}{4}}\left(\left|\frac{3}{2}, \frac{3}{2}\right\rangle \left|\frac{1}{2}, -\frac{1}{2}\right\rangle\right) - \sqrt{\frac{1}{4}}\left(\left|\frac{3}{2}, \frac{1}{2}\right\rangle \left|\frac{1}{2}, \frac{1}{2}\right\rangle\right) \\
\left|1, 0\right\rangle &\to \sqrt{\frac{1}{2}}\left(\left|\frac{3}{2}, \frac{1}{2}\right\rangle \left|\frac{1}{2}, -\frac{1}{2}\right\rangle\right) - \sqrt{\frac{1}{2}}\left(\left|\frac{3}{2}, -\frac{1}{2}\right\rangle \left|\frac{1}{2}, \frac{1}{2}\right\rangle\right) \\
\left|1, -1\right\rangle &\to \sqrt{\frac{1}{4}}\left(\left|\frac{3}{2}, -\frac{1}{2}\right\rangle \left|\frac{1}{2}, -\frac{1}{2}\right\rangle\right) - \sqrt{\frac{3}{4}}\left(\left|\frac{3}{2}, -\frac{3}{2}\right\rangle \left|\frac{1}{2}, \frac{1}{2}\right\rangle\right) ;
\end{aligned} \tag{A.6}$$

the T_3 values determine uniquely which nucleons are present within the system, although the $\left|1, 0\right\rangle$ system includes both p-n and n-p systems.

A.1.2 Δ Baryon Decay Branching

The mean lifetime for all varieties of Δ baryons is about 5.63×10^{-24} s. The Δ^{++} and Δ^{-} baryons have one main decay channel each. The Δ^{+} and Δ^{0} baryons can decay through two routes. The branching ratios for these decays are determined using Clebsch-Gordan coefficients. The final result for the decays is

$$\begin{aligned}
\left|\frac{3}{2},\frac{3}{2}\right\rangle &\to |1,1\rangle\left|\frac{1}{2},\frac{1}{2}\right\rangle \\
\left|\frac{3}{2},\frac{1}{2}\right\rangle &\to \sqrt{\frac{1}{3}}\left(|1,1\rangle\left|\frac{1}{2},-\frac{1}{2}\right\rangle\right)+\sqrt{\frac{2}{3}}\left(|1,0\rangle\left|\frac{1}{2},\frac{1}{2}\right\rangle\right) \\
\left|\frac{3}{2},\frac{-1}{2}\right\rangle &\to \sqrt{\frac{2}{3}}\left(|1,0\rangle\left|\frac{1}{2},-\frac{1}{2}\right\rangle\right)+\sqrt{\frac{1}{3}}\left(|1,-1\rangle\left|\frac{1}{2},\frac{1}{2}\right\rangle\right) \\
\left|\frac{3}{2},\frac{-3}{2}\right\rangle &\to |1,-1\rangle\left|\frac{1}{2},-\frac{1}{2}\right\rangle . \qquad \text{(A.7)}
\end{aligned}$$

A.1.3 Nucleon-Nucleon Collisions

Summarizing using particle notation, we have the production of Δ baryons from nucleon-nucleon collisions:

$$\begin{aligned}
p+p &\to \sqrt{\frac{3}{4}}\left(\Delta^{++}+n\right)-\sqrt{\frac{1}{4}}\left(\Delta^{+}+p\right) \\
n+p &\to \sqrt{\frac{1}{2}}\left(\Delta^{+}+n\right)-\sqrt{\frac{1}{2}}\left(\Delta^{0}+p\right) \\
n+n &\to \sqrt{\frac{1}{4}}\left(\Delta^{0}+n\right)-\sqrt{\frac{3}{4}}\left(\Delta^{-}+p\right) . \qquad \text{(A.8)}
\end{aligned}$$

We have the result of Δ baryon decays:

$$\begin{aligned}
&\Delta^{++} \to \pi^{+} + p \\
&\Delta^{+} \to \sqrt{\frac{1}{3}}(\pi^{+} + n) + \sqrt{\frac{2}{3}}(\pi^{0} + p) \\
&\Delta^{0} \to \sqrt{\frac{2}{3}}(\pi^{0} + n) + \sqrt{\frac{1}{3}}(\pi^{-} + p) \\
&\Delta^{-} \to \pi^{-} + n.
\end{aligned} \tag{A.9}$$

Putting this together, we have the pion production from nucleon-nucleon collisions:

$$\begin{aligned}
p + p \to & \sqrt{\frac{3}{4}}\left(\pi^{+} + p + n\right) - \sqrt{\frac{1}{4}}\left(\sqrt{\frac{1}{3}}(\pi^{+} + n + p) + \sqrt{\frac{2}{3}}(\pi^{0} + p + p)\right) \\
n + p \to & \sqrt{\frac{1}{2}}\left(\sqrt{\frac{1}{3}}(\pi^{+} + n + n) + \sqrt{\frac{2}{3}}(\pi^{0} + p + n)\right) \\
& -\sqrt{\frac{1}{2}}\left(\sqrt{\frac{2}{3}}(\pi^{0} + n + p) + \sqrt{\frac{1}{3}}(\pi^{-} + p + p)\right) \\
n + n \to & \sqrt{\frac{1}{4}}\left(\sqrt{\frac{2}{3}}(\pi^{0} + n + n) + \sqrt{\frac{1}{3}}(\pi^{-} + p + n)\right) - \sqrt{\frac{3}{4}}\left(\pi^{-} + n + p\right),
\end{aligned} \tag{A.10}$$

which simplifies to

$$\begin{aligned}
&p + p \to \sqrt{\frac{5}{6}}\left(\pi^{+} + p + n\right) - \sqrt{\frac{1}{6}}(\pi^{0} + p + p) \\
&n + p \to \sqrt{\frac{1}{6}}(\pi^{+} + n + n) + \sqrt{\frac{2}{3}}(\pi^{0} + n + p) + \sqrt{\frac{1}{6}}(\pi^{-} + p + p) \\
&n + n \to \sqrt{\frac{1}{6}}(\pi^{0} + n + n) - \sqrt{\frac{5}{6}}\left(\pi^{-} + n + p\right).
\end{aligned} \tag{A.11}$$

A.1.4 Pion Decay Branching Ratios

The partial decay widths for charged and neutral pion decays can be calculated using the branching ratios and total decay width for each pion flavor. The relevant equations involve the relation between decay width and partial decay widths

$$\Gamma = \frac{\hbar}{\tau} = \Gamma_1 + \Gamma_2 + ..., \tag{A.12}$$

and the definition of branching ratios,

$$BR_i = \frac{\Gamma_i}{\Gamma}. \tag{A.13}$$

Starting with $\pi^{\pm}$, the decay into μ^+ and μ^- leptons are respectively:

$$\begin{aligned} &\pi^+ \rightarrow \mu^+ + \nu_\mu \\ &\pi^- \rightarrow \mu^- + \bar{\nu}_\mu \end{aligned} \tag{A.14}$$

with a branching ratio of 0.999877. The other mode of decay is:

$$\begin{aligned} &\pi^+ \rightarrow e^+ + \nu_e \\ &\pi^- \rightarrow e^- + \bar{\nu}_e \end{aligned} \tag{A.15}$$

with a branching ratio of 0.000123. With charged pions having a mean lifetime of 2.6×10^{-8} s, the partial decay widths, $\Gamma_{\mu^{\pm}} = \frac{\hbar}{\tau_{\mu^{\pm}}}$ and $\Gamma_{e^{\pm}} \frac{\hbar}{\tau_{e^{\pm}}}$ are found to be

$$\begin{aligned} \Gamma_{\mu^{\pm}} &= \frac{\hbar}{2.6003 \times 10^{-8}\,\mathrm{s}} \\ \Gamma_{e^{\pm}} &= \frac{\hbar}{2.114 \times 10^{-4}\,\mathrm{s}}. \end{aligned} \tag{A.16}$$

The neutral pion (π^0) has a mean lifetime of about 8.4×10^{-17} s. Examining the three largest decay modes of the neutral pion decay,

$$\begin{aligned} &1)\ \pi^0 \to 2\gamma \\ &2)\ \pi^0 \to \gamma + e^- + e^+ \\ &3)\ \pi^0 \to e^- + e^+ + e^- + e^+, \end{aligned} \tag{A.17}$$

the partial decay widths are found to be

$$\begin{aligned} \Gamma_1 &= \frac{\hbar}{8.5 \times 10^{-17}\,\mathrm{s}} \\ \Gamma_2 &= \frac{\hbar}{7.16 \times 10^{-15}\,\mathrm{s}} \\ \Gamma_3 &= \frac{\hbar}{2.8 \times 10^{-12}\,\mathrm{s}}. \end{aligned} \tag{A.18}$$

BIBLIOGRAPHY

BIBLIOGRAPHY

[1] “NuDat2.” `https://www.nndc.bnl.gov/nudat2/`. Accessed July 3, 2019.

[2] M. B. Tsang, J. Estee, H. Setiawan, W. G. Lynch, J. Barney, M. B. Chen, G. Cerizza, P. Danielewicz, J. Hong, P. Morfouace, R. Shane, S. Tangwancharoen, K. Zhu, T. Isobe, M. Kurata-Nishimura, J. Lukasik, T. Murakami, and Z. Chajecki, “Pion production in rare-isotope collisions,” *Physical Review C*, vol. 95, p. 044614, Apr 2017.

[3] R. Shane, A. McIntosh, T. Isobe, W. Lynch, H. Baba, J. Barney, Z. Chajecki, M. Chartier, J. Estee, M. Famiano, B. Hong, K. Ieki, G. Jhang, R. Lemmon, F. Lu, T. Murakami, N. Nakatsuka, M. Nishimura, R. Olsen, W. Powell, H. Sakurai, A. Taketani, S. Tangwancharoen, M. Tsang, T. Usukura, R. Wang, S. Yennello, and J. Yurkon, “SπRIT: A time-projection chamber for symmetry-energy studies,” *Nuclear Instruments and Methods in Physics Research Section A: Accelerators, Spectrometers, Detectors and Associated Equipment*, vol. 784, pp. 513 – 517, 2015. Symposium on Radiation Measurements and Applications 2014 (SORMA XV).

[4] E. Pollacco, G. Grinyer, F. Abu-Nimeh, T. Ahn, S. Anvar, A. Arokiaraj, Y. Ayyad, H. Baba, M. Babo, P. Baron, *et al.*, “GET: A generic electronics system for TPCs and nuclear physics instrumentation,” *Nuclear Instruments and Methods in Physics Research Section A: Accelerators, Spectrometers, Detectors and Associated Equipment*, vol. 887, pp. 81–93, 2018.

[5] T. Isobe, G. Jhang, H. Baba, J. Barney, P. Baron, G. Cerizza, J. Estee, M. Kaneko, M. Kurata-Nishimura, J. Lee, W. Lynch, T. Murakami, N. Nakatsuka, E. Pollacco, W. Powell, H. Sakurai, C. Santamaria, D. Suzuki, S. Tangwancharoen, and M. Tsang, “Application of the Generic Electronics for Time Projection Chamber (GET) readout system for heavy Radioactive isotope collision experiments,” *Nuclear Instruments and Methods in Physics Research Section A: Accelerators, Spectrometers, Detectors and Associated Equipment*, vol. 899, pp. 43 – 48, 2018.

[6] S. Tangwancharoen, W. Lynch, J. Barney, J. Estee, R. Shane, M. Tsang, Y. Zhang, T. Isobe, M. Kurata-Nishimura, T. Murakami, Z. Xiao, and Y. Zhang, “A gating grid driver for time projection chambers,” *Nuclear Instruments and Methods in Physics Research Section A: Accelerators, Spectrometers, Detectors and Associated Equipment*, vol. 853, pp. 44 – 52, 2017.

[7] S. Tangwancharoen, *Design and construction of the SPiRIT TPC*. PhD thesis, 2016.

[8] “RIBF accelerator concept website.” `http://www.nishina.riken.jp/RIBF/accelerator/concept.html`. Accessed: 2019-04-14.

[9] T. Kubo, D. Kameda, H. Suzuki, N. Fukuda, H. Takeda, Y. Yanagisawa, M. Ohtake, K. Kusaka, K. Yoshida, N. Inabe, T. Ohnishi, A. Yoshida, K. Tanaka, and Y. Mizoi, "BigRIPS separator and ZeroDegree spectrometer at RIKEN RI Beam Factory," *Progress of Theoretical and Experimental Physics*, vol. 2012, no. 1, p. 03C003, 2012.

[10] H. Kumagai, T. Ohnishi, N. Fukuda, H. Takeda, D. Kameda, N. Inabe, K. Yoshida, and T. Kubo, "Development of Parallel Plate Avalanche Counter (PPAC) for BigRIPS fragment separator," *Nuclear Instruments and Methods in Physics Research Section B: Beam Interactions with Materials and Atoms*, vol. 317, pp. 717 – 727, 2013. XVIth International Conference on ElectroMagnetic Isotope Separators and Techniques Related to their Applications, December 2âĂŞ7, 2012 at Matsue, Japan.

[11] K. Kimura, T. Izumikawa, R. Koyama, T. Ohnishi, T. Ohtsubo, A. Ozawa, W. Shinozaki, T. Suzuki, M. Takahashi, I. Tanihata, T. Yamaguchi, and Y. Yamaguchi, "High-rate particle identification of high-energy heavy ions using a tilted electrode gas ionization chamber," *Nuclear Instruments and Methods in Physics Research Section A: Accelerators, Spectrometers, Detectors and Associated Equipment*, vol. 538, no. 1, pp. 608 – 614, 2005.

[12] G. Jhang, *Performance of the SπRIT TPC for the nuclear physics experiment at RIBF*. PhD thesis, Korea University, 2016.

[13] C. J. Horowitz, E. F. Brown, Y. Kim, W. G. Lynch, R. Michaels, A. Ono, J. Piekarewicz, M. B. Tsang, and H. H. Wolter, "A way forward in the study of the symmetry energy: experiment, theory, and observation," *Journal of Physics G: Nuclear and Particle Physics*, vol. 41, p. 093001, jul 2014.

[14] J. Piekarewicz and M. Centelles, "Incompressibility of neutron-rich matter," *Physical Review C*, vol. 79, no. 5, p. 054311, 2009.

[15] B.-A. Li, C. M. Ko, and Z. Ren, "Equation of State of Asymmetric Nuclear Matter and Collisions of Neutron-Rich Nuclei," *Physical Review Letters*, vol. 78, pp. 1644–1647, Mar 1997.

[16] M. B. Tsang, T. X. Liu, L. Shi, P. Danielewicz, C. K. Gelbke, X. D. Liu, W. G. Lynch, W. P. Tan, G. Verde, A. Wagner, H. S. Xu, W. A. Friedman, L. Beaulieu, B. Davin, R. T. de Souza, Y. Larochelle, T. Lefort, R. Yanez, V. E. Viola, R. J. Charity, and L. G. Sobotka, "Isospin Diffusion and the Nuclear Symmetry Energy in Heavy Ion Reactions," *Physical Review Letters*, vol. 92, p. 062701, Feb 2004.

[17] J. Piekarewicz, B. K. Agrawal, G. Colò, W. Nazarewicz, N. Paar, P.-G. Reinhard, X. Roca-Maza, and D. Vretenar, "Electric dipole polarizability and the neutron skin," *Physical Review C*, vol. 85, p. 041302, Apr 2012.

[18] P. Russotto, P. Wu, M. Zoric, M. Chartier, Y. Leifels, R. Lemmon, Q. Li, J. Łukasik, A. Pagano, P. Pawłowski, and W. Trautmann, "Symmetry energy from elliptic flow in 197Au+197Au," *Physics Letters B*, vol. 697, no. 5, pp. 471 – 476, 2011.

[19] B.-A. Li, G.-C. Yong, and W. Zuo, "Near-threshold pion production with radioactive beams," *Physical Review C*, vol. 71, p. 014608, Jan 2005.

[20] J. Hong and P. Danielewicz, "Subthreshold pion production within a transport description of central Au + Au collisions," *Physical Review C*, vol. 90, p. 024605, Aug 2014.

[21] N. Ikeno, A. Ono, Y. Nara, and A. Ohnishi, "Probing neutron-proton dynamics by pions," *Physical Review C*, vol. 93, p. 044612, Apr 2016.

[22] B.-A. Li, "Probing the High Density Behavior of the Nuclear Symmetry Energy with High Energy Heavy-Ion Collisions," *Physical Review Letters*, vol. 88, p. 192701, Apr 2002.

[23] H. Wieman, S. Abbott, A. Arthur, J. Bercovitz, F. Bieser, C. Harnden, R. Jones, S. Kleinfelder, K. Lee, H. Matis, M. Nakamura, C. McParland, G. Odyniec, D. Olson, H. Pugh, G. Rai, H. Ritter, T. Symons, M. Wright, R. Wright, and A. Rudge, "A TPC detector for the study of high multiplicity heavy ion collisions," *Nuclear Physics A*, vol. 525, pp. 617 – 620, 1991.

[24] J. C. Kintner, S. Albergo, F. Bieser, F. P. Brady, Z. Caccia, D. Cebra, A. D. Chacon, J. L. Chance, Y. Choi, S. Costa, J. B. Elliott, M. L. Gilkes, J. A. Hauger, A. S. Hirsch, E. L. Hjort, A. Insolia, M. Justice, D. Keane, M. A. Lisa, H. S. Matis, M. McMahan, C. McParland, D. L. Olson, M. D. Partlan, N. T. Porile, R. Potenza, G. Rai, J. Rasmussen, H. G. Ritter, J. Romanski, J. L. Romero, G. V. Russo, R. Scharenberg, A. Scott, Y. Shao, B. Srivastava, T. J. M. Symons, M. Tincknell, C. Tuvé, S. Wang, P. Warren, H. H. Wieman, T. Wienold, and K. Wolf, "Pion Flow and Antiflow in 1.15A GeV $Au + Au$," *Physical Review Letters*, vol. 78, pp. 4165–4168, Jun 1997.

[25] P. Danielewicz, "Determination of the mean-field momentum-dependence using elliptic flow," *Nuclear Physics A*, vol. 673, no. 1, pp. 375 – 410, 2000.

[26] P. Danielewicz and G. Bertsch, "Production of deuterons and pions in a transport model of energetic heavy-ion reactions," *Nuclear Physics A*, vol. 533, no. 4, pp. 712 – 748, 1991.

[27] J. Xu, L.-W. Chen, M. B. Tsang, H. Wolter, Y.-X. Zhang, J. Aichelin, M. Colonna, D. Cozma, P. Danielewicz, Z.-Q. Feng, A. Le Fèvre, T. Gaitanos, C. Hartnack, K. Kim, Y. Kim, C.-M. Ko, B.-A. Li, Q.-F. Li, Z.-X. Li, P. Napolitani, A. Ono, M. Papa, T. Song, J. Su, J.-L. Tian, N. Wang, Y.-J. Wang, J. Weil, W.-J. Xie, F.-S. Zhang, and G.-Q. Zhang, "Understanding transport simulations of heavy-ion collisions at 100A and 400A MeV: Comparison of heavy-ion transport codes under controlled conditions," *Physical Review C*, vol. 93, p. 044609, Apr 2016.

[28] T. Kobayashi, N. Chiga, T. Isobe, Y. Kondo, T. Kubo, K. Kusaka, T. Motobayashi, T. Nakamura, J. Ohnishi, H. Okuno, H. Otsu, T. Sako, H. Sato, Y. Shimizu, K. Sekiguchi, K. Takahashi, R. Tanaka, and K. Yoneda, “SAMURAI spectrometer for RI beam experiments,” *Nuclear Instruments and Methods in Physics Research Section B: Beam Interactions with Materials and Atoms*, vol. 317, pp. 294 – 304, 2013. XVIth International Conference on ElectroMagnetic Isotope Separators and Techniques Related to their Applications, December 2âĂŞ7, 2012 at Matsue, Japan.

[29] “Large-Acceptance Multi-Particle Spectrometer SAMURAI (Superconducting Analyzer for Multi-particle from Radio Isotope Beams) Construction Proposal.” Accessed March 10, 2018.

[30] W. Blum, W. Riegler, and L. Rolandi, *Particle detection with drift chambers*. Springer Science & Business Media, 2008.

[31] E. Pollacco, S. Anvar, H. Baba, P. Baron, D. Bazin, C. Belkhiria, B. Blank, J. Chavas, P. Chomaz, E. Delagnes, F. Druillole, P. Hellmuth, C. Huss, E. Galyaev, B. Lynch, W. Mittig, T. Murakami, L. Nalpas, J.-L. Pedroza, R. Raabe, J. Pibernat, B. Raine, A. Rebii, A. Taketani, F. Saillant, D. Suzuki, N. Usher, and G. Wittwer, “GET: A Generic Electronic System for TPCs for Nuclear Physics Experiments,” *Physics Procedia*, vol. 37, pp. 1799 – 1804, 2012. Proceedings of the 2nd International Conference on Technology and Instrumentation in Particle Physics (TIPP 2011).

[32] X. Grave, R. Canedo, J.-F. Clavelin, S. Du, and E. Legay, “NARVAL a modular distributed data acquisition system with Ada 95 and RTAI,” in *14th IEEE-NPSS Real Time Conference, 2005.*, pp. 5–pp, IEEE, 2005.

[33] V. Blinov, I. Popkov, and A. Yushkov, “Aging measurements in wire chambers,” *Nuclear Instruments and Methods in Physics Research Section A: Accelerators, Spectrometers, Detectors and Associated Equipment*, vol. 515, no. 1, pp. 95 – 107, 2003. Proceedings of the International Workshop on Aging Phenomena in Gaseous Detectors.

[34] K. Ackermann, N. Adams, C. Adler, Z. Ahammed, S. Ahmad, C. Allgower, J. Amonett, J. Amsbaugh, B. Anderson, M. Anderson, E. Anderssen, H. Arnesen, L. Arnold, G. Averichev, A. Baldwin, J. Balewski, O. Barannikova, L. Barnby, J. Baudot, M. Beddo, S. Bekele, V. Belaga, R. Bellwied, S. Bennett, J. Bercovitz, J. Berger, W. Betts, H. Bichsel, F. Bieser, L. Bland, M. Bloomer, C. Blyth, J. Boehm, B. Bonner, D. Bonnet, R. Bossingham, M. Botlo, A. Boucham, N. Bouillo, S. Bouvier, K. Bradley, F. Brady, A. Brandin, R. Brown, G. Brugalette, M. Burkes, R. Cadman, H. Caines, M. C. de la Barca SÃąnchez, A. Cardenas, L. Carr, J. Carroll, J. Castillo, M. Castro, D. Cebra, S. Chattopadhyay, M. Chen, W. Chen, Y. Chen, S. Chernenko, M. Cherney, A. Chikanian, B. Choi, J. Chrin, W. Christie, J. Coffin, L. Conin, C. Consiglio, T. Cormier, J. Cramer, H. Crawford, I. Danilov, D. Dayton, M. DeMello, W. Deng, A. Derevschikov, M. Dialinas, H. Diaz, P. DeYoung, L. Didenko, D. Dimassimo, J. Dioguardi, C. Drancourt, T. Dietel, J. Draper, V. Dunin, J. Dunlop, V. Eckardt, W. Ed-

wards, L. Efimov, T. Eggert, V. Emelianov, J. Engelage, G. Eppley, B. Erazmus, A. Etkin, P. Fachini, V. Faine, C. Feliciano, D. Ferenc, M. Ferguson, H. Fessler, K. Filimonov, E. Finch, Y. Fisyak, D. Flierl, I. Flores, K. Foley, D. Fritz, J. Fu, C. Gagliardi, N. Gagunashvili, J. Gans, L. Gaudichet, M. Gazdzicki, M. Germain, F. Geurts, V. Ghazikhanian, C. Gojak, J. Grabski, O. Grachov, M. Grau, D. Greiner, L. Greiner, V. Grigoriev, D. Grosnick, J. Gross, M. Guedon, G. Guilloux, E. Gushin, J. Hall, T. Hallman, D. Hardtke, G. Harper, J. Harris, M. Heffner, S. Heppelmann, T. Herston, D. Hill, B. Hippolyte, A. Hirsch, E. Hjort, G. Hoffmann, M. Horsley, M. Howe, H. Huang, T. Humanic, H. HÃijmmler, W. Hunt, J. Hunter, G. Igo, A. Ishihara, Y. Ivanshin, P. Jacobs, W. Jacobs, S. Jacobson, M. Janik, R. Jared, P. Jensen, I. Johnson, P. Jones, E. Judd, M. Kaneta, M. Kaplan, D. Keane, A. Khodinov, J. Kiryluk, A. Kisiel, J. Klay, S. Klein, A. Klyachko, G. Koehler, A. Konstantinov, I. Kotov, M. Kopytine, L. Kotchenda, A. Kovalenko, M. Kramer, P. Kravtsov, K. Krueger, T. Krupien, P. Kuczewski, C. Kuhn, A. Kulikov, G. Kunde, C. Kunz, R. K. Kutuev, A. Kuznetsov, L. Lakehal-Ayat, M. Lamont, J. Landgraf, S. Lange, C. Lansdell, B. Lasiuk, F. Laue, A. Lebedev, T. LeCompte, R. LednickÃ¡, W. Leonhardt, V. Leontiev, M. LeVine, Q. Li, C.-J. Liaw, J. Lin, S. Lindenbaum, V. Lindenstruth, P. Lindstrom, M. Lisa, F. Liu, L. Liu, Z. Liu, Q. Liu, T. Ljubicic, W. Llope, G. LoCurto, H. Long, R. Longacre, M. Lopez-Noriega, W. Love, D. Lynn, R. Maier, R. Majka, S. Margetis, C. Markert, L. Martin, J. Marx, H. Matis, Y. Matulenko, C. McParland, T. McShane, J. Meier, F. Meissner, Y. Melnick, A. Meschanin, M. Messer, P. Middlekamp, B. Miller, M. Miller, Z. Milosevich, N. Minaev, B. Minor, J. Mitchell, E. Mogavero, V. Moiseenko, D. Moltz, C. Moore, V. Morozov, M. de Moura, M. Munhoz, G. Mutchler, J. Nelson, P. Nevski, M. Nguyen, T. Nguyen, V. Nikitin, L. Nogach, T. Noggle, B. Norman, S. Nurushev, T. Nussbaum, J. Nystrand, G. Odyniec, A. Ogawa, C. Ogilvie, V. Okorokov, K. Olchanski, M. Oldenburg, D. Olson, G. Ott, D. Padrazo, G. Paic, S. Pandey, Y. Panebratsev, S. Panitkin, A. Pavlinov, T. Pawlak, V. Perevoztchikov, W. Peryt, V. Petrov, W. Pinganaud, S. Pirogov, E. Platner, J. Pluta, I. Polk, N. Porile, J. Porter, A. Poskanzer, E. Potrebenikova, D. Prindle, C. Pruneau, J. Puskar-Pasewicz, G. Rai, J. Rasson, O. Ravel, R. Ray, S. Razin, D. Reichhold, J. Reid, R. Renfordt, F. Retiere, A. Ridiger, J. Riso, H. Ritter, J. Roberts, D. Roehrich, O. Rogachevski, J. Romero, C. Roy, D. Russ, V. Rykov, I. Sakrejda, R. Sanchez, Z. Sandler, S. Salur, J. Sandweiss, A. Saulys, I. Savin, J. Schambach, R. Scharenberg, J. Scheblien, R. Scheetz, R. Schlueter, N. Schmitz, L. Schroeder, M. Schulz, A. SchÃijttauf, K. Schweda, J. Sedlmeir, J. Seger, D. Seliverstov, P. Seyboth, R. Seymour, E. Shahaliev, K. Shestermanov, S. Shimanskii, D. Shuman, V. Shvetcov, G. Skoro, N. Smirnov, L. Smykov, R. Snellings, K. Solberg, P. Sorensen, J. Sowinski, H. Spinka, B. Srivastava, E. Stephenson, R. Stock, A. Stolpovsky, N. Stone, M. Strikhanov, B. Stringfellow, H. Stroebele, C. Struck, A. Suaide, E. Sugarbaker, C. Suire, M. Åăumbera, T. Symons, A. S. de Toledo, P. Szarwas, A. Tai, J. Takahashi, A. Tang, A. Tarchini, J. Tarzian, J. Thomas, M. Thompson, V. Tikhomirov, M. Tokarev, M. Tonjes, S. Tonse, T. Trainor, S. Trentalange, R. Tribble, V. Trofimov, O. Tsai, K. Turner, T. Ullrich, D. Underwood, I. Vakula, G. V. Buren, A. VanderMolen, A. Vanyashin, I. Vasilevski, A. Vasiliev, S. Vigdor, G. Visser, S. Voloshin, C. Vu, F. Wang, H. Ward, J. Watson, D. Weerasundara, R. Weidenbach, R. Wells, T. Wenaus, G. Westfall, J. Whitfield, C. Whitten,

H. Wieman, R. Willson, K. Wilson, J. Wirth, J. Wisdom, S. Wissink, R. Witt, J. Wolf, J. Wood, N. Xu, Z. Xu, A. Yakutin, E. Yamamoto, J. Yang, P. Yepes, A. Yokosawa, V. Yurevich, Y. Zanevski, I. ZborovskÃ¡, H. Zhang, W. Zh, "STAR detector overview," *Nuclear Instruments and Methods in Physics Research Section A: Accelerators, Spectrometers, Detectors and Associated Equipment*, vol. 499, no. 2, pp. 624 – 632, 2003. The Relativistic Heavy Ion Collider Project: RHIC and its Detectors.

[35] "P10 Properties (Calculated)." `https://www.star.bnl.gov/public/tpc/hard/tpcrings/p10_magboltz1b.html`. Accessed: 2010-09-30.

[36] "Delta Packaging International Inc. Website." `https://deltapkg.us/`. Accessed: 2019-05-01.

[37] "RGEES Website." `https://rgees.com/index.php`. Accessed: 2019-05-01.

[38] "GEODETIC website." `https://www.geodetic.com/`. Accessed: 2019-04-18.

[39] M. Kurata-Nishimura, R. Shane, A. B. McIntosh, T. Isobe, J. Barney, J. Estee, G. Jhang, W. Powell, W. G. Lynch, M. B. Tsang, T. Murakami, S. Tangwancharoen, S. J. Yenello, *et al.*, "Status of SπRIT TPC," *RIKEN Accel. Prog. Rep.*, vol. 48, p. 206, 2015.

[40] I. Söderkvist and P.-Å. Wedin, "On condition numbers and algorithms for determining a rigid body movement," *BIT Numerical Mathematics*, vol. 34, no. 3, pp. 424–436, 1994.

[41] M. Kaneko, T. Murakami, T. Isobe, M. Kurata-Nishimura, W. G. Lynch, M. B. Tsang, J. Barney, J. Estee, G. Cerizza, C. Santamaria, *et al.*, "Kyoto Multiplicity Array for the SπRIT experiment," *RIKEN Accel. Prog. Rep.*, vol. 50, p. 172, 2017.

[42] S. Callier, C. D. Taille, G. Martin-Chassard, and L. Raux, "EASIROC, an Easy & Versatile ReadOut Device for SiPM," *Physics Procedia*, vol. 37, pp. 1569–1576, 2012.

[43] P. Lasko, M. Adamczyk, J. Brzychczyk, P. Hirnyk, J. Łukasik, P. Pawłowski, K. Pelczar, A. Snoch, A. Sochocka, Z. Sosin, J. Barney, G. Cerizza, J. Estee, T. Isobe, G. Jhang, M. Kaneko, M. Kurata-Nishimura, W. Lynch, T. Murakami, C. Santamaria, M. Tsang, and Y. Zhang, "KATANA âĂŞ A charge-sensitive triggering system for the SπRIT experiment," *Nuclear Instruments and Methods in Physics Research Section A: Accelerators, Spectrometers, Detectors and Associated Equipment*, vol. 856, pp. 92 – 98, 2017.

[44] "Raspberry Pi website." `https://www.raspberrypi.org/`. Accessed: 2019-04-08.

[45] Y. Zhang, J. Barney, M. Kaneko, M. Kurata-Nishimura, P. Lasko, J. Lukasik, P. Pawlowski, Z. G. Xiao, *et al.*, "The Veto Collimator for the SπRIT TPC," *RIKEN Accel. Prog. Rep.*, vol. 50, p. 170, 2017.

[46] A. Walenta, J. Heintze, and B. SchÃijrlein, “The multiwire drift chamber a new type of proportional wire chamber,” *Nuclear Instruments and Methods*, vol. 92, no. 3, pp. 373 – 380, 1971.

[47] K. Koch, J. Hoffmann, C. Ugur, and M. Heil, “A compact readout system for the R3B High-Resolution Neutron Time-of-Flight Spectrometer (NeuLAND),” in *2014 IEEE Nuclear Science Symposium and Medical Imaging Conference (NSS/MIC)*, pp. 1–4, IEEE, 2014.

[48] I. Gasparic, K. Boretzky, H. Tonqvist, T. Aumann, L. Atar, A. Horvat, Y. Leifels, D. Rossi, H. Simon, H. Scheit, *et al.*, “NeuLAND demonstrator performance in EOS experiments,” *RIKEN Accel. Prog. Rep.*, vol. 50, p. 176, 2017.

[49] Y. Kondo, “Calibration methods of the neutron detector array NEBULA,” *RIKEN Accel. Prog. Rep*, vol. 45, p. 131, 2012.

[50] H. Baba, T. Ichihara, T. Ohnishi, S. Takeuchi, K. Yoshida, Y. Watanabe, S. Ota, and S. Shimoura, “New data acquisition system for the RIKEN Radioactive Isotope Beam Factory,” *Nuclear Instruments and Methods in Physics Research Section A: Accelerators, Spectrometers, Detectors and Associated Equipment*, vol. 616, no. 1, pp. 65 – 68, 2010.

[51] X. Grave, R. Canedo, J. F. Clavelin, S. Du, and E. Legay, “NARVAL a modular distributed data acquisition system with Ada 95 and RTAI,” in *14th IEEE-NPSS Real Time Conference, 2005.*, pp. 5 pp.–, June 2005.

[52] H. Baba, T. Ichihara, T. Ohnishi, S. Takeuchi, K. Yoshida, Y. Watanabe, S. Ota, and S. Shimoura, “Common trigger firmware for GTO,” *RIKEN Accel. Prog. Rep.*, vol. 47, p. 235, 2014.

[53] Y. Higurashi, J. Ohnishi, T. Nakagawa, H. Haba, M. Tamura, T. Aihara, M. Fujimaki, M. Komiyama, A. Uchiyama, and O. Kamigaito, “Results of RIKEN superconducting electron cyclotron resonance ion source with 28 GHz,” *Review of Scientific Instruments*, vol. 83, no. 2, p. 02A308, 2012.

[54] O. Kamigaito, M. Kase, N. Sakamoto, Y. Miyazawa, E. Ikezawa, N. Fukunishi, S. Kohara, M. Fujimaki, M. Hemmi, T. Chiba, *et al.*, “Construction of a booster linac for the RIKEN heavy-ion linac,” *Review of scientific instruments*, vol. 76, no. 1, p. 013306, 2005.

[55] Y. Yano, “Status report on RIKEN Ring Cyclotron,” 1991.

[56] N. Inabe, N. Fukunishi, A. Goto, M. Kase, H. Ryuto, N. Sakamoto, S. Yokouchi, and Y. Yano, “Fixed-frequency ring cyclotron (fRC) in RIBF,” in *proceedings of the 17rh Int. Conf. on Cyclotrons and Their Applications, Yoyogi, Tokyo*, vol. 13, 2004.

[57] J. Ohnishi, M. Fujimaki, N. Fukunishi, A. Goto, K. Ikegami, O. Kamigaito, M. Kase, K. Kumagai, M. Nagase, H. Okuno, *et al.*, “Construction status of the RIKEN intermediate-stage ring cyclotron (IRC),” in *Cyclotrons*, vol. 4, pp. 197–199, 2004.

[58] H. Okuno, J. Ohnishi, K. Yamada, N. Fukunishi, K. Ikegami, T. Maie, H. Hasebe, M. Hamanaka, M. Kase, A. Goto, and Y. Yano, “The Superconducting Ring Cyclotron in RIKEN,” *IEEE Transactions on Applied Superconductivity*, vol. 17, pp. 1063–1068, June 2007.

[59] H. Okuno, T. Fujinawa, N. Fukunishi, A. Goto, Y. Higurashi, E. Ikezawa, O. Kamigaito, M. Kase, T. Nakagawa, J. Ohnishi, Y. Sato, and Y. Yano, “Heavy ion accelerators for riken RI beam factory and upgrade plans,” *HB 2008 - 42nd ICFA Advanced Beam Dynamics Workshop on High-Intensity, High-Brightness Hadron Beams*, 01 2008.

[60] D. J. Morrissey and B. M. Sherrill, *In-Flight Separation of Projectile Fragments*, pp. 113–135. Berlin, Heidelberg: Springer Berlin Heidelberg, 2004.

[61] T. Kubo, “In-flight RI beam separator BigRIPS at RIKEN and elsewhere in Japan,” *Nuclear Instruments and Methods in Physics Research Section B: Beam Interactions with Materials and Atoms*, vol. 204, pp. 97 – 113, 2003. 14th International Conference on Electromagnetic Isotope Separators and Techniques Related to their Applications.

[62] N. Fukuda, T. Kubo, T. Ohnishi, N. Inabe, H. Takeda, D. Kameda, and H. Suzuki, “Identification and separation of radioactive isotope beams by the BigRIPS separator at the RIKEN RI Beam Factory,” *Nuclear Instruments and Methods in Physics Research Section B: Beam Interactions with Materials and Atoms*, vol. 317, pp. 323 – 332, 2013. XVIth International Conference on ElectroMagnetic Isotope Separators and Techniques Related to their Applications, December 2âĂŞ7, 2012 at Matsue, Japan.

[63] H. Kumagai, A. Ozawa, N. Fukuda, K. SÃijmmerer, and I. Tanihata, “Delay-line PPAC for high-energy light ions,” *Nuclear Instruments and Methods in Physics Research Section A: Accelerators, Spectrometers, Detectors and Associated Equipment*, vol. 470, no. 3, pp. 562 – 570, 2001.

[64] H. Blok, E. Offermann, C. D. Jager, and H. D. Vries, “Path reconstruction and resolution improvement in magnetic spectrometers,” *Nuclear Instruments and Methods in Physics Research Section A: Accelerators, Spectrometers, Detectors and Associated Equipment*, vol. 262, no. 2, pp. 291 – 297, 1987.

[65] M. Berz, K. Joh, J. A. Nolen, B. M. Sherrill, and A. F. Zeller, “Reconstructive correction of aberrations in nuclear particle spectrographs,” *Physical Review C*, vol. 47, pp. 537–544, Feb 1993.

[66] D. Bazin, J. Caggiano, B. Sherrill, J. Yurkon, and A. Zeller, “The S800 spectrograph,” *Nuclear Instruments and Methods in Physics Research Section B: Beam Interactions*

with Materials and Atoms, vol. 204, pp. 629 – 633, 2003. 14th International Conference on Electromagnetic Isotope Separators and Techniques Related to their Applications.

[67] "RIBFDAQ ANAROOT website." `https://ribf.riken.jp/RIBFDAQ/index.php?Tools%2FAnalysis%2FANAROOT`. Accessed: 2019-04-26.

[68] CAEN Electronic Instrumentation, *Technical Information Manual*, 11 2016. Rev. 14.

[69] S. Henzler, "Time-to-digital converter basics," in *Time-to-digital converters*, pp. 5–18, Springer, 2010.

[70] O. Tarasov and D. Bazin, "LISE++: Exotic beam production with fragment separators and their design," *Nuclear Instruments and Methods in Physics Research Section B: Beam Interactions with Materials and Atoms*, vol. 376, pp. 185 – 187, 2016. Proceedings of the XVIIth International Conference on Electromagnetic Isotope Separators and Related Topics (EMIS2015), Grand Rapids, MI, U.S.A., 11-15 May 2015.

[71] Y. Shimizu, T. Kobayashi, T. Kubo, N. Chiga, T. Isobe, T. Kawabata, Y. Kondo, K. Kusaka, Y. Matsuda, T. Motobayashi, T. Murakami, T. Nakamura, J. Ohnishi, T. Ohnishi, H. Okuno, H. Otsu, H. Sakurai, H. Sato, Y. Satou, K. Sekiguchi, Y. Togano, and K. Yoneda, "SAMURAI project at RIBF," *Journal of Physics: Conference Series*, vol. 312, p. 052022, September 2011.

[72] G. Jhang, J. Barney, J. Estee, T. Isobe, M. Kaneko, M. Kurata-Nishimura, G. Cerizza, C. Santamaria, J. W. Lee, P. Lasko, *et al.*, "Beam commissioning of the SπRIT time projection chamber," *Journal of the Korean Physical Society*, vol. 69, no. 2, pp. 144–151, 2016.

[73] G. Jhang, J. W. Lee, G. Cerizza, T. Isobe, M. B. Tsang, *et al.*, "SpiRITROOT: an analysis framework for SπRIT experiment," *RIKEN Accel. Prog. Rep.*, vol. 49, p. 161, 2016.

[74] M. Al-Turany, D. Bertini, R. Karabowicz, D. Kresan, P. Malzacher, T. Stockmanns, and F. Uhlig, "The FAIRROOT framework," in *Journal of Physics: Conference Series*, vol. 396, p. 022001, IOP Publishing, 2012.

[75] J. Rauch and T. Schlüter, "GENFIT - a generic track-fitting toolkit," in *Journal of Physics: Conference Series*, vol. 608, p. 012042, IOP Publishing, 2015.

[76] W. Waltenberger, W. Mitaroff, and F. Moser, "RAVE - a Detector-independent vertex reconstruction toolkit," *Nuclear Instruments and Methods in Physics Research Section A: Accelerators, Spectrometers, Detectors and Associated Equipment*, vol. 581, no. 1, pp. 549 – 552, 2007. VCI 2007.

[77] The CMS Collaboration, S. Chatrchyan, G. Hmayakyan, V. Khachatryan, A. M. Sirunyan, W. Adam, T. Bauer, T. Bergauer, H. Bergauer, M. Dragicevic, J. ErÃű, M. Friedl, R. FrÃijhwirth, V. M. Ghete, P. Glaser, C. Hartl, N. Hoermann, J. Hrubec, S. HÃďnsel, M. Jeitler, K. Kastner, M. Krammer, I. M. de Abril, M. Markytan, I. Mikulec, B. Neuherz, T. NÃűbauer, M. Oberegger, M. Padrta, M. Pernicka, P. Porth, H. Rohringer, S. Schmid, T. Schreiner, R. Stark, H. Steininger, J. Strauss, A. Taurok, D. Uhl, W. Waltenberger, G. Walzel, E. Widl, C.-E. Wulz, V. Petrov, V. Prosolovich, V. Chekhovsky, O. Dvornikov, I. Emeliantchik, A. Litomin, V. Makarenko, I. Marfin, V. Mossolov, N. Shumeiko, A. Solin, R. Stefanovitch, J. S. Gonzalez, A. Tikhonov, A. Fedorov, M. Korzhik, O. Missevitch, R. Zuyeuski, W. Beaumont, M. Cardaci, E. D. Langhe, E. A. D. Wolf, E. Delmeire, S. Ochesanu, M. Tasevsky, P. V. Mechelen, J. D'Hondt, S. D. Weirdt, O. Devroede, R. Goorens, S. Hannaert, J. Heyninck, J. Maes, M. U. Mozer, S. Tavernier, W. V. Doninck, L. V. Lancker, P. V. Mulders, I. Villella, C. Wastiels, C. Yu, O. Bouhali, O. Charaf, B. Clerbaux, P. D. Harenne, G. D. Lentdecker, J. P. Dewulf, S. Elgammal, R. Gindroz, G. H. Hammad, T. Mahmoud, L. Neukermans, M. Pins, R. Pins, S. Rugovac, J. Stefanescu, V. Sundararajan, C. V. Velde, P. Vanlaer, J. Wickens, M. Tytgat, S. Assouak, J. L. Bonnet, G. Bruno, J. Caudron, B. D. Callatay, J. D. F. D. Jeneret, S. D. Visscher, P. Demin, D. Favart, C. Felix, B. Florins, E. Forton, A. Giammanco, G. Grégoire, M. Jonckman, D. Kcira, T. Keutgen, V. Lemaitre, D. Michotte, O. Militaru, S. Ovyn, T. Pierzchala, K. Piotrzkowski, V. Roberfroid, X. Rouby, N. Schul, O. V. der Aa, N. Beliy, E. Daubie, P. Herquet, G. Alves, M. E. Pol, M. H. G. Souza, M. Vaz, D. D. J. Damiao, V. Oguri, A. Santoro, A. Sznajder, E. D. M. Gregores, R. L. Iope, S. F. Novaes, T. Tomei, T. Anguelov, G. Antchev, I. Atanasov, J. Damgov, N. Darmenov, L. Dimitrov, V. Genchev, P. Iaydjiev, A. Marinov, S. Piperov, S. Stoykova, G. Sultanov, R. Trayanov, I. Vankov, C. Cheshkov, A. Dimitrov, M. Dyulendarova, I. Glushkov, V. Kozhuharov, L. Litov, M. Makariev, E. Marinova, S. Markov, M. Mateev, I. Nasteva, B. Pavlov, P. Petev, P. Petkov, V. Spassov, Z. Toteva, V. Velev, V. Verguilov, J. G. Bian, G. M. Chen, H. S. Chen, M. Chen, C. H. Jiang, B. Liu, X. Y. Shen, H. S. Sun, J. Tao, J. Wang, M. Yang, Z. Zhang, W. R. Zhao, H. L. Zhuang, Y. Ban, J. Cai, Y. C. Ge, S. Liu, H. T. Liu, L. Liu, S. J. Qian, Q. Wang, Z. H. Xue, Z. C. Yang, Y. L. Ye, J. Ying, P. J. Li, J. Liao, Z. L. Xue, D. S. Yan, H. Yuan, C. A. C. Montoya, J. C. Sanabria, N. Godinovic, I. Puljak, I. Soric, Z. Antunovic, M. Dzelalija, K. Marasovic, V. Brigljevic, K. Kadija, S. Morovic, R. Fereos, C. Nicolaou, A. Papadakis, F. Ptochos, P. A. Razis, D. Tsiakkouri, Z. Zinonos, A. Hektor, M. Kadastik, K. Kannike, E. Lippmaa, M. MÃijntel, M. Raidal, L. Rebane, P. A. Aarnio, E. Anttila, K. Banzuzi, P. Bulteau, S. Czellar, N. Eiden, C. Eklund, P. Engstrom, A. Heikkinen, A. Honkanen, J. HÃďrkÃűnen, V. KarimÃďki, H. M. Katajisto, R. Kinnunen, J. Klem, J. Kortesmaa, M. KotamÃďki, A. Kuronen, T. Lampén, K. Lassila-Perini, V. Lefébure, S. Lehti, T. Lindén, P. R. Luukka, S. Michal, F. M. Brigido, T. MÃďenpÃďÃď, T. Nyman, J. Nystén, E. Pietarinen, K. Skog, K. Tammi, E. Tuominen, J. Tuominiemi, D. Ungaro, T. P. Vanhala, L. Wendland, C. Williams, M. Iskanius, A. Korpela, G. Polese, T. Tuuva, G. Bassompierre, A. Bazan, P. Y. David, J. Ditta, G. Drobychev, N. Fouque, J. P. Guillaud, V. Hermel, A. Karneyeu, T. L. Flour, S. Lieunard, M. Maire, P. Mendiburu, P. Nedelec, J. P. Peigneux, M. Schneegans, D. Sillou, J. P. Vialle, M. Anfreville, J. P. Bard, P. Besson, E. Bougamont, M. Boyer,

P. Bredy, R. Chipaux, M. Dejardin, D. Denegri, J. Descamps, B. Fabbro, J. L. Faure, S. Ganjour, F. X. Gentit, A. Givernaud, P. Gras, G. H. de Monchenault, P. Jarry, C. Jeanney, F. Kircher, M. C. Lemaire, Y. Lemoigne, B. Levesy, E. Locci, J. P. Lottin, I. Mandjavidze, M. Mur, J. P. Pansart, A. Payn, J. Rander, J. M. Reymond, J. Rolquin, F. Rondeaux, A. Rosowsky, J. Y. A. Rousse, Z. H. Sun, J. Tartas, A. V. Lysebetten, P. Venault, P. Verrecchia, M. Anduze, J. Badier, S. Baffioni, M. Bercher, C. Bernet, U. Berthon, J. Bourotte, A. Busata, P. Busson, M. Cerutti, D. Chamont, C. Charlot, C. Collard, A. Debraine, D. Decotigny, L. Dobrzynski, O. Ferreira, Y. Geerebaert, J. Gilly, C. Gregory, L. G. Riveros, M. Haguenauer, A. Karar, B. Koblitz, D. Lecouturier, A. Mathieu, G. Milleret, P. Miné, P. Paganini, P. Poilleux, N. Pukhaeva, N. Regnault, T. Romanteau, I. Semeniouk, Y. Sirois, C. Thiebaux, J. C. Vanel, A. Zabi, J. L. Agram, A. Albert, L. Anckenmann, J. Andrea, F. Anstotz, A. M. Bergdolt, J. D. Berst, R. Blaes, D. Bloch, J. M. Brom, J. Cailleret, F. Charles, E. Christophel, G. Claus, J. Coffin, C. Colledani, J. Croix, E. Dangelser, N. Dick, F. Didierjean, F. Drouhin, W. Dulinski, J. P. Ernenwein,, "The CMS experiment at the CERN LHC," *Journal of Instrumentation*, vol. 3, pp. S08004–S08004, aug 2008.

[78] C. Adler, Z. Ahammed, C. Allgower, J. Amonett, B. Anderson, M. Anderson, G. Averichev, J. Balewski, O. Barannikova, L. Barnby, *et al.*, "Azimuthal anisotropy and correlations in the hard scattering regime at RHIC," *Physical Review Letters*, vol. 90, no. 3, p. 032301, 2003.

[79] S. Agostinelli, J. Allison, K. Amako, J. Apostolakis, H. Araujo, P. Arce, M. Asai, D. Axen, S. Banerjee, G. Barrand, F. Behner, L. Bellagamba, J. Boudreau, L. Broglia, A. Brunengo, H. Burkhardt, S. Chauvie, J. Chuma, R. Chytracek, G. Cooperman, G. Cosmo, P. Degtyarenko, A. Dell'Acqua, G. Depaola, D. Dietrich, R. Enami, A. Feliciello, C. Ferguson, H. Fesefeldt, G. Folger, F. Foppiano, A. Forti, S. Garelli, S. Giani, R. Giannitrapani, D. Gibin, J. G. Cadenas, I. GonzÃąlez, G. G. Abril, G. Greeniaus, W. Greiner, V. Grichine, A. Grossheim, S. Guatelli, P. Gumplinger, R. Hamatsu, K. Hashimoto, H. Hasui, A. Heikkinen, A. Howard, V. Ivanchenko, A. Johnson, F. Jones, J. Kallenbach, N. Kanaya, M. Kawabata, Y. Kawabata, M. Kawaguti, S. Kelner, P. Kent, A. Kimura, T. Kodama, R. Kokoulin, M. Kossov, H. Kurashige, E. Lamanna, T. LampÃľn, V. Lara, V. Lefebure, F. Lei, M. Liendl, W. Lockman, F. Longo, S. Magni, M. Maire, E. Medernach, K. Minamimoto, P. M. de Freitas, Y. Morita, K. Murakami, M. Nagamatu, R. Nartallo, P. Nieminen, T. Nishimura, K. Ohtsubo, M. Okamura, S. O'Neale, Y. Oohata, K. Paech, J. Perl, A. Pfeiffer, M. Pia, F. Ranjard, A. Rybin, S. Sadilov, E. D. Salvo, G. Santin, T. Sasaki, N. Savvas, Y. Sawada, S. Scherer, S. Sei, V. Sirotenko, D. Smith, N. Starkov, H. Stoecker, J. Sulkimo, M. Takahata, S. Tanaka, E. Tcherniaev, E. S. Tehrani, M. Tropeano, P. Truscott, H. Uno, L. Urban, P. Urban, M. Verderi, A. Walkden, W. Wander, H. Weber, J. Wellisch, T. Wenaus, D. Williams, D. Wright, T. Yamada, H. Yoshida, and D. Zschiesche, "GEANT4 - a simulation toolkit," *Nuclear Instruments and Methods in Physics Research Section A: Accelerators, Spectrometers, Detectors and Associated Equipment*, vol. 506, no. 3, pp. 250 – 303, 2003.

[80] W. Reisdorf, M. Stockmeier, A. Andronic, M. Benabderrahmane, O. Hartmann, N. Her-

rmann, K. Hildenbrand, Y. Kim, M. Kiš, P. Koczoń, *et al.*, “Systematics of pion emission in heavy ion collisions in the 1AGeV regime,” *Nuclear Physics A*, vol. 781, no. 3-4, pp. 459–508, 2007.